MULTISCALE PHYSICS-BASED MODELING OF FRICTION

BY

MELIH ERITEN

DISSERTATION

Submitted in partial fulfillment of the requirements
for the degree of Doctor of Philosophy in Mechanical Engineering
in the Graduate College of the
University of Illinois at Urbana-Champaign, 2012

Urbana, Illinois

Doctoral Committee:

Professor Andreas A. Polycarpou, Chair and Director of Research
Professor Lawrence A. Bergman
Professor Harley T. Johnson
Professor Arif Masud
Professor Alexander F. Vakakis

ABSTRACT

Frictional contacts between solids exist in nature and in a wide range of engineering applications. Friction causes energy loss, and it is the main source of wear and surface degradation which limits the lifetime of mechanical systems. Yet, friction is needed to walk, run, accelerate, slow down or stop moving systems. Whether desirable or not, friction is a very complex physical phenomenon. The behavior of systems with friction is nonlinear, and the physical mechanisms governing friction behavior span a wide range of spatial and temporal scales. A thorough study of friction should employ experimentalists and theoreticians in chemistry, materials science, tribology, mechanics, dynamics, and structural engineering. High spatial and temporal resolutions are required to capture and model essential physics of a frictional contact. However, such a detailed model is impractical in large-scale structural dynamics simulations; especially since frictional contacts can be numerous in a given application. Reduced-order models (ROMs) achieve broader applicability by compromising several aspects and accounting for the important physics. Hence, rather simple Coulomb friction is still the most ubiquitous model in the modeling and simulation literature. As an alternative, a reduced-order friction model built-up from micromechanics of surfaces is proposed in this work. Continuum-scale formulation of pre-sliding friction behavior is combined with material-strength-based friction coefficients to develop a physics-based friction model at asperity-scale. Then, the statistical summation technique is utilized to build a multiscale modeling framework. A novel joint fretting setup is designed for friction experiments in a practical setting, and the developed models are tested. Both asperity and rough surface friction models show good agreement with experimental data. The influences of materials, surface roughness and contact contamination on the friction are also studied. Finally, the developed models are incorporated in to a simple dynamical system to illustrate broader applicability. The models proposed in this work account for loading-history dependence, partial slip, gross slip, nonlinear stiffness and energy dissipation characteristics of frictional contacts. In doing so, the models require no curve-fit or look-up parameters. Instead, the formulations are developed from continuum mechanics, and the required parameters can be determined from simple tension/compression and surface roughness tests. In this sense, the developed models are physics-based and predictive. The parameters employed in the models depend on the contact conditions, surface roughness and material properties. For instance, the developed models use a dry-contact formulation at asperity-scale, and the macroscale friction predictions are tested only for dry contacts. However, the multiscale modeling approach can be applied to model the effect of lubrication provided that asperity-scale contact accounts for it. Besides, frictional contacts of certain materials exhibit severe adhesion, cold welding and galling behavior as demonstrated experimentally in this work. If these behaviors are modeled at asperity-scale, then the friction at rough contact scale can be obtained by the same procedure presented in this work. This flexibility is another significant advantage of the proposed modeling approach.

To my parents and wife

ACKNOWLEDGMENTS

This dissertation can be considered as the product of combined efforts provided by many people surrounding me. My advisors, Professor Andreas A. Polycarpou and Lawrence A. Bergman, guided me through essential steps of my doctoral research, read and edited nearly all of my written work. Their insight and experience assisted me mature as a researcher and academician. My committee members, Professor Arif Masud, Harley T. Johnson, and Alexander F. Vakakis provided guidance and support throughout my doctoral study. Visiting Professor Diana Lopez of National University of Colombia also agreed to serve in my committee and discussing research with all of my committee members was one of my favorites in this process. I owe very special thanks to the undergraduate and graduate students who helped me at different stages of this study. Without Luke Jungles, Joel Park, David Petlicki, Seung-min Yeo, and Antonis Vakis, this dissertation would cover half of what it covers now.

I am also grateful to the Departments of Mechanical Science and Engineering and Aerospace Engineering for offering me research and teaching assistantships. Most of my doctoral work was supported by the National Science Foundation under Grant CMMI 08-00208 and Sandia National Laboratories. I would also like to recognize the generous contributions of the Eugene and Lina Abraham Scholarship and Mavis Future Faculty Fellowship programs.

Boundless amount of thanks are due to my parents and wife to whom this dissertation is dedicated to, my sister, and numerous friends who tolerated, trusted and loved me during this difficult time period. Lastly, I would like to express my deepest gratitude to my uncles, *Müfit* and *Mete*, who not only has been encouraging me from my childhood on but also delivering continuous support through my mistakes and failures.

Table of Contents

List of Figures.....vii

List of Tables.....x

List of Symbols.....xi

CHAPTER 1: INTRODUCTION 1

1.1. Background 1

1.2. Motivation for a Multiscale Physics-based Friction Model 6

1.3. Outline of the Thesis 6

1.4. Figures 9

CHAPTER 2: MODELING APPROACH 10

2.1. Spherical (Asperity-scale) Contact 10

2.2. Material Strength vs. Sliding Inception 14

2.3. Multiscale Modeling: Asperity to Rough Surface Scale Contacts 17

2.4. Figures 19

CHAPTER 3: ASPERITY-SCALE FRICTION MODEL 21

3.1. Introduction 21

3.2. Spherical Contact 23

3.3. Proposed Model 34

3.4. Results 36

3.5. Comparison with Experiments and FEA 37

3.6. Conclusion 43

3.7. Figures 45

3.8. Tables 55

CHAPTER 4: MACROSCALE FRICTION MODEL 57

4.1. Introduction 57

4.2. Review of Utilized Models 59

4.3. Proposed Friction Model 65

4.4. Conclusion 70

4.5. Figures 72

4.6. Tables 79

CHAPTER 5: EXPERIMENTAL VALIDATION 80

5.1. Introduction 80

5.2. Review of Existing Setups and Limitations 83
5.3. Instrumentation 86
5.4. Calibration Experiments 90
5.5. Macroscale Friction Model vs. Experiments 98
5.6. Conclusion 105
5.7. Figures 107
5.8. Tables 114
CHAPTER 6: INFLUENCE OF ROUGHNESS & LUBRICATION 116
6.1. Introduction 116
6.2. Experimental Details 118
6.3. Results 122
6.4. Discussion 129
6.5. Conclusion 130
6.6. Figures 132
6.7. Tables 146
CHAPTER 7: APPLICATION OF THE FRICTION MODEL TO A SIMPLE DYNAMICAL SYSTEM 148
7.1. Introduction 148
7.2. Dynamical System 149
7.3. Friction Models 150
7.4. Results 154
7.5. Comparison 159
7.6. Conclusion 159
7.7. Figures 160
7.8. Tables 165
CHAPTER 8: CONCLUSIONS AND FUTURE WORK 167
REFERENCES 171
Appendix A 178
Appendix B 181
B.1. Normal Contact of Single (Spherical) Asperities 181
B.2. Tangential Contact of Single (Spherical) Asperities 182

List of Figures

Fig. 1.1. Multiscale modeling approach followed in the dissertation 9
Fig. 2.1. Spherical contact under partial slip contact 19
Fig. 2.2. Loading history for cyclic tangential loading of the spherical contact (a) and corresponding shear tractions (b) 19
Fig. 2.3. Load-displacement relations for monotonic (a) and cyclic (b) loading 20
Fig. 3.1. Spheres in contact under combined normal and tangential loading (a) and schematic of a typical loading history (b). The contact occurs in a circle of radius a and the stick region constitutes the core region of that contact with radius c. 45
Fig. 3.2. Dimensionless normal load vs interference for Hertz (elastic, frictionless); CEB and KE (elastic-plastic, perfect slip) and BKE (elastic-plastic, full stick) models. 46
Fig. 3.3. Fretting loops for spherical contacts under combined normal and tangential loading (purely elastic Cattaneo-Mindlin solution: dashed; fully plastic Ödfalk and Vingsbo model: dotted and Elastic-plastic model:solid line). 47
Fig. 3.4. Friction coefficient for CFC, CEB, KE and BKE models vs nondimensional normal penetration 48
Fig. 3.5. The flow of computation to obtain the proposed partial slip responses. 49
Fig. 3.6. Normalized tangential load vs. displacement obtained by the proposed models up to the onset of sliding. 50
Fig. 3.7. Fretting loops obtained by the proposed models. 51
Fig. 3.8. Energy dissipation vs maximum imposed tangential displacement for each partial slip model 51
Fig. 3.9. Comparison of the proposed models and micro-scale experiment 1 (a) and experiment 2 (b). 52
Fig. 3.10. Comparison of the proposed models and nano-scale experiment 1 (a) and experiment 2 (b). 53
Fig. 3.11. Dimensionless tangential load vs. dimensionless tangential displacement predicted by BKE model for different normal preloads. FEA results reproduced from Brizmer et al. [50]. 54
Fig. 4.1. Schematic representation of an equivalent rough surface and a rigid flat contact and, probability density function for asperity heights. 72
Fig. 4.2. Asperity behavior in statistical rough contact in relation to different regions of the probability density function of the asperity heights: a) loading, b) unloading. 73
Fig. 4.3. Computational flow chart for obtaining the fretting response for nominally flat rough surfaces using the advanced physics-based interfacial models and equations used at each step. 74
Fig. 4.4. Modeled results of fretting loops obtained from four different models under elastic contact conditions, $\psi = 0.5$). 75
Fig. 4.5. Modeled results of fretting loops obtained from different models under elastic-plastic contact conditions, $\psi = 1.0$). 76
Fig. 4.6. Modeled results of fretting loops obtained from different models under severe plastic contact conditions, $\psi = 2.0$). 77
Fig. 4.7. Modeled results of energy loss per cycle obtained from different models and different plasticity indices 78
Fig. 5.1. Schematic of the developed joint fretting apparatus 107
Fig. 5.2. Photographs of the developed joint fretting apparatus: (a) overall view, (b) close-up view of the joint halves 107
Fig. 5.3. Aluminum joint samples: a) monolithic, b) 1-bolt 108

Fig. 5.4. Typical force measurements from 1-bolt steel joint in three orthogonal directions: x (shear), y (normal to the joint interface) and z (orthogonal to x and y directions) under; (a) preload of 99 N and imposed tangential displacement of 9 μm, (b) preload of 993 N and imposed tangential displacement of 36 μm. 108
Fig. 5.5. Imposed, Δ_x; transmitted, δ_x and load cell, δ_{LC} displacements in the tangential direction for the 1-bolt aluminum sample under: (a) low preload ($F_p = 99\ N$), (b) high preload ($F_p = 993\ N$) 109
Fig. 5.6. Fretting loops with imposed and transmitted tangential displacements 109
Fig. 5.7. A 1DOF representation of the experimental apparatus 110
Fig. 5.8. Energy losses per fretting cycles (1-3-5-7-9th cycles) obtained from the monolithic and 1-bolt aluminum joints under different loading conditions 110
Fig. 5.9. Experimental fretting loops from bolted steel joint and the BKE model under different preloads 111
Fig. 5.10. Finite element analysis of the joint preloading: a) Meshed ABAQUS model of the joint, b) pressure between the bolt head and the upper joint surface, pbolt, and c) pressure over the contact interface between the two sides of the joint, pcon. Pressure values are normalized to the mean pressure observed between the bolt head and the upper joint surface. 112
Fig. 5.11. Energy losses per cycle obtained from 10 cycles of fretting experiments (box-plots) and prediction of BKE model (thick circles) 113
Fig. 6.1. Schematic of a typical fretting loop showing critical joint parameters. 132
Fig. 6.2. (a) Photograph of the smooth steel joint sample and (b) technical drawing (dimensions in mm) of the PZT half of the smooth steel joints. All joints are identical in geometry but have different surface roughness. 132
Fig. 6.3. Surface heights obtained from profile measurements of smooth and rough a) aluminum and b) steel joints. 133
Fig. 6.4. Imposed tangential displacement (PZT tip displacement) given in Eq.5.3. 133
Fig. 6.5. Average fretting loops obtained from the smooth aluminum and steel joint samples under various loading and dry conditions. 134
Fig. 6.6. Average fretting loops obtained from the rough aluminum and steel joint samples under various loading and dry conditions. 135
Fig. 6.7. SEM images of aluminum samples after dry fretting experiments. Arrows show typical machining marks and circled areas show mild galling. 136
Fig. 6.8. SEM images of steel samples after fretting experiments. Arrows indicate typical machining marks. 137
Fig. 6.9. Average fretting loops obtained from the smooth aluminum and steel joint samples under various loading and boundary/mixed lubricated contact conditions. 138
Fig. 6.10. Average fretting loops obtained from the rough aluminum and steel joint samples under various loading and boundary/mixed lubricated contact conditions. 139
Fig. 6.11. Tangential joint stiffness values for aluminum and steel joints under various loading and contact conditions. 140
Fig. 6.12. Energy dissipation per fretting cycle versus maximum tangential force for aluminum and steel joint samples (0.192 Nm bolt torque). 141
Fig. 6.13. Energy dissipation per fretting cycle versus maximum tangential force for aluminum and steel joint samples (0.305 Nm bolt torque). 142

Fig. 6.14. Energy dissipation per fretting cycle versus maximum tangential force for aluminum and steel joint samples (0.418 Nm bolt torque). 143
Fig. 6.15. Comparison between model predictions (Chapter 4) and experiments with the smooth joint samples under dry contact conditions. 144
Fig. 6.16. Comparison between model predictions (Chapter 4) and experiments with the rough joint samples under dry contact conditions. 145
Fig. 7.1. Single degree-of-freedom dynamical system with friction 160
Fig. 7.2. Multiscale modeling approach proposed by Bjorklund [78] 160
Fig. 7.3. Power spectra of the impulse response of the mass with Coulomb and Dankowicz friction models (no friction case is given for reference) 161
Fig. 7.4. Power spectra of the impulse response of the mass with EPB friction applied to rough and smooth surfaces (no friction case is given for reference) 161
Fig. 7.5. Ramp response of the mass-spring-damper system with different friction models, and soft and hard structural stiffness 162
Fig. 7.6. Phase-portraits of the steady-state harmonic response of the mass with the Coulomb (a) and Dankowicz (b) friction models, and the corresponding friction forces as a function of position, c) and d), respectively. 163
Fig. 7.7. Phase-portraits of the steady-state harmonic response of the mass with the EPB friction model using smooth (a) and rough (b) contact parameters, and the corresponding friction forces as a function of position, c) and d), respectively. 164

List of Tables

Table 3.1. Mechanical properties and geometry of contacting materials used in micro-scale experiments documented in Varenberg et al. [71]. Combined values are listed for reference to calculations done in this chapter. 55
Table 3.2. Model parameters derived from the micro-scale experiments documented in Varenberg et al. [71]. 55
Table 3.3. Mechanical properties and geometry of contacting materials used in nano-scale experiments documented in Varenberg et al. [71]. Combined values are listed for reference to calculations done in this chapter. 55
Table 3.4. Model parameters derived from the nano-scale experiments documented in Varenberg et al. [71]. 56
Table 4.1. Friction coefficients predicted by each model at different plasticity indices 79
Table 5.1. Design requirements for joint fretting apparatus 114
Table 5.2. Torque input on the bolt and corresponding preload obtained from Eq. (5.2) 114
Table 5.3. Chemical composition and mechanical properties of the materials used in joints 114
Table 5.4. Surface roughness properties of the individual and combined joint samples (PZT and load cell halves) 115
Table 5.5. Torque input on the bolt and corresponding preload obtained from Eq. (5.2) 115
Table 5.6. PZT actuator tip motion, maximum tangential displacement measured at the PZT half of the joint, and friction coefficient values measured from the fretting loops 115
Table 6.1. Chemical composition and mechanical properties of the aluminum and steel alloys. 146
Table 6.2. Roughness parameters for each joint half (PZT and load cell (LC) halves) as well as for the equivalent surface (Comb.) before and after fretting experiments. 146
Table 6.3. Bolt torque values used in the experiments, and corresponding normal preloads and mean pressures 147
Table 6.4. Average friction coefficient values for dry and lubricated contact conditions. 147
Table 7.1. Base excitation and corresponding equation of motion in non-dimensional form 165
Table 7.2. Parameters used in simulations 165
Table 7.3. Comparison table for the friction models studied (*Only with velocity-dependent parameters) 166

List of Symbols

Chapter 4

- *Asperity-level*

$v_{1,2}$ Poisson's ratios of contacting materials
$E_{1,2}$ Young's moduli of contacting materials
E^* Combined Young's modulus
$G_{1,2}$ Shear moduli of contacting materials
G^* Combined shear modulus
K Hardness factor
s Shear strength
H Hardness of softer material
$R_{1,2}$ Radii of contacting spheres
R Combined radius
P Normal contact force
ω Penetration
a Contact radius
Q Tangential force
δ Tangential displacement
μ Friction coefficient
ΔW Energy dissipated per fretting cycle
Subscripts "c" and "max" denotes critical and maximum parameter values, respectively

- *Dimensionless values*

$$\tilde{Q} = Q/(\mu P)$$

$$\tilde{\delta} = 16G^* a\delta/(3\mu P)$$

$$\Delta\tilde{W} = \frac{10G^* a}{9(\mu P)^2}\Delta W$$

$$z^* = z/\sigma_s$$

$$d^* = d/\sigma_s$$

$$\delta^* = \delta/\sigma_s$$

$$Q_{flat}^{*l}(\delta^*;\lambda) = \frac{Q_{flat}^{l}}{KHA_0}$$

$$Q_{flat}^{*unl}(\delta^*;\lambda) = \frac{Q_{flat}^{unl}}{KHA_0}$$

- *Flat rough surfaces*

z_i Height of asperity "i" measured from the mean of asperity heights
d Separation between the mean of asperity heights and the rigid flat
A_0 Nominal contact area

η	Areal density of asperities
$\phi(z)$	Probability density function of asperity heights
σ_a	Standard deviation of asperity heights
σ_s	Standard deviation of surface heights
β	Roughness parameter
ψ	Plasticity index
$z_{1,2}$	Limiting heights for tangential response of contacting asperities
λ	Parameter set for tangential force formulation
P_{flat}	Normal force
Q_{flat}^{l}	Tangential force under loading
Q_{flat}^{unl}	Tangential force under unloading
Q_{flat}^{rel}	Tangential force under reloading
W_{flat}^{*}	Energy loss per fretting cycle

- *Experiments*

Tin	Input torque on the bolts
k	Nut factor
D	nominal diameter of the bolts
p_{mean}	Mean pressure on the jointed interface
Δ_x	PZT tip displacement
A	Loading rate of the ramp signal
f	Frequency of the harmonic signal
θ	Adhesion parameter
$\Delta\gamma$	Work of adhesion

Chapter 7

m	Mass
k	Stiffness
c	Damping Coefficient
μ	Friction Coefficient
k_{tan}	Slope of Coulomb Friction Model
F_{max}	Friction Force at Gross Sliding
P	Normal Load
d	Separation btw. Mean of Asperity Heights and Rigid Flat
x(t)	Vibrations of the Joint Interface
y(t)	External Structural Vibrations
A	Amp. of External Vibrations
f	Freq. of External Vibrations
δ	Maximum Microslip
E(G*)*	Combined Young's (Shear) Modulus for Contacting Materials
υ	Poisson's Ratio of the Softer Material
H	Hardness of the Softer Material
σ_{rms}	Root-mean-square Roughness
R	Mean Asperity Tip Radius

η	Areal Density of Asperities
A_0	Nominal Contact Area
z	Asperity Heights
$\phi(z)$	Probability Density Function of Asperity Heights

CHAPTER 1: INTRODUCTION

1.1. Background

Frictional contacts between solids exist in nature and in a wide range of engineering applications. Frictional sliding of tectonic plates along a fault causes earthquakes; tribo-electrical frictional contact of clouds results in lightning; and high-friction force between a gecko's feet and a surface enables it to scamper along ceilings. An incomplete list of engineering applications where frictional contacts constitute a critical aspect includes turbine blade joints, electric motor drives, wheel/rail contact in mass transit systems, machine tool/work piece systems, bolted and riveted joints in assembled structures, bow-string interaction in a violin, and brake systems. Frictional contacts cause energy loss; therefore, energy needed for material processing and driving electric motors and mass transit systems increases significantly. Friction is the main source of wear and surface degradation, which limit the lifetime of mechanical systems. Increasing surface to volume ratio in micro/nanomechanical systems intensifies the hazardous effects of friction and causes serious performance and reliability issues. Frictional losses account for up to 1.6 % of the GDP of developed countries [1]. In contrast, friction is needed to walk, run, accelerate, slow down or stop moving systems. Many string instruments use stick-slip vibrations caused by friction to generate sound. Besides, frictional contacts behave as shock absorbers and damp out severe vibrations in assembled structures, electric motor drives and turbine blade joints.

Whether desirable or not, friction is an important and very complex physical phenomenon. The behavior of system with friction is nonlinear, and the physical mechanisms involved span a wide range of spatial and temporal scales. A thorough study of friction should employ experimentalists and theoreticians in chemistry, materials science, tribology, mechanics, dynamics, and structural engineering. This nonlinear, multiscale and multidisciplinary nature limits the current understanding of friction. High spatial and temporal resolutions are required to capture and model essential physics of a frictional contact.

However, such a detailed model lacks practicality; especially since frictional contacts are numerous in a given application. Reduced-order models (ROMs) achieve broader applicability by compromising several aspects and accounting for the important physics. Reduced-order models can be classified in two categories: phenomenological and physics-based models. The former class of models utilizes experimental observations of tangential force and relative displacement between contacting bodies to describe global friction behavior. Phenomenological models show great variability due to the nonlinear and complex nature of friction. In addition, such models depend heavily on experimental conditions and, thus, they lack predictive capability and are difficult to generalize. In contrast, physics-based friction models study essential aspects of interface chemistry, mechanics and material properties, and develop a global behavior of friction from the local physics. Due to the multiscale nature of friction, physics-based models can span length scales from nanometer to meter, and time scales from microseconds to minutes. Therefore, developing a reduced-order friction model from interface physics is a challenging task.

There exist numerous phenomenological models for friction contacts. Coulomb friction is the most commonly-used phenomenological description of friction. This model in its original version quantifies the friction force acting on the surfaces while sliding against each other as a constant proportion of the normal contact force. The proportionality constant is referred to as the friction coefficient [2]. The Coulomb friction coefficient has no physical meaning other than being the tangential force normalized to normal contact force. Friction coefficients measured from various experiments are tabulated in many resources, yet with significant variability. Besides, the need for determining a friction coefficient value a priori degrades the predictive capability of the Coulomb model. When a tangential load is applied to the contact, elastic-plastic deformations and slip occur over the contact patch, and these physical events affect the frictional behavior [3,4]. None of these pre-sliding physics is modeled in the Coulomb friction model. To remedy these drawbacks, state-space-based dynamic friction models are proposed. To list a few of such models: Dahl [5], LuGre [6], and Dankowicz [7] treat the frictional interface as the contact of numerous surface irregularities called asperities, and assume an internal state variable to track the average

deformation of these asperities. Since the parameterization for the average deformation is achieved by experimental observations, this modeling approach is also phenomenological. Regularization of the Coulomb friction model [8] and elasto-slip models (Iwan Beam Elements [9]) using discrete stick-slip elements assumes an empirical friction coefficient and limiting friction force, and therefore, compromises the physical basis. The model proposed by Valanis [10] is physics-based for endochronic plasticity, but when it is applied to frictional contact problem, the modeling parameters lose their physical meaning.

Physics-based reduced-order friction models use constitutive approaches relating stress and strain fields, and the parameters employed can be extracted from the basic or fundamental behavior of materials. In the 1950s, Bowden and Tabor [11] attempted the first physics-based friction description. Initially, they observed that the real area of contact occurring at asperity tips corresponds to a few percent of the nominal contact area. Then, they defined friction coefficient of a junction at asperity scale as the ratio of materials' shear strength and hardness. The assumption that material strength under normal and tangential loading is decoupled was the main deficiency of this model. In the last three decades, there were numerous attempts at remedying this deficiency: by analytical studies of elastic-plastic spherical contacts [12–14] or by finite element analyses under various contact conditions [15–18]. The final product of these attempts is a material-strength-based description of sliding inception at continuum scale [11]. Some relate the sliding inception to fracture of the junction and some to softening behavior due to increasing plastic deformation. The last two decades or so have seen growing numbers of attempts at explaining the sliding inception at asperity-scale by the effects of chemistry (atomistics, [19,20]) and inelastic deformation due to dislocation glide (discrete dislocation dynamics, [21–23]). Note that the physics-based friction modeling at asperity-scale spans a wide scale of lengths (nanometer to 100 microns) and relates the sliding inception (maximum friction force/displacement) to fundamental surface and material properties such as hydrocarbons trapped on the contact surface, densities of dislocation sources and obstacles, yield strength and hardness. The most critical challenge awaiting researchers in applying this modeling approach to engineered surfaces is experimental validation. Modeling and simulation tools are being

developed to explain friction force at asperity-scale, but developments in reliable experimental instrumentation for testing such models are still at an early stage.

The approach of relating friction coefficient or sliding inception with material strength at the asperity-scale still does not explain pre-sliding behavior. Cattaneo [3] and Mindlin [4] independently studied the elastic contact of spheres under normal and tangential loading, and formulated the pre-sliding behavior for an asperity junction. Their analysis of fully-adhered contact showed that the tangential tractions over the contact edges tend to infinity, and thus there must be a stress-relaxation mechanism. They both assigned local slippage emanating from the contact edges and showed that this mechanism ensures the necessary stress-relaxation. This contact condition, where the middle part of the contact patch fully adheres and the surrounding part towards the contact edges slips is referred to as partial slip. Partial slip results in local deformations and a nonlinear increase in friction force before gross sliding occurs. This force-deformation relation resembles a softening spring behavior. The Cattaneo-Mindlin solution assumed fully elastic normal contact (first solved by Hertz) and Coulomb friction for the local slippage along the contact edges (shear traction is proportional to the normal traction through a constant friction coefficient). Constant friction coefficient assumption at asperity-scale holds better than macroscale contacts, but the elasticity assumption is barely true when two asperities contact each other. The localized nature of the contact results in stress concentrations and, thus, plastic deformations are inevitable [2]. Many researchers extended the elastic Hertzian solution to elastic-plastic normal loading [24,25] and Odfalk and Vingsbo [26] introduced plasticity to the tangential loading response. Practically, when two surfaces are brought into contact, the loading on the contact is in an arbitrary direction, and thus repeated loading and unloading is expected to occur in both normal and tangential directions. Cyclic loading in the normal direction results in immediate plastic deformations for the first few cycles, and the contact area at the asperity tips increases (junction growth), and the mean contact pressure drops to values within the elastic limits. The same argument is true for the tangential loading case, where cyclic loading in the tangential direction triggers plastic flow for a few cycles and then the contact becomes fully elastic again

[27]. Therefore, understanding elastic contact with junction growth in normal loading is sufficient to study steady contact behavior at asperity scale.

One of the major limitations of physics-based friction models is the difficulty in developing a bottom-up multiscale model for macroscale contacts. At asperity-scale (10 nm – 100 microns), the boundaries and conditions of contact are well-defined and controlled. However, the nature of the engineered surfaces at the macroscale becomes uncertain with random distributions of surface asperities, contamination of the contact, and changing material properties over multilayers (oxides, work-hardened, etc.) [28]. There are three main approaches to extend asperity-scale contact formulations to macroscale, multiasperity contacts: i) statistical summation, ii) fractal characterization and iii) discrete models. Statistical summation uses distribution of asperity heights over the nominal contact area to add the contributions of individual asperities [29]. In this approach, asperity-scale contacts are assumed not to interact with each other, and the surfaces are isotropic. Height distribution and related parameters are obtained through surface roughness measurements. Though defined by international standards, roughness measurements and parameters extracted vary with changing measurement length, instrument resolution and post-processing. Besides, superposition of stress-strain fields under elastic-plastic contact conditions is not physical, but more of an empirical practice inherently assuming isolated localized asperity contacts surrounded by a large elastic material (substrate). Fractal characterization of the surface roughness remedies the problems associated with the sampling length and instrument resolution; however, the filtering for parameter extraction is still arbitrary, and reduces the physical basis of those models [30]. However, both statistical summation and fractal models provide a simple and modular technique to bridge length scales between asperities and macroscale frictional contacts. A more direct way is to model actual asperities either as discrete contact patches [31] or in a finite element framework [32]. This approach defeats the purpose of reduced-order modeling, especially since a large nominal area can contain millions of asperities to model. Next, an example justifying the immediate need for a physics-based reduced-order friction model is presented.

1.2. Motivation for a Multiscale Physics-based Friction Model

A practical and reliable friction model should be as simple as possible while capturing most of the interfacial physics. Discrete multiscale models would satisfy the second criterion especially with the significant enhancement of computational capabilities, yet would still fail practically. To illustrate this point, let us take a lap joint with 10 x17 mm nominal contact area (identical to the joints used in the experiments presented in this work). When checked under a scanning electron microscope, fine details of asperities at length scales of tens of microns can be observed. Regular cutting and milling processes would produce root-mean-square (rms) roughness on the order of a few microns if no special surface treatment is employed. When the two sides of this lap joint are bolted together and oscillated in the tangential direction, the contact patch at the asperity tips would be on the order of a few microns, and partial slip along the contact edges would vary between a few percent of the contact radius due to large clamping loads used in practice. Therefore, for a mesh to capture the fine details of partial slip contact at asperity-scale, the maximum element size should be smaller than a few percent of a few microns; i.e., less than 100 nm. The localized stress and strain fields are encapsulated within a depth of approximately the length of the contact patch; therefore, the fine meshing should at least continue for a material segment of a rectangular prism with sides 10 mm x 17 mm and depth of a few microns. That already necessitates tens of billions of elements. Considering that in an assembled structure, there can exist a large number of these lap joints, a structural dynamics simulation with this finite element model would computationally be intractable. Instead, a reduced-order friction model which accounts for asperity-scale physics and can replace each lap joint with a rather simple force-deformation law would be more practical and favorable. With this motivation, a multiscale physics-based modeling approach for frictional contacts is proposed.

1.3. Outline of the Thesis

The modeling approach followed in this work starts with continuum mechanics formulations at asperity scale and utilizes statistical representation of surface roughness to model friction in macroscale applications. The models at each length scale are validated by experiments designed and traced from the

literature. The friction models are also transformed into compact forms and applied to a simple dynamical system. Collaborations with colleagues in Civil and Environment Engineering at UIUC enabled incorporation of the developed friction model into a variationally-consistent finite element model. Both of these applications validate the practicality and broader applicability of the proposed friction models at the continuum scale. In addition, the proposed modeling approach can easily be extended to micro/nanoscale contact problems. Future work will consist of friction modeling for small asperities with characteristic dimension of less than a few microns, where discrete dislocations and molecular interactions are expected to play a major role in contact behavior.

The work contained herein can be grouped in three main sections: i) asperity-scale contact, ii) rough contact, and iii) macroscale contact applications, as shown in Figure 1.1. The first section, covered in Chapters 2 and 3, formulates the details of the friction model at asperity-scale and sets the stage for the multiscale modeling (Eriten et al., [33]). Asperity-scale contact is modeled after spherical contacts under combined normal and tangential loading. Normal load is kept constant while the tangential load is oscillated. This type of loading is referred to as fretting. Fretting is a simple and useful loading condition in testing many aspects of a frictional contact such as history-dependence, hysteresis, and energy dissipation. Theoretical formulations and experimental observations of spherical contacts under fretting loading are provided in these chapters. During my doctoral work, my contributions to asperity-scale contact continued with modeling the effects of contamination (lubrication) [34] and investigating the effects of friction and adhesion on inelastic contact behavior [35]. However, these works do not fit in a common multiscale modeling framework presented in this dissertation and, hence, are not included.

The second section, Chapters 4, 5 and 6, deals with the challenge of modeling macroscale frictional rough contacts (Eriten et al., [36]), experimental validation (Eriten et al., [37]) and effect of surface roughness and lubrication (Eriten et al., [38]), respectively. A statistical summation procedure is used to develop this multiscale friction model for macroscale contacts (Chapter 4). An experimental setup is designed and developed to test flat-on-flat contacts of centimeter size (practical length scale) under

fretting conditions (Chapter 5). Effects of different materials, roughness and surface conditions are investigated in Chapter 6. Both presliding and sliding behaviors of these contacts are studied throughout these chapters. Additional works (not included in this dissertation) elucidating the static friction in rough surfaces with asymmetric asperity height distributions [39], the effects of roughness on frictional energy dissipation [40], and the asperity interaction in normal contact of rough surfaces [41] are my supplementary contributions to the rough contact mechanics.

The last section consists of Chapter 7 where the friction model developed is applied to a simple dynamical system (Eriten et al., [42]). As mentioned above, the friction models are also shown to be suitable for consistent embedding in finite element models (see Truster et al., [43]). Another study in application-level frictional contact investigates the measurement techniques for tangential stiffness of mechanical joints before sliding occurs [44]. These studies are not included in this dissertation.

1.4. Figures

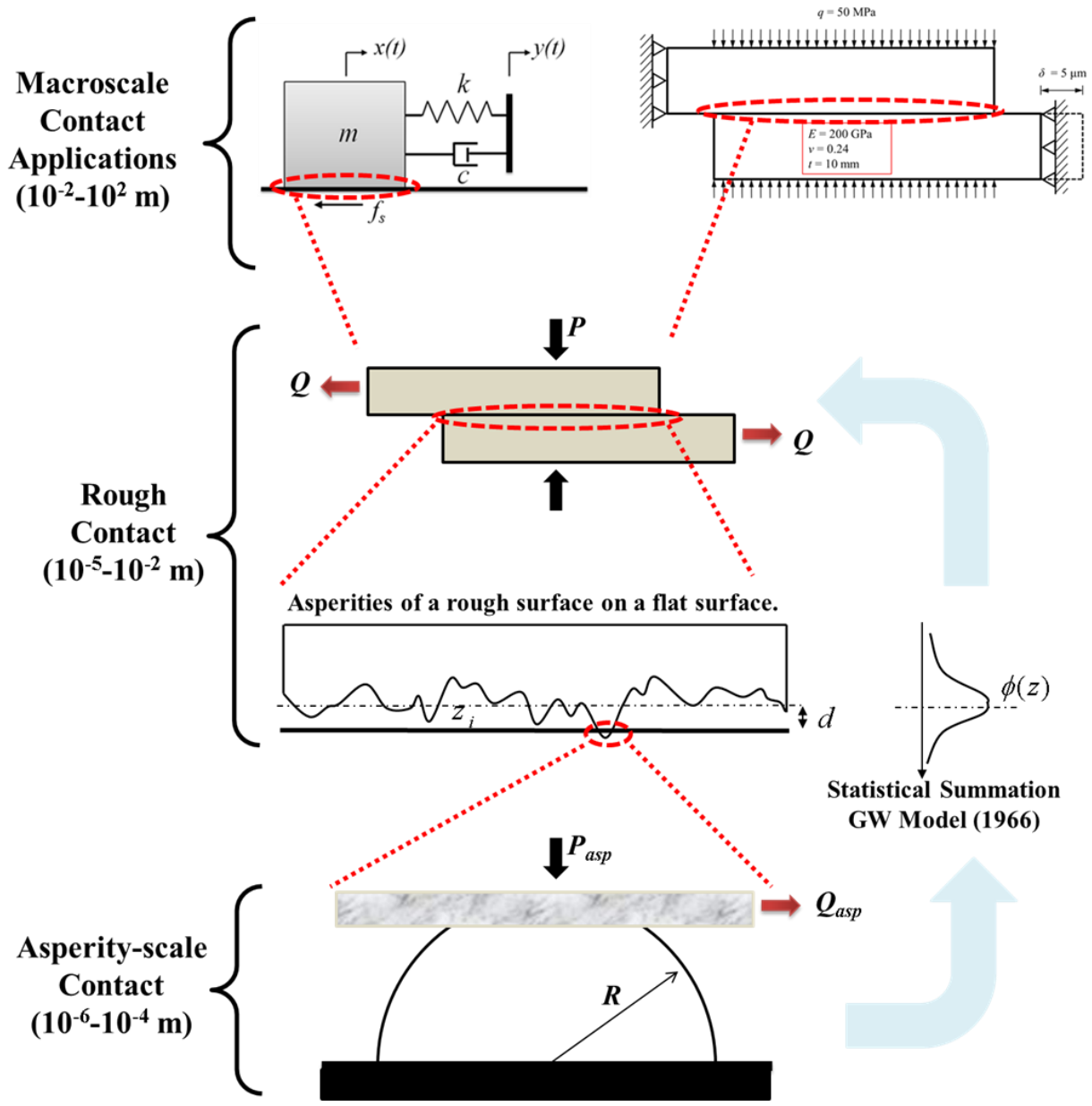

Fig. 1.1. Multiscale modeling approach followed in the dissertation

CHAPTER 2: MODELING APPROACH

2.1. Spherical (Asperity-scale) Contact

Continuum Formulation

Spherical contacts are favorable in studying contact loading of materials for both theoretical and experimental reasons. Theoretically, spherical contacts under normal loading can be treated as an axisymmetric boundary value problem, and governing kinematic and kinetic equations simplify significantly when compared to 3D contact cases. This axisymmetric contact assumption holds up to a reasonable accuracy when a minute amount of tangential loading is applied. Considering that the tangential force resulting from partial slip contact is small, the axisymmetric contact assumption can be used for frictional contact of spheres. Another immediate advantage of spherical contacts over wedge and flat contact configurations appears when stress and strain fields are studied. Spherical contacts result in continuous stresses and strains, so when material behavior is of concern, one needs not worry about singularities. The experimental advantage of spherical contacts over flat-on-flat or cylindrical contacts is that they do not cause alignment problems. Besides, spherical contacts are classified as incomplete in the sense that the contact area depends on the applied loading, and thus single spherical contact is enough to study what happens with varying contact area experimentally [45]. In this thesis, asperity-scale interactions are treated as spherical contacts to benefit from these advantages. Though there are other approaches modeling asperities as cones and bristles, the spherical contact assumption is widely employed due to the large radius to height ratio of asperities on engineered surfaces.

Next, the continuum formulation of the spherical contact problem is presented. This section is by no means a comprehensive primer for contact mechanics, but focuses on spherical contacts and bypasses the details. For more comprehensive coverage, readers are referred elsewhere [27,28]. Two spheres under combined normal and tangential loading are shown in Fig. 2.1. The following boundary conditions apply on each sphere:

$$
\begin{aligned}
&|x| > a \Rightarrow \sigma_z = \tau_{xz} = 0 \\
&|x| < a \Rightarrow \begin{cases} \sigma_z = -p(x) \\ \sigma_x = -q(x) \end{cases} \\
&\lim_{x,z\to\infty} (\sigma_x, \sigma_z, \tau_{xz}) = 0
\end{aligned}
\tag{2.1}
$$

where a is the contact radius, $p(x)$ is the contact pressure and $q(x)$ is the contact shear traction. Potential theory can be used to express the stress and displacement fields [28]. The displacement field over the contact patch takes the form

$$
\begin{aligned}
u_r^*(r) &= r\int_r^a \frac{q(s)\,ds}{\sqrt{s^2 - r^2}} - \gamma \int_0^r \frac{sp(s)\,ds}{\sqrt{r^2 - s^2}} \\
u_z^*(r) &= \int_r^a \frac{sp(s)\,ds}{\sqrt{s^2 - r^2}} - \gamma \left\{ \int_0^a q(s)\,ds - r\int_0^r \frac{q(s)\,ds}{\sqrt{r^2 - s^2}} \right\}
\end{aligned}
\tag{2.2}
$$

where γ is the Dundurs' parameter showing the extent of elastic mismatch between contacting materials, and the adjusted displacements on the left-hand side are expressed as

$$
\begin{aligned}
u_r^*(r) &= -\frac{E}{2(1-\nu^2)} \left\{ \int_0^r \frac{\left[su_r(s) \right]' ds}{\sqrt{r^2 - s^2}} \right\} \\
u_z^*(r) &= -\frac{E}{2(1-\nu^2)} \frac{d}{dr} \left\{ \int_0^r \frac{su_z(s)\,ds}{\sqrt{r^2 - s^2}} \right\}
\end{aligned}
\tag{2.3}
$$

Since the displacement field over the contact is easier to predict than contact tractions, Eqs. (2.2) and (2.3) are critical in the formulation of contact mechanics problems.

Normal Contact

When the overlap of elastically similar contacting bodies ($\gamma = 0$) in normal loading $h(r) = u_z^1(r) + u_z^2(r)$ is computed, the resulting equation is

$$
h^*(r) = -A\int_r^a \frac{sp(s)\,ds}{\sqrt{s^2 - r^2}} \tag{2.4}
$$

where $h^*(r)=\dfrac{d}{dr}\left\{\int_0^r \dfrac{su_z(s)ds}{\sqrt{r^2-s^2}}\right\}$ and $A=\dfrac{2\left(1-\nu_1^2\right)}{E_1}+\dfrac{2\left(1-\nu_2^2\right)}{E_2}$. Elastic spherical contact was first studied by Hertz in 1881 [46]. He assumed that the contact radius would be a small fraction of the radius of each sphere, and the normal deformation profile would resemble an inverted parabola of the form

$$h(r)=\omega-\frac{1}{2R}r^2 \tag{2.5}$$

where $R=\left(\dfrac{1}{R_1}+\dfrac{1}{R_2}\right)^{-1}$ is the combined radius of the spheres, and $\omega=\dfrac{a^2}{R}$ (this result follows from geometry with the assumption of $a<<R$) is the approach of two remote points on each sphere (i.e., applied or measured displacement in contact problems). Substituting this deformation profile in Eq.(2.4) yields the contact pressure

$$p(r)=-p_0\sqrt{1-(r/a)^2} \tag{2.6}$$

where $p_0=\dfrac{4a}{\pi AR}$ is the maximum contact pressure. Integrating this pressure over the contact area gives the total load, P, carried by the contact in the normal direction; i.e.,

$$P=-\int_0^a p(\xi)2\pi\xi d\xi=p_0\int_0^a 2\pi\xi\sqrt{1-(\xi/a)^2}d\xi=p_0\frac{2\pi a^2}{3} \tag{2.7}$$

Therefore, the maximum contact pressure can be expressed in terms of the applied load as $p_0=\dfrac{3P}{2\pi a^2}$. Equating the two maximum pressure expressions yields the contact radius in terms of the applied load

$$p_0=\frac{4a}{\pi AR}=\frac{3P}{2\pi a^2}\Rightarrow a=\left(\frac{3PAR}{8}\right)^{1/3} \tag{2.8}$$

and the load-displacement ($P-\omega$) relation follows by the substitution of Eq.(2.8) in $\omega=\dfrac{a^2}{R}$;

$$\omega = \frac{a^2}{R} = \left(\frac{3PA}{8R^{1/2}} \right)^{2/3} \tag{2.9}$$

When referred to for the remainder of this thesis, Eq.(2.9) will serve as the Hertzian load-deformation (displacement) relation.

Tangential Contact

First studies of tangential contact of elastic spheres assume subsequent tangential loading of a Hertzian contact. The Cattaneo and Mindlin (CM) solution starts by assuming fully adhered contact under tangential loading. This assumption results in a displacement field similar to the axisymmetric flat punch contact over the contact area, and thus creates a shear traction singular at the contact edges (can be calculated from Eqs. (2.2) and (2.3)); i.e.,

$$q(r) = \frac{Q}{2\pi a^2} \left[1 - (r/a)^2 \right]^{-1/2} \tag{2.10}$$

and the load-displacement relation

$$\delta = \frac{Q}{8G^* a} \tag{2.11}$$

where $G^* = \left((2-\nu_1)/G_1 + (2-\nu_2)/G_2 \right)^{-1}$ and Q is the monotonically increasing tangential loading. Shear traction growing unboundedly towards the contact edges is unrealistic, and a stress-relaxation mechanism in the material response is expected. The Cattaneo-Mindlin solution assigns local slippage (microslip) and assumes that a local Coulomb friction law bounds the shear traction towards the contact edges. That shear traction produces the load-displacement relation

$$\delta = \frac{3\mu P}{16G^* a} \left(1 - \left(1 - \frac{Q}{\mu P} \right)^{2/3} \right) \tag{2.12}$$

where μ is the friction coefficient and P is the normal load on the contact. In case of cyclic loading, the reverse slip initiates immediately after the load is decreased, and the reverse slip region enlarges by

further decrease; and once the load is completely reversed, the shear traction keeps the same form as in loading case but with opposite direction. The evolution of the shear tractions throughout the loading and unloading period is shown in Fig. 2.2, and the mathematical expressions for shear tractions for both monotonic and cyclic loading cases can be found elsewhere. Corresponding load-displacement relations are given as

$$\delta = \begin{cases} \dfrac{3\mu P}{16G^{*}a}\left(2\left(1-\dfrac{Q_m - Q}{2\mu P}\right)^{2/3} - \left(1-\dfrac{Q_m}{\mu P}\right)^{2/3} - 1\right) & \dot{Q} < 0 \\ -\dfrac{3\mu P}{16G^{*}a}\left(2\left(1-\dfrac{Q_m + Q}{2\mu P}\right)^{2/3} - \left(1-\dfrac{Q_m}{\mu P}\right)^{2/3} - 1\right) & \dot{Q} > 0 \end{cases} \tag{2.13}$$

where Q_m is the maximum tangential load applied on the contact. Note that Eqs.(2.12) and (2.13) are valid only when the maximum tangential load applied is less than the maximum friction force the contact can carry; i.e., they describe presliding friction behavior.

Fig. 2.3 presents the load-displacement curves for monotonic and cyclic loading conditions. These load-displacement relations model the softening contact behavior before sliding inception. Note that the friction coefficient in these expressions is a look-up parameter and assumed constant. An alternative approach is to relate the sliding inception and, thus, friction coefficient to material strength.

2.2. Material Strength vs. Sliding Inception

The major drawback of the Cattaneo-Mindlin solution is the difficulty of building a physical understanding for the friction coefficient used to couple normal tractions to shear tractions. At asperity-scale contact, friction experiments can be conducted to obtain a friction coefficient. However, the friction coefficients obtained will heavily depend on experimental conditions, loading, and material strength and micro/nanostructure. An alternative approach is to associate sliding inception of a frictional contact to these critical factors. In this thesis, the effects of loading and material strength on the friction behavior are modeled using this alternative approach. The effects of environment and contact conditions are studied

experimentally, but are not accounted for in modeling. Therefore, the friction models developed in this thesis hold for dry contacts under normal environmental conditions (no thermal effects or contamination) and neglect the influence of micro/nanostructure on the sliding inception.

The approach of associating sliding inception with material failure, plastic deformations in particular, dates back to the 1940s when Bowden and his collaborators re-defined the onset of frictional sliding as the breaking of asperity junctions with "distortion" (plastic deformations) or "tearing" (fracture) of the contacting bodies to a considerable depth beneath the contact patch [11,47]. This redefinition resulted from their experimental observations, and McFarlane and Tabor [48] attempted to explain the sliding in a frictional contact as the plastic flow according to the von Mises yield criterion. Similarly, Burwell and Rabinowicz [49] proposed a simple model for the maximum normal (indentation load, $P_{\max} = A_r H$, A_r is the real area of contact and H is the hardness of the softer material in contact) and tangential load ($Q_{\max} = A_r s$, s is the shear strength of the softer material in contact) a junction can carry and formulated the friction coefficient as

$$\mu = \frac{Q_{\max}}{P_{\max}} = \frac{s}{H} \tag{2.14}$$

For ductile materials, hardness is approximately five times the shear strength, resulting in a friction coefficient value of 0.2. However, many metal-on-metal contacts are documented to have larger friction coefficients than 0.2. There are three possible reasons for this mismatch in theory and practice: i) surface layers in metals can have oxides and work-hardened sections with larger shear strength, ii) tangential loading of the contact increases the real area of contact by junction growth mechanism, so the real area of contact in the maximum tangential load calculation is larger than in the maximum normal load calculation, iii) normal and tangential strength of the contacting materials are not independent of each other; for instance, if a contact is loaded with a small normal force, then the maximum tangential load this contact can carry is large. The first of these problems can be solved by measuring the mechanical

properties of the surface layers carefully. The other two have been studied by Chang et al. [13], Kogut and Etsion [15], and Brizmer et al. [50]. Chang et al. [13] applied the volume conservation after the inception of plastic deformation in spherical contacts and estimated the maximum tangential load these contacts can carry until the first instance of plasticity. This approach resulted in very low friction coefficient values when compared to experimental values mainly because materials in practice are capable of carrying more shear even after the inception of plasticity. Kogut and Etsion [15] utilized a finite element model of sphere-on-flat contact and associated the sliding inception with the complete yielding of the contact surface. Recently, Brizmer et al. [50] used a finite element model of a fully-adhered spherical contact and detected the sliding inception as the vanishing tangential stiffness of the junction.

These continuum scale friction models provided friction coefficient values as a function of normal loading, geometry of the contact and mechanical properties of materials (Young's modulus, Poisson's ratio, yield strength). These mechanical properties can be found from well-established experiments (simple tensile testing), or from atomistic simulations. Therefore, the friction models are predictive and physics-based at continuum scale. In this thesis, these friction models are incorporated in the Cattaneo-Mindlin solution to remedy the non-physical local Coulomb friction assumption. In this approach, presliding friction behavior is still dominated by the slippage towards the contact edges, but the shear tractions resulting from this slippage are coupled to the normal tractions through the physics-based friction models. In other words, instead of a local Coulomb law, plasticity is used to determine the sliding inception along the contact surface. The applicability of the developed friction models is limited to ductile materials with asperity sizes larger than a few microns, for which the continuum plasticity holds. Discrete dislocation effects start playing a major role for \ asperities less than this size [51]. Besides, molecular interactions and adhesion become more pronounced as the size of contact decreases. In this thesis, some of these effects are documented as observed in experiments, but the friction models developed do not account for these effects. Future work will include the extension of the modeling approach to nanoscale

asperities. Some essential features to include in a nanoscale asperity-scale friction model consist of the effects of dislocation source and obstacle densities, grain boundaries in polycrystalline materials, crystal orientation and surface contamination/chemistry.

2.3. Multiscale Modeling: Asperity to Rough Surface Scale Contacts

As mentioned above, the models developed in this thesis hold for asperity-scale contacts of larger than a few microns characteristic length up to rough surfaces of centimeter size. The reasons for the lower bound are given in the preceding discussion. The upper bound is limited by practical considerations such as uniform contact loading in the normal direction and isotropic surface assumptions. If both conditions are satisfied, the upper bound on the length scale can be increased further. The experiments presented in this thesis are valid up to centimeter scale, and the corresponding friction models are generated by the statistical summation multiscale modeling technique.

The statistical summation technique was first introduced by Greenwood and Williamson in 1966 [29] for a nominally flat rough contact problem and extended to the rough spherical contact problem a year later by Greenwood and Tripp [52]. In this approach, the asperity peaks are modeled as identical spheres with randomly-distributed heights. Let the probability density function for the asperity heights be given by $\phi(z)$; then, the number of asperities with heights $z_1 < z_i < z_2$ is calculated as

$$n(z_1 < z_i < z_2) = N\int_{z_1}^{z_2} \phi(\zeta)d\zeta \tag{2.15}$$

where *N* is the total number of asperities calculated out of surface roughness measurements.

For the surfaces with randomly-distributed asperity heights, the Gaussian distribution can be used for the probability density function

$$\phi(z) = \frac{1}{\sqrt{2\pi}\sigma_a}\exp\left(-0.5\left(\frac{z}{\sigma_a}\right)^2\right) \tag{2.16}$$

where σ_a is the root-mean-square roughness (standard deviation of the asperity heights). Once the contact formulation at asperity-scale is achieved, the statistical summation yields the total normal and tangential loads carried by the rough contact as

$$P_{total} = N\int_d^\infty P_{asp}\phi(\zeta)d\zeta$$
$$Q_{total} = N\int_d^\infty Q_{asp}\phi(\zeta)d\zeta \tag{2.17}$$

where *d* is the distance between the means of asperity heights of the rough surfaces in contact. Note that the upper bound of these integrals is infinity due to the choice of Gaussian distribution given in Eq.(2.16). This non-physical upper bound is due to mathematical representation, but when summed with all other asperities, the effect of this unbounded height discrepancy vanishes.

The statistical summation technique was utilized for the multiscale modeling for three main reasons: i) common manufacturing techniques such as turning, grinding, cutting, abrading and shot peening generate surface asperities with randomly-distributed heights, ii) the surfaces experimented with contain a sufficiently large number of asperities, so when statistical summation is applied, the local discrepancies and variations are smoothed out and an effective equivalent expression for the global load-deformation relations is obtained (i.e., smoothing and predictive effects of the moving average in a large collections of data), iii) the multiscale modeling parameters (number of asperities, root-mean-square roughness of asperity height distributions, mean radius of asperities) are easy to obtain through standard roughness measurements and post-processing techniques. The details of roughness measurements, post-processing of surface height data, and application of the statistical summation technique are given in Chapters 4, 5 and 6 of this thesis.

2.4. Figures

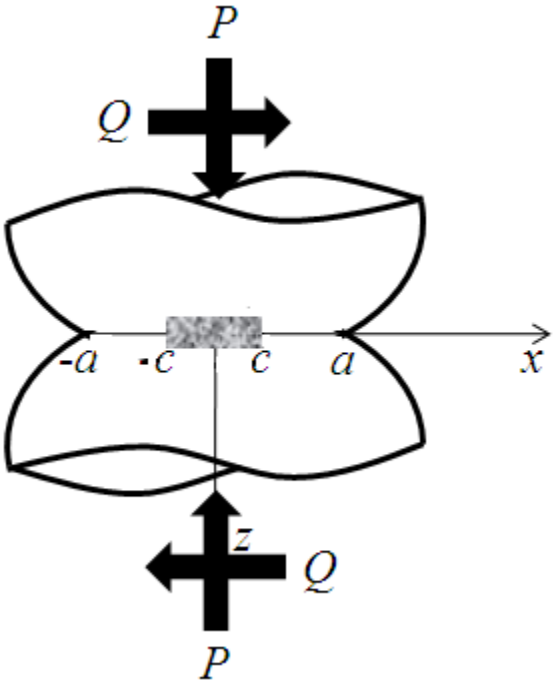

Fig. 2.1. Spherical contact under partial slip contact

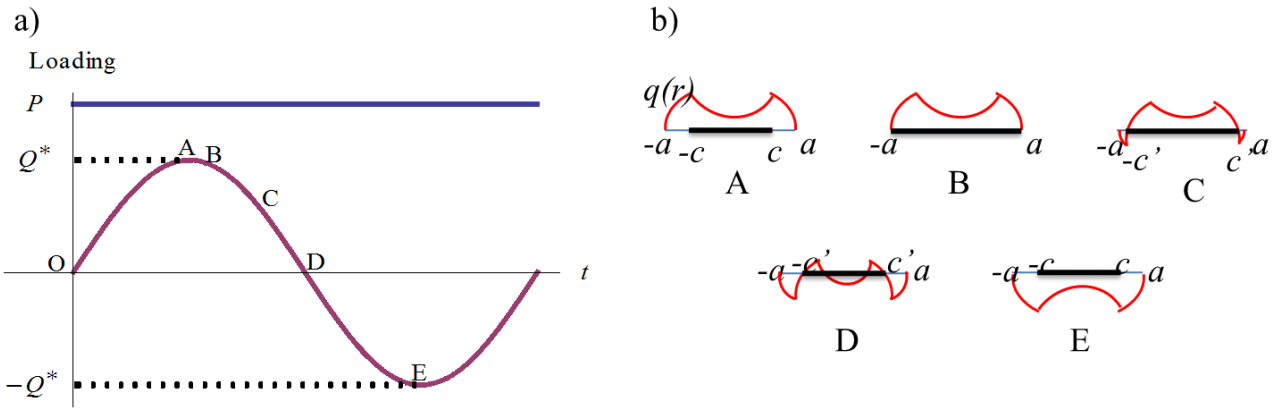

Fig. 2.2. Loading history for cyclic tangential loading of the spherical contact (a) and corresponding shear tractions (b)

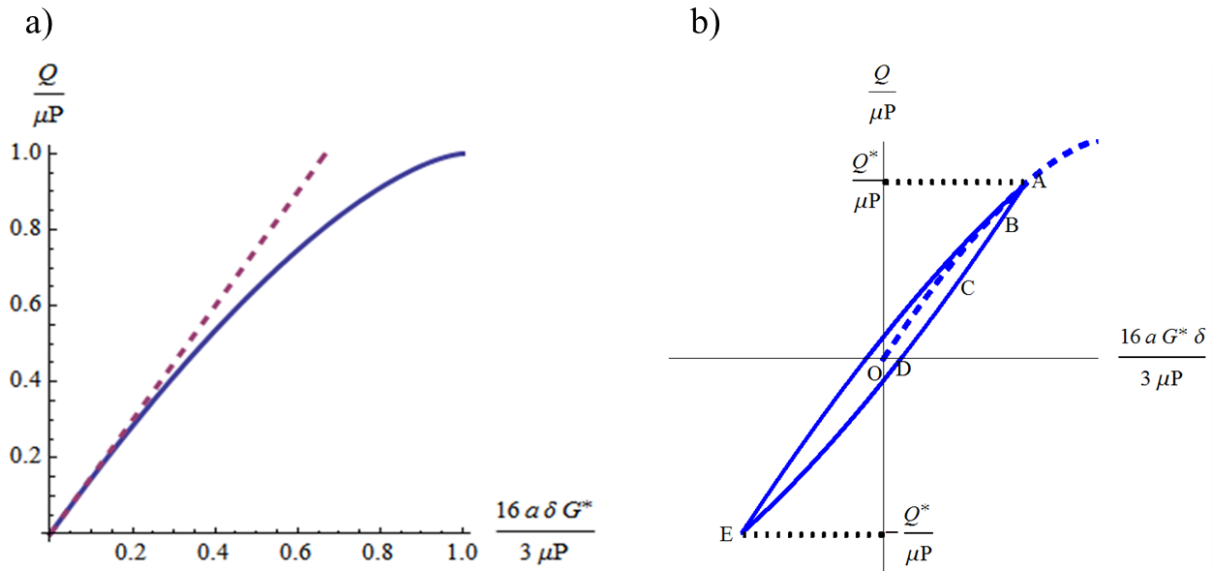

Fig. 2.3. Load-displacement relations for monotonic (a) and cyclic (b) loading

CHAPTER 3: ASPERITY-SCALE FRICTION MODEL

3.1. Introduction

Contact of spheres is a large subset of axi-symmetric contacts seen in practice. Particle handling, sealing, electrical conductivity, MEMS and magnetic storage systems are only a few examples where spherical contact governs the interaction between different parts. Besides, the contact of nominally flat rough surfaces can be modeled as numerous spherical contacts assuming spherical asperity tips. Therefore, understanding the normal and tangential loading of spherical contacts is critical in modeling, design and control of many engineering systems, such as interference fits of rotating or vibrating assemblies, rolling bearings, wire ropes, turbine blades, and mechanical joints (bolted, lap, dovetail, etc.).

As fundamental as the combined loading of spherical contact is, it is complicated to analyze due to three major reasons. Firstly, although many engineering systems containing interfaces are brought into contact by a prescribed clamping load, both tangential and normal loading vary throughout system operation. Nevertheless, assuming a constant normal clamping load and proceeding with varying tangential loading simplifies the problem considerably while providing insight about the problem. Normal loading under different contact conditions has been analyzed extensively by many researchers (elastic frictionless contact, [46]; elastic fully-adhered contact, [53,54]; elastic-plastic frictionless contact, [12,55]; elastic-plastic fully adhered contact, [25].

Secondly, even though the normal loading problem can be accurately solved, a physics-based mechanism relating known normal load to unknown tangential load in combined loading problems is difficult to solve. Local Coulomb friction law assumes an either tabulated or experimentally determined constant friction coefficient value in order to couple the normal and tangential tractions on a sliding contact [56]. Similarly, power law coupling needs experimentally determined non-physical coefficients [57]. By treating the plastic yielding as the trigger for sliding, friction force and friction coefficient can be related to physical quantities; however, the results proposed by several researchers vary significantly

depending on the contact modeling assumptions (elastic contact, [13,49]; elastic-plastic contact with partial slip, [15]; fully-adhered elastic-plastic contact, [17].

Thirdly, the tangential loading of spherical contacts is not as well understood as normal loading. This is because the contact condition (fully adhered, lubricated, sliding, etc.) used in modeling affects the results. The first modeling attempts by Cattaneo [3], and independently by Mindlin [4], assumed fully adhered purely elastic contact and showed that tangential loading would produce unreasonably high tangential tractions toward the edge of the spherical contact. For relaxation of this growing stress, they suggested "slip" and assumed that tangential tractions inside the slip region would obey the local Coulomb friction law. This contact condition, for which a slipping annular region encapsulates a sticking core in the contact patch, is named "partial slip." Mindlin et al. (1952) expanded the same approach to solve the oscillating tangential loading response of spherical contact under partial slip [58]. The partial slip contact under oscillating tangential loading is also referred to as fretting contact. Mindlin's elastic partial slip model has been shown to agree with fretting experiments of steel ball and flat contact under moderate normal loads [59]. However, the energy dissipation measured during each unloading/reloading (fretting) cycle deviates considerably from the theoretical calculation. In addition, Johnson (1955) points at four basic assumptions of Mindlin's elastic model to be approached critically, [59]: 1) Contacting bodies are perfectly elastic, 2) Contacting surfaces are smooth and thus the contact is continuous, 3) Infinite shear stress due to the fully stick contact condition is relieved by relative slipping over an annulus (partial slip), and 4) Shear stress over the slip annulus obeys the local Coulomb friction law . Ödfalk and Vingsbo (1992) challenged the perfect elasticity assumption and suggested that plastic displacements should be added to the elastic displacements in order to account for plasticity [26]. Specifically, they suggested a parallelogram-shaped load-displacement curve for plastic regime loading. However, their formulation needs two experimentally-determined parameters, namely "fretting yield point" and "fretting hardening coefficient", which in turn compromises the physical basis of predictive fretting modeling.

The purpose of this chapter is to explain the approach challenging the first and fourth assumptions listed above by combining elastic and elastic-plastic normal loading and preload-dependent friction coefficient models with the Cattaneo-Mindlin elastic solution to obtain physics-based partial slip responses for spherical contact. The models developed by this approach are compared with data existing in the literature. Furthermore, the limitations and assumptions—elastic similarity, smoothness, adhesion and plasticity— of this modeling approach are discussed.

3.2. Spherical Contact

We review elastic and elastic-plastic spherical contact (incomplete) models in this section. In doing so, we mention only normal and tangential loading/deformation responses. For more details about flat-on-flat fretting contact (complete), contact stresses, surface tractions, and their evolution during loading; the reader is referred elsewhere, e.g. [27,28,45,60–62].

Normal Loading

When two elastic spheres are pressed to each other (see Fig. 3.1), the contact is enclosed within a circle whose radius is dependent on the applied load, P (incomplete contact). With the assumption that the contact radius is considerably smaller than the radii of the spheres, Hertz (1881) offered the first analytical solution to the load-penetration problem of elastic spheres under frictionless (perfect slip) contact [46]. Subsequently researchers relaxed the assumptions needed by the Hertzian solution. Sneddon (1965) relaxed the small contact radius assumption by solving the problem of a rigid punch pressed into an elastic half-space under frictionless contact [63]. Spence relaxed the frictionless contact assumption and solved first the fully-adhered rigid punch problem and then the same problem with finite Coulomb friction [54,64]. Noting that plastic deformations either on or below the contact surface are inevitable, especially for heavier loading conditions and stress intensification due to geometry, Chang et al. (1987) —CEB Model— proposed an elastic-plastic solution to the frictionless sphere-on-flat contact by assuming volume conservation during plastic deformations [12]. To solve this problem with minimal assumptions, Kogut and Etsion, [55]—KE Model— utilized finite element analysis (FEA), and Brizmer

et al. [25]—BKE Model— investigated the effects of contact conditions (fully-adhered or frictionless) and material properties on the normal contact, also by FEA.

We assume small contact radius throughout this study, so the Sneddon and Spence solutions will only serve as extreme cases. Hence, we summarize the load-penetration ($P-\omega$) relationships offered by Hertz, CEB, KE and BKE models in Eqs. (1-4), respectively as

Hertz:
$$P^* = \omega^{*3/2} \tag{3.1}$$

CEB:
$$P^* = \begin{cases} \omega^{*3/2} & \omega^* \le 1 \\ 3\left(\omega^* - 0.5\right) & \omega^* > 1 \end{cases} \tag{3.2}$$

KE:
$$P^* = \begin{cases} \omega^{*3/2} & \omega^* \le 1 \\ 1.03\omega^{*1.425} & 1 < \omega^* \le 6 \\ 1.4\omega^{*1.263} & 6 < \omega^* \le 110 \end{cases} \tag{3.3}$$

BKE:
$$P^* = \frac{\bar{l}_c}{\bar{\delta}_c^{3/2}} \begin{cases} \omega^{*3/2} & \omega^* \le \bar{\delta}_c \\ \omega^{*3/2}\left(1 - \exp\left(\frac{\bar{\delta}_c^{\alpha}}{\bar{\delta}_c^{\alpha} - \omega^{*\alpha}}\right)\right) & \omega^* > \bar{\delta}_c \end{cases} \tag{3.4}$$

where $P^* = P / P_c$ and $\omega^* = \omega / \omega_c$ are the normalized load and penetration. Chang et al. [13] defines the critical interference, ω_c, contact radius, a_c, and normal load, P_c, at the inception of plastic deformation as functions of Poisson's ratio, ν; hardness factor, $K = 0.454 + 0.41\nu$; hardness of the softer material in contact, H; combined Young's modulus, $E^* = \left((1-\nu_1^2)/E_1 + (1-\nu_2^2)/E_2\right)^{-1}$; and combined radius of curvature, $R = \left(1/R_1 + 1/R_2\right)^{-1}$ as

$$\omega_c = \left(\frac{\pi KH}{2E^*} \right)^2 R$$
$$a_c = \sqrt{\omega_c R} = \frac{\pi KHR}{2E^*}$$
$$P_c = \frac{2}{3} KH \pi a_c^2 \tag{3.5}$$

Note that $\bar{l}_c = 8.88\nu - 10.13\left(\nu^2 + 0.089\right)$, $\bar{\delta}_c = 6.82\nu - 7.83\left(\nu^2 + 0.0586\right)$, and $\alpha = 0.174 + 0.08\nu$ are given in Brizmer et al. [25].

Fig. 3.2 depicts the normalized loads, P^*, given by Eqs. (3.1)-(3.4) as a function of normalized penetration, ω^*, for $\nu = 0.3$. As seen in Fig. 3.2, both CEB (Eq. (3.2)) and KE (Eq. (3.3)) models possess discontinuities at the transitionary penetration values and this is not physical. For instance, CEB model calculates normalized loads of 1 and 1.5 and normalized contact stiffnesses of 1.5 and 3 before and after the yielding ($\omega^* = 1$). This non-physical transition is due to the fact that CEB model assumes the volume of the sphere is conserved while plastically deforming, although elastic contact is not volume-conserving. Evseev et al. [65] studied the elastic-plastic deformation of a spherical contact experimentally and recommended a general model to fix the discontinuity observed in CEB model. Zhao et al. [66], on the other hand, utilized mathematical smoothening to express a continuous transition in CEB formulation. Since we use CEB's normal load model in conjunction with CEB's static friction model with vanishing friction coefficient at $\omega^* = 1$, the partial slip model developed is not affected from this discontinuity. Therefore, we used the original CEB formulation. The discontinuities in KE model appear in two transition penetration, $\omega^* = 1, 6$, both of which are associated to the curve-fitting process of FEA results. These artificial discontinuities are bounded within 3 % for normalized load and 10 % for normalized contact stiffness. Therefore, the use of the original KE formulation should not affect the partial slip response either.

Note that, for a wide range of practical normal penetration values, i.e. $\omega^* < 5$, the elastic-plastic normal loading results given by the frictionless KE and fully-adhered BKE models remain very close to each other and within 10 % of the purely elastic response (Hertz). Furthermore, the fully adhered BKE solution deviates from the frictionless Hertz solution by only 3 % within the elastic loading regime. These observations lead us to an early remark: friction's effect on the load-penetration response of the spherical contact is negligible. This remark has been shown to hold by Spence [54]. Spence's analysis of a fully-adhered rigid punch pressed into an elastic half-space led to a $5\ \%$ increase in load compared to the frictionless punch solution of Sneddon with a Poisson's ratio of 0.3. This increase is more than the BKE/Hertz yields, due to the fact that both BKE and Hertz (CEB and KE, as well) assume small penetrations and, thus, small contact radii. Larger penetrations result in stronger surface tractions, and, hence, the ratio of loads under different contact conditions increases. Nevertheless, it is reasonable to conclude that the contact condition under normal loading has negligible effect on the load-penetration response.

Tangential Loading

Subsequent application of a tangential load, Q, on a spherical contact normally preloaded by a constant load, P, disturbs the axi-symmetric nature of the problem. Additionally, tangential loading causes physical complications such as junction growth and change in normal tractions, and the nature of contact (frictionless, fully-adhered or finite friction) affects the tangential load-displacement response (even though we don't study them, the contact and bulk stresses also depend on the contact conditions). Starting from fully-adhered elastic contact and continuing with finite friction (friction coefficient, μ), Cattaneo [3] and Mindlin [4] independently proposed the same solution to the elastic spherical contact under constant normal and increasing tangential loading . Furthermore, Mindlin et al. [58] proposed a solution to cyclic tangential loading (unloading/reloading) of spherical contacts under partial slip. A maximum tangential load, Q_m, which is not sufficient to cause gross sliding, is applied to the contacting

bodies repeatedly (see Fig. 3.1) and superposition is used to obtain solutions for the tangential load-displacement, $Q-\delta$, while unloading/reloading. Eqs. (6-9) summarize these findings.

Full Stick:
$$\delta = \frac{Q}{8G^{*}a} \tag{3.6}$$

Partial Slip (increasing Q):
$$\delta = \frac{3\mu P}{16G^{*}a}\left(1-\left(1-\frac{Q}{\mu P}\right)^{2/3}\right) \tag{3.7}$$

Partial Slip (unloading Q):
$$\delta = \frac{3\mu P}{16G^{*}a}\left(2\left(1-\frac{Q_m-Q}{2\mu P}\right)^{2/3}-\left(1-\frac{Q_m}{\mu P}\right)^{2/3}-1\right) \tag{3.8}$$

Partial Slip (reloading Q):
$$\delta = -\frac{3\mu P}{16G^{*}a}\left(2\left(1-\frac{Q_m+Q}{2\mu P}\right)^{2/3}-\left(1-\frac{Q_m}{\mu P}\right)^{2/3}-1\right) \tag{3.9}$$

where $G^{*}=\left(\left(2-\nu_1\right)/G_1+\left(2-\nu_2\right)/G_2\right)^{-1}$ is the combined shear modulus and a is the contact radius. Observing that plastic flow causes additional tangential displacement without a considerable force increase, Ödfalk and Vingsbo [26] relaxed the elastic assumption of Mindlin's tangential unloading/reloading solution. They suggested a simple superposition of a parallelogram-shaped load-displacement relation, Eq.(3.10), with Mindlin's elastic solution, Eq.(3.8).

Plastic Slip (cyclic Q):
$$\delta_p = \beta\left(\gamma\frac{Q+Q_{ty}}{k_p}+\frac{Q_m-Q_{ty}}{2k_p}\right) \tag{3.10}$$

, where $\beta=\begin{cases}1 & \text{when } Q_m > Q_{ty}\\ 0 & \text{when } Q_m \le Q_{ty}\end{cases}$ and $\gamma=\begin{cases}1 & \text{when } |Q|>Q_{ty} \text{ and } \dfrac{dQ}{dt}Q>0\\ 0 & \text{else}\end{cases}$.

There are two critical parameters to be determined in this model, namely "fretting yield point," Q_{ty}, and "fretting hardening coefficient," k_p. The fretting yield point is described as the load needed for the

inception of plastic yield due to increasing tangential load. This parameter depends on the contact geometry, material properties of the contacting bodies, and the normal preload. The fretting hardening coefficient depends on the mean strain rate and, hence, on the fretting frequency. Both parameters are obtained experimentally and could not be generalized. In addition, both Mindlin and Ödfalk and Vingsbo use a local Coulomb friction law, with a pre-determined, constant friction coefficient. Therefore, one could argue that neither the Mindlin nor the Ödfalk and Vingsbo model is entirely physics-based.

The dashed curve in Fig. 3.3 shows Mindlin's partial slip response (hysteresis curve or fretting loop) under cyclic tangential loading. The dynamical behavior of the contact can be completely characterized by the fretting loop. For instance, the slope of the hysteresis curve at the beginning of the loading and unloading regimes suggests a measure of the tangential contact stiffness. Essentially, both machine support and contact stiffnesses contribute to that slope. Provided that a careful experimentalist isolates the contact stiffness, through use of a relatively rigid attachment to the machine support, the slope coincides with the tangential contact stiffness. Mathematically, this can be described as

$$\frac{1}{K_T} = \left.\frac{d\delta_{OA}}{dQ}\right|_{Q=0} = \left.\frac{d\delta_{AB}}{dQ}\right|_{Q=Q_m} = \frac{d\delta_{stick}}{dQ} = \frac{1}{8G^*a} \tag{3.11}$$

Fig. 3.3 also shows a purely plastic fretting loop (dotted curve) representing the Ödfalk and Vingsbo partial slip model. The elastic-plastic fretting loop (solid curve) is obtained by summing the elastic and plastic displacements calculated for the same tangential load, and, hence, this model shows a larger range of tangential motion when compared to Mindlin's purely elastic solution (dashed curve). However, the tangential contact stiffness remains the same as Mindlin's prediction.

Another critical phenomenon which can be observed from fretting loops is damping. Even though Mindlin's model assumes purely elastic contact, the reloading response does not follow the unloading *response* in Fig. 3.3 (hysteretic behavior). The energy needed to reload the contact is more than the energy released by unloading because of the frictional losses incurred by slippage toward the contact

edges. The energy dissipated during one cycle of unloading/reloading is given by the area inside the fretting loop. This area can be calculated via the difference of the work done by reloading (Eq.(3.9)) and unloading (Eq.(3.8)) as

$$\Delta W = \frac{9\mu^2 P^2}{10G^* a}\left(1-\left(1-\frac{Q_m}{\mu P}\right)^{5/3} - \frac{5Q_m}{6\mu P}\left(1+\left(1-\frac{Q_m}{\mu P}\right)^{2/3}\right)\right) \tag{3.12}$$

The elastic-plastic model shown in Fig. 3.3 indicates a broader fretting loop and thus more energy dissipation per cycle compared to the purely elastic model. This is due to the additional energy dissipation incurred by plasticity.

Friction Coefficient Models

As mentioned above, both the elastic Mindlin and elastic-plastic Ödfalk and Vingsbo models assume a local Coulomb friction law. Accordingly, the partial slip region enlarges by increasing tangential load, and, once the tangential load reaches a pre-determined fraction of the normal load, gross sliding occurs. This pre-determined fraction is referred to as the static friction coefficient and is usually available from engineering handbooks. Rabinowicz [67] lists time and speed of sliding, loading conditions, and degree of vacuum as factors affecting the friction coefficient values obtained through experiments. Experimentally-measured friction coefficient values tabulated in different sources vary drastically, and their practical significance thus diminishes. To exemplify, let's study the friction coefficients tabulated for unlubricated (dry) steel on steel contact. Rabinowicz [67] tabulates values for metal-on-metal contact as a function of the metallurgical compatibility of the metals. For identical metals, the friction coefficient is 0.8, whereas for incompatible metals, 0.35. Similarly, Bowden and Tabor [2] documents 0.8 for mild and 0.4 for tool steel. On the other hand, Gieck and Gieck [68] provides a range of values for static ($0.15-0.3$) and sliding friction coefficients ($0.1-0.3$). Concise Metals Data Handbook by Davis [69] tabulates 0.31 for the static friction coefficient of stainless steel 1032 and twice that value (0.62) for mild steel. Clearly,

there is a large uncertainty and variation in friction coefficient values pre-determined from experiments and that uncertainty influences the partial slip model responses significantly.

An alternative approach to pre-determined friction coefficient values starts by attributing yielding mechanisms to the origins of sliding inception. Since both sliding inception and plastic yielding are physical phenomena, the static friction coefficient, defined as the ratio of the maximum tangential load that a junction can carry (static friction force) to the normal pre-load, can be found directly from a physics-based methodology. A simple example of this approach is achieved by assigning average shear, τ_{Av}, and normal compressive strengths, H, to the junction. Since the maximum loads in the shear and normal directions are related to the shear and normal strengths by the real contact area, A_r, the ratio of the loads, and thus friction coefficient, is the ratio of shear and normal strengths of the junction. It is customary to assume that the shear and normal strengths of the junction cannot exceed those of the weaker bulk material in contact (Burwell and Rabinowicz, [49]). Thus, this simple approach yields a constant friction coefficient (CFC) equal to the ratio of the shear strength, s, and hardness, H, of the softer material in contact (Bowden and Tabor, [47]).

CFC:
$$\mu = \frac{Q_{\max}}{P_{\max}} = \frac{\tau_{Av} A_r}{H A_r} = \frac{\tau_{Av}}{H} \approx \frac{s}{H} \tag{3.13}$$

This approach assumes that each shear and normal loading independently causes plastic yielding of the junction. In reality, some invariant combination of shear and normal stresses (von Mises, Tresca, etc.) is related to the plastic yielding. Therefore, the friction coefficient estimate given in Eq.(3.13) does not hold for most engineering applications.

To alleviate the above-mentioned limitation of this physics-based approach, recent works used Hamilton's sub-surface stress calculations and numerical methods (FEA) to calculate the maximum static friction force (and hence friction coefficient) at sliding inception. Chang et al. [13] treated sliding inception as the first occurrence of plastic yield either on or below the contact area. In this model, the von

Mises yielding criterion is used as the equivalent stress needed for plastic yield. The effect of normal tractions is subtracted from the equivalent stress, and the remaining stress is assumed to be caused by tangential loading only, without any interaction between normal and tangential loading. Therefore, this model assumes that tangential loading following a constant preload has no effect on the normal contact stresses, the shape, and dimensions of the contact area. This assumption infers that tangential loading does not cause junction growth, or a change in the plasticity inception location (this point is shown to be on the axis of symmetry, $x, y = 0$, for purely elastic normal loading and slightly deviating from that point toward the direction of tangential loading for normally loaded sliding contacts, by Hamilton [70].

Since, the model treats the first occurrence of plasticity, whether in the contacting bodies or on the contacting surface, as sliding inception, and additional tangential loading has no effect on the preceding normal loading, the Hertz solution is safely used for normal loading response. The stress field under the contact is taken from Hamilton's formulation for sliding contact, and the maximum tangential load needed for the inception of plastic yield and, thus, sliding is calculated. In contrast to Chang et al. [13], Kogut and Etsion [15] combined an analytical solution with FEA results and calculated sliding inception of a spherical contact under both purely elastic and elastic-plastic loading. This model assumes that the normal preload is not sufficient to produce any plastic yielding, and, thus, the additional tangential force causes the first yield to occur at the contact interface because the shear stress due to the fact that tangential loading is higher on the contact surface. Employing a similar methodology as Chang et al. [13], and stress distributions obtained from FEA, the authors proposed two relationships for the friction coefficient, one for elastic and the other for elastic-plastic contact conditions.

Brizmer et al. [17] studied via FEA elastic-plastic fully-adhered contact of a deformable sphere with a rigid flat under combined normal and tangential loading. The authors relaxed the assumptions of Kogut and Etsion [15] about constant interference, contact pressure and area due to normal loading by imposing fully-adhered contact conditions (thus allowing junction growth and further interference due to tangential loading). According to this model, sliding is assumed to initiate when the contact cannot carry any

additional tangential force; i.e., when the tangential stiffness approaches zero. Using this criterion, the FEA results were curve-fitted to a nonlinear function to obtain the friction coefficient. Eqs. (14-16) summarize the results of the physics-based friction coefficient modeling efforts as

CEB:
$$\mu = \min\left(\frac{0.2045}{K|c_1|}\left(\frac{1}{\omega^*}-1\right)^{1/2}, \frac{-c_4+\sqrt{c_4^2-4c_3c_5}}{2c_3} \right) \tag{3.14}$$

KE:
$$\mu = \begin{cases} 0.536\omega^{*-0.5} - 0.0186\omega^{*0.5} & \omega^* \le 1 \\ -0.007\omega^{*3} + 0.085\omega^{*2} - 0.389\omega^* + 0.822 & 1 \le \omega^* \le 6.2 \end{cases} \tag{3.15}$$

BKE:
$$\mu = 0.26\coth\left(0.27\bar{\delta}_c^{-1}\omega^{*0.46}\right) \tag{3.16}$$

where $c_1 = -1+\frac{3}{2}\zeta\tan^{-1}(1/\zeta) - \frac{\zeta^2}{2(1+\zeta^2)}$, $c_2 = (1+\nu)\left(\zeta\tan^{-1}(1/\zeta)-1\right) + \frac{3}{2(1+\zeta^2)}$,

$c_3 = \frac{9\pi^2}{16}\left(2-\frac{\nu}{2}+\frac{7}{8}\nu^2\right)$, $c_4 = \frac{9\pi}{4}(1-2\nu)(1-\nu/2)$ and $c_5 = \frac{3}{2}(1-2\nu)^2 - \frac{0.56}{K^2\omega^*}$. Note that ζ is the normal direction location of the plastic yield normalized by the contact radius and is approximately found to be 0.48 with Poisson's ratio of 0.3.

Fig. 3.4 shows the friction coefficient of AISI 304N stainless steel ($s = 186MPa$ and $H = 655MPa$ from MatWeb material property database) found as $\mu \approx 0.284$ by Eq.(3.13) and from penetration-dependent models defined in Eqs. (3.14)-(3.16). Unlike the constant friction coefficient, since the penetration-dependent models treat the sliding inception as a failure mechanism of the contact, i.e. plastic yielding, the friction coefficient values reduce as the normal penetration increases. CEB and KE models use the stress field presented by Hamilton [70] in the elastic loading regime to compute the additional tangential load needed for plastic yield. The difference between the models in the elastic loading regime, i.e. $\omega^* < 1$, stems from the modeling assumptions. The CEB model assumes that plastic yielding, even at a

single point beneath or on the contacting surface, would cause the sliding inception; however, the KE model necessitates that all the points in the contacting region should reach plastic yield. Therefore, the KE model predicts higher static friction force and coefficient values than the CEB model. In practice, the CEB model's assumption that no additional tangential load can be carried after the plastic yielding of a single point beneath or on the surface leads to a significant underestimation of the static friction force and coefficient because the plastically-yielded point is still surrounded by a large elastic region, which is capable of carrying additional tangential load. Accordingly, the CEB model unrealistically predicts zero friction coefficient after the inception of plastic yielding due to normal preload, whereas the KE model predicts nonzero values up to $\omega^* = 6.2$. At $\omega^* = 6.2$, the central elastic core is surrounded by a plastic region, and, thus, any additional tangential load causes that elastic island to float rather than showing resistance. On the other hand, the BKE model predicts higher friction coefficient values than the KE model, and the friction coefficient never vanishes (instead approaching an asymptotic value of 0.26). This occurs because the inception of sliding inception under the full-adhered contact condition is caused by a vanishing tangential stiffness. It is important to note that the BKE model relaxes many assumptions of the CEB and KE models by assuming a fully-adhered contact condition. However, in practice, the fully-adhered condition is difficult to establish and maintain (slip due to surface contamination, wear debris, etc.), and, hence, the friction coefficient values predicted by this model should generally serve as an upper bound for the actual values.

In developing the plasticity-based friction coefficients, the assumptions about the scale of the contact and material properties are crucial to be mentioned. While introducing the plasticity-driven formulation of the CFC model, Burwell and Rabinowicz [49] assume macroscopic contact and provide an estimate for friction coefficient of a dry clean contact. The CEB, KE and BKE models, in contrast, are developed by analyzing a smooth, dry and clean spherical contact at asperity scale. To carry the results of these models to the macroscopic contact is a difficult task because the real contacting surfaces contain asperities, contamination and third-bodies (wear debris). One needs to verify each assumption about the contact

conditions carefully, and, contact conditions are specifically complicated to control in macroscopic applications. That is why micro and nano-scale experiments are chosen for comparison. Even so, the assumptions of smoothness and the effect of adhesion in each experiment are checked before proceeding with the conclusions. In addition, plastic response of the material will affect the comparisons. The CEB model uses the von Mises yielding criterion as the limit for static friction. Therefore, material response after yielding is not needed in formulation. However, the KE and BKE models develop friction coefficient formulation involving elastic-plastic response of the softer material beyond the von Mises yielding surface. Both models inherently assume that the harder material behaves elastically during contact. However, this assumption fails to hold when two identical materials is in contact. The KE model treats the softer material as an elastic-perfectly plastic material with identical response in tension and compression, whereas the BKE model uses elastic linear isotropic hardening with a tangent modulus 2 % of the Young modulus. Note that the materials used in experiments, bearing steel and silicon, show different responses in plastic deformation. Many steel grades show work-hardening, whereas silicon exhibits almost no plastic deformation at room temperature. Therefore, one needs to be careful in using the KE and BKE models for these materials under plastic deformation. The experiments used in this chapter involve only elastic deformation, and, hence, the validity of the comparison with the models presented in this section.

3.3. Proposed Model

Cattaneo-Mindlin's approach and formulation of tangential displacement-load relationships (Eq.(7) for increasing and Eq.(8) for oscillating tangential loads) and energy dissipation per cycle (Eq.(12)) under partially slipping contact are combined with elastic-plastic normal loading and preload-dependent friction coefficient models (presented above) to obtain physics-based models for partial-slip. The portion of the models involving plasticity violates the elasticity assumption of Cattaneo-Mindlin. Therefore, only the elastic portion can safely be tested against experimental results. Nevertheless, the Cattaneo-Mindlin

formulation qualitatively represents the weakening of the junction due to plasticity (softening spring behavior) and, hence, can be used for qualitative comparison.

It is worth mentioning the fact that the proposed partial slip models are no different than the Cattaneo-Mindlin function except for the physics-based formulation of the friction coefficient. In fact, the presented friction models predict a constant friction coefficient value for each set of material properties, sphere radius and loading condition. Moreover, the normal preload and penetration responses of each model are shown to agree quite well with the Hertzian solution for small penetration values (see Fig. 3.2). Therefore, the contact pressure is safely assumed to follow Hertzian pressure. As a result, the proposed models conform to the Cattaneo-Mindlin formulation of the superposed surface tractions and the stick-slip regions in the elastic loading regime. In plastic loading, Hertzian pressure assumption fails to hold, and since the Cattaneo-Mindlin formulation is valid for only elastic deformations, the proposed approach has no physical meaning. The proposed procedure to obtain the partial slip response is summarized in Fig. 3.5.

For instance, via the proposed methodology shown in Fig. 3.5, we obtain Eqs. (3.17)-(3.21) for the tangential load-displacement response to increasing tangential loading (see the Appendix A for expressions of cyclic loading and energy dissipation per cycle),

CFC:

$$\delta^* = 0.284\omega^*\left(1-\left(1-\frac{3.52Q^*}{\omega^{*3/2}}\right)^{2/3}\right) \tag{3.17}$$

CEB:

$\omega^* \le 0.95 \Rightarrow$

$$\delta^* = \omega^*\left(-0.112+0.047\sqrt{-4.5+\frac{72}{\omega^*}}\right)\left(1-\left(1+\frac{Q^*}{0.112\omega^{*3/2}-0.047\omega^*\sqrt{-4.5\omega^*+72}}\right)^{2/3}\right) \tag{3.18}$$

$\omega^* > 0.95 \Rightarrow$

$$\delta^* = 1.245\omega^* \sqrt{-1+\frac{1}{\omega^*}} \left(1-\left(1-\frac{0.803Q^*}{\omega^*\sqrt{1-\omega^*}}\right)^{2/3}\right) \tag{3.19}$$

KE: $$\delta^* = \left(0.536\omega^{*1/2} - 0.0186\omega^{*3/2}\right)\left(1-\left(1-\frac{1.87Q^*}{\omega^*\left(1-0.035\omega^*\right)}\right)^{2/3}\right) \tag{3.20}$$

BKE: $$\delta^* = 0.267\omega^* \coth\left(0.306\omega^{*0.46}\right)\left(1-\left(1-\frac{3.75Q^*\tanh\left(0.306\omega^{*0.46}\right)}{\omega^{*3/2}}\right)^{2/3}\right) \tag{3.21}$$

where $\delta^* = 16G^* a_c \delta/(3P_c)$, $Q^* = Q/P_c$. The response to cyclic loading and energy dissipation per cycle are expressed in the Appendix B in a similar way. Note that the constant friction coefficient model uses $\mu = 0.284$, i.e. the friction coefficient calculated for AISI 304N stainless steel. The expressions in Eqs. (3.17)-(3.21) correspond to the elastic loading conditions only. The elastic-plastic formulation is too untidy to be shown in compact forms; however, can be obtained by the same procedure outlined in Fig. 3.5 with conditional statements on the normalized penetration.

3.4. Results

In this section, the responses resulting from the proposed models are summarized. The procedure outlined in Fig. 3.5 is used to generate the results depicted in Figs.3.6-8. Fig. 3.6 shows the normalized responses of the proposed models to increasing tangential loading up to sliding inception with a normalized penetration of (this value is specifically selected to match the first set of experiments shown in the next section). Note that each model predicts similar tangential loading for small displacements and, hence, the same tangential contact stiffness. However, the maximum loading and deformation responses vary significantly due to the variation in predicted friction coefficients. Sliding inception occurs at the highest tangential load-displacement for the BKE model and the lowest for the CFC.

In Fig. 3.7, the cyclic tangential loading responses are shown for the same maximum normalized tangential displacement. The normalized penetration is again set to 0.6. All fretting loops except for CFC

showed partial slip only, whereas CFC predicted mixed gross and partial slip behavior. This is mainly because CFC uses a constant friction coefficient value of 0.284, and this friction coefficient is not sufficient to prevent gross slip for higher tangential loads. Another observation is that the higher the friction coefficient value, the more the fretting behavior approaches the full-stick model. In other words, the fretting loop predicted by BKE has the smallest enclosed area; i.e., the contact is almost fully-adhered.

To analyze the energy dissipation (damping) predictions of the proposed models, we vary the maximum normalized tangential displacements and obtain the normalized energy dissipation, $\Delta W^* = G^* a_c \Delta W / P_c^2$ at each fretting cycle. The results (Fig. 3.8) show nonlinear relationships between the energy dissipation and the maximum tangential displacements for each model under partial slip regimes and a linear relationship after gross slip is reached. The energy dissipation for small tangential displacements decreases with increasing friction coefficient; however, the opposite is true for large displacements and tangential loads. Note that the tangential load remains constant at μP in gross slip regime and the further increase in tangential displacements $\Delta\delta$ increase the energy dissipation by $\mu P \Delta\delta$, and, hence, the linear slope equals to μP in gross slip regime. Since the preload is fixed, higher friction coefficients result in steeper slopes in gross slip regime. This is essentially why CFC and BKE respectively predict the highest and lowest energy losses (and thus damping) per fretting cycle in partial slip regime, but the roles interchange for gross slip.

3.5. Comparison with Experiments and FEA

Next, the partial slip models are tested against two sets of experimental results reported in Varenberg et al. [71]. The first set includes a spherical contact with mm-scale geometry and μm-scale deformations, whereas the second set involves μm-scale geometry and nm-scale deformations. The experiments are referred to by the scale of deformations occurring, and, thus, the first set is denoted “micro-scale” and the second set “nano-scale.” In addition to experiments, FEA results from the literature are also used to assess the “BKE” model.

Micro-scale experiments

In the experiments, a standard bearing-steel ball specimen is fretted against an AISI 52100 flat steel specimen hardened to 63-67 HRC. The exact material properties are not specified by the authors. The values tabulated in Table 3.1 are found from the literature (MatWeb). Combined radius and shear and Young's moduli are computed as described above whereas softer material properties are used as the combined Possion's ratio and hardness.

For the first experiment, the normal preload was set to 35 N and the maximum tangential displacement to 1.5 μm. Using Eq.(3.5) with the material properties and geometry given above, the critical contact radius, penetration and load are found to be 0.136 mm, 7.41 μm and 152.8 N, respectively. The normal contact is elastic since the penetration for all the models is estimated to be 2.77 μm, which is nearly 1/3 of the critical value for plastic yielding (see Table 3.2). The average roughness of the specimens used was documented to be 0.04-0.05 μm. Roughness-to-penetration ratio, R_a / ω is less than 2 %, and, therefore, it is safe to assume that smooth sphere-on-flat contact analysis would apply to model the experiments (according to Johnson (1987) the threshold is at 5 %). Moreover, adhesion is assumed to be insignificant in preloading the contact because the intermolecular separation-to-critical penetration ratio, ε / ω_c is very small (less than 0.01 % for a typical intermolecular separation value of 0.4 nm (Kogut and Etsion, [72]).

In the second set of experiments, normal loading was set at 23 N and maximum tangential displacement to 10 μm. That means normal preload did not cause any plastic yielding (since the preload was even less than the preload used in the previous elastic experiments). The penetration is estimated to be 2.1 μm for this case, and, hence, the roughness-to-penetration ratio validates the smooth spherical contact assumption. The adhesion force is negligible as in the first experiment, since the intermolecular distance-to-critical penetration ratio does not depend on applied load but rather on material properties and radius of the sphere. Under the given loading conditions, friction coefficient values predicted by the CEB, KE and BKE models are also tabulated in Table 3.2.

Fig. 3.9a and b provide a comparison of the models proposed and the micro-scale experiments 1 and 2 respectively. As clearly seen, CEB matches the broadness (the width of the hysteresis loops) of the experimental results, whereas the maximum tangential loads obtained by this model are almost 15 % less than those from the experiments. In addition, the tangential stiffness predicted by the experiments (17.1 N/μm) compares well with the value predicted by the Cattaneo-Mindlin solution (Eq.(3.11)); i.e. 16.17 N/μm for the first set of experiments and 14.06 N/μm for the second. Given that commercial load transducers possess stiffness values on the order of 1000 N/μm and the contact usually appears in a series configuration to the force transducer and machine support, the tangential contact stiffness should be 2-5 % higher than the measured tangential stiffness (corresponds to 17.44-17.96 N/μm). Overall, the stiffness values obtained by the Cattaneo-Mindlin solution are within 20 % error.

The proposed models other than CEB cannot replicate the behavior observed in the experiments due to several modeling limitations. CFC overestimates the broadness of the loop and underestimates the maximum tangential loading, whereas BKE does completely the reverse. The KE model predicts the maximum tangential load quantitatively as well as CEB, but fails to predict the broadness of the experimental fretting loops.

The differences discussed above essentially stem from the assumptions each model employs in order to determine the friction coefficient. Since CFC uses a lower friction coefficient, sliding occurs at lighter loads. In contrast, BKE uses the BKE friction model for a fully-adhered contact condition and, hence, predicts considerably larger tangential loads before sliding. This observation can be attributed to difficulties in maintaining a full-stick contact condition under laboratory conditions. At a relative humidity reported as 47 % by Varenberg et al. [71], contamination might induce slip within the contact area. The assumptions used in CEB and KE friction models seem more appropriate in matching the experimental conditions due to the fact that they both allow partial-slip contact in model development and employ the sliding-contact sub-surface stress field found analytically.

Nano-scale Experiments

In addition to micro-scale experiments, Varenberg et al. [71] present results from nano-scale fretting experiments. In these experiments silica microspheres of radius 1.55 μm are first glued to the end of an AFM cantilevers and fretted against silicon (100) flat specimens. The material and geometry values for contacting bodies are tabulated in Table 3.3 (MatWeb). With these parameters, the critical penetration, contact radius, and load are calculated as 12.67 nm, 0.14 μm and 105.9 μN, respectively.

Three main differences should be kept in mind before applying the previously proposed models to nano-scale experiments. First of all, the elastic models presented assume the contact of elastically similar materials, and, thus, the normal tractions do not cause tangential relative motion or shear tractions. In the micro-scale experiments, a bearing-steel ball was fretted against hardened flat steel; thus, the shear modulus and Poisson's ratios of the contacting materials were the same. Therefore, the elastic similarity assumption is met, and the normal and tangential tractions can be assumed to be safely decoupled. Unlike these experiments, the elastic mismatch between silica microspheres and a silicon flat specimen is large; hence, the normal and tangential tractions are highly coupled. Effects of elastic mismatch and fretting models accounting for it can be found elsewhere ([73–75]). Secondly, the silicon flat specimen is documented to have an average roughness of 0.5-0.7 nm. Roughness-to-penetration ratio calculated for both experiments 1 and 2 (0.99 and 0.94, see Table 3.4) is an order of magnitude higher than the critical value of 0.05 documented in Johnson [27]. As a consequence, we cannot safely apply the partial slip models for smooth spherical contact. Instead, models accounting for roughness on sphere or flat can be used, as done in Greenwood and Tripp [52]; however, it is beyond the scope of our modeling. The third complication stems from growing adhesion effects as the size of the spherical contacts decrease. In this set of experiments, the intermolecular separation-to-critical penetration ratio is 3.2 % which is considerably higher than the critical ratio of 0.01 % for a typical intermolecular separation value of 0.4 nm. The adhesion force obtained by the Kogut and Etsion [72] adhesion model reaches three times the applied load for each nano-scale experiment. In that case, the effect of adhesion on friction, and hence the fretting characteristics, cannot be ignored. It is evident that the partial slip models proposed in this work

are not applicable to all experimental or practical situations where fretting occurs. Three main assumptions elastic similarity, smoothness, and non-adhesive contact, play important roles in the development of the models presented and should therefore be met before application of these models to experiments.

Fig. 3.10 depict the proposed models and results from nanoscale experiments 1 and 2 of Varenberg et al. [71], respectively. Although the loading conditions for both experiments are within elastic limits, the models match neither the broadness nor maximum tangential load results from the experiments.

The friction coefficient for experiment 1 cannot be predicted directly from the data since gross-sliding is not reached. However, the value should be greater than 1 since the maximum tangential load to applied preload ratio is almost 1 under the partial slip regime, seen in Fig. 3.10a. The friction coefficient for experiment 2 is 0.583. The CFC friction model gives $\mu = 0.259$ with the shear strength and hardness values of silica found in the literature, and CEB, KE and BKE models predict friction coefficient values greater than 1.7 for both experiments (Table 3.4). These high values explain the discrepancy at high maximum tangential loads obtained by the models. The tangential stiffness for both experiments (203-539 N/m) is smaller than model predictions (2356-2426 N/m). This disagreement might stem from the low stiffness values of AFM cantilevers dominating the overall tangential stiffness. As a conclusion, the experimental conditions should match modeling assumptions of the proposed models for direct comparison and correlation between models and experiments.

FEA: Fully-adhered Spherical Contacts

As mentioned above, the tangential loading response is greatly influenced by the contact condition. According to Cattaneo-Mindlin, the partial-slip contact condition occurs immediately after a tangential load is applied to a normally preloaded spherical contact as a stress relaxation mechanism. Although the CEB and KE models agree with this, the BKE model instead assumes that the contact region formed by the preload is under full-stick condition and remains so throughout subsequent tangential loading. This

assumption is associated with highly-adhesive contacts, which is difficult to justify for metallic interfaces under light and moderate loading. The FEA results of Brizmer et al. [17] for tangential loading of a sphere-on-flat contact under full-stick condition show a softening spring behavior of the interface as the tangential loading curve of Cattaneo-Mindlin's partial slip solution demonstrated in Fig. 3.3 (the material behavior is assumed as elastic linear isotropic hardening with a tangent modulus 2 % of the Young modulus). The physical basis behind this softening behavior is a weakening junction due to increasing plasticity rather than interfacial slip. Despite that fundamental difference, the proposed BKE model combines the BKE friction coefficient model with Cattaneo-Mindlin partial-slip model to account for the weakening junction.

Fig. 3.11 shows the BKE model predictions for a tangential loading history with various preloads, Mindlin stick model, as well as Brizmer et al. [17]'s FEA results. The partial slip curves labeled with normalized preloads 1, 10 and 100 compare reasonably well with the FEA curves. In addition to the weakening junction behavior, the dependence on normal preload is well mimicked by this model. Note that, as the normal preload decreases, the tangential loading curves approach Mindlin's stick model. This occurs because the model response with lower normal preloads stays within the elastic limit for wider ranges of tangential displacements (for instance, for $P^* = 0.1$, only 10 % of the critical load is reached before tangential loading, and the contact behaves elastically for larger imposed tangential displacements).

It is crucial to note that the formulation of BKE model is achieved by combining the elastic Cattaneo-Mindlin approach with the friction coefficient and preload values which were obtained from fully-adhered elastic-plastic contact analyses. There are two main inconsistencies in this approach: elastic-plastic formulation and contact conditions. Despite these physical inconsistencies, the BKE model results compare well with the FEA. There two reasons for that "non-physical" match. First, the BKE friction model is originally developed from the same FEA results. Hence, the tangential loads at the onset of sliding inevitably matches with the ones obtained through FEA. Secondly, be it because of partial slip or a

plastic deformation, the junction uniformly weakens while loading (softening spring behavior). In addition, both Cattaneo-Mindlin partial slip approach and elastic-plastic FEA should give the same tangential contact stiffness as the Mindlin Stick Model at the initial stages of loading and zero tangential stiffness at the onset of sliding. Ultimately, the problem of expressing the FEA results of BKE simplifies to a problem of finding a uniformly-behaving softening spring with certain stiffness values at specified forces ($K_T = 8G^*a$ and 0 at $Q = 0$ and Q_m). Obviously, this problem cannot be solved uniquely without further physical arguments. However, having the same derivatives as FEA results at specified values, BKE was a natural candidate of such solutions. As can be seen in Fig. 3.11, the junction behavior is mimicked quite well except for differences in maximum tangential displacement. As a conclusion, better physics-based models employing elasticity and plasticity theory to solve the tangential loading of spherical contact are still to be developed.

3.6. Conclusion

In this chapter, purely elastic and elastic-plastic behavior of spherical contacts under combined normal and tangential loading are studied, and a physics-based partial slip modeling approach is proposed and compared with both experiments and FEA results. The proposed modeling approach essentially incorporates elasto-plastic normal loading response and preload-dependent friction coefficient models into the elastic Cattaneo-Mindlin solution. Although very promising, Ödfalk and Vingsbo's elastic-plastic partial slip model is briefly discussed but not used in this study, primarily because this model uses experimentally determined parameters (phenomenological model). The proposed models do not utilize any empirical data or curve-fit coefficients. As we employ physics-based parameters and variables, we call this approach "physics-based partial slip modeling." The physics-based partial slip models –CFC, CEB, KE, and BKE— and the tangential stiffness values have been tested against experimental results existing in the literature, and the CEB has been shown to correlate reasonably well with micro-scale experiments. These experiments correspond to the elastic loading regime, and, thus, the plastic loading

portion of the CEB and KE models is not tested in this chapter. Additionally, tangential contact stiffness predicted by the models compared reasonably well with available data at the micro-scale. However, large differences between model predictions and experiments at the nano-scale are observed. Although the deformations in these nano-scale experiments are calculated to be just above break-down of continuum theory, the modeling assumptions effectively contribute to the discrepancies between experimental data and modeling results. Three major modeling simplifications (elastic similarity, smoothness and non-adhesive contact) used in our approach are shown to be critical assumptions to be validated before application of these models for comparison with experimental results. The nano-scale experiments, where silica microspheres were fretted against silicon flat surfaces, essentially violated all three assumptions and, hence, the proposed models cannot be used to simulate nano-scale fretting behavior.

Finally, the BKE model proposed in this chapter is tested against FEA results. The comparison shows that the BKE model developed by our approach matches reasonably well with FEA results in mimicking the softening spring behavior of the junction during loading. Therefore, the "non-physical" approach of combining the purely elastic Cattaneo-Mindlin partial-slip solution with elastic-plastic models seems to replicate full-stick contact weakening due to plasticity.

3.7. Figures

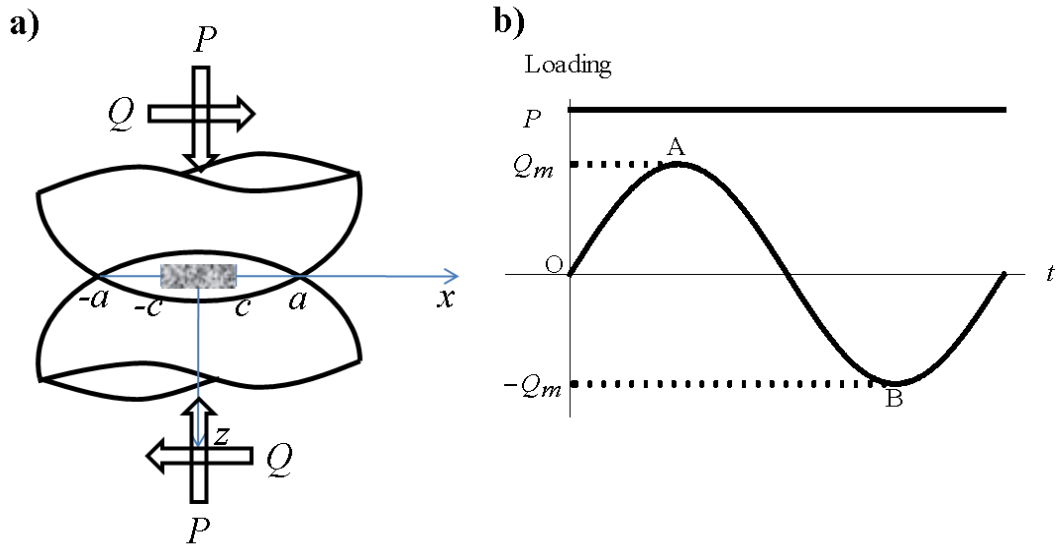

Fig. 3.1. Spheres in contact under combined normal and tangential loading (a) and schematic of a typical loading history (b). The contact occurs in a circle of radius a and the stick region constitutes the core region of that contact with radius c.

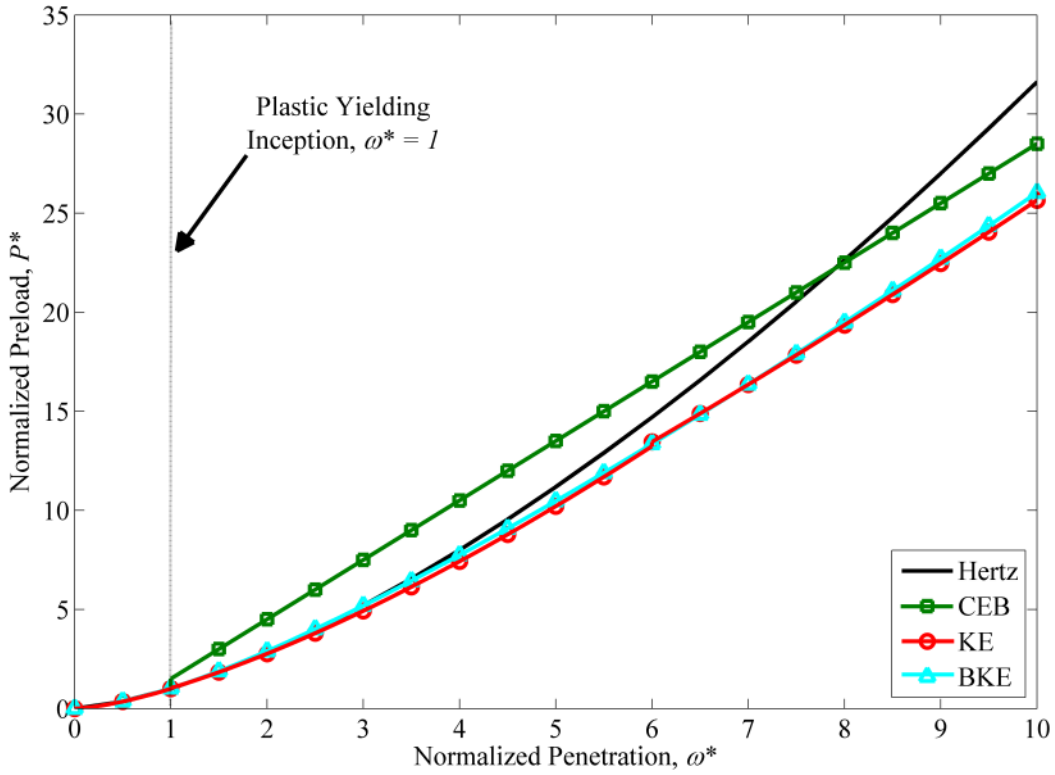

Fig. 3.2. Dimensionless normal load vs interference for Hertz (elastic, frictionless); CEB and KE (elastic-plastic, perfect slip) and BKE (elastic-plastic, full stick) models.

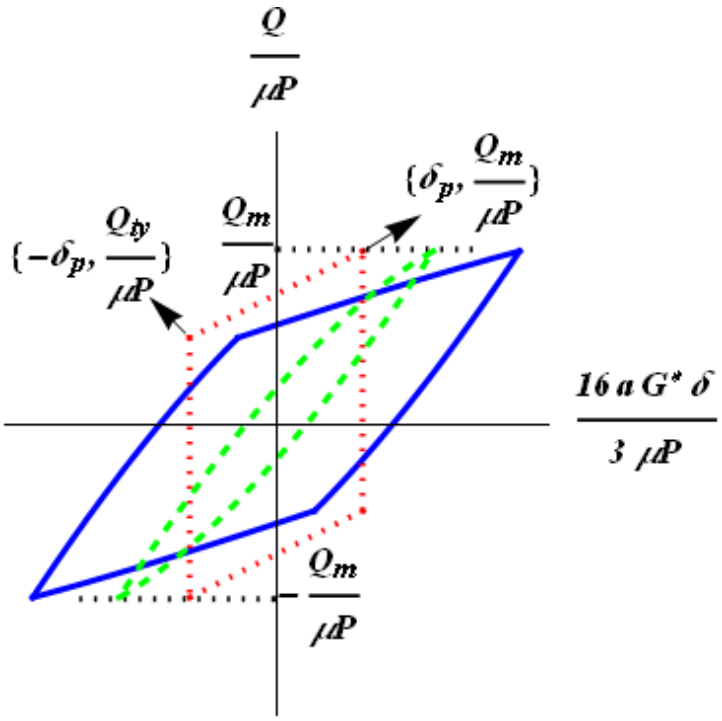

Fig. 3.3. Fretting loops for spherical contacts under combined normal and tangential loading (purely elastic Cattaneo-Mindlin solution: dashed; fully plastic Ödfalk and Vingsbo model: dotted and elastic-plastic model:solid line).

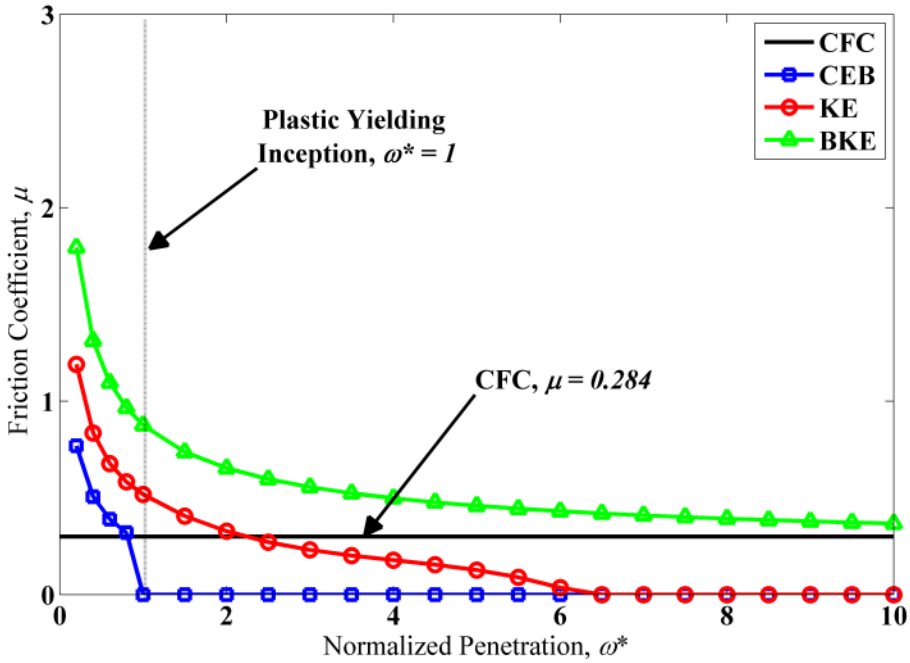

Fig. 3.4. Friction coefficient for CFC, CEB, KE and BKE models vs nondimensional normal penetration.

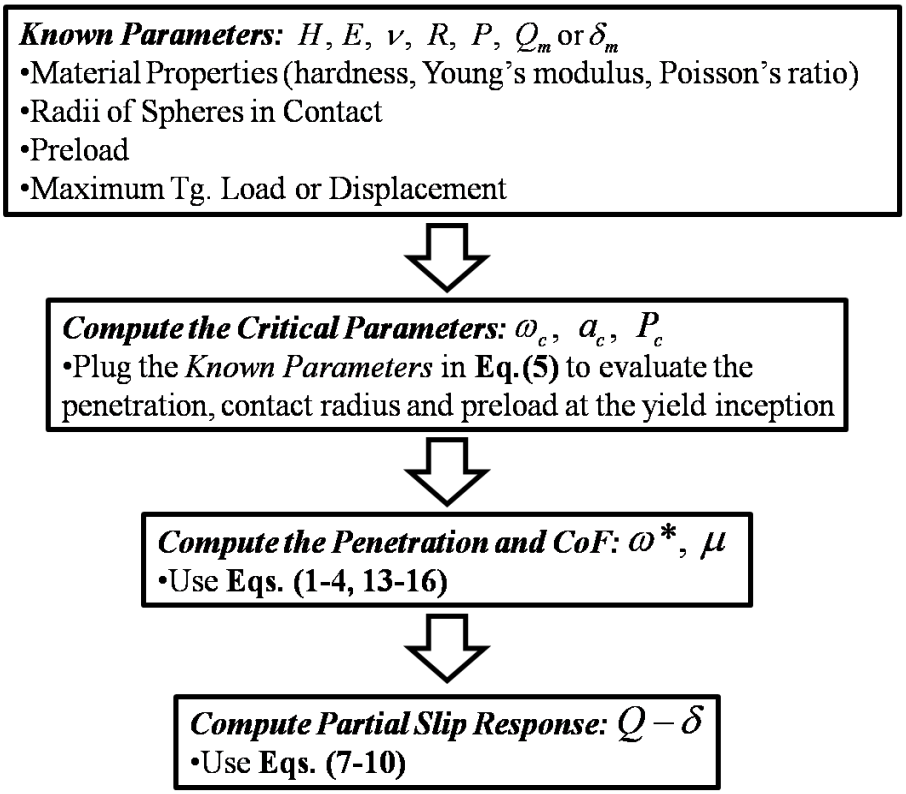

Fig. 3.5. The flow of computation to obtain the proposed partial slip responses.

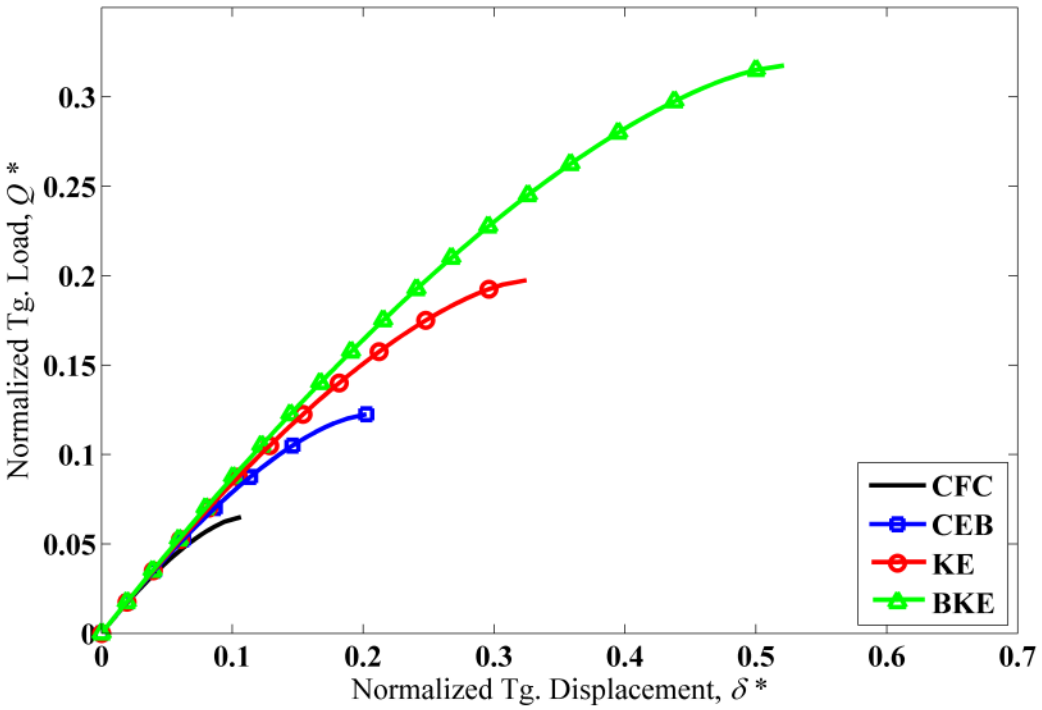

Fig. 3.6. Normalized tangential load vs. displacement obtained by the proposed models up to the onset of sliding. .

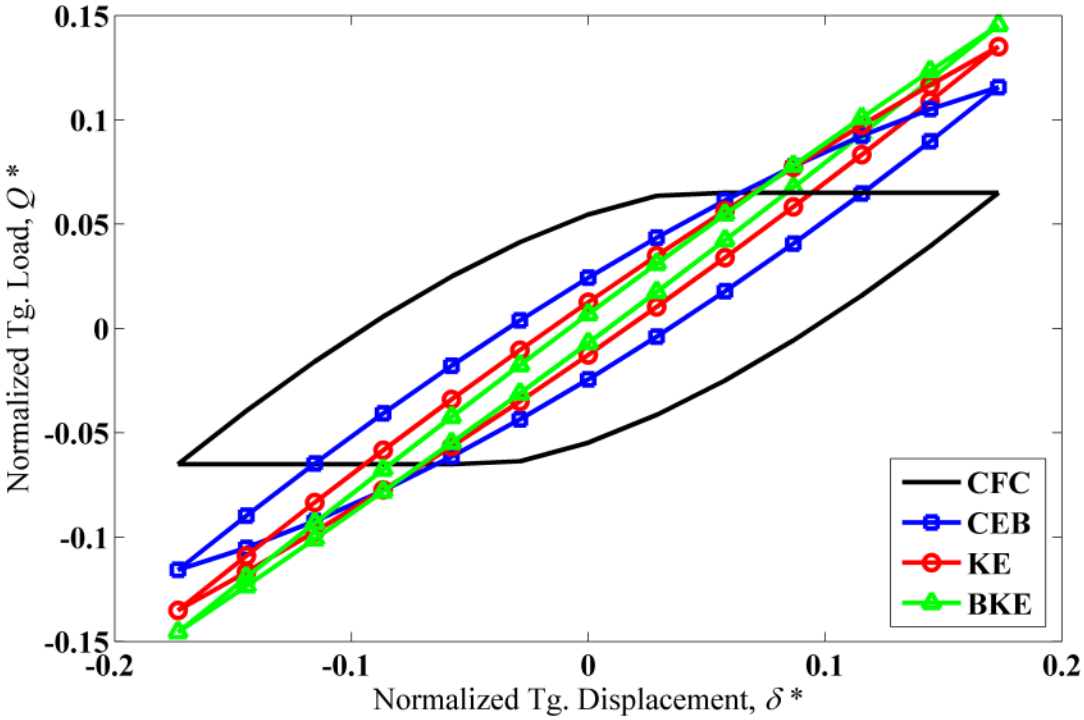

Fig. 3.7. Fretting loops obtained by the proposed models.

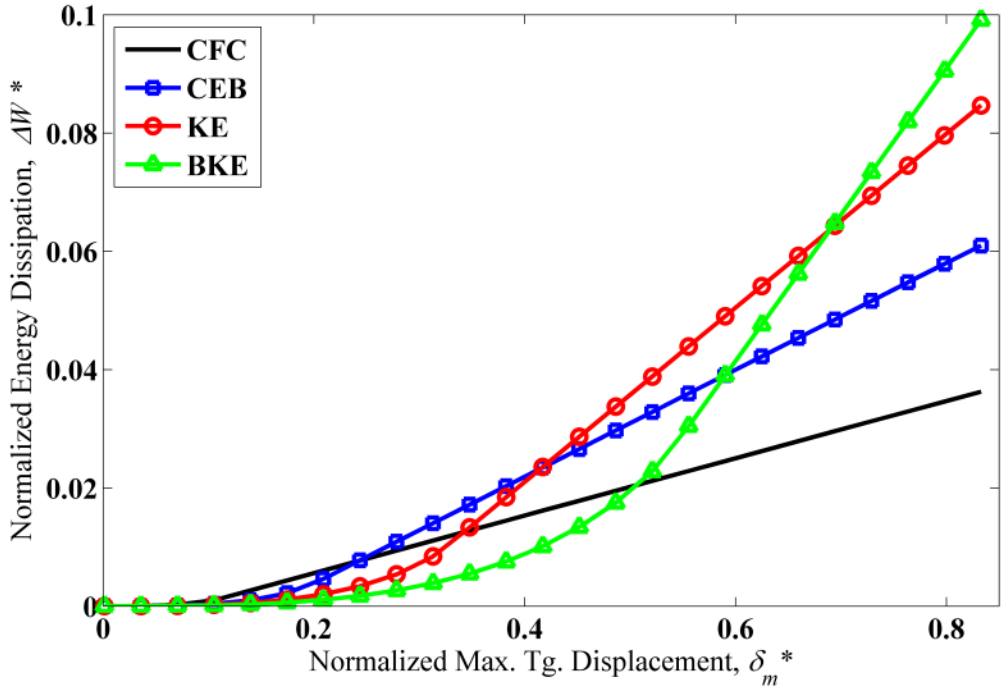

Fig. 3.8. Energy dissipation vs maximum imposed tangential displacement for each partial slip model.

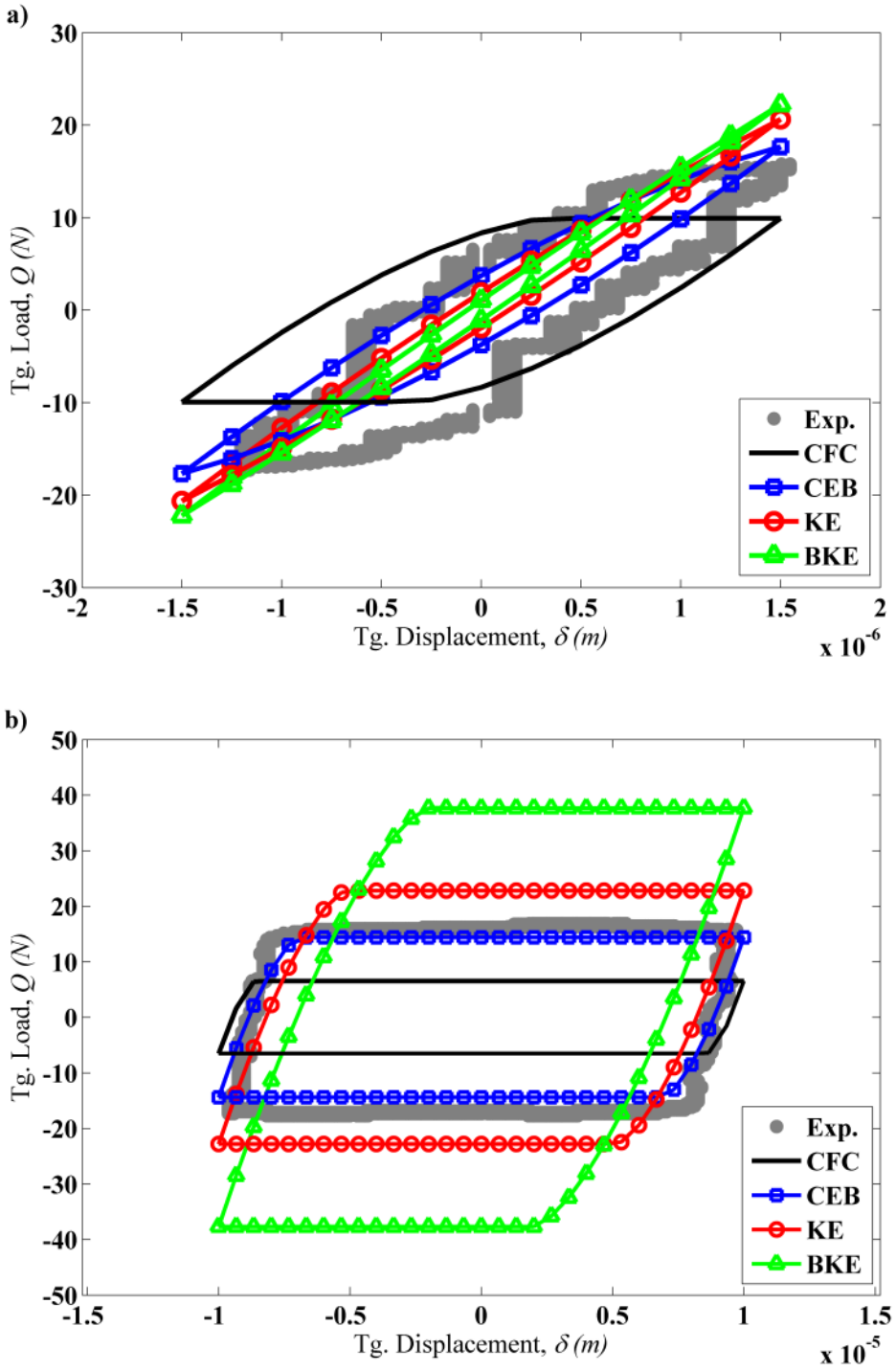

Fig. 3.9. Comparison of the proposed models and micro-scale experiment 1 (a) and experiment 2 (b).

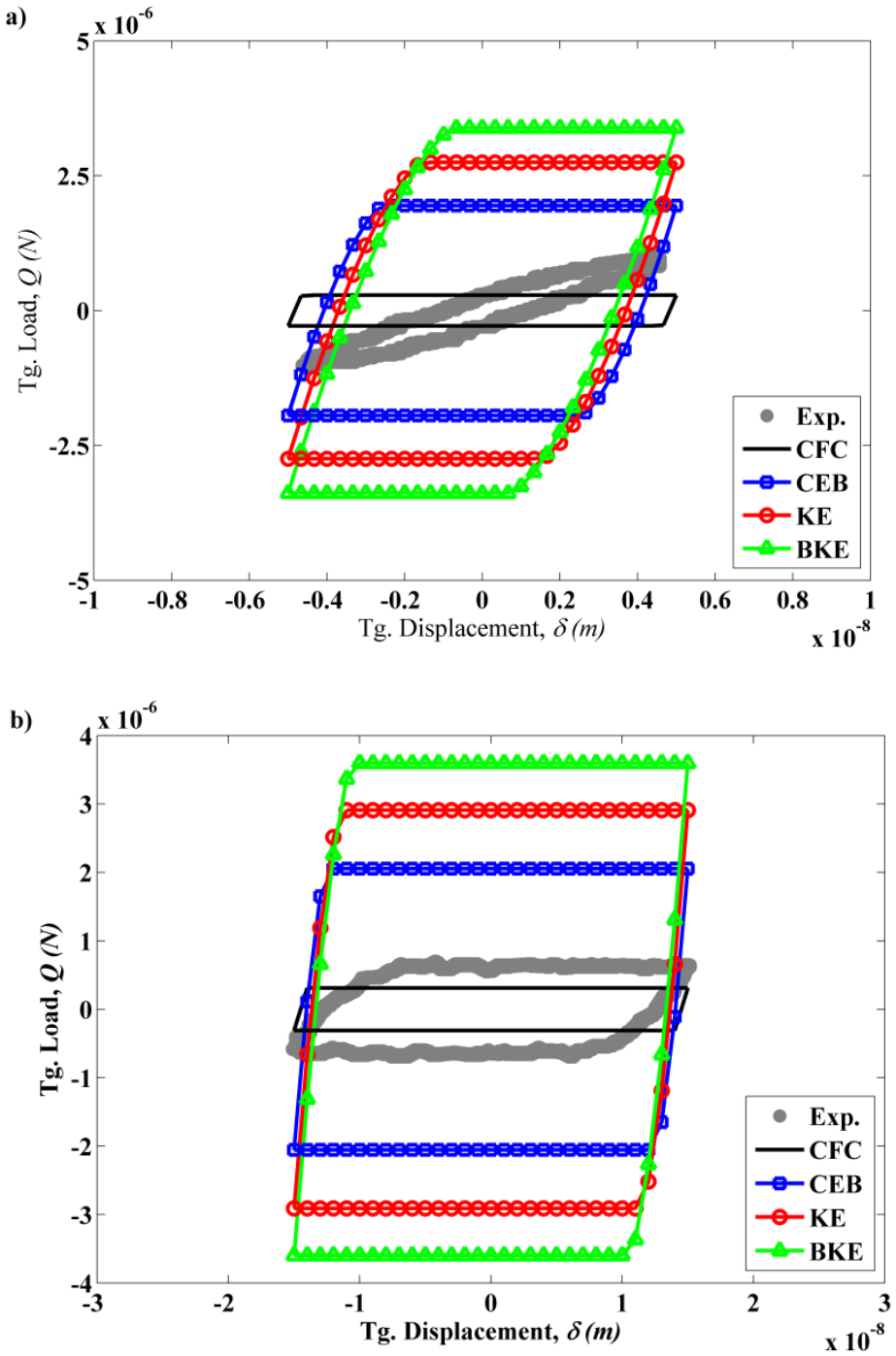

Fig. 3.10. Comparison of the proposed models and nano-scale experiment 1 (a) and experiment 2 (b).

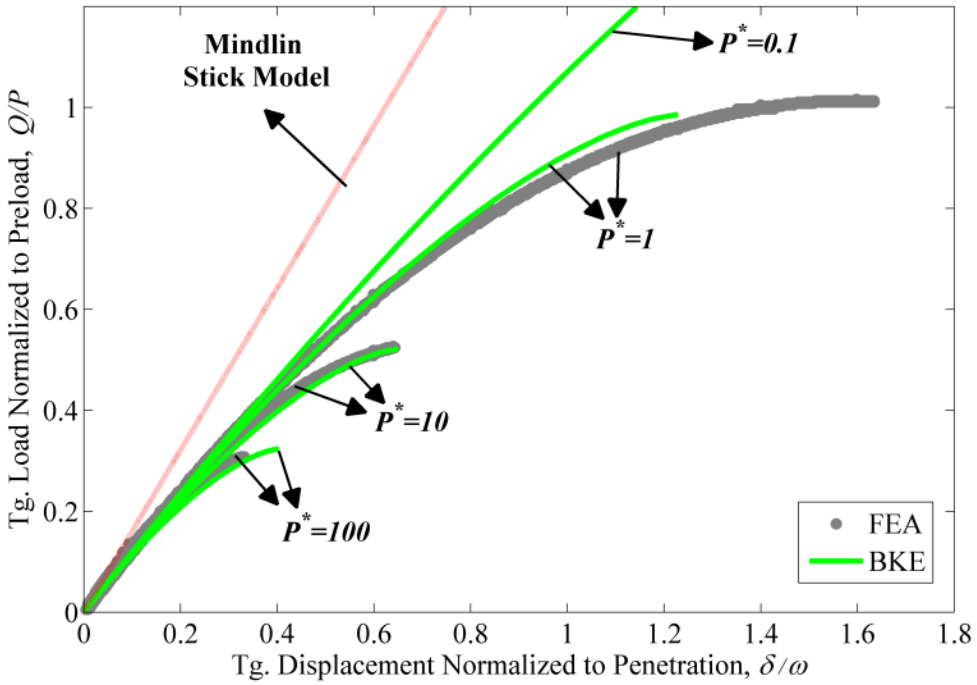

Fig. 3.11. Dimensionless tangential load vs. dimensionless tangential displacement predicted by BKE model for different normal preloads. FEA results reproduced from Brizmer et al. [50].

3.8. Tables

Table 3.1. Mechanical properties and geometry of contacting materials used in micro-scale experiments documented in Varenberg et al. [71]. Combined values are listed for reference to calculations done in this chapter.

Material	Poisson's ratio, ν	Shear Modulus, G (GPa)	Young's Modulus, E (GPa)	Hardness, H (HRC/GPa)	Geometry (Radius, mm)
Flat Steel (hardened)	0.3	82.7	207	63 / 7.48	Flat (∞)
Bearing Steel (SAE 52100)	0.3	82.7	207	60 / 6.83	Sphere (2.5)
Combined	0.3	24.3	113.8	60 / 6.83	Flat-on-sphere (2.5)

Table 3.2. Model parameters derived from the micro-scale experiments documented in Varenberg et al. [71].

Experiment	*P (N)*	δ_m *(μm)*	ω^*	R_a / ω	ε / ω_c	*μ (CFC, CEB, KE, BKE)*
Exp 1	35	1.5	0.374	0.02	5.4e-5	(0.284, 0.528, 0.858, 1.444)
Exp 2	23	10	0.283	0.024	5.4e-5	(0.284, 0.626, 0.992, 1.639)

Table 3.3. Mechanical properties and geometry of contacting materials used in nano-scale experiments documented in Varenberg et al. [71]. Combined values are listed for reference to calculations done in this chapter.

Material	Poisson's ratio, ν	Shear Modulus, G (GPa)	Young's Modulus, E (GPa)	Hardness, H (GPa)	Geometry (Radius, μm)
Flat Silicon (100)	0.28	43.9	112.4	11.3	Flat (∞)
Silica microspheres	0.19	28.0	68.0	4.8	Sphere (1.55)
Combined	0.19	9.6	44.7	4.8	Flat-on-sphere (1.55)

Table 3.4. Model parameters derived from the nano-scale experiments documented in Varenberg et al. [71].

Experiment	*P (μ N)*	δ_m *(nm)*	ω^*	R_a / ω	ε / ω_c	*μ (CFC, CEB, KE, BKE)*
Exp. 1	1.1	5	0.048	0.99	3.2e-2	(0.259, 1.769, 2.498, 3.077)
Exp. 2	1.2	15	0.051	0.94	3.2e-2	(0.259, 1.714, 2.424, 2.996)

CHAPTER 4: MACROSCALE FRICTION MODEL

4.1. Introduction

When a low-amplitude oscillatory tangential displacement or force is imposed on a preloaded contact, fretting occurs. During fretting, the contact can be under partial slip (some portion of the contact area is fully adhered whereas the remaining area slips) or both partial and gross slip conditions. This pre-sliding response was worked out first for preloaded spherical contacts by Cattaneo [3] and independently by Mindlin [4]. The response to cyclic loading was presented by Mindlin et al. [58] for elastic contacts and it was subsequently extended to the elastic-plastic contact case by Ödfalk and Vingsbo [26].

In all these works, *the Coulomb law of dry friction,* which couples normal to tangential tractions by a constant, μ, called the friction coefficient, is employed. This constant can be determined from experiments or found in look-up tables; alternatively, it can be varied arbitrarily to investigate the effect of frictional coupling on the response. Eriten et al. [33] incorporated preload-dependent friction coefficient models into Mindlin's model to formulate *physics-based* models for partial slip behavior of spherical contacts. The approach presented in Eriten et al. does not require any curve-fit or experimentally-determined parameters and assumes that constitutive material models hold for the contacting materials (i.e., Young's modulus, shear modulus, Poisson's ratio and yield strength can be defined from standard techniques). In these models, material and geometric properties of the contacting materials are needed to determine the load-deformation response of the spherical contact under partial slip condition.

Nominally flat contacts are found in many applications such as shrink fits, bolted joints and brakes. Modeling the fretting of a smooth flat-on-flat contact is more challenging than of a spherical contact due to the stress concentrations at the contact edges [45]. An early attempt to solve the flat-on-flat frictional contact problem with stress singularities was made by Comninou [76], where the contact between the wedge and elastic half space was assumed to be complete and smooth. However in practice, it is nearly

impossible to machine a perfectly smooth engineering surface (except for mica surfaces). Surface geometry will involve micro irregularities, called asperities, which essentially look like peaks and valleys on the surface. When such two nominally flat rough surfaces are brought into contact, contact occurs at asperity tips, and the real contact area constitutes only a few percent of the nominal contact area. Furthermore, the contact, and, thus, traction distribution over the contact patch becomes discontinuous, which drastically complicates the boundary value problem. Besides, stress intensification occurs at the asperity tips, and plastic yielding initiates even in the presence of very low normal loads. Therefore, purely elastic models are unable to model all the physics of fretting contact. In this study, we employ elastic-plastic models presented in Eriten et al. [33] to account for the effect of surface roughness on fretting of nominally flat rough surfaces.

Using various methods, researchers have long attempted to build-up contact models for nominally flat rough surfaces from asperity-scale mechanics. Four commonly used methods are as follows: analytical solutions by assuming regular roughness profiles such as contact of surfaces filled with periodic undulations [27]; numerical solutions or Finite Element Analysis (FEA) with a limited number of asperities [31,77]; numerical solutions for the contact of rough surfaces characterized by scale-independent fractal parameters [30]; and numerical and analytical solutions obtained by statistical summation of individual asperity contacts [16,29,78,79]. The last method is widely employed because it provides an efficient way to incorporate surface roughness parameters such as standard deviation of asperity heights, curvature of asperity tips and areal density of asperities into the contact load and deformation calculations. The contact models developed by the statistical method are shown to correlate well with experiments [80].

The aim of this chapter is to present a physics-based modeling approach for fretting behavior of nominally flat rough surfaces. The physics-based models developed by Eriten et al. [33] are used in the formulation of individual asperity-scale contact, and the flat contact forces are obtained by the statistical summation procedure outlined by Björklund [78].

4.2. Review of Utilized Models

Normal Contact of Nominally Flat Rough Surfaces

When two nominally flat rough surfaces are brought into contact; the contact occurs at the asperity tips and there is a normalized gap between the reference planes formed by the means of asperities of both surfaces. Assuming these reference planes stay parallel to each other over the whole contact area, the contact can be equivalently represented as contact between a smooth rigid flat surface and a rough surface with combined roughness. A variety of asperity height distributions are observed on engineering surfaces, with the normal distribution being the most common one for surfaces manufactured by abrasive and/or generic cumulative removal processes. Although running-in surfaces (produced by honing, lapping and superfinishing) usually exhibit asymmetrical surface height distributions (such as skewed and bimodal), asperity heights continue to exhibit distributions quite close to normal distribution [32,81–83].

The pioneering work of Greenwood and Williamson [29] —GW Model— introduced the statistical summation concept for the contact of nominally flat rough surfaces. The GW model essentially calculates the total normal contact load via a statistical summation of individual contributions of asperities carrying the load. The rough surface is assumed to be isotropic over a nominally flat area of A_0, which consists of spherical asperities with uniform areal density η and radius R. In addition, asperities are assumed to be distributed far apart over the contact surface, and, thus, there is no interaction between them.

Roughness of the two nominally flat surfaces can be combined using the approach documented in McCool [84], so that the contact problem is reduced to the contact of a rough surface with a rigid flat, as depicted in Fig. 4.1. The flat surface and the reference plane defined by the mean of asperity heights are separated by a distance, d. Therefore, an asperity makes contact with the flat surface and carries load provided that its height relative to the reference plane, z_i is greater than the separation, d; i.e. its interference is positive, $\omega_i = z_i - d > 0$. Assuming that the probability that a particular asperity has a height

between z and $z+dz$ is $\phi(z)$, and that the probability density function for asperity heights follows a Gaussian distribution with standard deviation of σ_a

$$\phi(z) = \frac{1}{\sqrt{2\pi}\sigma_a} \exp\left(-0.5\left(\frac{z}{\sigma_a} \right)^2 \right) \tag{4.1}$$

Normalizing the density function with the standard deviation of surface heights σ_s gives

$$\phi^*(z^*) = \frac{\sigma_s}{\sqrt{2\pi}\sigma_a} \exp\left(-0.5\left(\frac{\sigma_s}{\sigma_a} \right)^2 (z^*)^2 \right) \tag{4.2}$$

where $z^* = z/\sigma_s$, $\sigma_a/\sigma_s = \sqrt{1 - \frac{3.717\text{x}10^{-4}}{\beta^2}}$, and $\beta = \sigma_s R\eta$ is the roughness parameter which varies between 0.02 and 0.06 for many engineering surfaces. Following with the assumption that the sphere and rigid flat contact formulation, summarized in the Appendix B, holds for individual asperity contacts with the rigid flat, the total normal contact force for the flat surface, P_{flat}, can be expressed as

$$\begin{aligned} P_{flat}(d^*; \nu, H, A_0, \beta, \omega_c^*) &= \eta A_0 \int_d^\infty P(z-d; P_c, \omega_c, \nu)\phi(z)dz \\ &= \eta A_0 \int_{d^*}^\infty P(z^*-d^*; P_c, \omega_c^*, \nu)\phi(z^*)\sigma_s dz^* \\ &= \eta A_0 P_c \int_{d^*}^\infty f(z^*-d^*; \omega_c^*, \nu)\phi^*(z^*)dz^* \\ &= \frac{2\pi}{3} KHA_0 \beta\omega_c^* \int_{d^*}^\infty f(z^*-d^*; \omega_c^*, \nu)\phi^*(z^*)dz^* \end{aligned} \tag{4.3}$$

where $f(z^*-d^*; \omega_c^*, \nu) = P/P_c$ is the normalized asperity contact force given in Eqs. (B.1)-(B.4). Normalizing the contact force with material yield strength (KH) and nominal surface area A_0 leads to the expression

$$P_{flat}^*(d^*; \beta, \omega_c^*, \nu) = \frac{P_{flat}}{KHA_0} = \frac{2\pi}{3}\beta\omega_c^* \int_{d^*}^\infty f(z^*-d^*; \omega_c^*, \nu)\phi^*(z^*)dz^* \tag{4.4}$$

Note that Eq.(4.4) is a function of Poisson's ratio, roughness parameter β, dimensionless critical interference ω_c^*, and dimensionless separation between the rigid smooth surface and the mean of asperity

heights d^*. The dimensionless critical interference is a material- and geometry-dependent parameter showing the limit of elastic deformation of each asperity. Greenwood and Williamson introduced the plasticity index as a measure of the ratio of the plastically yielded areas to the total contact area for the contact of nominally flat rough surfaces. At low plasticity indices ($\psi < 0.6$), unrealistically high contact pressures are needed to cause considerable plastic yield at the nominally flat rough contact interface. In contrast, for large plasticity indices ($\psi > 1$), very light loads are shown to cause plastic flow, so the contact is said to be highly plastic. What happens in between, $0.6 < \psi < 1$, is considered to be elastic-plastic contact in this work, and the models described in the Appendix A cover that contact regime, as well as purely elastic contact. The plasticity index is shown to relate to the asperity critical interference by [29]

$$\psi = \frac{2E^*}{\pi KH}\sqrt{\frac{\sigma_s}{R}} = \left(\frac{\omega_c}{\sigma_s}\right)^{-1/2} = \left(\frac{\sigma_s}{\sigma_a}\omega_c^*\right)^{-1/2} \tag{4.5}$$

According to Eq.(4.5), rougher and softer surfaces are expected to have higher plasticity indices, and hence the contact of such surfaces is predominantly plastic. In contrast, smoother and harder surfaces exhibit lower plasticity indices and, thus, mostly elastic contact occurs.

Tangential Contact of Nominally Flat Rough Surfaces

Provided that the nominally flat surfaces slide against each other, the static friction force can be obtained by the same procedure as normal loading. This is essentially because all of the asperities show gross sliding behavior, and their reaction to tangential loading is assumed to be governed by a local Coulomb friction law. Note that, since the friction coefficient models, except for CFC—constant friction coefficient—, depend on the interference, the friction coefficient remains in the integrand of the statistical summation integral as

$$Q_{flat}^{\max} = \eta A_0 \int_d^\infty \mu P \phi(z) dz \tag{4.6}$$

and in nondimensional form as

$$Q_{flat}^{*\max}\left(d^*;\beta,\omega_c^*,\nu\right)=\frac{Q_{flat}^{\max}}{KHA_0}=\frac{2\pi}{3}\beta\omega_c^*\int_{d*}^{\infty}\mu\left(z^*-d^*;\omega_c^*,\nu\right)f\left(z^*-d^*;\omega_c^*,\nu\right)\phi^*(z^*)dz^* \quad (4.7)$$

One of the assumptions made in this formulation is that asperity scale friction is modeled after Coulomb friction. Hurtado and Kim [21] showed that friction stress is contact-size dependent by employing a dislocation model of frictional slip. According to the Hurtado and Kim model, the friction stress reduces an order of magnitude from nanoscale contact to microscale contacts and becomes size-independent for contact sizes larger than 10 μm. The inherent assumption of our modeling approach is that asperity scale contact falls in this size-independent regime and experimental conditions should comply with this assumption (the scale of the nominally flat rough surfaces in contact should be at least on the order of millimeters and the mean radius of asperities should not be lower than 10 μm).

When the tangential load is insufficient to cause gross sliding, the response of each asperity is coupled to the normal loading. Shorter asperities carry less normal load and hence slide more easily than taller asperities. Also, the loading history affects the tangential response of each asperity: As can be seen in Eqns. (3.7)-(3.9), individual asperity responses to loading, unloading and reloading differ due to history-dependence of tangential loading. Fig. 4.2 shows the different response regions for asperities with varying heights during a) loading and b) unloading conditions. In Fig. 4.2 a and b, the probability density of asperity heights on a rough surface is described by a normal distribution, and the separation between two rough surfaces is set to a normalized distance *d* from the mean of asperity heights. Therefore, asperities with heights greater than *d* are in contact and assumed to carry normal and tangential load. The asperities in contact can be separated into two groups while loading and three groups while unloading: slip-slip, slip-stick and stick-stick according to the asperities' response to loading-unloading as described elsewhere [31,78,85]. Under initial loading, while taller asperities stick and contribute to the tangential stiffness of the contact, shorter asperities slip and cause frictional energy dissipation. A subsequent unloading of the contact results in three different asperity behaviors. The asperities which stick through initial loading remain stuck while unloading, since the contact force on these asperities prevents any

slippage. In contrast, while unloading the asperities which slip while loading can either slip or stick, depending on their heights. This is mainly due to a decrease in tangential force upon unloading. Since the preload on these asperities does not change throughout tangential loading/unloading, the limiting tangential force is constant. Therefore, a decrease in tangential force results in some of the asperities carrying tangential force of less than the limiting force, and, thus, they start sticking while unloading. As expected, the shorter asperities among these previously slipping asperities continue slipping, whereas the taller asperities stick.

This approach assumes that the asperities carry the tangential load as parallel springs, and, hence, the imposed displacement on the nominally flat contact is fully transferred to each asperity. Therefore, it is beneficial to express the tangential response for individual spheres given in Eqs. (3.6)-(3.9) as tangential force rather than displacement. Expressing the nondimensional displacement in terms of normal penetration using the elastic portion of Eqns.(3.1)-(B.8) and the critical parameters in Eq.(3.5), we arrive at the expression

$$\tilde{\delta} = \frac{16G^* a\delta}{3\mu P} = \frac{16G^* a_c \left(\omega/\omega_c\right)^{0.5}\delta}{3\mu P_c \left(\omega/\omega_c\right)^{1.5}} = \frac{4G^*\delta}{\mu E^* \left(z-d\right)} = \frac{4G^*\delta^*}{\mu E^* \left(z^*-d^*\right)} \tag{4.8}$$

When elastic-plastic penetration regimes are involved, the ratio a/P differs from the expression used in Eq.(4.8). However, the actual expressions calculated by Eqs. (A.1)-(A.8) causes at most 10% error, and, hence, the expression for fully elastic contact is adopted by the modeling approach in this chapter. The tangential force for the asperities in the slip (loading) and slip-slip (unloading) zones is assumed to obey the Coulomb friction law with a constant friction coefficient. The tangential force for the asperities in the slip-stick and stick-stick regions, on the other hand, is given by the partial slip solution to cyclic loading proposed by Mindlin et al. [58]. The following expressions are obtained by substituting Eq.(4.8) in Eqs.(3.7)-(3.9) and solving for the tangential force in terms of nondimensional tangential displacement δ^*:

Partial Slip (loading):

$$Q\left(z^*,\delta^*;\lambda\right)=\mu P\begin{cases}1-\left(1-\dfrac{4G^*\delta^*}{\mu E^*\left(z^*-d^*\right)}\right)^{3/2} & z^*\le z_0^*\\ 1 & z^*>z_0^*\end{cases} \tag{4.9}$$

Here, $z_0^*=d^*+\dfrac{4G^*\delta^*}{\mu E^*}$, and $\lambda=\{G^*,E^*,\mu,P,d^*\}$ is the parameter set. The statistical summation utilizing the normal distribution of asperity heights gives the tangential force for flat on flat contact as

$$Q_{flat}^{l}\left(\delta^*;\lambda\right)=\eta A_0\int_{d^*}^{\infty}Q\left(z^*,\delta^*;\lambda\right)\phi^*(z^*)dz^*\Rightarrow$$

$$Q_{flat}^{*l}\left(\delta^*;\lambda\right)=\frac{Q_{flat}^{l}}{KHA_0}=\frac{2\pi}{3}\beta\omega_c^*\left\{\int_{d^*}^{z_0^*}\mu f\left[1-\left(1-\frac{4G^*\delta^*}{\mu E^*\left(z^*-d^*\right)}\right)^{3/2}\right]\phi^*dz^*+\int_{z_0^*}^{\infty}\mu f\phi^*dz^*\right\} \tag{4.10}$$

Partial Slip (unloading):

$$Q\left(z^*,\delta^*,\delta_{\max}^*;\lambda\right)=\mu P\begin{cases}-1 & z^*\le z_1^*\\ 2\left(1-\dfrac{2G^*\left(\delta_{\max}^*-\delta^*\right)}{\mu E^*\left(z^*-d^*\right)}\right)^{3/2}-1 & z_1^*\le z^*<z_2^*\\ 2\left(1-\dfrac{2G^*\left(\delta_{\max}^*-\delta^*\right)}{\mu E^*\left(z^*-d^*\right)}\right)^{3/2}-\left(1-\dfrac{4G^*\delta_{\max}^*}{\mu E^*\left(z^*-d^*\right)}\right)^{3/2}-1 & z_2^*\le z^*\end{cases} \tag{4.11}$$

Here, $\delta_{\max}^*$ is the maximum tangential displacement (tangential displacement at tangential force $\tilde{Q}_{\max}$) and limiting heights $z_1^*=d^*+\dfrac{2G^*\left(\delta_{\max}^*-\delta^*\right)}{\mu E^*}$, $z_2^*=d^*+\dfrac{4G^*\delta_{\max}^*}{\mu E^*}$. Statistical summation yields the tangential force for nominally flat surfaces under tangential unloading as

$$Q_{flat}^{unl}\left(\delta^*,\delta_{\max}^*;\lambda\right)=\eta A_0\int_{d^*}^{\infty}Q\left(z^*,\delta^*,\delta_{\max}^*;\lambda\right)\phi^*(z^*)dz^*\Rightarrow$$

$$Q_{flat}^{*unl}=\frac{Q_{flat}^{unl}}{KHA_0} \tag{4.12}$$

$$=\frac{2\pi}{3}\beta\omega_c^*\begin{Bmatrix}-\int_{d^*}^{z_1^*}\mu f\phi^*dz^*+\int_{z_1^*}^{z_2^*}\mu f\left[2\left(1-\frac{2G^*\left(\delta_{\max}^*-\delta^*\right)}{\mu E^*\left(z^*-d^*\right)}\right)^{3/2}-1\right]\phi^*dz^*+\\ \int_{z_2^*}^{\infty}\mu f\left[2\left(1-\frac{2G^*\left(\delta_{\max}^*-\delta^*\right)}{\mu E^*\left(z^*-d^*\right)}\right)^{3/2}-\left(1-\frac{4G^*\delta_{\max}^*}{\mu E^*\left(z*-d*\right)}\right)^{3/2}-1\right]\phi^*dz^*\end{Bmatrix}$$

The same process that occurs during unloading also occur in reloading, but in the reverse direction, and, hence, the tangential force for nominally flat surfaces in reloading can be found from the unloading response simply by reversing the directions of force and displacement.

Partial Slip (reloading): $$Q_{flat}^{*rel}\left(\delta^*,\delta_{\max}^*;\lambda\right)=-Q_{flat}^{*unl}\left(-\delta^*,\delta_{\max}^*;\lambda\right) \tag{4.13}$$

Contacts under partial slip and gross slip experience frictional energy losses. The loss per each fretting cycle is important in the calculation of the damping characteristics of the nominally flat contact and can be found by the difference of work done during reloading and energy recovered during unloading. In other words, the area inside each fretting loop yields the energy loss in that cycle. Therefore, the energy loss per fretting cycle can be obtained in nondimensional form as

$$W_{flat}^*\left(\delta_{\max}^*;\lambda\right)=\int_{-\delta_{\max}^*}^{\delta_{\max}^*}\left(Q_{flat}^{*rel}-Q_{flat}^{*unl}\right)d\delta^* \tag{4.14}$$

4.3. Proposed Friction Model

The models proposed in this chapter employ the physics-based formulation for fretting behavior of sphere-on-flat contact [33] for the response of each asperity and sum these responses using the statistical framework proposed by Greenwood and Williamson [29] to obtain the fretting response for elastic/plastic contact of nominally flat rough surfaces. Use of statistical summation is common in modeling normal preload [12,29] and tangential loading response [18,78,86] of flat surfaces. However, a physics-based

friction and elastic-plastic loading model for asperity level contact has not previously been used, to the authors' knowledge, in modeling fretting of flat surfaces. This physics-based modeling approach allows the study of the influence of surface roughness (statistical representation of roughness) on fretting.

In this approach, the contact between two nominally flat rough surfaces is replaced by the contact of a smooth rigid surface and a deformable flat surface with combined roughness properties. The following parameters are needed in the model: First, the combined material properties (hardness, Poisson's ratio, Young's and shear moduli) are computed from material properties of each contacting material as described in the previous section. Second, combined roughness parameters (rms roughness, areal density, and mean radius of asperities) are determined from the surface profile measurements of each contacting surface. An example of the second step can be found in the next chapter, where combined roughness parameters of lap joints are calculated. Last, the preload and maximum tangential displacement imposed on the flat contact should be known prior to calculation of the fretting response. In fretting experiments, the preload is usually kept constant, and either maximum tangential displacement or force is imposed on the contact. The formulation given above and our experiments with lap joints assume constant preload and tangential displacement as the known loading conditions. This formulation can readily be converted to the maximum tangential force using Eq.(B.15).

The next step after determining the modeling parameters is to find the normalized separation, between the rigid flat and mean of asperities as shown in Fig. 4.1. Using the material and surface roughness properties, the critical interference and preload are computed using Eq. (B.9). Assuming a constant preload is imposed on the contact during each experiment, Eq. (4.3) is employed to obtain the normalized separation, which is needed to determine how much each asperity is compressed during normal loading. Furthermore, the tangential response of each asperity depends on the amount of compression it experiences, which is mathematically modeled using the conditional statements in Eqs. (4.9) and (4.11). Employing the maximum tangential displacement imposed in the experiments in Eqs. (4.9) and (4.11), the tangential response of each asperity under loading and unloading conditions can then

be found. Finally, the fretting response of the flat follows from the statistical summation procedure outlined in Eqs. (4.10), (4.12) and (4.13). As given in Eq. (4.14), another integration is needed to compute energy loss per fretting cycle. Note that the flat contact models are named after the asperity-level contact and friction models they use; i.e., the Kogut and Etsion (KE) model is essentially found from Eqs. (4.10), (4.12) and (4.13) with the asperity load-penetration relation given in Eq. (B.3) and friction coefficient given in Eq. (B.12). Only the CFC model is an exception to this naming. The CFC model uses the Hertzian load-penetration relation and a constant coefficient of friction. Blau [87] documents friction coefficient values ranging from 0.2 to 1.5 for metal-on-metal contacts. Specifically, the friction coefficient value for steel-on-steel (1032) is given as 0.31. In accordance with that value, 0.3 is used in the following simulations. The CFC model is essentially identical to Björklund's model [78], and is used as a basis of comparison for the advanced physics-based models proposed in this chapter. Fig. 4.3 summarizes the above-mentioned steps in a flow chart and gives the necessary equations explicitly for the BKE model. The other models can be obtained using the same computational flow.

Fig. 4.4 presents the normalized fretting responses calculated by each model using the computational flow chart given above. The contact is simulated under highly elastic conditions (plasticity index is 0.5), and the roughness parameter β is 0.04. The normalized preload and maximum tangential displacement used in the simulations are 0.001 and 0.6, respectively. This normalized preload corresponds to 531 N for the steel joint sample used in the experiments described in the next chapter. The normalized tangential displacement of 0.6 is chosen such that all models remain in the partial slip fretting regime (note that the CFC model enters the gross slip regime for displacements larger than 0.6). By comparison, the CFC model predicts the smallest friction force for flat contact. The maximum normalized force approaches 0.0003 at the inception of gross slip for the CFC model, which assumes a constant friction coefficient of 0.3 for each asperity ($Q^*_{flat} = 0.3P^*_{flat}$). As expected, the maximum tangential force for the flat contact increases by increasing the friction coefficient at the asperity-scale. The increase in the maximum tangential force for the flat contact from the CEB, KE and BKE models is due to this asperity-scale

increase. The fretting loops become narrower approaching a single line (such as in elastic non-dissipative contact) as the maximum tangential force predicted by the models increases. This result is physically sound since friction force is the mechanism balancing the tangential force carried by the flat contact, and the friction force increases with friction coefficient. In the limit, when friction coefficient goes to infinity, the flat contact becomes fully-adhered and elastic in the case of plasticity indices lower than 0.6. Fully-adhered elastic contact does not result in energy loss during the tangential loading and unloading cycling, and therefore a linear force-displacement relationship is expected. The BKE model in the case of plasticity index 0.5 approaches this fully-adhered elastic contact behavior.

Fig. 4.5 and 6 show the evolution of fretting loops when the plasticity index increases to 1 and 2, respectively; i.e., the flat contact becomes significantly plastic. Note that the CFC model predictions remain nearly identical to the elastic loading case. This is because neither the friction coefficient nor the normal preload function used for the CFC model depends on the extent of plastic deformation. However, increasing plasticity index means softer material in contact and thus larger penetration of the rigid flat. Mathematically, the separation *d* between surfaces (see Eq.(4.4)) decreases by increasing plasticity under the same normal preload. This decrease will expand the slip region seen in the height distributions shown in Fig. 4.2. The variation of the separation *d* with changing plasticity index is negligibly small so its effect on fretting loops is barely noticeable in Fig. 4.4-6. For all other models, the maximum tangential force decreases by increasing plasticity and, thus, the contact starts to experience gross slip fretting rather than the partial slip seen in the elastic case.

A more dramatic decrease in the maximum tangential force is seen in the case of $\psi = 2$, shown in Fig. 4.6. As the contact tends to fully plastic, i.e., $\psi \to \infty$, the friction coefficient predictions of the CEB and KE models vanish, as do the fretting loops. Vanishing friction coefficient in the CEB model is due to the assumption that sliding inception is tied to plastic yield inception. Similarly, the KE model associates sliding inception with the plastic yielding reaching the contact patch. However, this behavior is unlikely to be observed in reality because, no matter how plastic the contact under normal loading may be, there

will always exist a tangential force as a reaction to loading in the shear direction, as long as elastic material is present. Tangential force can be expected to vanish only when sufficient portion of the contact patch and material surrounding that patch yield [88]. In line with this observation, the response of the BKE model seems physically more sound in friction coefficient modeling for highly plastic contacts. However, maintaining fully adhered contact conditions under laboratory conditions is difficult, and gross and partial slip responses are inevitable, in which the CEB and KE models can be more favorable than the BKE model [39]. Table 4.1 shows the friction coefficients predicted by each models at different plasticity indices.

Evidently, the plasticity index is a critical parameter in the proposed modeling approach. However, the plasticity index is not constant during the life cycle of an interface and is influenced by the running-in conditions. The more fretting cycles a contact surface is exposed to, the more plastic deformation and wear occurs at the asperity tips (asperity tip flattening). Accordingly, the rms roughness decreases whereas the average radius of asperities increases. Therefore, the plasticity index decreases as can be seen from Eq.(4.5), and the contact becomes more elastic. That, in turn, results in narrower fretting loops with the lapse of time in a fretting contact. Similar observations were made by Zhou et al. [89], where Al-Li alloy specimens were fretted through a sphere-on-flat contact. Frictional "logs" (3D plots of tangential force vs. displacement vs. number of cycles) obtained from these experiments show that the friction loops become narrower as the number of cycles increases. Surface degradation and wear caused by plastic deformations are presented as the main causes of the shrinkage in these loops. We believe that the proposed modeling approach, which builds the fretting response from asperities to flat contact captures this running-in behavior.

Fig. 4.7 presents energy loss per cycle predictions for each model and the three different plasticity indices, 0.5, 1 and 2 (the maximum normalized tangential displacement is varied from 0 to 1 in these simulations). There are basically two different parts in each of these energy loss curves: a nonlinear part corresponding to low tangential displacements, and a linear part for higher tangential displacements.

Under low tangential displacements, the flat contact does not slide, but remains in the partial slip fretting regime. Since the extent of sliding is limited in partial slip regime, energy dissipation is lower than for the gross slip regime. The nonlinear relationship between energy loss and tangential displacement stems from the cubic nonlinearity that is predicted in sphere-on-flat asperity scale contacts (see Eq.(B.20)). In the gross slip fretting regime the relationship becomes linear since the maximum tangential force remains constant and, thus, a further increase in displacement adds a rectangular area to the energy dissipation. Hence, the maximum tangential force determines the slope in the linear energy loss regime.

Note that energy losses predicted by the CFC model do not vary significantly with plasticity index because of the same reason as to why fretting loops look almost identical for the same model. The simulations for the remaining models show that energy loss increases with plasticity index under partial slip regime. This result is in line with the observations of Johnson [59] and Ödfalk and Vingsbo [26], which essentially state that plastic deformations at the asperity scale can significantly increase the energy dissipation for contacts under partial slip. Furthermore, the transition to the gross slip regime occurs earlier for higher plasticity indices. This early transition means lower maximum tangential force and, hence, lower slopes in the linear energy loss regime seen for gross slip fretting. Therefore, although it might appear counterintuitive, the energy loss results obtained by this modeling approach suggest that there exists a tangential displacement at which the elastic contact under gross slip fretting starts to dissipate more energy than the plastic one.

4.4. Conclusion

We proposed physics-based models for fretting of nominally flat rough surfaces and demonstrated their validity and limitations by comparing simulations with experimental results. The models employ Mindlin's partial slip response to monotonous and cyclic loading response and couple it with elastic-plastic preload and preload-dependent friction coefficient models. Associating sliding inception with plastic yielding and junction weakening, the models predict the tangential response for spherical contacts using only material and geometric properties. Furthermore, individual physics-based spherical contact

models are summed statistically with probability density of asperity heights to obtain forces for nominally flat rough surfaces. This enables physics-based build-up from micromechanics of asperity deformation to surface roughness of flat contact.

4.5. Figures

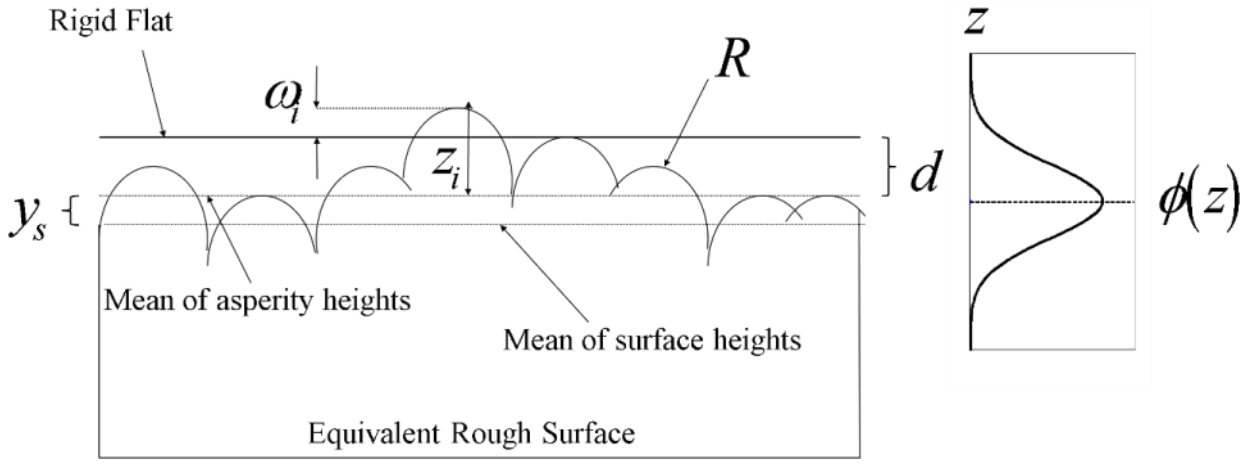

Fig. 4.1. Schematic representation of an equivalent rough surface and a rigid flat contact and, probability density function for asperity heights.

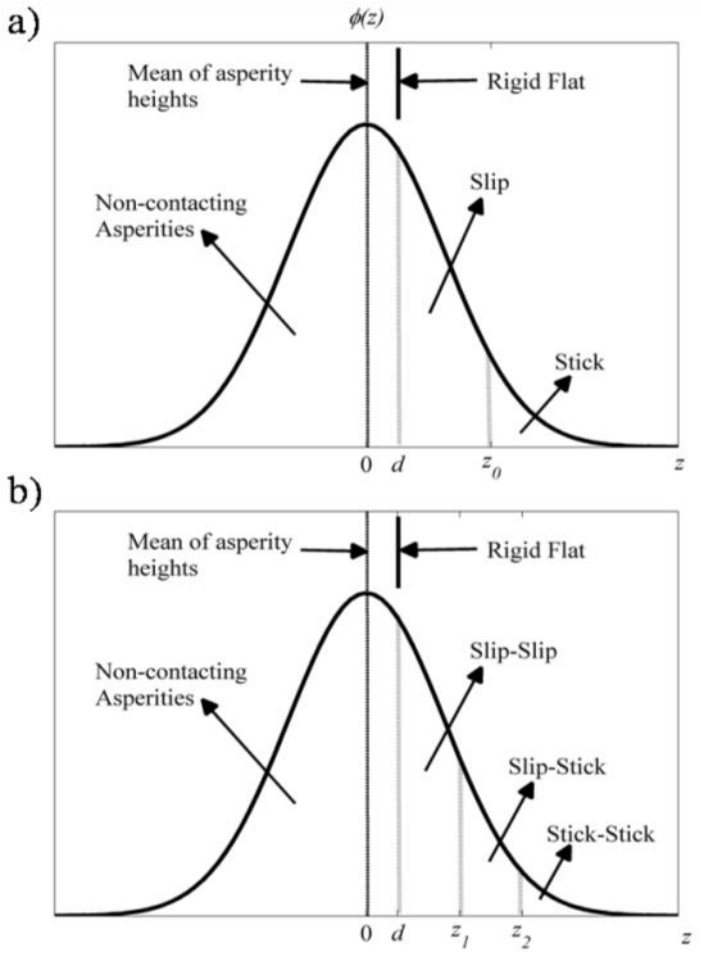

Fig. 4.2. Asperity behavior in statistical rough contact in relation to different regions of the probability density function of the asperity heights: a) loading, b) unloading.

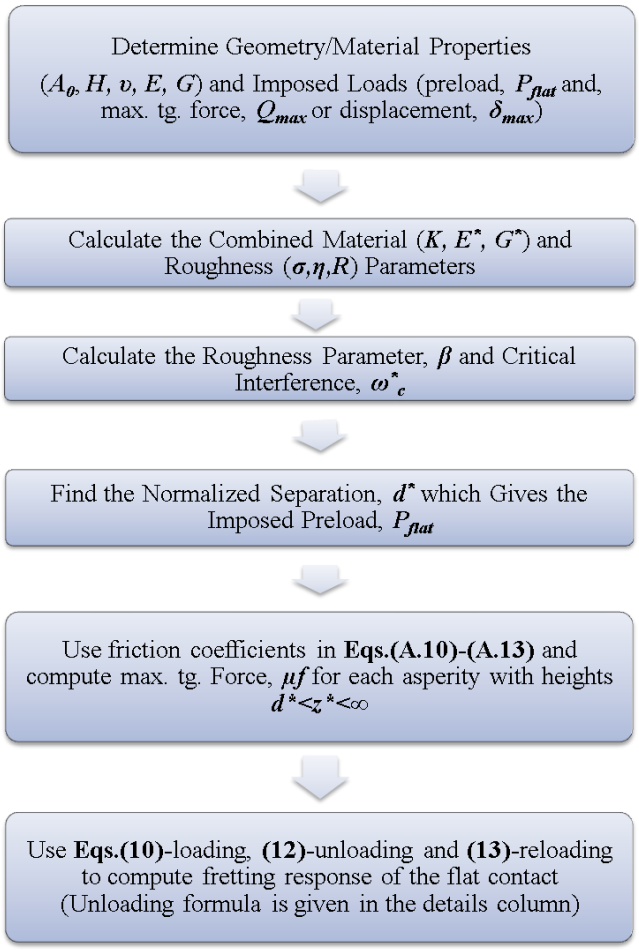

Material properties: supplier datasheet, material databases or uniaxial tension/compression and indentation tests
Imposed Loads: measured from experiments or generic values specific to flat contact application

$$K = 0.454 + 0.41\nu, \quad E^* = \left((1-\nu_1^2)/E_1 + (1-\nu_2^2)/E_2\right)^{-1}$$

$$G^* = \left((2-\nu_1)/G_1 + (2-\nu_2)/G_2\right)^{-1}$$

Roughness parameters: Surface height data from each surface can be combined with the procedure given in **Eq. 15**.

Roughness parameter and the critical interference is calculated by $\beta = \eta R\sigma, \quad \omega_c^* = \left(\frac{\pi KH}{2E^*}\right)^2 \frac{R}{\sigma}$

$$P_{flat} = \frac{2\pi}{3} KHA_0 \beta \omega_c^* \int_{d^*}^{\infty} f\left(z^* - d^*; \omega_c^*, \nu\right) \phi^*(z^*) dz^*$$

where $f = P/P_c$ in Eqs. (A.1-4) –the function for the BKE model is given as example

$$f_{BKE} = P_{BKE}/P_c = \frac{\bar{I}_c}{\bar{\delta}_c^{1.5}} \begin{cases} (\omega/\omega_c)^{1.5} & \omega/\omega_c \le \bar{\delta}_c \\ (\omega/\omega_c)^{1.5}\left(1 - \exp\left(\bar{\delta}_c^{\alpha} / \left(\bar{\delta}_c^{\alpha} - (\omega/\omega_c)^{\alpha}\right)\right)\right) & \omega/\omega_c > \bar{\delta}_c \end{cases}$$

and, $\phi^*\left(z^*\right) = \frac{\sigma_s}{\sqrt{2\pi}\sigma_a} \exp\left(-0.5\left(\frac{\sigma_s}{\sigma_a}\right)^2 \left(z^*\right)^2\right)$

For instance, the BKE model friction coefficient predictions are given as

$$\mu_{BKE}(\omega, \omega_c, \nu) = 0.26 \coth\left(0.27\left(\bar{\delta}_c^{-1}\omega/\omega_c\right)^{0.46}\right)$$

$$Q_{flat}^{unl} = \frac{2\pi}{3} KHA_0 \beta \omega_c^*$$

$$\begin{cases} -\int_{d^*}^{z_1^*} \mu f \phi^* dz^* + \int_{z_1^*}^{z_2^*} \mu f \left[2\left(1 - \frac{2G^*\left(\delta_{\max}^* - \delta^*\right)}{\mu E^*\left(z^* - d^*\right)}\right)^{3/2} - 1\right] \phi^* dz^* + \\ \int_{z_2^*}^{\infty} \mu f \left[2\left(1 - \frac{2G^*\left(\delta_{\max}^* - \delta^*\right)}{\mu E^*\left(z^* - d^*\right)}\right)^{3/2} - \left(1 - \frac{4G^*\delta_{\max}^*}{\mu E^*\left(z^* - d^*\right)}\right)^{3/2} - 1\right] \phi^* dz^* \end{cases}$$

Fig. 4.3. Computational flow chart for obtaining the fretting response for nominally flat rough surfaces using the advanced physics-based interfacial models and equations used at each step.

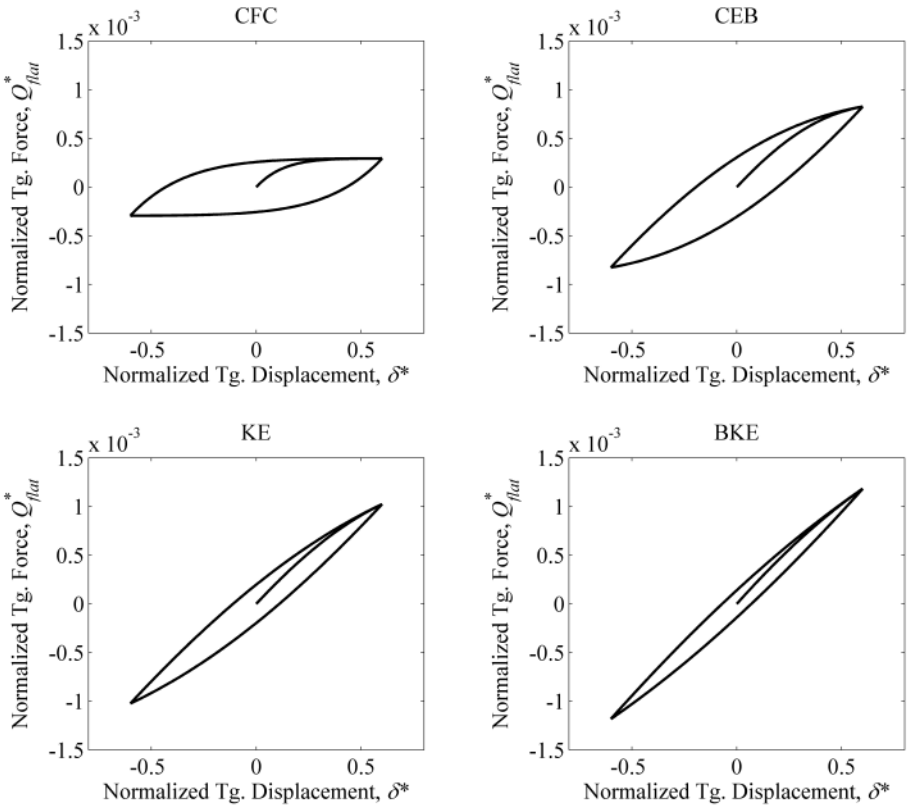

Fig. 4.4. Modeled results of fretting loops obtained from four different models under elastic contact conditions, $\psi = 0.5$).

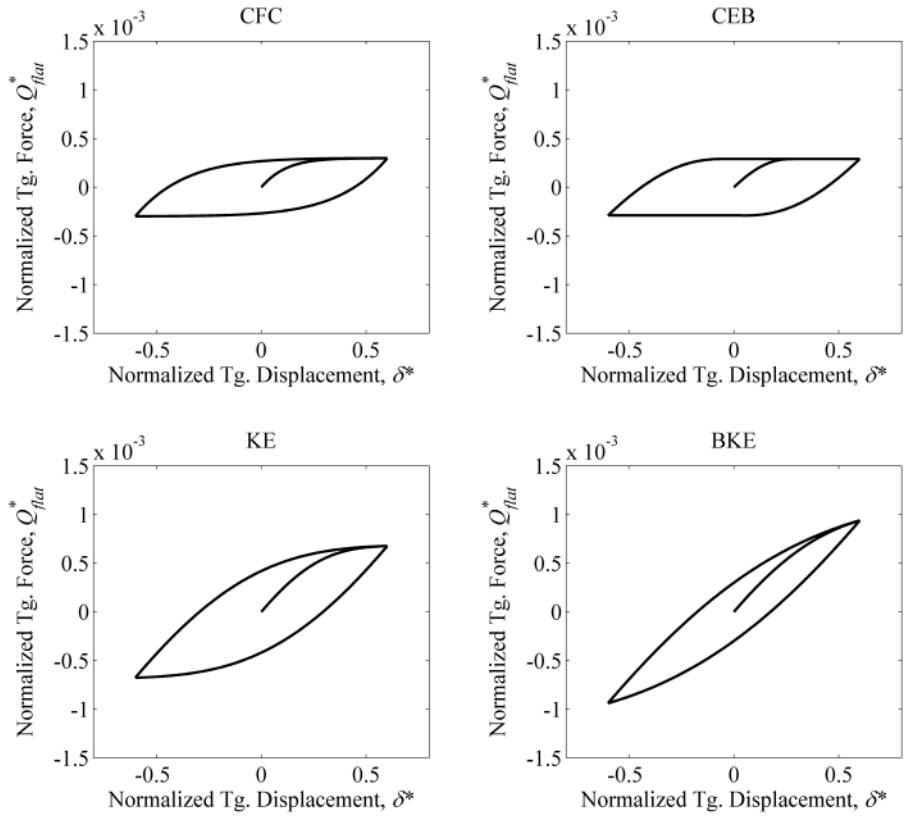

Fig. 4.5. Modeled results of fretting loops obtained from different models under elastic-plastic contact conditions, $\psi = 1.0$).

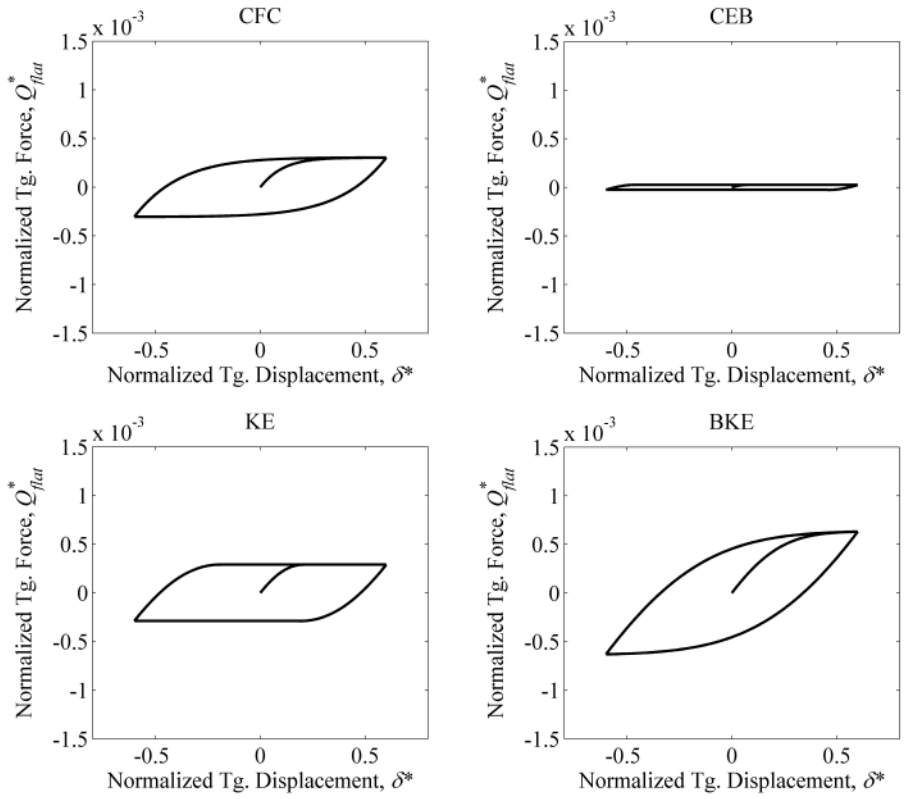

Fig. 4.6. Modeled results of fretting loops obtained from different models under severe plastic contact conditions, ψ = 2.0).

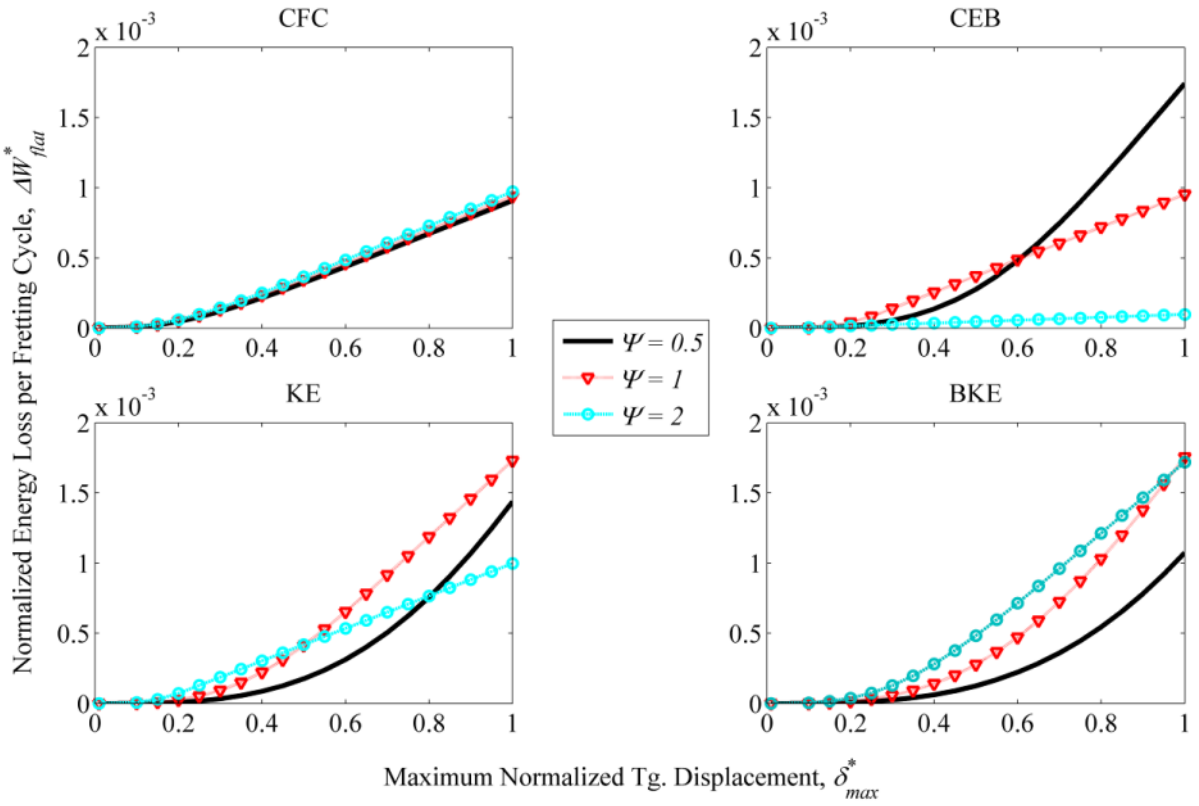

Fig. 4.7. Modeled results of energy loss per cycle obtained from different models and different plasticity indices.

4.6. Tables

Table 4.1. Friction coefficients predicted by each model at different plasticity indices

Models	$\psi = 0.5$	$\psi = 1$	$\psi = 2$
CFC	0.3	0.3	0.3
CEB	0.83	0.29	0.03
KE	1.02	0.68	0.29
BKE	1.18	0.94	0.63

CHAPTER 5: EXPERIMENTAL VALIDATION

5.1. Introduction

Oscillatory loads due to vibration of a structural component containing joints may induce small oscillating displacements across jointed interfaces. Contacts under these loading conditions can exhibit partial slip or both partial slip and gross slip behaviors. This type of contact is known as fretting. Fretting can cause crack nucleation/propagation and wear debris, which in turn degrade the overall operation of the jointed components [90,91]. Moreover, slippage during fretting of the joint interface is the major source of frictional energy loss and, hence, damping associated with joints. It is common to report the stiffness and damping of the jointed interface by obtaining fretting responses from an apparatus, simultaneously imposing constant normal and oscillatory tangential loads. Fretting response is generally characterized by a force-displacement loop (fretting loop); i.e., relative displacement across the joint halves versus the tangential force transmitted by the interface friction in response to this relative displacement.

In fretting experiments, tangential loading is generally imposed by either controlled displacement or controlled force on one side of the contact, and resistive force is measured from the opposite side. In addition, the displacement of contact surfaces relative to each other should be accurately known to fully determine the fretting response. Normal loading, on the other hand, can be imposed by dead weights or by a clamping method such as bolting, welding, or riveting (specifically for mechanical joints). It is reported that up to 50 variables influence the fretting response [90], where friction coefficient, magnitude of slip, and contact pressure are identified as the "primary" set of variables directly affecting fretting response. The so-called "secondary" variables (humidity, lubricant, contamination, residual stresses, work-hardening, microstructure, etc.) influence the fretting response by altering the primary variables. The fretting response is also influenced by loading history, surface finish and underlying material composition [45]. An application where many of these factors play an important role in fretting behavior is head-stem interface of a typical hip replacement [92]. Activities like walking, running, squatting and jumping

imposes cyclic loads on the head-stem interface of the hip joint, whereas the physiological fluid surrounding the tissue introduces a corrosive environment. Surface roughness of these modular implants is shown to be changed by both residual stress development and stress-assisted dissolution, which in turn results in surface degradation/wear/contamination and influence the fretting response [92]. Clearly, to capture the effect of each parameter on fretting behavior, precise and accurate measurement of fretting loops is necessary.

Since the relative displacements observed in fretting contact are very small (typically less than 50 μm) [93], obtaining accurate fretting response of a contact is challenging. In addition, the following three requirements should be met for measurement reliability and validity: 1) high reliability of the imposed displacement or imposed force, 2) high accuracy of interfacial displacement measurement, and 3) high accuracy of interfacial force measurement [94] (see Table 5.1). The first of these requirements is usually limited by the actuation mechanism used because reliability in imposed tangential loading is related to repeatability and precision of actuation. Closed-loop actuation mechanisms are commonly utilized to fulfill this requirement. Requirements 2 and 3 usually compete against each other. High accuracy interfacial displacement measurements require fixation of the contact interface to the test fixture as rigidly as possible, whereas force measurements are more accurate with low rigidity. Therefore, meeting all three requirements simultaneously in a fretting apparatus design is particularly challenging and only possible with recent advances in instrumentation.

Fretting experiments specifically with mechanical lap joints add two more challenges to the list of design requirements: 4) minimal misalignment and minimal out-of-plane motions, and 5) operation under high-frequency tangential loading. The fourth requirement is due to the flat-on-flat contact configuration that takes place in lap joints. A sphere-on-flat contact configuration, for example, does not need precise alignment in the fretting direction for reliable measurements. The fifth requirement is a result of experimental observations from structures containing mechanical joints. In experiments with nominally identical jointed structures, shock response spectra are shown to deviate considerably at mid-to-high frequencies (higher than 2 kHz [95]). This observation is associated with uncertainties introduced by the

joints since identical monolithic structures exhibit minimal variations in their shock spectra. To understand the effect of frequency on fretting response, dynamic fretting experiments at high frequencies need to be conducted. Table 5.1 summarizes the aforementioned design requirements for a candidate joint fretting apparatus.

Fulfillment of the first three requirements is crucial for reliable joint compliance measurements, which influence the overall dynamical response of the jointed structures in helicopters, aircrafts, trains, ships, automobiles, farm machinery, engines, construction equipment, etc. [96]. In addition to stiffness, joint damping response is highly influenced by the accuracy of displacement and force measurements. The area inside the fretting loops give a measure of the loss factor and damping associated to joints [97]. If the fretting loop obtained contains additional slippage and compliance stemming from the instrumentation, the joint damping predictions will be erroneous, too. Considering the fact that many jointed structures are prone to dynamical loading, safe and economical design, manufacturing and operation necessitates better physical models for the joints, especially because the behavior of the structures can be accurately modeled without the joints, and joints complicate the dynamical response [95,98]. The dynamical response gets even more complicated when mid-to-high frequency operation is studied. Even nominally identical jointed structures show different responses due to changes in complex interfacial phenomena such as friction, slip, roughness, wear, etc. [95,98]. Therefore, a complete picture about the joint response cannot be obtained without mid-to-high frequency testing, and thus requirement 5 follows. The fourth requirement is associated to the challenges of maintaining flat-on-flat contact and it is common in any tribological testing (e.g. see the influence of misalignment on wear tests with flat pin on disk [99]).

An experimental apparatus using direct force and displacement measurements to obtain fretting loops from mechanical lap joints is presented in this chapter, and is referred to as the “joint fretting apparatus.” This apparatus is tested with fretting experiments on metallic joints and shown to meet all five requirements listed above without any data filtering or post-processing. The developed apparatus can also be used for fretting of lap joints with different materials (such as metals, polymers and mica), and

preloading methods (such as bolts, rivets, and welding), and under various loading and contact conditions (oscillation amplitude/frequency, dry/lubricated/contaminated, etc.). A comparison with the recently developed fretting setups is given in the next section to emphasize the novelty of the joint fretting apparatus. After introducing the instrumentation and calibration of the joint fretting apparatus, the fretting loops obtained from the experiments and the models presented in Chapter 4 are compared in the following sections.

5.2. Review of Existing Setups and Limitations

Research on fretting response and damping of mechanical joints dates back to Ungar's work in 1964 [100]. He conducted experiments with riveted, bolted and welded plates and panels to investigate the damping characteristics of aerospace joints. In his experimental apparatus, he utilized decay rate of the structural responses of the joints to determine the damping. The experiments of Rogers and Boothroyd [101] were capable of producing fretting loops from the contact of metallic interfaces. Frequency effects (up to 200 Hz), break-in effects (elastic shakedown in the first several fretting cycles), and time-histories were investigated by the same researchers [97]. Recent experimental efforts focus on the dynamic response of joints, particularly on measuring damping characteristics [102,103]. Gaul proposed an experimental apparatus (termed resonator) which accommodated a lap joint between two lumped masses [104,105]. By exciting longitudinal or torsional vibration modes of these masses, the relative motion across the joint interface was measured. Both parts of this resonator are suspended by flexible nylon cords, and a shaker excites one of the masses. The force input by the shaker is measured by piezo-electric pickups, whereas both the displacement and friction force calculations are derived from measured acceleration data (using frequency domain integration techniques). Sandia National Laboratories has an established research program on mechanical joints utilizing an apparatus similar to Gaul's longitudinal resonator [95]. In Sandia's resonator, four accelerometers are used to collect reliable axial motion data from each mass, and these four acceleration signals are synchronously time-averaged to obtain the

average acceleration and friction force. These experimental methods require post-processing of the acquired data to obtain fretting loops and, hence, are referred to as “indirect” methods.

Contrary to indirect methods mentioned above, direct measurements of forces and relative displacements were performed in fretting experiments by Varenberg et al. [106] and Ovcharenko et al. [107]. The experimental apparatus described in [103] utilizes a piezoactuator to impose controlled displacements on the flat sample and measures the relative displacements between the sphere and flat samples by a proximity sensor. The friction force is measured directly by a load cell whereas the normal force is imposed by dead weights. With this experimental apparatus, no further post-processing of the collected data is needed to obtain fretting responses. Therefore, we classify this method as the “direct” method.

Kartal et al. [108] studied fretting of titanium and nickel alloys using direct force and indirect displacement measurements (we call this method “semi-direct” in reference to the above discussion). In this apparatus, normal preload on the flat-on-flat contact is imposed by hydraulic actuators connected to the flat fretting pads, and tangential force is directly measured by a load cell to which the specimen is attached. The relative tangential displacement, on the other hand, is determined using digital image correlation (DIC) techniques. Images of the interface are taken from the center of the contact, and the relative motion of the specimen and the fretting pads is determined by correlating certain surface features at each frame. In addition to the DIC technique, a linear variable differential transformer (LVDT) is used to measure the displacement between the specimen mounting and the cast iron block which contains the fretting pads and hydraulic actuator.

Note that both direct and indirect methods have advantages and disadvantages in fulfilling the requirements listed in Table 5.1. Starting with the indirect methods (specifically, the longitudinal resonator), it is acknowledged that acceleration data is easier to obtain with current accelerometer designs (easy-installation by adhesives or tape). Despite being prone to considerable noise, the measurements can be obtained without any complication stemming from structural vibrations at higher fretting frequencies. However, both time and frequency domain integration of noisy acceleration data might yield erroneous

velocity and displacement results. In addition, accuracy of friction force calculations from Newton's second law ($F = ma$) heavily relies on the accuracy of the acceleration measurements and the accuracy of the actuation at the correct mode of the resonator. The desired mode of the resonator is the longitudinal mode (fretting), which generally corresponds to the fifth mode. Therefore, the resonator should be designed accordingly so that its axial mode is sufficiently isolated from neighboring modes and transient effects during loading are minimal. Otherwise, misalignment and out-of-plane forces might drastically change the fretting behavior.

Direct methods (specifically Ovcharenko et al.'s apparatus [107]), in contrast, do not suffer from errors introduced by post-processing since fretting loops are measured directly. However, the conflict between requirements 2 and 3 and high frequency operation need special attention. The former problem has been resolved by direct relative displacement measurements in Ovcharenko et al.'s apparatus [107]. With direct relative displacement measurements, the rigidity requirement in imposing displacements is satisfied. High frequency operation using direct measurement methods is the most challenging aspect of the design because an apparatus consists of rigid and compliant assemblies each of which further complicates the dynamic response. The misalignment requirement needs to be checked and monitored throughout the experiments. Ovcharenko et al.'s apparatus [107] was designed for quasi-static fretting experiments with sphere-on-flat contacts. Therefore, requirements 4 and 5 were not considered in their design. Semi-direct measurement methods, e.g., [108], satisfy requirements 1 and 3. However, the accuracy of interfacial displacement measurements depends highly on the resolution and size of the images taken as well as on the accuracy of the DIC technique. Kartal et al. [108] used images taken from a 1.8 x 1.4 mm area in the center of the contact with a pixel size of 1.8 μm. Considering that this region covers a small portion of the contact patch (8 mm in length) and 1.8 μm pixel resolution is too low for image correlations especially in the partial slip fretting regime, the relative displacement measurements might lack sufficient accuracy. Despite the fact that misalignment issues and high frequency operation are present in turbine blade applications, requirements 4 and 5 were not considered in [108].

Direct measurement methods were employed in the joint fretting apparatus to eliminate post-processing, signal processing and filtering steps in determining the fretting loops as well as to meet the first 3 requirements as achieved by Ovcharenko et al.'s design [107]. A minor compromise in meeting the first requirement is inevitable due to the inherent compliance of the apparatus. Although accurate displacement measurements in the proximity of the actual interface lessens the effect of this compromise, the applied displacement on a joint sample changes due to normal preload and frictional properties. The proposed joint fretting apparatus needs to fulfill requirement 4 for quasi-static loading and both 4 and 5 for high-frequency fretting experiments on mechanical joints. The experimental data obtained with the proposed joint fretting apparatus clearly show that all the above-mentioned requirements were met. The details of the apparatus and discussion about the calibration, noise and misalignment issues follow in subsequent sections in addition to typical fretting loops obtained from aluminum and steel bolted lap joints. The measured fretting loops and the obtained stiffness and damping results agree well with data existing in the literature. Lastly, a comparison between the predictions of the models introduced in Chapter 4 and the measured fretting response of a steel lap joint with two bolts is presented in this chapter. The model is shown to agree reasonably well with the experimental fretting loops and energy dissipation per fretting cycle.

5.3. Instrumentation

The joint fretting apparatus allows studying the fretting behavior of mechanical joints under quasi-static and dynamic loading conditions. The proposed design fulfills the requirements listed in Table 5.1 and possible misalignment errors are continuously (in-situ) monitored by this apparatus. In addition, fretting loops can be obtained from the raw force-displacement data; i.e. no further post-processing of the data is needed. The effects of damping and compliance originating from the joint apparatus are shown to be minimal, and thus the physics of the contact interface is accurately captured. To our knowledge, no experimental apparatus overcoming these challenges of fretting experiments with actual mechanical joints by direct force-displacement measurements has been documented in the literature.

Fig. 5.1 shows a sketch of the proposed joint fretting apparatus. Points A and D are fixed on a thick steel frame (machined from a monolithic component), which is placed on a vibration isolation table, at side D. The piezoactuator or piezotranslator (PZT), load cell and joint samples are assembled on line A-D and attached to the steel frame, whereas the laser nanosensor (LNS) measuring the local imposed displacement δ_x is directly attached to the vibration isolation table. Signal conditioners and a workstation are situated on a separate table. Photographs of the assembly of the joint fretting apparatus are seen in Fig. 5.2. The specifications of each component and discussion about the requirements regarding the input and measured quantities follow.

As mentioned above, the joint fretting apparatus provides direct measurement of force-displacement data from mechanical joints. The relative motion on the joint interface is imposed by the PZT actuator. The force is measured by the load cell, and the actual relative motion across the joint interface is measured by the LNS.

Piezotranslator (PZT)

Various types of actuators have been utilized in fretting experiments. Servo-hydraulic actuators [109] are typically used for high stress fretting studies, whereas rotational to linear motion mechanisms [110] (involving a DC motor, an eccentric cam, and a crank drive) are preferred by some researchers due to convenience, robustness and low cost. Electromagnetic actuators [111] are used for larger ranges of slip amplitude and frequency studies, while piezoelectric actuators [107] are used for high frequency small fretting amplitude experiments.

A linear preloaded piezoactuator, P-845.60 (Physik Instrument, PI), is chosen for the joint fretting apparatus because it enables fast response (high frequency operation, requirement 5 in Table 5.1) with sub-nanometer resolution (high accuracy during loading, requirement 1). Theoretically, the resolution of the piezoactuator is not limited by stiction or friction: rather, the amplifier used (PI, E-505) introduces a noise voltage restricting the resolution to 1.8 nm in closed-loop mode. The travel range of this actuator's tip is 90 μm, which is sufficient to cover the partial slip fretting regime for the mechanical joints of

interest. The actuator's tip motion is measured by an integrated strain gauge sensor (SGS) and closed-loop operation is sustained by a position servo-controller (PI, E-509.x1). The push and pull force capacities of the PZT actuator are 3000 and 700 N, respectively. The static large signal (average over a long actuation period) stiffness ranges from 30 to 45 N/ μm, whereas the dynamic small signal (at the beginning of loading/unloading) stiffness is 30 % higher.

From these specifications, it is clear that the selected PZT actuator satisfies the first requirement in Table 5.1 as it provides high resolution displacement and measures this displacement through a high-accuracy SGS allowing for closed-loop operation. Knowledge of the imposed displacement is critical, as it is the first requirement in any fretting apparatus design. In many apparatus employing direct methods of measurements, the actuator motion is accurately monitored and assumed to be the relative motion across the contact [106,112]. However, the displacement (or force) imposed by the actuator might transfer to the other parts of the apparatus rather than the interface contact. This is the reason that a laser nanosensor is also employed to determine the "actual" relative displacement imposed on the joint samples.

Laser Nano Sensor (LNS)

The laser nano sensor (LNS 18/120, LMI Technologies B.V) provides high-precision displacement measurement within an effective range of ± 60 μm and a practical resolution without averaging of 50 nm (sensitivity: 130 mV/ μm). It uses a semi-conductor laser as a light source and measures the displacement by sensing the reflections of that light. Therefore, the object whose displacement is to be detected should be mirror polished, or a reflective tape should be used. Metal joints do not satisfy this requirement unless they are finely-machined to have sub-nanometer root-mean-square roughness. Hence, a small mirror of 4.3 g is attached to one end of the joint with an adhesive mounting wax (Petro Wax from PCB). This particular wax offers a convenient attachment without altering the high-frequency response. Since the mirror is very light and small in size, it does not affect the dynamic response of the joints. The most complicated part of using the LNS to measure the displacement is that the object to be measured should be kept at a precise standoff distance of 18 mm with almost perfect perpendicularity (90 ± 1^{o}) with the

laser beam to ensure high-sensitivity measurements. The laser spot size at the specified standoff distance is 4 μm and not visible with a naked eye. This challenge is overcome by a lengthy assembly process. The LNS is attached to a 3-axis translation stage. Once one side of the lap joint is attached to the PZT tip, and the mirror is assembled by the adhesive wax, the levels of the LNS and mirror are checked and matched each other to ensure perpendicularity. Finally, the standoff distance is varied by the z-translation of the LNS and open-loop sinusoidal motion of the PZT tip is used to calibrate and obtain the sensitivity listed in the LNS specifications. Note that open-loop motion of the PZT is measured accurately by the internal SGS and this motion is completely transferred to the attached joint half since the other side of the lap joint is not attached and thus no reaction force exists. With this known motion, calibration of the standoff distance is precise, but quite lengthy.

Once assembled and calibrated, the LNS provides displacement measurements with a wide dynamic bandwidth (DC to 250 kHz). Other non-contact measurement methods are possible, such as using a laser Doppler vibrometer, which however does not offer true DC measurements. Should a resolution better than 50 nm be needed, LNS 18/120 can trivially be replaced with LNS 2.3/8.8 or 7/26 (resolutions 2.5 and 10 nm, respectively) since the LNS assembly is not an integral part of the main frame of the apparatus. Alternative displacement sensors such as linear variable differential transformers or proximity probes can be used without affecting the design requirements.

Dynamic Force Transducer (Tri-axial Load Cell)

To achieve high accuracy in force measurements, a highly sensitive and stiff tri-axial piezocrystal load cell (dynamic force transducer) is chosen (ICP-260A01, PCB Piezotronics). The force measurement from each direction is delivered to the workstation through 484B Series ICP sensor signal conditioners. This specific model can measure up to 4450 N (with 0.56 mV/N sensitivity) along the x axis and 2225 N (with 2.25 mV/N sensitivity) along the y and z axes (Fig. 5.1). The cross-talk between the x, y and z axes measurements is less than 2.5 % when the preload on the load cell is sufficiently large (22250 N preload is recommended). The needed preload on the load cell is applied by a high-precision torque wrench. The

stiffness of the load cell in the x direction is typically 1750 N/μm, whereas y and z directions exhibit less than half of that stiffness (700 N/μm). The load cell has a natural frequency of 90 kHz under "unloaded" conditions. This value drops to 5-6 kHz depending on the loading conditions used for mechanical joints. Nevertheless, the load cell enables force measurements within a wide bandwidth ranging from DC to 5-6 kHz in the current assembly (requirement 5). Note that force measurements in the normal (y) and out-of-plane (z) directions allow for precise monitoring of possible misalignment during the experiments.

Data Acquisition

A 12-bit data acquisition board (DAQ, National instruments PCI-6110) is used to acquire force data from the load cell and displacement data from the LNS. The PZT actuator tip displacement is imposed by the output channel of the same DAQ. Actual tip displacement is obtained from the data acquired from the internal SGS of the PZT. The actual displacement matches the imposed PZT tip displacement in closed-loop mode. Full synchronization and control of the experimental apparatus is done using LabVIEW 8.0 software on a workstation. The virtual test environments developed in LabVIEW allow for amplitude and frequency modulation for the imposed displacement signal and sampling rate modulation for the dynamic forces and SGS data. All the input and output data presented in this chapter are sampled at 1 kHz, and no analog or digital filtering or post-processing is employed to obtain the fretting loops.

5.4. Calibration Experiments

Calibration of the instrumentation is done individually for each component of the joint fretting apparatus. After assembly, misalignment and noise measurements are performed using preliminary experiments with an aluminum monolithic joint (calibration sample) and 1-bolt aluminum and steel joint samples, shown in Fig. 5.3. The monolithic and 1-bolt joint samples are identical in configuration: the monolithic sample is a solid piece without any contact interface and is used as an instrument calibration sample as it has no interface compliance. The contact configuration for the 1-bolt joints is flat-on-flat with a nominal contact area of 165 mm^2. Roughness measurements from the contacting surfaces of the joints is taken by a portable roughness tester (Marsurf PS 1, Mahr Federal Inc. using 5.6 mm long profilometric

scans). Since the surfaces are prepared by milling, the contacting surfaces show anisotropic roughness patterns. To determine a combined roughness, four profilometric scans (2 along the machining marks, 2 perpendicular) from different locations of each joint half interface (PZT and load cell sides) are collected first. Then, two orthogonal directions yielding maximum and minimum surface height slopes on the contacting surfaces are found and zeroth spectral moments are calculated from the surface heights data $y(x)$ along these orthogonal directions. Finally, combined zeroth spectral moment is calculated by summation of the zeroth moments of each side of the joint and the rms roughness, σ follows from the square root of that combined moment (see the analyses of McCool [84] for further details). A summary of this computation process is given as follows

$$\left.\begin{array}{l}\text{Spectral Moments}\\ m_0 = AVG\left[y^2\right]\end{array}\right\} \Rightarrow \left.\begin{array}{l}\text{Equivalent spectral}\\ \text{moments from max/min}\\ \text{slopes}\\ m_{0e} = \left(m_0^{\max} + m_0^{\min}\right)/2\end{array}\right\} \Rightarrow \left.\begin{array}{l}\text{Combined spectral}\\ \text{moments (PZT}\\ \text{and Load Cell sides)}\\ m_0^{comb} = m_0^{PZT} + m_0^{LC}\end{array}\right\} \Rightarrow \begin{array}{l}\text{Combined rms}\\ \text{roughness}\\ \sigma = \sqrt{m_0^{comb}}\end{array} \tag{5.1}$$

Using this process, the combined root-mean-square roughnesses of the 1-bolt aluminum and steel joint samples are calculated as 1.65 and 1.75 μm, respectively. The samples are cleaned according to ASTM G115-04 standard to ensure dry contact and to remove any wear debris and loose particles from the surfaces (ultrasonic cleaning with acetone).

The joint samples are clamped using a #4-48 UNF bolt. The preload on the bolt is imposed by either torque drivers (for imposed torques of 0.5 and 1.5 lb-in—0.057 and 0.17 N-m) or torque wrenches (for imposed torque of 5 lb-in—0.565 N-m) with dials and memory needles to detect the exact values (Precision Instruments). The following torque-preload relationship is used to determine the normal load F_p at the contact [113]

$$T_{in} = K F_p D \tag{5.2}$$

where T_{in} is the input torque, K is the nut factor (taken as 0.2 for the stainless steel #4-48 UNF bolts used), and D is the nominal diameter (2.845 mm for #4-48 UNF bolts). Table 5.2 lists the torque input for different preload values used in the experiments and the corresponding mean contact pressure values p_{mean}. Note that in practical lap joint applications, mean contact pressures vary between 5 to 20 MPa [97] and gross slip is not commonly observed unless in reduced friction cases such as bolt loosening, contamination, and lubrication. The range of preloads listed in Table 2 is intentionally chosen to show the capability of the fretting apparatus in handling all fretting regimes, for the dry metallic joints used in preliminary tests.

The aluminum joint sample is made of 6061-T6 alloy whereas a grade 420 stainless steel is used for the steel sample. The chemical composition and mechanical properties for each material, as obtained from the suppliers, are given in Table 5.3.

Calibration

Static weights were used to calibrate the load cell. Ten different weights ranging from 0.2 to 20 lbs—0.89 to 89 N were systematically imposed on the load cell, and force readings were recorded. The sensitivity obtained from these experiments fell within 10% of the sensitivities listed in the specifications of the load cell. Therefore, no further calibration was done. The PZT was recently calibrated by the manufacturer, so only closed and open loop modes were checked under various loads on the tip. Closed-loop mode was shown to work almost identically to open-loop mode up to 300 N force at the tip. Additional loading caused time-delay and attenuation at the tip motion. This limitation is due to the amplifier, which is not capable of delivering sufficient power for heavy loading conditions. For our application, though, the current amplifier is acceptable. Lastly, the LNS was calibrated by the PZT tip motion. Since the SGS of the PZT delivers the actual tip motion data, the measurements from the LNS were calibrated against these data. The sensitivities from the calibration experiments and the

specifications sheet matched within 15% maximum deviation for a range of motion from 1 to 60 μm (maximum deviation occurs under full range of motion, 60 μm).

Noise and Misalignment

The noise level was checked by conducting experiments with the aluminum monolithic joint sample. The displacement input imposed on one half of the joint by the PZT actuator is given by a continuous function of time (*s*)

$$\Delta_x(t) = \begin{cases} At & 0 \le t \le 0.5 \\ 0.5A(1+\sin 2\pi ft) & 0.5 \le t \le 10.5 \\ A(10.5-t) & 10.5 \le t \le 11 \end{cases} \tag{5.3}$$

where A and f are the loading rate of the ramp signal (*μm/s*) and frequency of the harmonic signal, respectively. Note that, at the beginning and end of the harmonic portion, the signal ramps up and down. The purpose of these half second loading and unloading periods is to determine the response of the joint interface to monotonic loading and unloading conditions as part of the cyclic loading experiments. The experiments with monolithic joints employed a loading rate of A=0.56 μm/s and ramp signal duration of t^*=4 s to ensure quasi-static loading conditions (harmonic signal frequency is 1 Hz). These loading conditions resulted in an imposed harmonic displacement with peak-to-peak amplitude of 4.5 μm. The SGS signal reproduced the imposed displacement signal given by Eq.(5.3) almost perfectly; i.e., with more than 100:1 signal-to-noise ratio. Note that the displacement measured by the SGS was not fully transferred to the monolithic joint due to the motion of the other parts of the joint fretting apparatus. The LNS measurements from the PZT side of the monolithic joint captured the actual joint motion since the load cell part of the joint was rigid (this will be shown in the next subsection). The LNS measurements showed noise levels of 0.1 μm, so experiments with sub-micron imposed displacements were prone to lower signal-to-noise ratio. The tangential force, f_x, followed the same pattern as the SGS signal, whereas misalignment and out-of-plane forces, f_y and f_z, varied negligibly compared to f_x ; i.e., they remained less than 3% of f_x . Taking the specified 2.5% cross-talk between the load cell channels into consideration, the

measured 3% suggested that misalignment was not an issue with the current joint fretting apparatus. The noise level on the f_y and f_z measurements corresponded to 1 N error. Considering the fact that the tangential forces seen in these experiments increase with increasing imposed tangential displacements, 1 N error in force measurements constitutes less than 2% of the tangential forces of interest.

Although measurements with the monolithic joint showed negligible misalignment, the problem can manifest itself when bolted joints are used for the experiments. To check this, tri-axial force measurements from the load cell were compared. The inherent assumption made here was that any misalignment would cause forces in the y and/or z directions, since the joint halves were bolted together and the PZT and the load cell connections with the joint halves were rigid in the y and z directions. Therefore, any misalignment would create moments and reaction forces on the load cell.

Fig. 5.4 shows raw force measurements from two typical fretting experiments with a 1-bolt steel joint under preloads of a) 99 N and imposed displacement of 9 μm, and b) 993 N and imposed displacement of 36 μm. The steel joint and the aforementioned conditions were specifically chosen since they showed the largest amount of misalignment, which did not exceed 2% of the tangential force, f_x, at any instant during the experiments. This level of misalignment is also within the cross-talk limit of the load cell channels as in the monolithic case. Therefore, no complexity due to misalignment is expected during the fretting experiments. Even if an unexpected misalignment occurs, it can easily be captured by the load cell, and such experiments could be discarded.

Imposed vs. Actual Tangential Displacements

As discussed above, the imposed tangential displacement signal given by Eq.(5.3) cannot be fully transmitted to the joint half due to the stiff nature of the joints under investigation and the inherent compliance of the experimental apparatus. Closed-loop operation of the PZT actuator with a powerful driver guarantees that the PZT tip moves the same amount as the imposed input signal; however, possible relative motion between the PZT and apparatus connections reduces the displacement transmitted to the joint. Experiments with the 1-bolt aluminum joint under different bolt preloads were conducted to

illustrate this phenomenon. Fig. 5.5 shows the PZT tip displacement (Δ_x) measured by the SGS of the PZT, the LNS measurements (δ_x) obtained directly from the joint half and the displacement of the load cell half of the joint (δ_{LC}) calculated by f_x / k_{LC} (f_x is the resistive tangential force measured by the load cell, and k_{LC} is the stiffness of the load cell listed in its specifications).

The data presented in Fig. 5.5 was collected from two separate experiments with the maximum tangential loading condition used in the preliminary tests (imposed peak-to-peak displacement of 36 μm) and with low ($F_p = 99N$, Fig. 5.5a) and high ($F_p = 993N$, Fig. 5.5b) preload values. High preload means that the tangential force transmitted by the joint interface is expected to be high. Therefore, the difference between the imposed PZT tip displacement and the joint half displacement measured by the LNS was higher for the case of $F_p = 993N$ than for the $F_p = 99N$ preload. As seen in Fig. 5.5b, that difference reached up to 3 times the actual displacement transmitted to the joint half. However, the displacements on the side of the load cell joint did not change significantly as a function of the preload. In fact, they were approximately zero for both cases, indicating that the measured LNS displacement is the actual joint interface displacement. Independent displacement measurements from the load cell half of the joint were taken to verify these observations. The range of motion measured on the load cell was limited to sub-micron level, even for the most severe loading conditions.

Fig. 5.6 shows the fretting loops averaged over ten cycles with the imposed and actual interface displacements. It is clearly seen that both stiffness and damping obtained from the fretting loop with the imposed displacement would diverge far from the actual joint stiffness and damping. Stiffness is underestimated due to the compliance caused by the apparatus, and damping is overestimated due to additional apparatus-originated energy losses. Thus, ensuring correct interface displacement measurements is critical for obtaining accurate fretting loops.

Stiffness and Damping of the Apparatus

Full transfer of the imposed displacement at the PZT actuator tip to the joint samples is nearly impossible due to the inherent compliance of the different parts of the apparatus. The imposed displacement is accommodated by different parts of the apparatus along the line A-D (Fig. 5.1). Measuring the motion at point B eliminates any possible compliance effects originating from the PZT-end of the apparatus. Direct measurement of relative motion of points B and C or a separate displacement sensor measuring the displacement of point C would remove the effect of equipment compliance. In this work a relatively stiff load cell was chosen to simplify the design for relative motion measurements. The simpler design eliminated the possible issues with synchronization and efficacy of simultaneous measurements using two separate LNS. The attachment between the joint and the load cell holder was accomplished through two #4.48 UNF bolts. Since the bolt-to-joint stiffness ratio for these bolts and attachment was around 0.2, bolt stiffnesses were assumed to have negligible influence on the compliance along the friction direction. Fig. 5.7 shows a simplified representation of the compliance of the apparatus sketched in Fig. 5.1 with only 1 degree of freedom along the friction direction.

The motion of point D was taken to be zero since the apparatus was connected at that point to a vibration isolation table, and we confirmed that its motion was indeed approximately zero. The combined stiffness of the steel connector block (8890 N/μm) and the load cell (1750 N/μm) was 1462 N/μm. Noting that the stiffness of the PZT was only 38 N/μm and the stiffnesses of the experimented joints ranged from 10 to 300 N/μm, the load cell part of the joint barely experienced any motion. Therefore, the rigidity assumption for the load cell is valid. Nevertheless, all three components of the displacement corresponding to the PZT, joint, and load cell can be recorded for each experiment, and can be accounted for when obtaining fretting loops and joint stiffness/damping.

As an example of the displacement analysis, let us consider the experimental results shown in Fig. 5.5. The tangential forces approached 70 N for the loading conditions in (a) and 500 N for (b). The 1 DOF representation given in Fig. 5.7 resulted in 1.85 (70/38) and 13.2 (500/38) μm motion on the PZT side of

the apparatus for these loading conditions; i.e., relative motion of points A and B. These values matched the maximum deviation of the SGS and LNS measurements ($\Delta_x - \delta_x$) in Fig. 5.5.

Since the joint interface experiences relative slip, there are energy losses due to friction. Energy dissipation in linear systems scales with the square of the maximum applied force. Goodman's [114] and Mindlin's [58] analyses suggested that the energy dissipation scales with the third power of the maximum tangential force, in the case of frictional energy losses under slipping and partially slipping contact conditions; i.e., $\Delta W \sim \left(f_x^{\max} \right)^3$. Smallwood et al. [115] and Hartwigsen et al. [116] experimentally found that the exponent ranges between 2 and 3 depending on the nonlinearity effects. Since there is a substantial amount of motion on line A-D of the joint fretting apparatus that is not coming from the joint interface, associating the joint samples as the only source of observed damping could be incorrect. To validate that moving parts of the apparatus did not significantly contribute to the total energy loss per fretting cycle, energy losses obtained from the monolithic and 1-bolt aluminum joints were compared. Energy loss per fretting cycle was calculated by the difference of the work done while reloading and work recovered during unloading; i.e., the area inside a fretting loop. Fig. 5.8 presents energy losses obtained from cycles 1, 3, 5, 7 and 9 of each fretting experiment as a function of the maximum tangential force (the maximum applied force is estimated as the average of the absolute values of the minimum and maximum forces obtained in a fretting cycle and the energy dissipation is calculated using trapezoidal integration of the tangential force with respect to the tangential displacement). In total, 32 experiments and 160 data points are presented in Fig. 5.8. In these experiments, eight different tangential displacements (ranging from 4.5 to 36 μm peak-to-peak amplitude) were imposed on the monolithic and 1-bolt joint samples under different preloads. Note that the energy loss for the monolithic joint was negligibly small compared to the losses for the 1-bolt joint regardless of the loading conditions. This result leads us to the conclusion that the energy losses and, hence, damping associated with the apparatus are minimal compared to the energy dissipation caused by the fretting of joints. Therefore, the area inside each fretting loop can be safely used to determine joint damping.

Another observation that can be made from Fig. 5.8 is that the energy loss for the first fretting cycle (darker data points) is always larger than for the remaining 4 cycles. The change in the energy loss decreases and finally settles into a constant steady-state value. This phenomenon is known as the process of shakedown [27]. Recently, Ovcharenko and Etsion [117] observed similar energy dissipation behavior from fretting experiments with copper and steel spherical samples.

5.5. Macroscale Friction Model vs. Experiments

A multiscale physics-based friction model was introduced in the last chapter, and four variations of this model are presented (CFC, CEB, KE, and BKE). Using different asperity-scale contact, the CEB, KE and BKE models predict different (and physically more correct) behavior than the simple CFC model. Moreover, as expected, the three physics-based models predict slightly different behavior, since the KE model is an improvement of the CEB model (both models assume full slip conditions) and the BKE model is based on the assumption of full stick contact conditions. Away from theoretical arguments alone, one needs to experimentally validate the applicability of these models to practical contact problems (such as bolted lap joints) and determine which one more accurately represents realistic fretting loop behavior. Thus, experiments with a steel lap joint were conducted to demonstrate the use of the proposed fretting models in a realistic flat-on-flat contact problem.

The joint fretting apparatus with a 2-bolt steel joint is used in the experiments. The grade 420 stainless steel joint sample possesses a 10x17 mm^2 nominally flat rectangular contact area as shown in the photograph in Fig. 5.3. The chemical composition and mechanical properties for the steel, obtained from the supplier (Precision-Marshall Steel Company), are tabulated in Table 5.3. The joint halves are cleaned according to ASTM G115-04 standard to remove the presence of any wear debris and ensure dry contact conditions (ultrasonic cleaning with acetone). Roughness characteristics of the joint surfaces were obtained from surface height measurements (4 mm long line scans) taken by a portable contact profilometer (Marsurf PS 1, Mahr Federal Inc.). To obtain accurate surface roughness measurements,

high-frequency noise and low-frequency waviness were filtered by a band-pass filter with low and high-pass cutoff wavelengths of 0.8 and 0.02 mm, respectively. These cutoff wavelengths vary due to the scale of the application. The values chosen for our application comply with internationally recognized standards [118,119]. Furthermore, since the surfaces are prepared by milling with variable feed rates, the contacting surfaces show anisotropic roughness patterns. As suggested by the analyses of McCool [84] for anisotropic surfaces, three steps are followed to extract the roughness parameters used in the proposed statistical models: (i) find two orthogonal directions yielding maximum and minimum surface height slopes on the contacting surfaces; (ii) compute the spectral moments of the surface heights data $y(x)$ obtained from the two orthogonal directions; and (iii) compute the combined spectral moments and roughness parameters, R, η, σ. The flow of computations to determine roughness parameters from surface heights data is summarized in Eq.(5.1). The combined surface roughness parameters as well as the individual roughness parameters for the joint samples attached onto the PZT and load cell halves before and after fretting experiments are given in Table 5.4. Note that the plasticity index for the initial untested (as machined) flat-on-flat contact with combined parameters is found to be 4.725. The joint surfaces were machined with a common machining method for joints, namely milling, without any special surface treatment, producing high plasticity indices on virgin surfaces [39,120]. To obtain surfaces with lower plasticity indices, smoother and harder surfaces should be machined. Such special surface machining techniques could introduce residual stresses and change the material hardness, and thus compromising the ductility of the contacting materials, both of which are shown to influence fretting behavior [45]. Future experiments will utilize residual stress removal techniques such as heat treatment to remedy these challenges. The plasticity index value decreases slightly after the experiments due to the plastic deformations of the asperity tips (asperity tip flattening). Therefore, a major portion of the asperity tip contacts in this chapter are under plastic flow. The CEB and KE models predict diminishing friction coefficient for highly plastic spherical contacts, and, hence, their prediction for fretting of the flat contact will show a diminishing tangential force. However in practice, there always exists a reaction force to

shear, no matter how high the plasticity index is. Therefore, the CEB and KE model predictions lose validity for highly plastic contact conditions in fretting.

The joint halves are clamped by two steel M3 bolts. The preload on each bolt is imposed by a torque driver (Precision Instruments) with a dial and memory needle to measure the torque input. The same torque-preload relationship employed in the calibration experiments is used to determine the normal load on the contact (Eq.(5.2)). Note that the nut factor used (0.2) is an experimental constant, where all the factors influencing torque-preload relationship such as friction, torsion, bending and plastic deformation of the threads in a bolt are lumped. Hence, its value shows variation depending on the material, lubrication, and temperature. Bickford [113] surveyed nut factor values and found a mean value of 0.199 and minimum and maximum values of 0.158 and 0.267 for steel bolts on steel joints applications. In accordance with this, a value of 0.2 is used for the nut factor in our experiments. In addition to the variability of the nut factor, bolting by torque driver can introduce ± 30 % preload scatter and the preload can change during operation [113]. The scatter for the specific torque driver we used in our work is documented not to exceed 2 % by the manufacturer. To check the constant preload assumption, torque on the bolts was measured before and after each set of experiments and a mean difference of 5 % was observed. Despite these checks, it is important to remember that the preload values documented in this work are prone to some scatter, which is one of the limitations of the conducted experiments. To remedy this, strain-gauged bolts could be used in future experiments. Table 5.5 lists the torque input for different preload values used in the experiments and the corresponding mean contact pressure p_{mean} values. This range of preloads is intentionally chosen to encompass gross to partial slip fretting regimes.

The experiments were carried out under laboratory conditions of room temperature of 21-23 ^{o}C and relative humidity of 40-45%. The displacement input imposed on one half of the joint by the PZT actuator is given by Eq.(5.3). Note that the PZT actuator tip displacement given in Eq. (5.3) is not fully transferred to the PZT half of the joint due to compliance of the fixture.

Table 5.6 presents magnitudes of the PZT tip motion and the measurements from the LNS, which is the actual maximum tangential displacement on the moving joint half. The maximum tangential displacement decreases steadily as the preload on the contact increases. This occurs because the maximum tangential force transferred by the contact increases with increasing preload, resulting in less slip.

Following the proposed modeling approach summarized in Fig. 4.3, simulations of fretting response for the flat contact under the experimental conditions listed in Table 5.6 were conducted. Fig. 5.9 presents fretting loops obtained from the experiments (averaged over 10 cycles) and the BKE model simulations. The BKE model results are more favorably-compared to the experiments than those of other models. Since the plasticity index is fairly high, both the CEB and KE models predict zero friction coefficient for many of the asperities on the joint interface. Hence, the maximum tangential force predictions of these models are approximately an order of magnitude lower than the experimental values. In addition, the friction coefficient varies with changing preload on the joint interface.

Table 5.6 shows the friction coefficient values obtained from each experiment. The experimental friction coefficients vary due to changing preload. The CFC model is not capable of accounting for this change, and, thus, even if matched for one experimental condition, fails to predict the others. On the other hand, the BKE model predicts a more physical fretting behavior with preload-dependent non-zero friction coefficient. The friction coefficient values predicted by the BKE model are 0.354, 0.334, 0.335, and 0.347. The friction coefficient values measured in the experiments with preloads of 526 N and 721 N match the model predictions whereas up to 50 % deviation is observed for the others.

The BKE model predictions for maximum tangential force deviate from the experimental values, up to approximately 40% (for the case with preload of 331 N). We hypothesize two possible reasons for this mismatch: (1) non-uniform pressure due to the bolts, and (2) omission of adhesion effects in the models. The models presented in the last chapter assume that the mean of asperity heights of nominally flat rough

surfaces remain parallel throughout normal and tangential loading. Therefore, it is expected to have higher pressures around taller asperities. However, the areal distribution of the asperities is assumed to be uniform, and thus no distinctive stress concentration over the interface is modeled.

In experiments with bolted joints, the contact pressure between the bolt head or nut and the joint surface is shown to vary between 0.6 to 3 times the mean pressure balancing an identical bolt preload provided the bolt/nut has no sharp edges causing further pressure discontinuity [113]. This pressure is shown in Fig. 5.10b as a normalized quantity, p_{bolt}/p_{mean}. A finite element analysis taking this non-uniform pressure distribution as boundary condition over the two bolt head regions was conducted to study the pressure distribution over the joint interface (the finite element ABAQUS model is shown in Fig. 5.10a). Fig. 5.10c shows the contact pressure distribution along the longitudinal direction (x direction in Fig. 5.1). The contact pressure between the bolt holes is fairly constant. However, the pressure drops rapidly towards the edges creating a non-uniform pressure distribution along the longitudinal direction. Along the orthogonal direction, the pressure is expected to vary as it varies nearby the edges in Fig. 5.10c. This non-uniform pressure necessitates use of an areal distribution in the proposed models and thus will result in double (isotropic surface) or even triple (anisotropic surface) integrals. These more complicated models are currently being studied.

The second possible reason, adhesion, becomes important only when the surfaces in contact are very smooth. Fuller and Tabor [121] proposed a dimensionless parameter to determine the importance of adhesion in elastic contact of rough surfaces as

$$\theta = \frac{E^* \sigma}{\Delta\gamma} \sqrt{\frac{\sigma}{R}} \tag{5.4}$$

where $\Delta\gamma$ is the work of adhesion between the steel surfaces (typical values range from 5 to 0.5 J/m^2, [14,122]). If the adhesion parameter exceeds 10, the adhesion force becomes negligible compared to elastic deformation forces. Using the material and surface characteristics of the surfaces used in the experiments, the adhesion parameter is calculated to range from 17000 to 170000. Therefore, neglecting

adhesion in the proposed modeling approach does not cause a significant problem in the elastic loading regime. In the plastic loading regime (many of the asperities are plastically deformed in the experiments), stronger metal-metal bonds are formed, and the adhesion force shows a logarithmic increase with the applied preload on the interface [122]. The preloads used in the experiments vary less than several orders of magnitude. Therefore, a drastic change in the influence of adhesion, even in plastic loading regime, is unlikely.

Another discrepancy between the models and experiments is the tangential stiffness predictions. As seen in Fig. 5.9, the models predict steeper increase/decrease in the tangential force while reloading/ unloading, when compared to the experiments. This difference is due to the fact that the elastic tangential response formulated by Mindlin et al. [58] is used for both elastic and elastic-plastic loading conditions. As shown by Johnson [59] and Bryggman and Söderberg [123], the tangential displacements observed in the experiments are larger than the Mindlin et al. [58] predictions. Based on this observation, Ödfalk and Vingsbo [26] proposed an elastic-plastic fretting model for spherical contacts. Their model uses two experimentally-determined parameters: fretting yield point and hardening coefficient. These critical parameters determine the amount of additional plastic flow over the contact patch. Since experimental data is used to determine these parameters, we did not employ this elastic-plastic tangential response model. Our modeling approach does not use fitting parameters or friction coefficients determined from the fretting experiments, but instead builds up from the asperity-scale (micro-scale) to macro-scale contact with first principles and material/surface properties. We are aware that such a model for elastic-plastic loading conditions is still missing, and our future work will focus on this aspect.

In addition to plasticity, asperity interactions can also play a role in the tangential stiffness mismatch between experiments and the model. Ciavarella et al. [124] showed that normal contact stiffness decreases with the inclusion of asperity interaction in the classical GW model. Yeo et al. [125] utilized an iterative numerical solution to rough surface contact with asperity interaction and found further decrease in normal contact stiffness. This decrease results in smaller separation values for the surfaces, and, thus, the slip

zones in Fig. 4.2 expand, implying more slippage over the contact. Therefore, tangential stiffness for the flat contact is expected to decrease with the inclusion of asperity interaction. However, this explanation omits the direct influence of asperity interaction on tangential response, and to the best knowledge of the authors; there exists no model in the literature accounting for this effect in tangential loading.

Fig. 5.11 presents a comparison of the energy losses per fretting cycle at different preloads. The circles essentially represent the values predicted by the best-matching fretting model, the BKE model (the area inside the solid fretting loops presented in Fig. 5.9). On the other hand, box-whiskers data points show the statistical distribution of energy loss over 10 experimental fretting cycles. On each box, the bottom and top edges correspond to the 25^{th} and 75^{th} percentiles, respectively. The whiskers, on the other hand, extend to minimum and maximum energy losses observed within 1.5 times the inter-quartile range under each preload. The data located outside the 1.5 times inter-quartile range are plotted individually as plus (+) signs in this figure. Omitting the outliers, the energy loss data at each preload stay within ± 20 % of the median values. This low degree of dispersion in energy loss data suggests the repeatability of the fretting experiments. The two outliers and upper extreme of whiskers correspond to the energy losses during the first few fretting cycles. Ovcharenko and Etsion [117] provide experimental results showing that the energy dissipation at the early stages of fretting of spherical contacts (steel and copper materials) is higher than the rest of the cycles; this is attributed to the plastic shakedown mechanism. Although the proposed models cannot account for this mechanism, the results obtained from the experiments with nominally flat bolted joints clearly supply evidence for plastic shakedown phenomena. Therefore, the proposed models can only be used for steady-state fretting behavior where no additional plastic deformation or residual stresses accumulate.

Energy loss decreases with increasing preload on the joints, since the maximum tangential displacement and slip decrease, as shown in Fig. 5.11. The BKE model predictions match the experimental data well for low preloads, whereas at high preloads the error exceeds 100%. This discrepancy stems from the limitations of the model to represent highly plastic contacts. Note that the

models presented in this work are described as *physics-based* models because they do not require experimental data or fitting parameters. Despite discrepancies with the experimental results, especially at higher preloads, the modeling approach seems quite promising.

5.6. Conclusion

The design and construction of an instrumented experimental apparatus for fretting experiments of mechanical lap joints is presented. The apparatus satisfies the following four design requirements specific to fretting of mechanical joints: (1) high reliability of the applied displacement or applied force, (2) high accuracy of interfacial displacement measurements, (3) high accuracy of interfacial force measurements, and (4) minimal misalignment and out-of-plane motions. Calibration experiments conducted with monolithic and 1-bolt aluminum and steel joints verify that the joint fretting apparatus meets these requirements. Direct measurements of force and displacement close to the joint halves constitute the uniqueness of the design and help meet the second and the third requirements. Measuring the imposed PZT actuator displacement with a high-accuracy internal sensor of the actuator and 3-axis dynamic force measurements assist in fulfilling the first and fourth requirements. The fifth requirement (operation under high-frequency tangential loading) cannot be evaluated with the current PZT amplifier due to power limitations. However, by using a more powerful amplifier, experiments up to 3-4 kHz can be conducted reliably since each component of the apparatus has higher operational frequency limits, and the rigid assembly of the instrument is not expected to introduce lower dynamic modes which might influence the experimental results.

After calibration of the setup, fretting experiments are conducted with a nominally flat bolted steel joint and the models presented in Chapter 4 are compared to the experimental data. Two bolts are used to clamp the joint interface to obtain fairly constant nominal pressures over the contact, which makes for better comparisons with the models. The results show that the plasticity index is the dominant parameter influencing the model predictions. The CEB and KE models predict vanishing fretting loops for highly plastic contacts, which is unrealistic. The CFC model uses a constant friction coefficient and cannot

account for changes in friction coefficient due to preload conditions. The BKE model appears to be the most successful in matching the experimental results. At low preloads, the model captures the fretting cycles and energy loss per cycle seen in experiments quite well, whereas for high preloads the correlation worsens. We hypothesize that a similar approach with better physics-based tangential response models accounting for plastic flow of the material will improve correlation with the experiments at high loads.

5.7. Figures

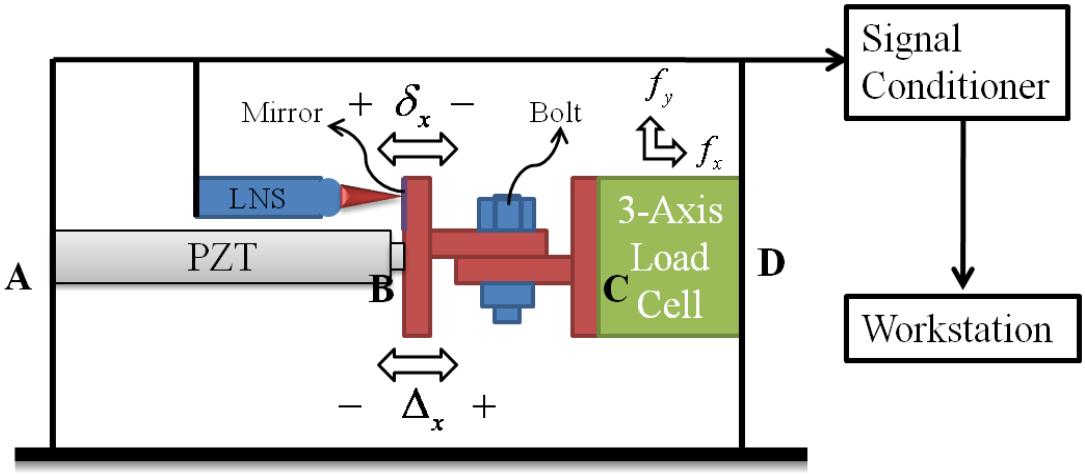

Fig. 5.1. Schematic of the developed joint fretting apparatus

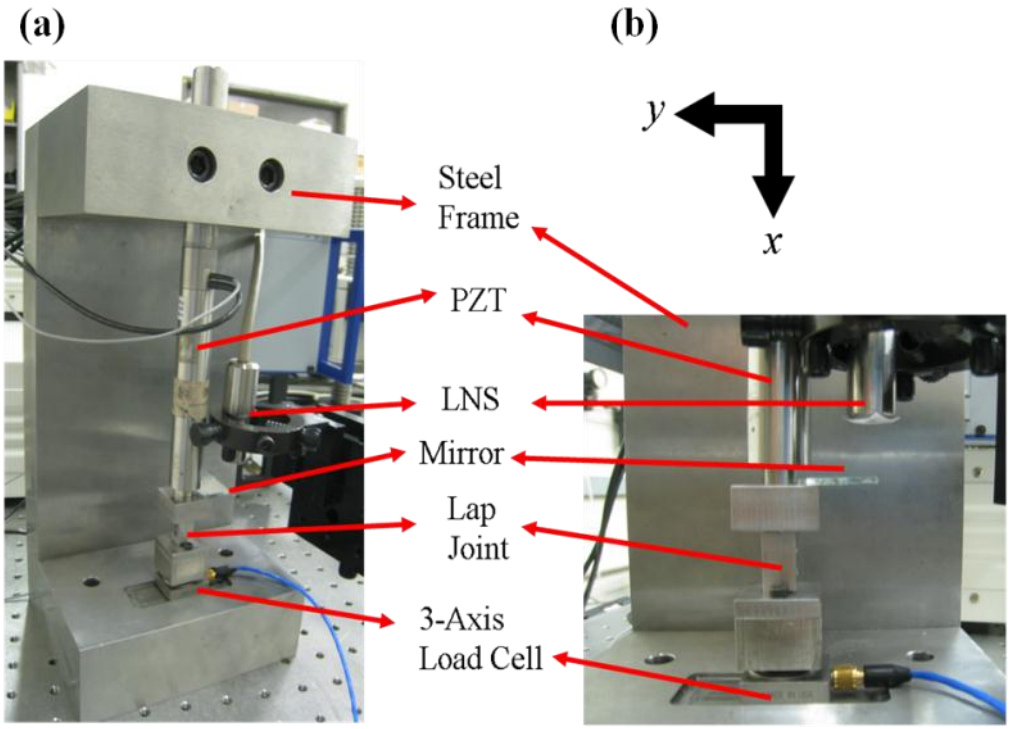

Fig. 5.2. Photographs of the developed joint fretting apparatus: (a) overall view, (b) close-up view of the joint halves

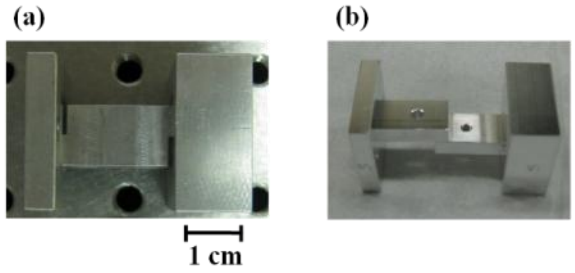

Fig. 5.3. Aluminum joint samples: a) monolithic, b) 1-bolt

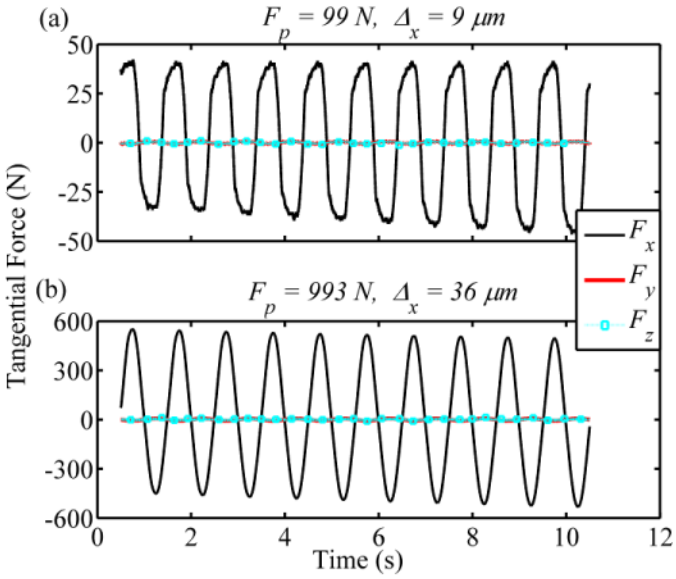

Fig. 5.4. Typical force measurements from 1-bolt steel joint in three orthogonal directions: x (shear), y (normal to the joint interface) and z (orthogonal to x and y directions) under; (a) preload of 99 N and imposed tangential displacement of 9 μm, (b) preload of 993 N and imposed tangential displacement of 36 μm

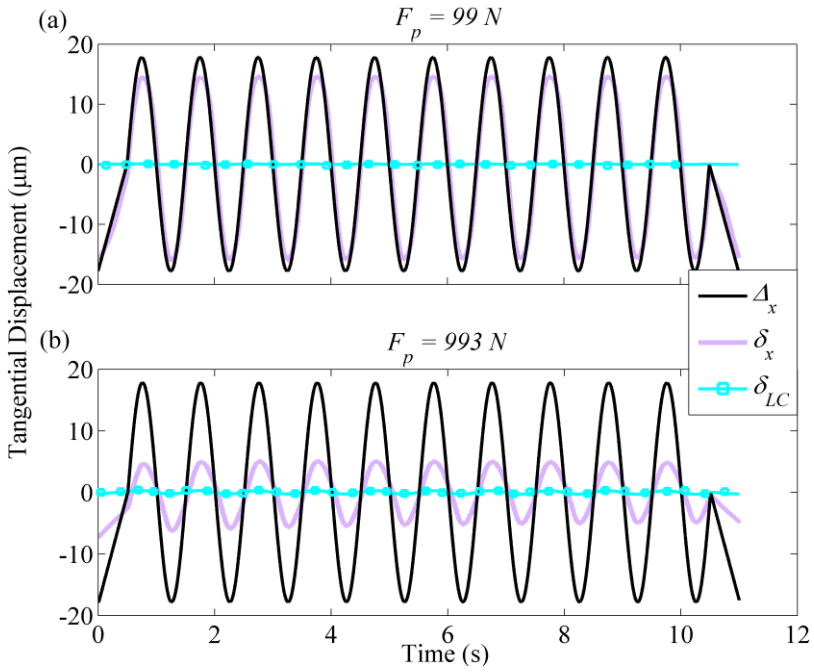

Fig. 5.5. Imposed, Δ_x; transmitted, δ_x and load cell, δ_{LC} displacements in the tangential direction for the 1-bolt aluminum sample under: (a) low preload (F_p = 99 N), (b) high preload (F_p = 993 N)

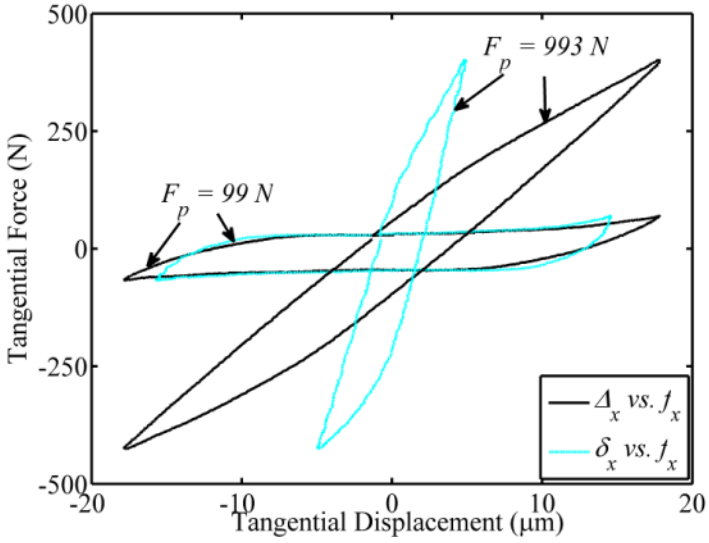

Fig. 5.6. Fretting loops with imposed and transmitted tangential displacements

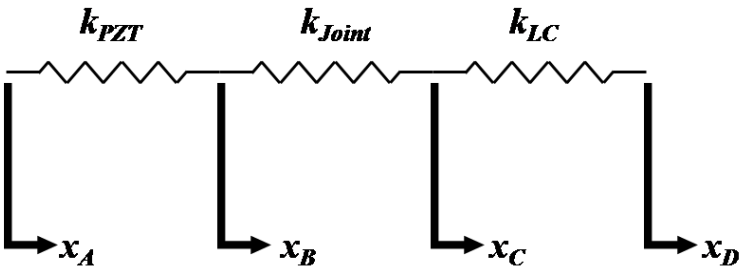

Fig. 5.7. A 1DOF representation of the experimental apparatus

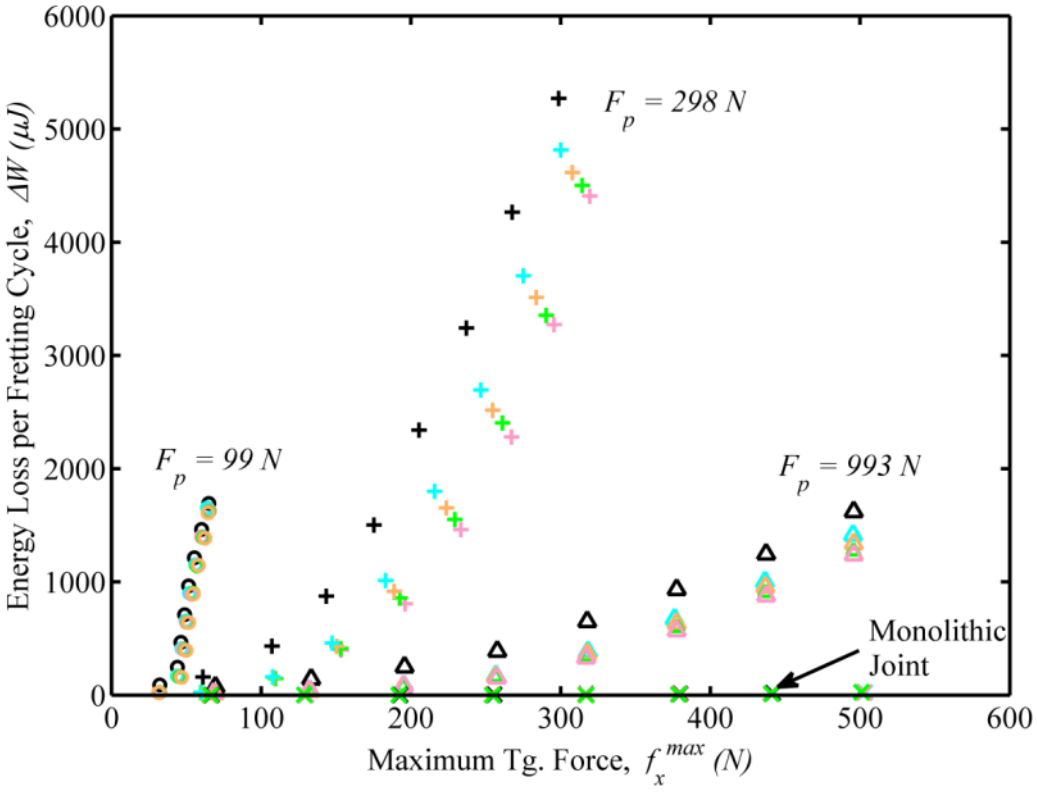

Fig. 5.8. Energy losses per fretting cycles (1-3-5-7-9th cycles) obtained from the monolithic and 1-bolt aluminum joints under different loading conditions

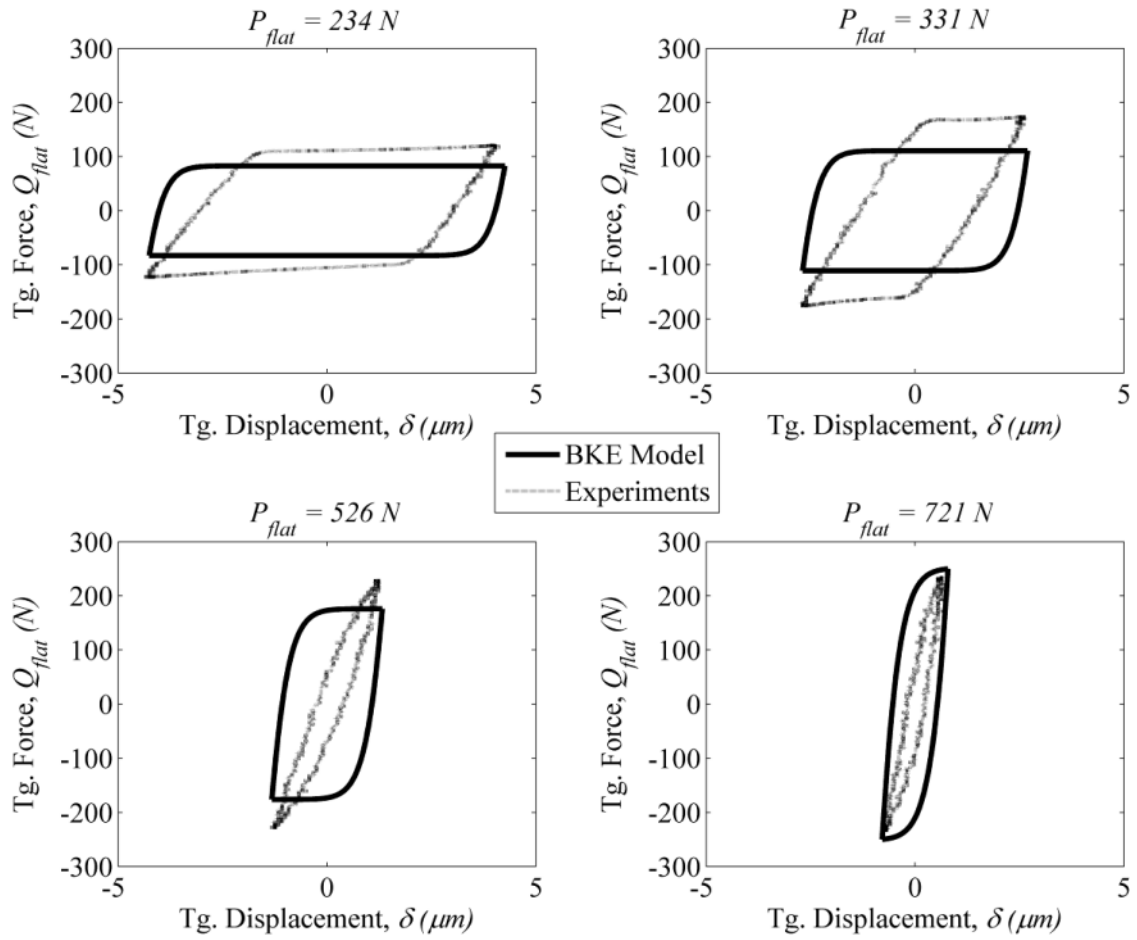

Fig. 5.9. Experimental fretting loops from bolted steel joint and the BKE model under different preloads

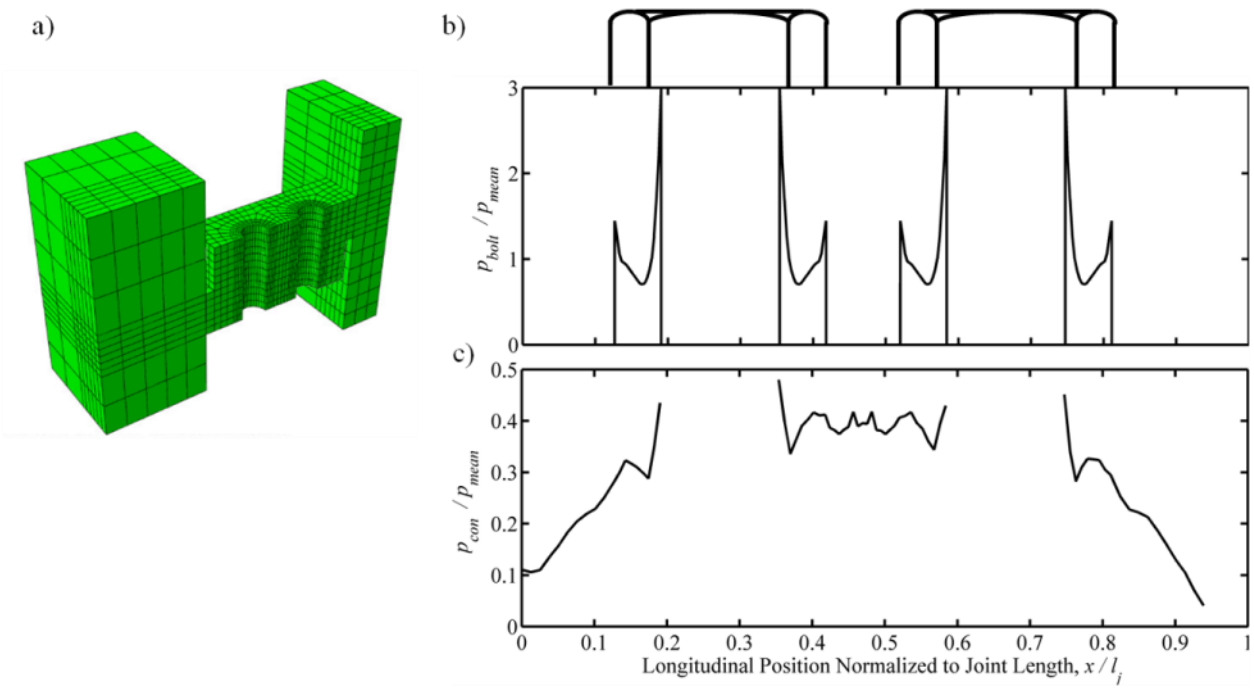

Fig. 5.10. Finite element analysis of the joint preloading: a) Meshed ABAQUS model of the joint, b) pressure between the bolt head and the upper joint surface, pbolt, and c) pressure over the contact interface between the two sides of the joint, pcon. Pressure values are normalized to the mean pressure observed between the bolt head and the upper joint surface.

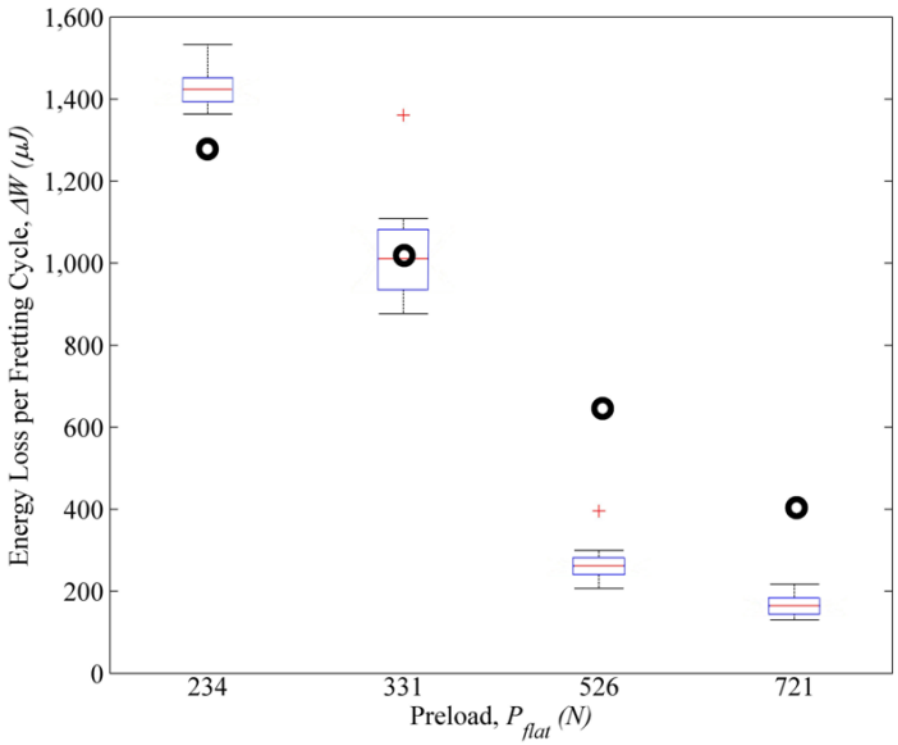

Fig. 5.11. Energy losses per cycle obtained from 10 cycles of fretting experiments (box-plots) and prediction of BKE model (thick circles)

5.8. Tables

Table 5.1. Design requirements for joint fretting apparatus

Experimental Apparatus Design Requirements
1. High reliability of the applied displacement or force
2. High accuracy of interfacial displacement measurement
3. High accuracy of interfacial force measurement
4. Minimal misalignment and out-of-plane motion
5. Operation under high-frequency tangential loading

Table 5.2. Torque input on the bolt and corresponding preload obtained from Eq. (5.2)

T_{in} *(lb-in)*	T_{in} *(Nm)*	F_p *(N)*	p_{mean} *(MPa)*
0.5	0.057	99	0.6
1.5	0.170	298	1.8
5	0.565	993	6.1

Table 5.3. Chemical composition and mechanical properties of the materials used in joints

	Aluminum Alloy 6061-T6	**Grade 420 Stainless Steel**
% Chemical Composition	Si(0.6), Fe(0.35), Cu(0.28), Mn(0.15), Mg(0.08), Cr(0.19), Zn(0.13), Ti(0.08), Other(0.1), Al(98.04)	C(0.35), Ni(0.14), Cu(0.04), Mn(0.44), N(0.06), Cr(12.34), P(0.02), Mo(0.03), Other(0.06), Fe_3C(86.52)
Poisson's Ratio	0.33	0.24
Young's Mod. (GPa)	69	200
Shear Modulus (GPa)	26.2	80.7
Yield Strength (MPa)	280	1360
Ult. Tensile Str. (MPa)	310	2025
% Elongation	14.6	25

Table 5.4. Surface roughness properties of the individual and combined joint samples (PZT and load cell halves)

Roughness	**Joint Half (before experiments)**			**Joint Half (after experiments)**		
Parameters	*PZT*	*LC*	*Comb.*	*PZT*	*LC*	*Comb.*
σ **(μm)**	1.763	2.015	2.677	1.859	1.847	2.620
η **(μm^{-2})**	$3.34\text{x}10^{-4}$	$2.51\text{x}10^{-4}$	$2.91\text{x}10^{-4}$	$2.87\text{x}10^{-4}$	$2.68\text{x}10^{-4}$	$2.77\text{x}10^{-4}$
***R* (μm)**	40.76	44.77	30.14	44.75	47.37	32.53
β	0.024	0.023	0.023	0.024	0.023	0.024
ψ	3.374	3.230	4.725	3.284	3.122	4.534

Table 5.5. Torque input on the bolt and corresponding preload obtained from Eq. (5.2)

T_{in} **(lb in)**	T_{in} **(N m)**	P_{flat} **(N)**	p_{mean} **(MPa)**
1.2	0.136	234	1.4
1.7	0.192	331	2
2.7	0.305	526	3.2
3.7	0.418	721	4.4

Table 5.6. PZT actuator tip motion, maximum tangential displacement measured at the PZT half of the joint, and friction coefficient values measured from the fretting loops

Amplitude of the sinusoidal motion of the PZT tip (μm)	δ_{max} **(μm), μ**			
	P_{flat}*=234 N*	P_{flat}*=331 N*	P_{flat}*=526 N*	P_{flat}*=721 N*
6.75	4.26, 0.479	2.69, 0.508	1.32, 0.420	0.79, 0.323

CHAPTER 6: INFLUENCE OF ROUGHNESS & LUBRICATION

6.1. Introduction

Joints constitute an important component of many assembled structures such as, for example, airplanes, gas turbine engines and hip joint implants. They make assembly, disassembly, and maintenance easier; enable the mating of different materials, and provide frictional damping for limiting hazardous resonance effects in structures. Along with the benefits, joints are usually associated with detrimental effects such as wear, corrosion, reduced fatigue life and strong nonlinearities. Complex interfacial phenomena (friction, slip, contamination, wear, roughness, etc.) introduced by the jointed surfaces complicate modeling which, in turn, increase design, manufacturing and maintenance costs. A thorough understanding of jointed interface physics will improve current state-of-the-art joint modeling.

The important interfacial phenomena listed above play a significant role in mechanical lap joints. Specifically, a joint can be loaded in normal (via, for example, bolts, rivets, welding, adhesive bonding, or accelerations due to high-speed rotation) and tangential (structural vibrations, rolling, cyclic operation) directions relative to the contact surface, and the interface mechanics involve friction, slip, wear particles, contamination, etc. Out of many different loading scenarios, the most simplified and realistic one occurs when the joint is preloaded by a constant force in the normal direction and oscillated by small tangential force or displacement. This contact is referred to as “fretting” in the literature [45]. Fretting response is usually characterized by a force-displacement loop (fretting loop), i.e., relative displacement of the joint halves versus the tangential force transmitted by the interface in response to this relative displacement. At the initial stages of gradual tangential loading, the interface response is linear elastic since the shearing traction is insufficient to cause slippage. When the tangential loading reaches a certain level which produces shear tractions larger than the friction force, microscopic slip of adjacent points on both sides of the interface occur. Such a partially slipping contact, results in a “softening spring” behavior until all the points on the interface start sliding relative to each other (i.e., gross sliding occurs). While gross sliding,

the friction force remains fairly constant and equal to the static friction force value unless severe asperity ploughing and bolt/rivet pinning occur.

Tangential unloading (compared to loading), initiates a sudden full stick behavior on the sliding interface. Essentially, the same physical events occurring during loading are also encountered during unloading, but in the opposite direction. A schematic of a generic fretting loop is depicted in Fig. 6.1. Tangential force and displacement are denoted by Q and δ, respectively, with maximum values designated by the subscript "max." To distinguish partial slip and gross sliding regimes, the tangential displacement is separated into two components: (a) sliding displacement, δ_s and (b) partial slip, δ_{max}- δ_s. Joint stiffness is the slope of the initial linear elastic response, k_{joint}, and energy loss per fretting cycle is given by the area inside the fretting loop, ΔW.

It is reported that up to 50 different parameters influence fretting response [93], where friction coefficient, magnitude of slip and contact pressure are identified as "primary" sets of parameters directly affecting fretting response. The so-called "secondary" parameters (such as humidity, lubricant, residual stresses, work-hardening, microstructure) influence the fretting response by altering the primary parameters. The fretting response is also influenced by loading history, surface treatments/finishes, and the underlying (bulk) materials [45].

In this chapter, we investigate the effects of roughness and boundary lubrication on the fretting loops during the initial stages of cyclic loading in mechanical lap joints. Once these effects are thoroughly understood, initial roughness and contact conditions of the jointed interface can be optimized for a specific application. Previously, it was found that roughness influences sliding conditions [126], friction [127] and fretting wear [127–129]. Recently, Kubiak et al. [130] studied the evolution of fretting loops for a sphere-on-flat contact of steel samples with various surface roughness conditions, and found that initial roughness and machining processes influence the friction coefficient, partial slip displacement, and surface degradation. Kubiak and Mathia [131] investigated the effect of boundary lubrication with the

same set of surface roughness conditions and showed that initial roughness was influential on fretting response under lubricated conditions, as well. A review article by Zhou and Vincent [132] pointed out that solid lubricants were more effective in the partial slip fretting regime, whereas oil and grease were more beneficial in the gross sliding regime.

Studies focused on dynamic modeling of joints utilize fretting loops to determine stiffness and damping (loss factor) associated with lap joints [95,97,105,133]. The effects of adhesive bonding [134,135] on the joint stiffness and hole lubrication [136] on fretting fatigue life of lap joints have also been studied. A thorough investigation of the influence of surface roughness and lubrication on the early stages of fretting behavior of mechanical lap joints is missing from the literature. In this work, we study the effects of loading conditions, surface roughness and lubrication on friction force, partial slip displacement, tangential joint stiffness and energy dissipation per fretting cycle, measured from aluminum and steel lap joints. Limited number of fretting cycles and mild loading conditions are studied so that we have better control over contact roughness and lubrication. It is important to note that surface roughness and lubrication contamination are variables in practical applications since much severer loading conditions for larger number of cycles are imposed on the joints. Our study aims to understand fundamental mechanisms influencing contact friction, stiffness and damping at all possible contact responses (i.e., partial and gross slip) but do not attempt to study the evolution of contact parameters. In addition to qualitative study of the experimental data, the predictions of the models presented in Chapter 4 are compared with the dry contact experiments for smooth and rough aluminum and steel samples. This way, the applicability of the models is validated through a range of surface roughness and material properties.

6.2. Experimental Details

Joint fretting apparatus

A fretting apparatus was designed to obtain fretting loops from lap joints (Fig. 5.1). A tri-axial load cell (ICP-260A01, PCB Piezotronics) was used to measure the in-situ forces in three orthogonal

directions throughout the experiments; by comparing the relative amplitudes of the out-of-plane forces (normal to the joint interface, f_y, and perpendicular to the fretting motion, f_z) with the friction force, the extent of misalignment was found. The misaligned forces did not exceed 5 % of the measured friction force in any of the experiments presented in this chapter. A piezo-stack actuator, PZT (P-845.60, Physik Instruments) was utilized to precisely impose the tangential displacement. Imposed displacement, Δ, was measured by the internal strain gauge of the PZT. In addition to the PZT's internal strain gauge, a laser nanosensor (LNS 18/120, LMI Technologies B.V.) was employed for measuring the relative displacement of the joint halves, δ. Synchronization and control of the experimental setup was performed with LabVIEW 8.0 software. The virtual test environments developed in LabVIEW allowed for amplitude and frequency modulation of the imposed displacement and sampling rate modulation for all sensor and actuation signals. Further details of the fretting apparatus can be found elsewhere [137].

Joint samples

Smooth (root-mean-square (rms) roughness 0.5-0.8 μm) and rough (rms roughness 2.3-2.9 μm) aluminum and steel joint samples (total of four different lap joints) were built with identical machining techniques and geometries. Smooth and rough surfaces were obtained by changing only the milling cutter radius and keeping the rest of the machining parameters the same. Therefore, any possible mismatch of residual stresses due to machining was prevented. The geometry of the samples results in a flat-on-flat contact configuration preloaded by two stainless steel M3 socket head bolts (165 mm^2 nominally flat rectangular contact area as shown in Fig. 6.2).

The chemical composition and mechanical properties for the aluminum and steel alloys are listed in Table 6.1 (as obtained from the suppliers: Central Steel and Wire, and Precision-Marshall Steel, respectively). Both alloys are sufficiently strong and are, thus, suitable for highly stressed structural components [69,138]. The joint halves were cleaned according to ASTM G115-10 standard to remove the presence of any wear debris and ensure dry contact conditions (ultrasonic cleaning with acetone).

Roughness measurement and characterization

The roughness characteristics of the joint surfaces were obtained from surface height measurements (4 mm long line scans) taken by a portable contact profilometer (Marsurf PS 1, Mahr Federal Inc.). High-frequency noise and low-frequency waviness were filtered by a band-pass filter with low and high-pass cutoff wavelengths of 0.8 mm and 0.02 mm, respectively. The cutoff values chosen for our application comply with internationally recognized standards (ASME B46.1). Furthermore, since the surfaces were prepared by milling, the contacting surfaces show anisotropic roughness patterns. When preparing the smooth and rough samples, we tried to obtain "extreme" roughness parameters with milling; i.e., smoothest and roughest surfaces possible. The rms roughness values we obtained are similar to the lap joint roughness values used by other researchers [95]. We chose not to change the surface preparation method to ensure that the residual stresses introduced through manufacturing are comparable for all joint samples. Typical surface height profiles for smooth (rms roughness 0.5-0.8 μm) and rough (rms roughness 2.3- 2.9 μm) aluminum and steel joints are presented in Fig. 6.3.

As suggested by the analyses of McCool [84] for anisotropic surfaces, three steps were followed to extract the equivalent roughness parameters: (i) find two orthogonal directions yielding maximum and minimum surface height slopes on the contacting surfaces; (ii) compute the spectral moments of the surface height data $y(x)$ obtained from the two orthogonal directions; and (iii) compute the combined spectral moments and roughness parameters (average radius of asperity tips, R; areal density of asperities, η; and rms roughness, σ). The flow of computations to determine roughness parameters from surface heights data is summarized in Eq.(5.1). The combined surface roughness parameters as well as the individual roughness parameters for the joint samples attached onto the PZT and Load Cell (LC) halves before and after fretting experiments are given in Table 6.2. Note that each sample was exposed to 800 fretting cycles in total, half of which were under boundary/mixed lubricated conditions. The changes in surface roughness of all samples after fretting experiments were not significant because of the relatively low number of fretting cycles. Nevertheless, there was a nearly 10 % decrease in rms roughness for each sample.

Loading conditions

The joint halves were clamped by two stainless steel M3 socket head bolts. The preload on each bolt was imposed by a torque driver (Precision Instruments) with a dial and memory needle to measure the torque input. The normal load on the contact is determined by Eq.(5.2). Note that the nut factor in this equation is an experimental constant, where all the factors influencing the torque-preload relationship such as friction, torsion, bending and plastic deformations of the threads in a bolt are lumped. Hence, its value shows variation depending on the material, lubrication, and temperature. Bickford [113] surveyed nut factor values and found a mean value of 0.199 and minimum and maximum values of 0.158 and 0.267, respectively, for steel bolts. In accordance with this, a value of 0.2 was used for the nut factor in our experiments. In addition to the variability of the nut factor, bolting by torque driver can introduce preload scatter, and the preload can also change during operation [113]. The scatter for the specific torque driver we used in our work is documented not to exceed 2 % by the manufacturer. To check the constant preload assumption, the torque on the bolts was measured before and after each set of experiments, and a mean difference of 5 % was observed. Note that for high-cycle fretting fatigue or wear studies, surface degradation and run-in processes can also result in variation of normal preload. Since in this work we studied the initial stages of fretting and surface degradation is not a main variable at these stages, further change in the bolt torque values due to run-in processes is not observed. Despite these checks, it is important to remember that the preload values documented in this work were prone to some scatter, which is also the case in practical joint applications. Table 6.3 lists the total bolt torque input; corresponding preloads, P_{flat} and mean contact pressures, p_{mean}. This range of preloads is intentionally chosen to capture gross to partial slip fretting regimes. In practice, the mean pressure values at jointed interfaces vary from 5 to 200 MPa [97] and, hence, gross slip is not encountered unless unexpected reduction in clamping pressure occurs.

The experiments were carried out under laboratory conditions at a temperature of 21-23 ^{o}C and a relative humidity of 40-45%. The displacement input imposed on one half of the joint by the PZT actuator is given by Eq.(5.3). In these experiments, the fretting frequency was chosen as 1 Hz to ensure

quasi-static contact conditions. Fig. 6.4 shows a typical tangential displacement signal imposed on the PZT tip. Eight different maximum tangential displacements (2.25 μm to 18 μm with 2.25 μm increments) were used for each bolt preload. Therefore, each sample was fretted for 240 cycles (3 preloads x 8 maximum tangential displacements per each preload x 10 cycles per each maximum tangential displacement). When presenting the fretting loops, time averaging of certain number of fretting loops is utilized. Since the input frequency is fixed to 1 Hz, the forces and displacements read from the sensors are divided in to cycles of 1 second duration, and then arithmetic mean of forces and displacements are computed for a chosen number of cycles.

6.3. Results

Dry contact fretting loops

The fretting loops obtained from each experiment (10 cycles per experiment as given in Eq. (5.3)) were averaged over time. No post-processing or filtering was utilized to generate these averaged fretting loops; i.e., raw data was reliable and repeatable without any need for averaging. Note that the actual relative displacement of the joint halves differed from the maximum tangential displacement imposed by the PZT tip due to the compliance of the joint fretting apparatus. As a result, higher joint stiffness resulted in less joint motion at a particular imposed displacement.

Fig. 6.5 and 6.6 show the average fretting loops obtained using aluminum and steel joint samples under the bolt preloads listed in Table 6.3 and maximum imposed tangential displacements of 9 μm and 18 μm with smooth and rough surface features, respectively. These displacements were chosen to exhibit both partial and gross slip fretting responses, depending on the preload. Increasing preload increased the tangential joint stiffness and hence resulted in reduction of the displacement transferred to the joint. This reduction was minimal for the smooth aluminum sample since the joint stiffness did not vary significantly when the preload was increased. The friction (tangential) force increased with increasing preload. Increase in friction force for smooth and rough steel samples was proportional to increasing preload whereas for aluminum, the friction force showed a sudden increase between bolt preloads of 0.192 Nm

and 0.305 Nm. This sudden increase was due to an increase in the real area of contact and higher adhesive properties of the aluminum surfaces. In addition, the rough aluminum sample also showed a sudden increase in tangential stiffness.

Another important observation from Fig. 6.5 and 6.6 is that rough joint samples exhibited larger partial slip which extended up to 10 μm for aluminum and 5 μm for steel joints. The partial slip regime is particularly important since high bolt pressures prevent gross slip in real life applications, so all the stiffness and energy dissipation in practice can be explained by partial slip behavior unless loss of contact pressure occurs (via bolt loosening, debonding, etc.). Note that the partial slip behavior is intertwined with the friction force and tangential stiffness of the joint. Increasing friction force with constant tangential stiffness means more slippage will be observed when the static friction force is reached. Increasing tangential stiffness with a constant friction force, in contrast, results in less slippage. For both the steel and aluminum samples under low bolt preload of 0.192 Nm, the smooth samples showed higher tangential stiffness and lower friction force, meaning shorter partial slip regime than the rougher interfaces. However, higher preloads triggered sharp increase in tangential stiffness through galling process, in the case of the rough aluminum joint. Thus, the smooth aluminum sample started to exhibit more slippage than the rough sample.

A qualitative analysis using microscopy was conducted to investigate the sudden increase in friction force and tangential stiffness observed in aluminum joint samples. Fig. 6.7 and 6.8 present typical 70X micrographs of the rough and smooth aluminum and steel joint surfaces obtained using a JEOL 6060LV Scanning Electron Microscope (SEM) after the fretting experiments. Note that in each of these figures, four joint surfaces are presented: two surfaces (of the load cell and the PZT halves) for each smooth and rough joint sample. Each micrograph shows a 1.8 mm x 1.2 mm region in the middle of the two bolt holes, where the pressure was highest during the fretting experiments. The fretting direction is shown with the horizontal double arrow whereas the machining marks are shown by the smaller arrows placed directly on the micrographs. Note that the machining marks are not aligned along the fretting direction,

but create anisotropy both in texture and roughness. As clearly seen from Fig. 6.7, the rough aluminum sample exhibits scratches along the fretting direction (indicated as a circled region). These scratches are signs of possible galling occurred at the asperity junctions. Note that the scratches are spread over the whole contact area, but they are more densely visible over the regions shown in these micrographs due to the high contact pressure. Although the maximum relative motion of the aluminum joint halves is measured as 22 μm (in the smooth surface case under the lowest bolt torque), the length of the scratch shown in the micrograph reaches 1 mm in the middle of the contact. This indicates that all of the asperity junctions around this scratch line experienced galling behavior and this is due to the highest level of contact pressure imposed by the bolt torque, in this region. Further zoom-in on the scratch shows discrete lines of scratches over these junctions. The rough steel sample exhibits plastic deformation, but does not show any signs of possible galling behavior (i.e., no adhesive wear or scratches). Given the fact that the virgin surfaces did not have any significant features along the fretting direction, these SEM images suggest that fretting loops using aluminum joints were highly influenced by mild galling. Consequently, joint stiffness and energy loss per fretting cycle for the rough aluminum sample varied significantly with changing loading conditions.

Boundary/mixed lubricated contact fretting loops

To study the effects of joint contamination in the presence, for example, of lubrication, a few drops (5 mg) of a polyolester (POE) synthetic lubricant (grade EMKARATE, RL68H, Nu-Calgon Wholesaler, Inc.) was applied on each sample, and fretting experiments with the same set of bolt preloads and maximum tangential displacements were conducted. POE lubricants exhibit excellent solubility, thermal and chemical stability, and long life, which make them suitable for use in refrigeration systems, for example [139]. Besides, POE lubricants are shown to reduce friction and wear, and thus increase the scuffing life of metal-on-metal contacts [140]. Therefore, the POE lubricant used in this work is an appropriate choice to prevent the unpredictable effects of galling, which were clearly displayed in fretting of the rough aluminum samples under dry (unlubricated) contact conditions.

Fig. 6.9 and 6.10 show the averaged fretting loops under boundary/mixed lubricated contact conditions for smooth and rough joint samples, respectively. For the case of smooth samples (Fig. 6.9), the fretting loops for aluminum and steel joints had nearly identical maximum tangential force and displacement, but the steel joint showed stiffer response in the partial slip regime. This suggested that friction and sliding characteristics were mainly controlled by the traces of the fluid film and that the tangential stiffness was still influenced by the solid material properties.

Note that 60 % or more of the maximum imposed displacement was transferred to the smooth aluminum and steel joint samples under lubricated conditions; i.e., $\delta_{max} > 0.6\,\Delta_{max}$ (91 % for T_{bolt} = 0.192 Nm, 73 % for T_{bolt} = 0.305 Nm, 61 % for T_{bolt} = 0.418 Nm). This ratio dropped to 27 % for the dry contact case shown in Fig. 6.5. This difference was due to the decrease in tangential stiffness and friction force with the use of lubrication. Partial slippage observed in smooth lubricated joints was less than 5μm in aluminum and 2 μm in steel; i.e., less than half compared to the dry contact conditions.

Similar observations can be made for fretting of rough steel samples depicted in Fig. 6.10, whereas major differences appear for aluminum samples. The rough aluminum samples showed a sudden increase in tangential stiffness and friction force when the bolt preload was increased from 0.192 to 0.305 Nm. This suggests that the small amount of lubricant used was not as effective in avoiding solid-solid contact at higher contact pressures. To test this hypothesis, the average friction coefficient values were calculated as the ratio of the average maximum tangential force to the normal contact force, obtained from Eq.(5.2) for each bolt torque:

$$\mu = \frac{Q_{\max}^{av}}{P_{flat}} \tag{6.1}$$

This formulation coincides with the static friction coefficient only when the joints are in the gross sliding fretting regime. The obtained average friction coefficient values are tabulated in Table 6.4 for both dry and lubricated contact conditions. Friction coefficient values for steel and smooth aluminum samples under boundary/mixed lubrication decreased to almost one third of the values under dry contact

conditions. However, the friction coefficient did not drop significantly in the rough aluminum case under lubricated conditions and exhibited a sharp increase when the bolt preload increased from 0.192 to 0.305 Nm, as in the dry contact case. These observations provided further evidence that boundary lubrication was not sufficient in preventing galling in rough aluminum joints. Considering the facts that full film lubrication with POEs reduces the friction coefficient well below 0.1 for many engineering surfaces [141] and the observed friction coefficients listed in Table 6.4 are all greater than 0.1 assured that asperity (solid) interactions played a major role, which was expected for boundary, mixed and starved lubricated conditions.

Joint stiffness

Tangential joint stiffness is an important parameter in structural modeling of jointed structures and can be directly extracted from the fretting loops as the slope of the tangential force curve when the loading is reversed (i.e., the slope at the sharp edges of the fretting loops). Tangential stiffness depends on the normal preload but not on the tangential load (neither the tangential displacement nor the tangential force). Fig. 6.11 shows the stiffness values obtained from the fretting experiments under different conditions. Aluminum stiffness values varied from 30 to 65 N/μm under dry contact conditions whereas that range extends up to 200 to 275 N/μm for steel. Owens and Lee-Sullivan [134] showed that the stiffness of aluminum-to-aluminum shear lap joints was around 40 N/μm. Stiffness values ranging from 100 to 500 N/μm were reported in the literature [95,97,105] for steel lap joints under various loading conditions. Thus, the values obtained from the fretting loops in this study were in line with the literature. For all joints, lubrication reduced the joint stiffness by 20 to 50 %. The smooth steel joint under all preloads and the aluminum joint under the preload of 0.192 Nm exhibited stiffer response independent of the contact conditions (possibly due to larger real area of contact and higher adhesion), whereas the stiffness of the rough aluminum joint almost doubled and overtook the smooth aluminum joint stiffness when the preload was set to 0.305 Nm. This behavior can be explained by the initiation of galling in aluminum due to high contact pressure. The influence of surface roughness on the dry joint stiffness was preserved in lubricated joints, too. Similar observations were made by Kubiak and Mathia [131], where it

was shown that roughness played an important role in both dry and boundary lubricated sphere-on-flat fretting contact. To repeat, these observations are only valid for boundary and mixed lubrication regimes, where solid-to-solid contact still has a significant contribution to overall contact parameters.

Energy dissipation

As clearly observed in Fig. 6.5, 6.6, 6.9, and 6.10, the joint samples demonstrated hysteretic response to fretting; i.e., the energy needed to reload the contact was higher than the energy recovered by unloading. The energy loss per fretting cycle is mainly due to frictional losses incurred by partial slip on the joint interface and can be computed from the area inside the fretting loops. Energy dissipation in linearly varying friction force ($Q \sim k\delta$, *k-constant*) scales with the square of the maximum tangential force. Goodman's [114] and Mindlin et al.'s [58] analyses suggested that the energy dissipation scales with the third power of the maximum tangential force, in the case of frictional energy losses under partial slip contact conditions; i.e., $\Delta W \sim Q_{\max}^3$. Smallwood et al. [115] and Hartwigsen et al. [116] experimentally found that the exponent ranges between 2 and 3 depending on the nonlinearity effects. The energy losses obtained from the four joint samples under various tangential displacements (forces) are presented as logarithmic plots in Fig. 6.12-14 for bolt preloads of 0.192, 0.305 and 0.418 Nm, respectively. Each curve represents a joint sample under dry or lubricated conditions, and there are 8 data points for each curve. Each of these data points corresponds to the averaged (over ten cycles) energy dissipation obtained by different maximum tangential displacement imposed on the joint. In addition to these energy losses, straight lines with slopes of 2 and 3 are plotted for comparison with the above-mentioned literature. The curves for all preloads exhibited slopes between 2 and 3 except for the curves representing gross slip behavior, such as the curves for the lubricated contact conditions and parts of the curves corresponding to higher tangential forces. For these exceptions, the energy loss increased significantly without any significant increase in tangential force since the tangential force reached the static friction force and the whole contact started to slide; i.e., the joint sliding displacement increased, and thus the energy dissipation increased by the amount of increase in tangential displacement.

With the exception of aluminum under bolt preload of 0.192 Nm, lubricated contacts dissipated considerably higher energy than their dry equivalents. For aluminum under a bolt preload of 0.192 Nm, the energy loss responses are similar for low tangential forces, with lubricated contact dissipating more energy at higher forces. In addition, the smooth (rms roughness 0.5- 0.8 μm) samples dissipated more energy than their rough (rms roughness 2.3-2.9 μm) equivalents under both dry and lubricated contact conditions. Since slip damping is an essential source of structural damping needed to keep resonant vibration stresses within reasonable limits, boundary/mixed lubricated smooth joint interfaces can be used in many engineering applications. Note that lubricated contacts dissipate energy by enabling more slippage throughout the jointed interface. Excessive slippage may cause wear and corrosion, both of which degrade the surface and may reduce the operational life of the joints. However, in lubricated contacts, the friction force decreases considerably as seen in Table 6.4. Hence, the hazardous effects of slippage over the contact would be less compared to the dry contact slippage. Since the increase in slippage is more than the decrease in friction force, the lubricated contact dissipates more energy than the dry equivalent case.

Another important observation from Fig. 6.12-14 is the shift of the energy dissipation curves to the right, meaning that for the same amount of energy dissipation, more tangential force was needed. More accurately stated, for the same maximum imposed tangential force, joints under heavier loading conditions dissipated less energy due to an increase in friction force, thus preventing slip.

The comprehensive findings from Sandia National Laboratories, published as a handbook in 2009 [95], matched well, both qualitatively and quantitatively, with our energy dissipation results. Sandia used three roughness scales on a stepped flat steel lap joint with a contact area of 200 mm^2 (close to the contact area used in this work). Out of these roughness scales, the fine scale was nearly identical to our rough scale, and the 0.418 Nm bolt torque case was closer to their loading conditions except that their normal preloading was greater. Sandia's energy dissipation results ranged from 10 to 1000 μJ with maximum tangential forces ranging from 200 to 1000 N, which correspond to a curve of nearly identical slope with

our “dry & rough” curve for the steel joint presented in Fig. 6.14. The only difference was that their curve was shifted further to the right with respect to our results, and this was mainly due to the decrease in energy dissipation caused by the increase in normal force as mentioned before. Thus, a quantitative correlation with the existing literature was possible.

6.4. Discussion

In Chapter 5, a validation of the friction models developed in Chapter 4 is presented with a steel joint of a given surface roughness (rms roughness of 2.7 μm) under various tangential and normal loading conditions. To test the broader applicability of the models, the experiments presented in this chapter can be utilized especially since they cover a range of roughness values (0.57-2.87 μm) and two materials (aluminum alloy 6061-T6 and grade 420 stainless steel).

Fig.6.15 presents a comparison between the dry contact fretting experiments and the predictions of the BKE model presented in Chapter 4 for smooth aluminum and steel surfaces. The model predictions correlate well with the experimental observations for the steel sample. However, the model deviates considerably in the aluminum surface case. The main reason for this discrepancy is the galling behavior mentioned above. Note that, if the friction modeling approach outlined in Chapter 4 is supported with an asperity-scale contact accounting for galling behavior observed in aluminum surfaces, the model predictions might improve. The current dry contact formulations cannot account for galling or cold-welding phenomena. Another observation one can make from Fig 6.15 is that the correlations between the model and experiments worsen by increasing normal load. This is due to increasing plastic deformations and limitation of the current modeling approach to account for severe plasticity over the contact. This argument becomes clearer when rough surface equivalent of Fig 6.15 is studied in Fig 6.16. As the roughness increases, the plasticity index and hence the plastic deformations over the contact increases. Therefore, the model predictions for both aluminum and steel surfaces worsen when compared to the smooth case. Nevertheless, the model predicts the friction response of steel joint samples under fretting loading upto a reasonable accuracy. Note that the modeling approach described utilizes a multi-scale

physics-based methodology and do not require any curve-fit parameters. Therefore, these models are predictive unless the material response at asperity-scale is governed by adhesive and chemical properties of the surfaces (as in aluminum case).

6.5. Conclusion

The influence of surface roughness and the presence of lubrication on the early stages of fretting response of mechanical, specifically Al 6061-T6 and Grade 420 stainless steel, joints were experimentally studied. Fretting loops obtained from a joint fretting apparatus developed by the authors were utilized in analyses. Special attention was directed to changes in friction force, partial slip, tangential stiffness and energy dissipation with changing roughness, loading and contact interface conditions. The experimental results obtained match well with data existing in the literature. In addition, a comparison of the dry-contact experimental results and the models developed in Chapter 4 is presented. The models are found to predict the friction behavior for the steel samples under fretting loading. The following conclusions summarize the findings of this experimental study:

- An increase in bolt preload increases the friction force and tangential joint stiffness, but decreases partial slip and energy dissipation.

- An increase in tangential displacement imposed on the joints, increases the friction force under partial slip. Although friction force remains constant under gross sliding, slippage continues to increase with increasing imposed displacement, and thus energy dissipation increases without noticeable increase in friction force. Tangential stiffness is shown to be independent of tangential loading.

- Friction force is higher in smoother aluminum and rougher steel joint samples.

- Smoother (rms roughness 0.5-0.8 μm) joints exhibit stiffer tangential response unless galling occurs. Rougher (rms roughness 2.3-2.9 μm) joints show more compliant response and, thus,

larger partial slip displacements, which reaches up to 10 μm for aluminum and 5 μm for steel joints under dry conditions.

- Smoother (rms roughness 0.5-0.8 μm) joints dissipate more energy under greater normal preload (partial slip regime) conditions.

- Galling occurs in aluminum joints under greater normal preload conditions and causes a sharp increase in both tangential force and joint stiffness.

- Traces of POE lubricant (boundary and mixed lubrication regimes) reduce the differences between smooth (rms roughness 0.5-0.8 μm) and rough (rms roughness 2.3-2.9 μm) joint responses but do not completely eliminate them. The roughness effects for dry contacts mentioned above prevail for lubricated contacts too.

- Boundary/mixed lubrication reduces the friction force by approximately one third, tangential joint stiffness and partial slip displacements by half, and increases energy dissipation per cycle up to an order of magnitude. Galling continues to be influential on the friction force and tangential joint stiffness under boundary/mixed lubrication.

- Smooth steel samples under dry contact and greater preloading conditions provide stiff joint responses with little damping, whereas lubricated smooth joints under light preloads provide high damping and resonance control to the jointed structures.

6.6. Figures

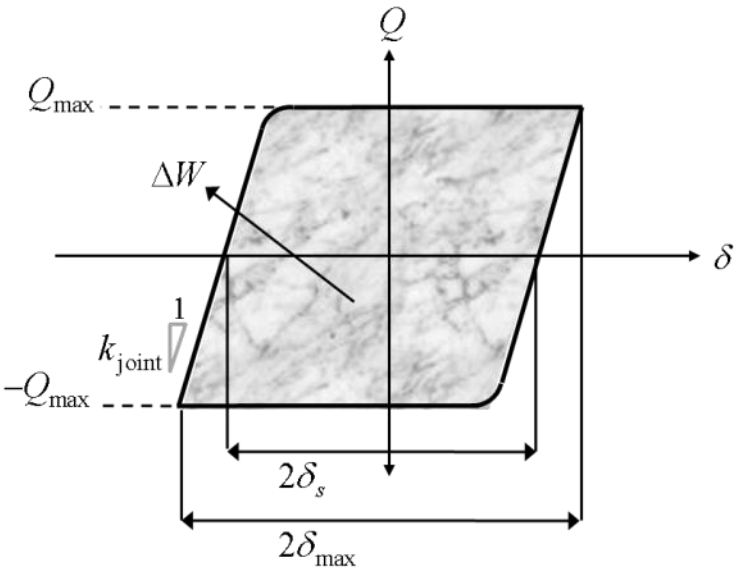

Fig. 6.1. Schematic of a typical fretting loop showing critical joint parameters.

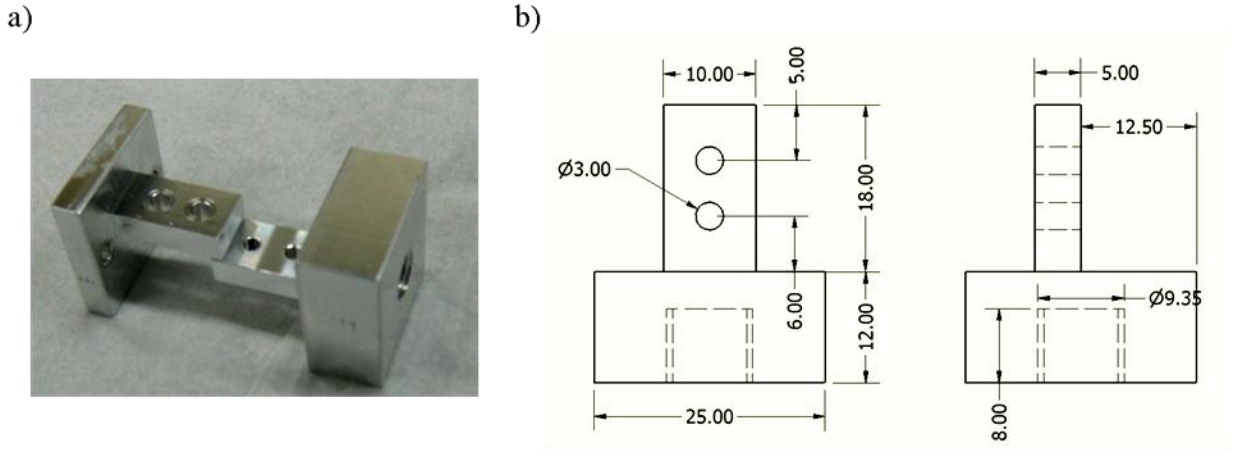

Fig. 6.2. (a) Photograph of the smooth steel joint sample and (b) technical drawing (dimensions in mm) of the PZT half of the smooth steel joints. All joints are identical in geometry but have different surface roughness.

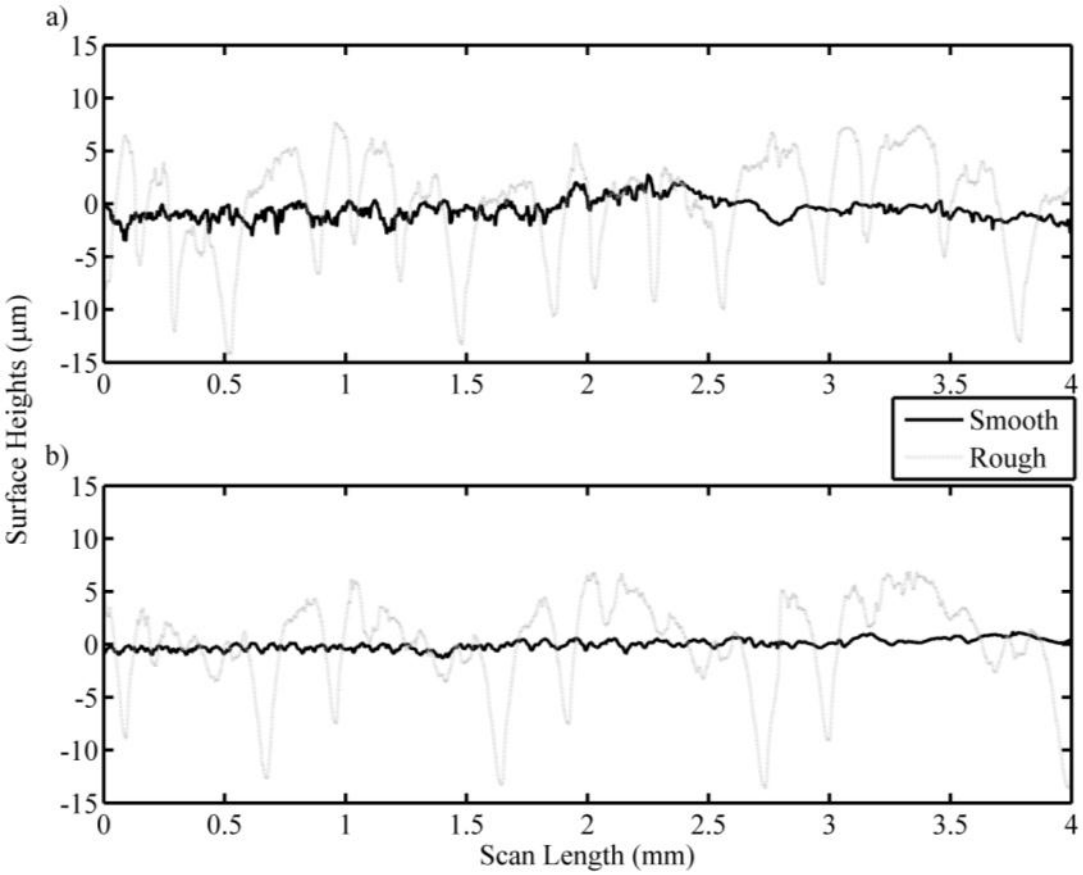

Fig. 6.3. Surface heights obtained from profile measurements of smooth and rough a) aluminum and b) steel joints.

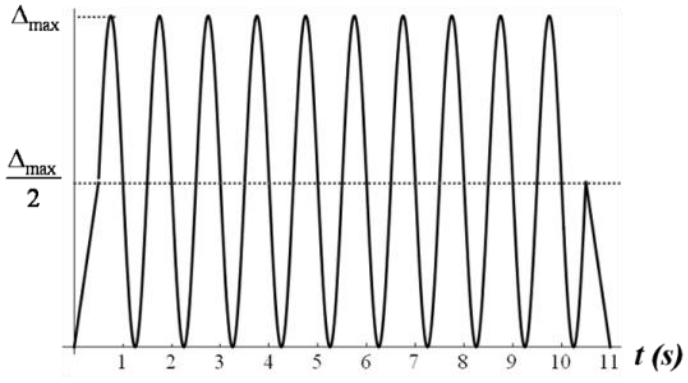

Fig. 6.4. Imposed tangential displacement (PZT tip displacement) given in Eq.5.3.

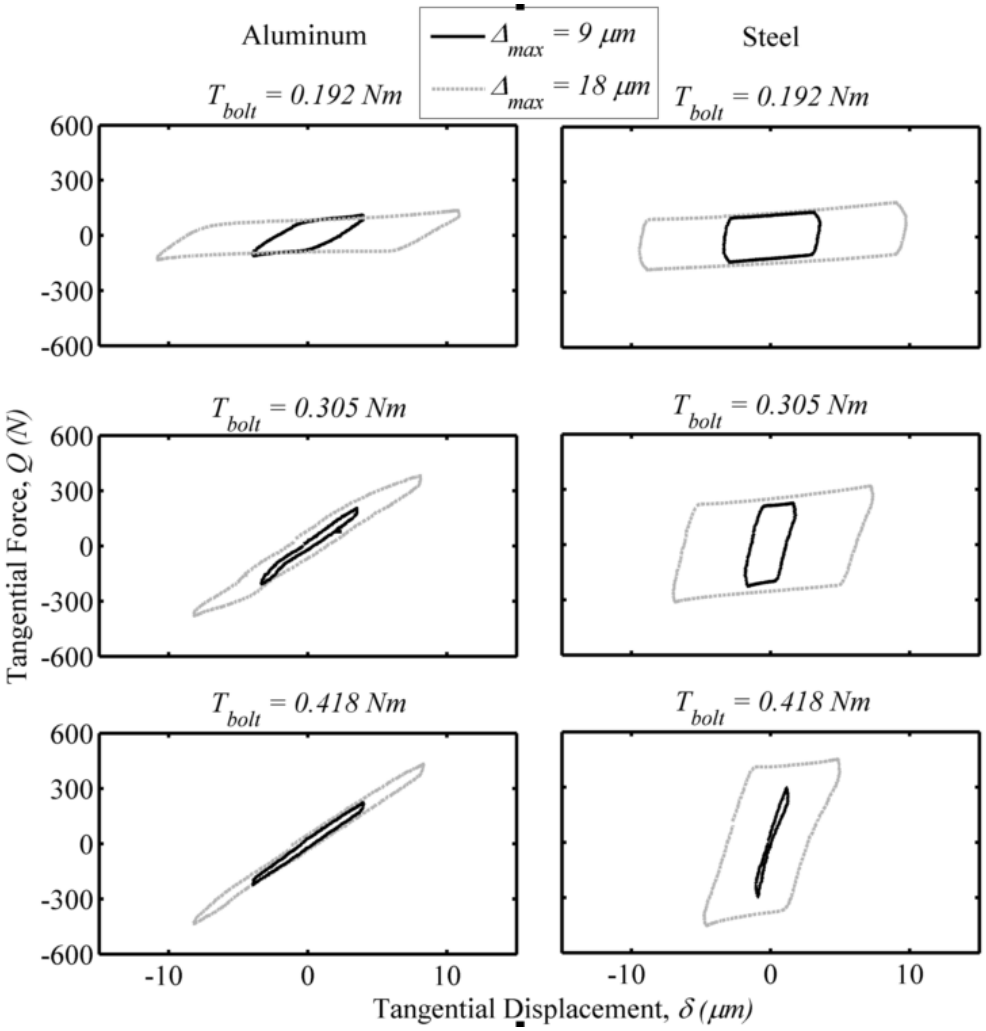

Fig. 6.5. Average fretting loops obtained from the smooth aluminum and steel joint samples under various loading and dry conditions.

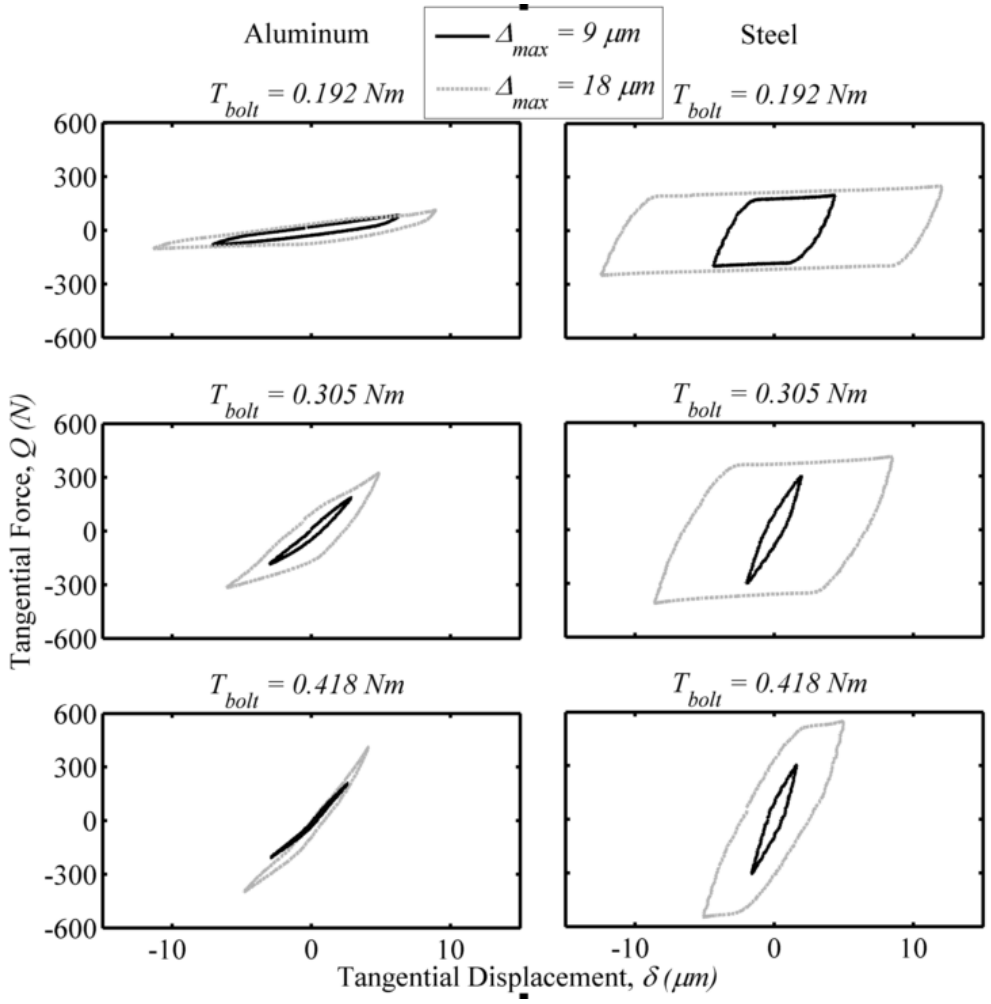

Fig. 6.6. Average fretting loops obtained from the rough aluminum and steel joint samples under various loading and dry conditions.

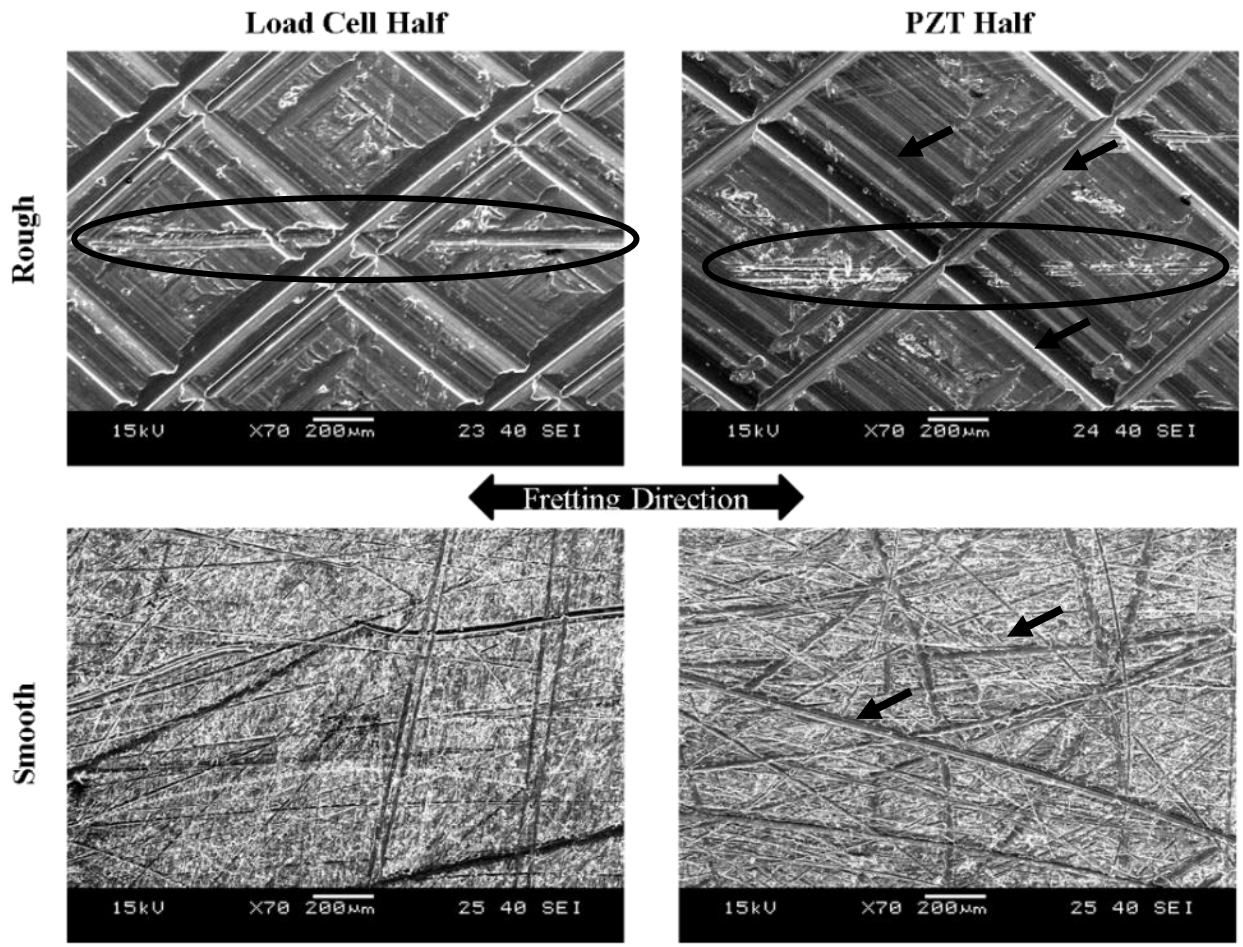

Fig. 6.7. SEM images of aluminum samples after dry fretting experiments. Arrows show typical machining marks and circled areas show mild galling.

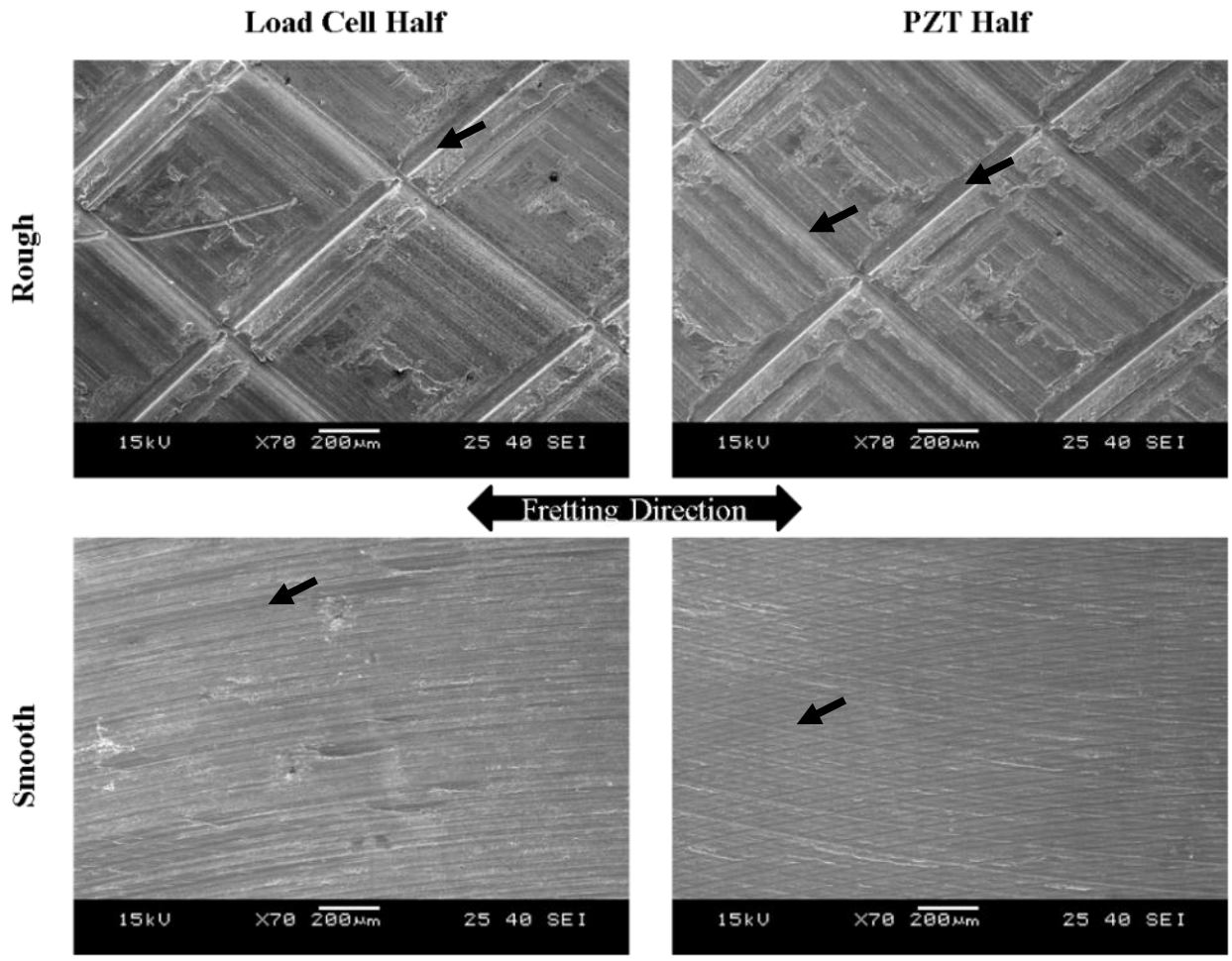

Fig. 6.8. SEM images of steel samples after fretting experiments. Arrows indicate typical machining marks.

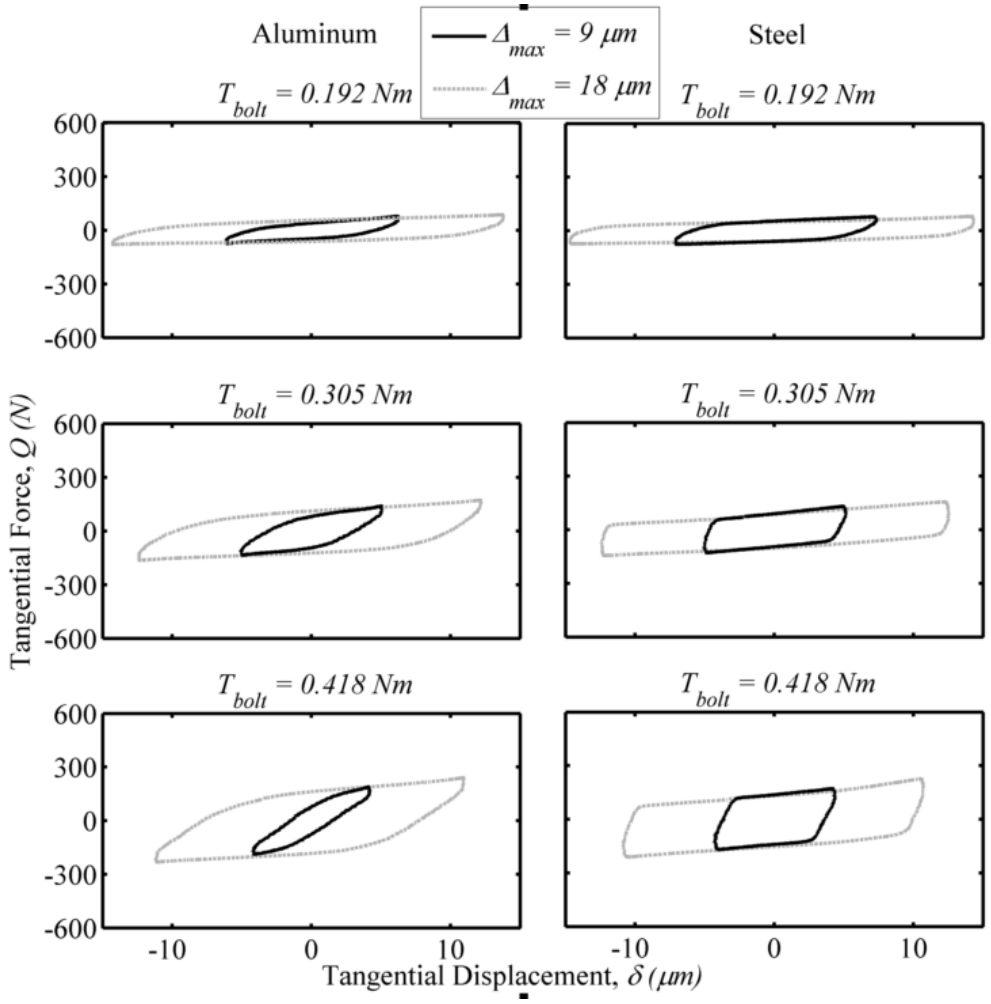

Fig. 6.9. Average fretting loops obtained from the smooth aluminum and steel joint samples under various loading and boundary/mixed lubricated contact conditions.

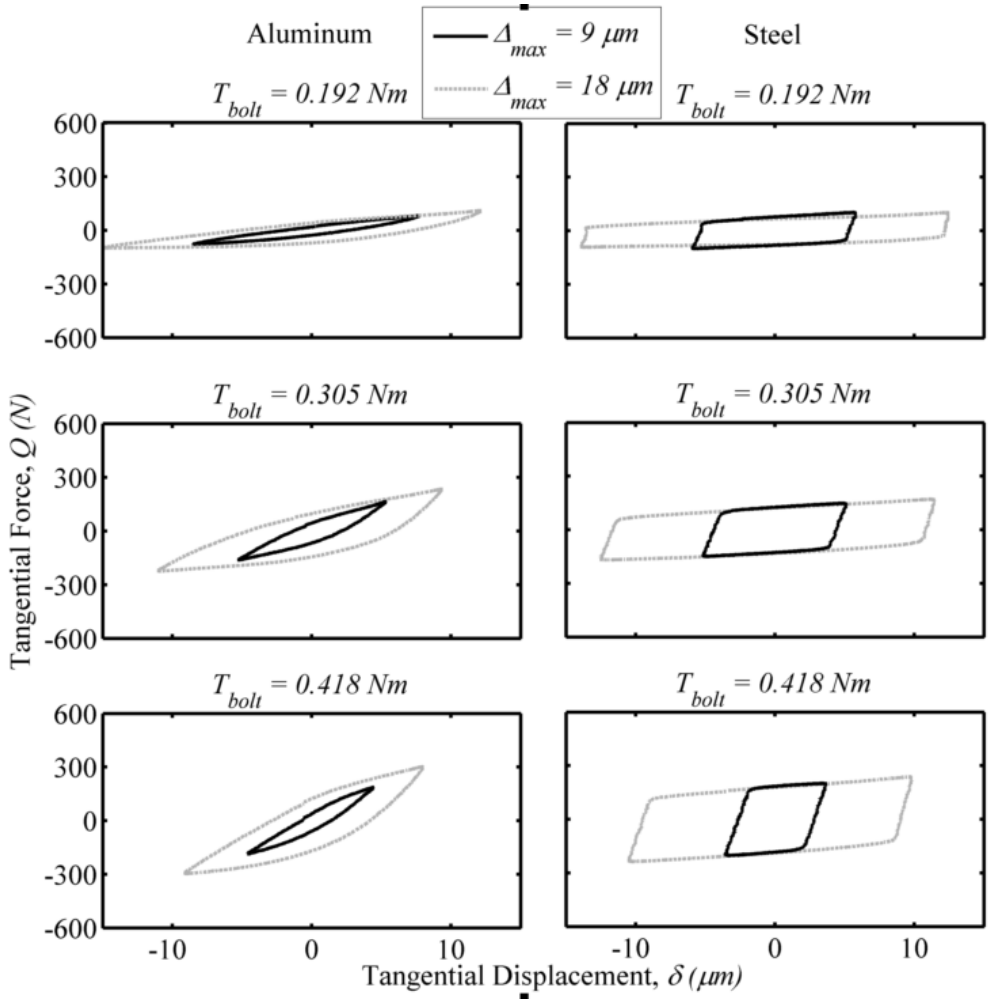

Fig. 6.10. Average fretting loops obtained from the rough aluminum and steel joint samples under various loading and boundary/mixed lubricated contact conditions.

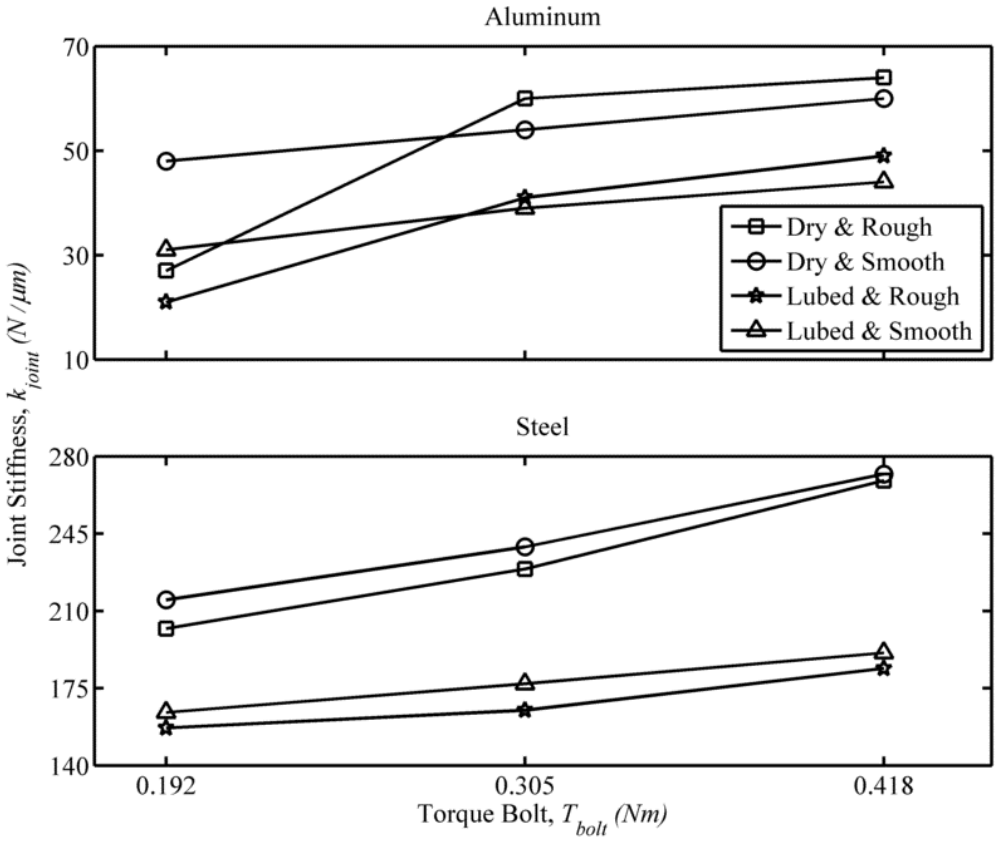

Fig. 6.11. Tangential joint stiffness values for aluminum and steel joints under various loading and contact conditions.

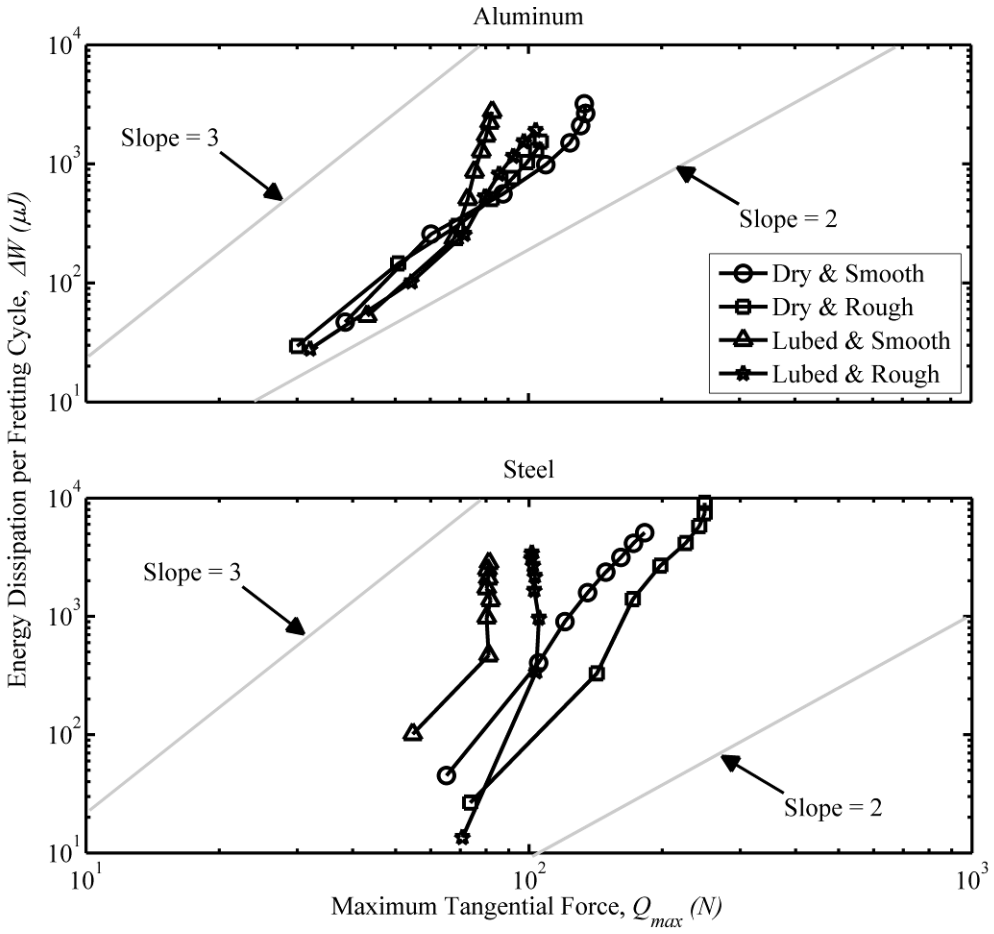

Fig. 6.12. Energy dissipation per fretting cycle versus maximum tangential force for aluminum and steel joint samples (0.192 Nm bolt torque).

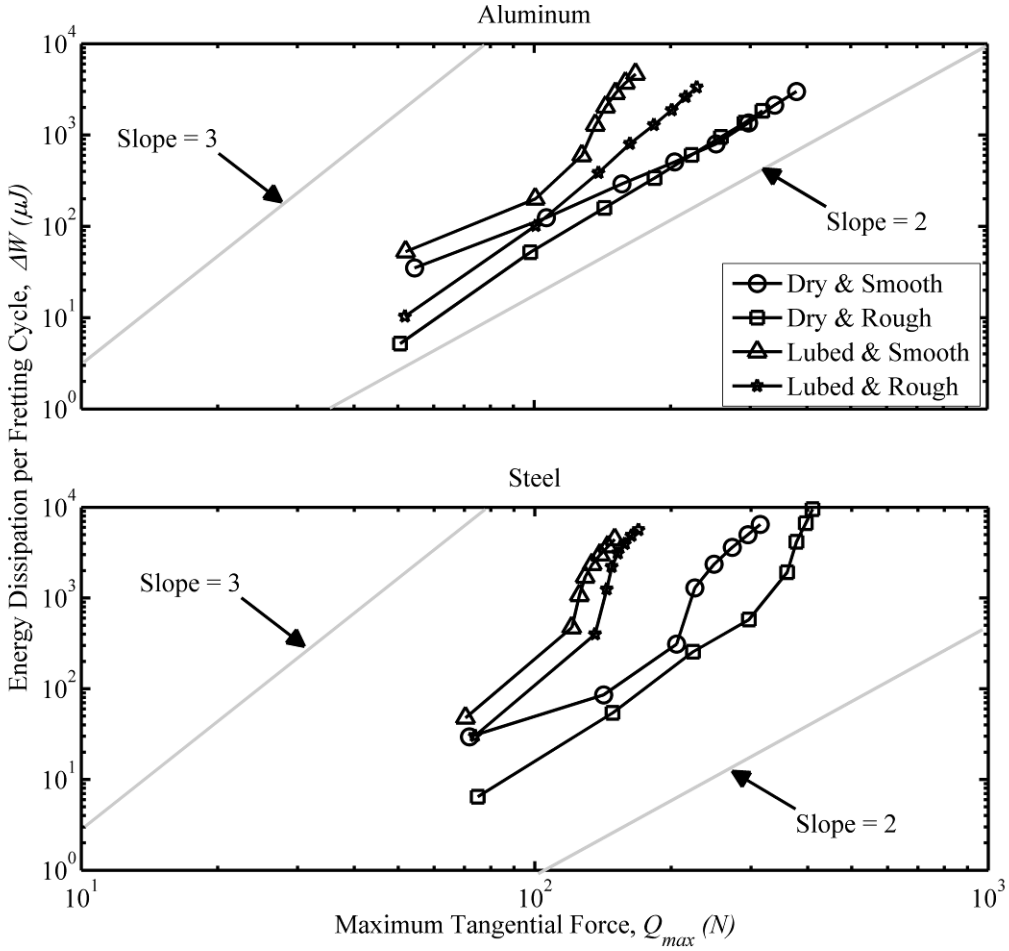

Fig. 6.13. Energy dissipation per fretting cycle versus maximum tangential force for aluminum and steel joint samples (0.305 Nm bolt torque).

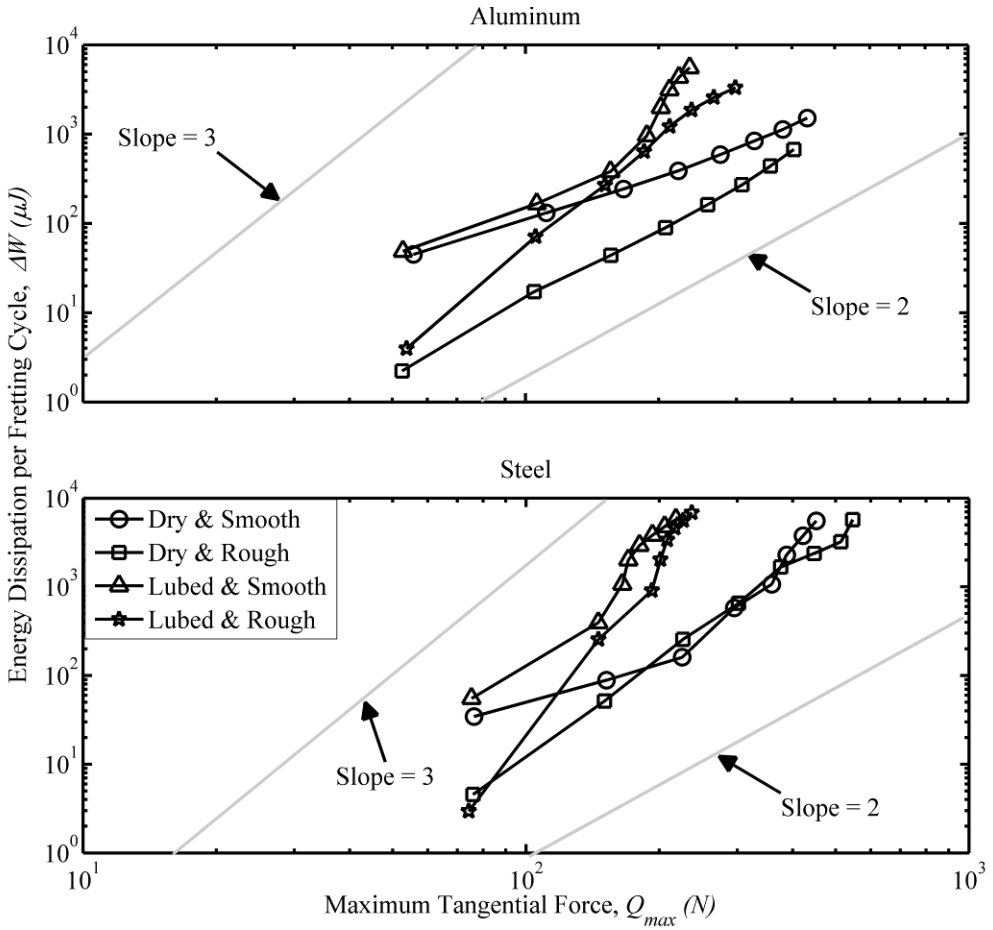

Fig. 6.14. Energy dissipation per fretting cycle versus maximum tangential force for aluminum and steel joint samples (0.418 Nm bolt torque).

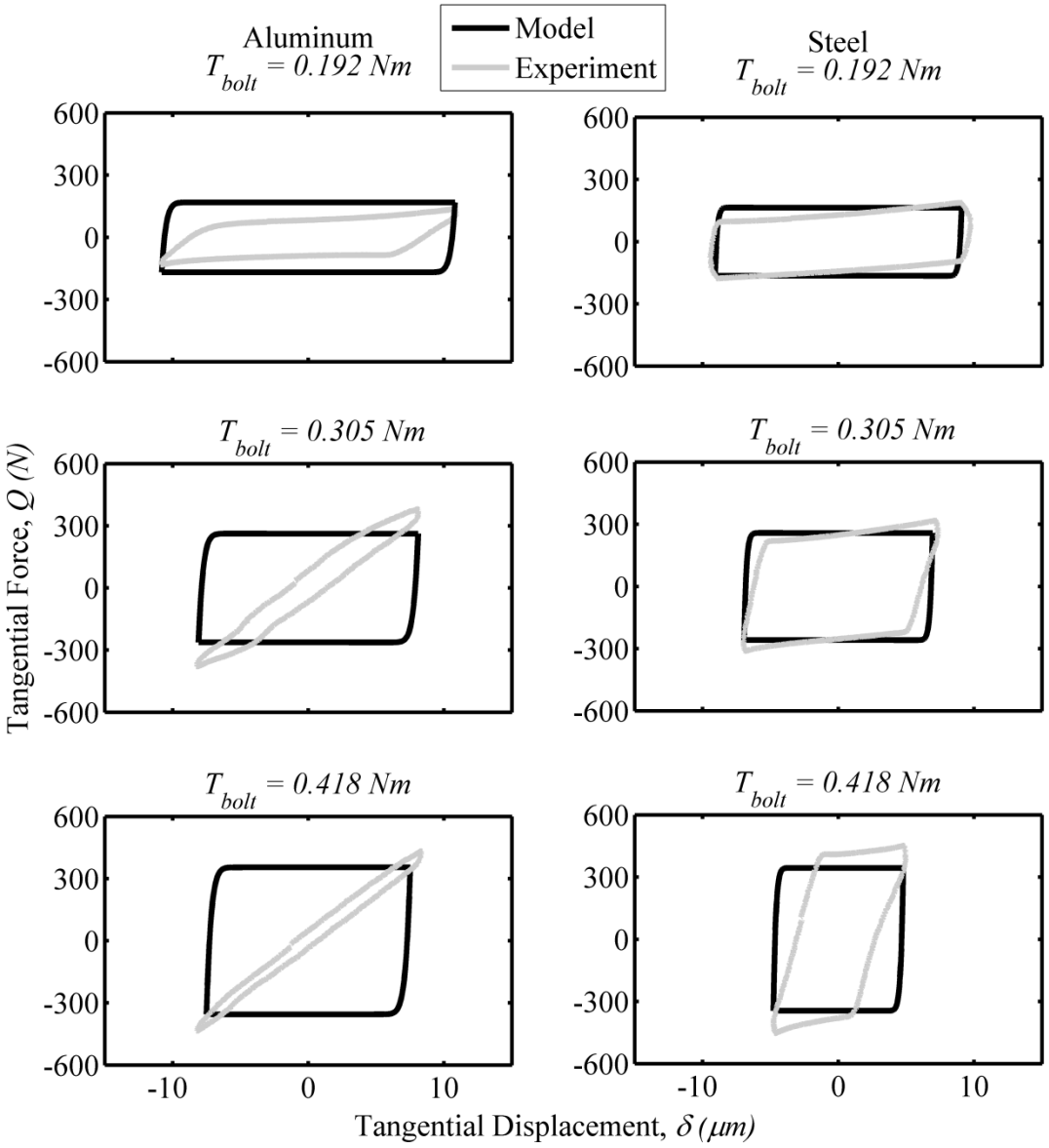

Fig. 6.15. Comparison between model predictions (Chapter 4) and experiments with the smooth joint samples under dry contact conditions.

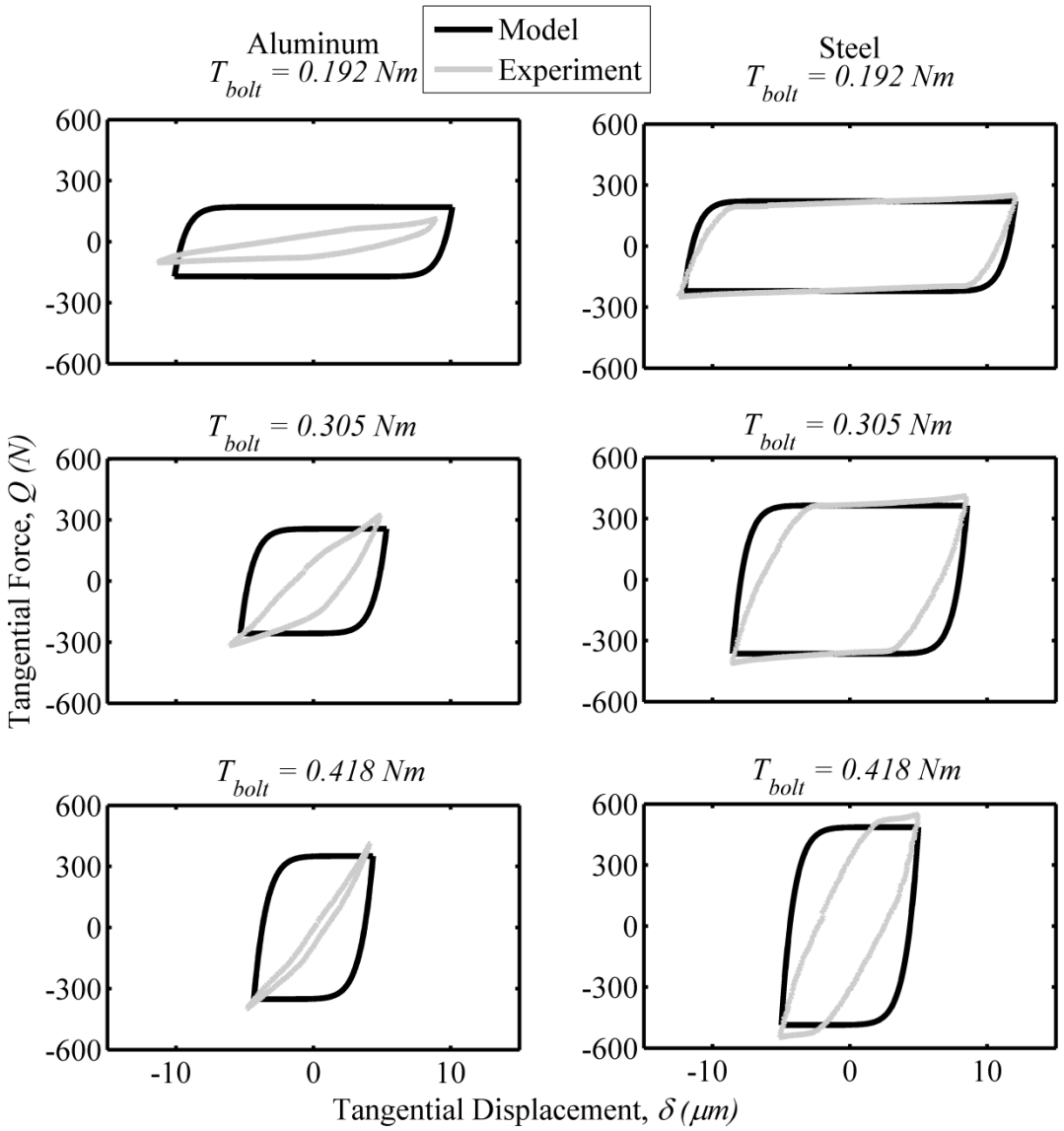

Fig. 6.16. Comparison between model predictions (Chapter 4) and experiments with the rough joint samples under dry contact conditions.

6.7. Tables

Table 6.1. Chemical composition and mechanical properties of the aluminum and steel alloys.

	Aluminum Alloy 6061-T6	**Grade 420 Stainless Steel**
% Chemical Composition	Si(0.6), Fe(0.35), Cu(0.28), Mn(0.15), Mg(0.08), Cr(0.19), Zn(0.13), Ti(0.08), Other(0.1), Al(98.04)	C(0.35), Ni(0.14), Cu(0.04), Mn(0.44), N(0.06), Cr(12.34), P(0.02), Mo(0.03), Other(0.06), Fe_3C(86.52)
Poisson's Ratio	0.33	0.24
Young'sMod. (GPa)	69	200
Shear Mod. (GPa)	26.2	80.7
Yield Str. (MPa)	280	1360
Ult. Ten. Str. (MPa)	310	2025
% Elongation	14.6	25

Table 6.2. Roughness parameters for each joint half (PZT and load cell (LC) halves) as well as for the equivalent surface (Comb.) before and after fretting experiments.

Smooth	**Joint Half (before experiments)**			**Joint Half (after experiments)**		
Aluminum	*PZT*	*LC*	*Comb.*	*PZT*	*LC*	*Comb.*
σ (μm)	0.507	0.655	0.828	0.506	0.537	0.738
η (μm^{-2})	3.87E-04	3.26E-04	3.59E-04	4.09E-04	3.58E-04	3.83E-04
R (μm)	129.451	152.867	98.788	130.186	138.147	94.745
Rough	**Joint Half (before experiments)**			**Joint Half (after experiments)**		
Aluminum	*PZT*	*LC*	*Comb.*	*PZT*	*LC*	*Comb.*
σ (μm)	2.243	1.791	2.870	1.903	1.812	2.628
η (μm^{-2})	3.00E-04	3.35E-04	3.16E-04	3.12E-04	3.28E-04	3.20E-04
R (μm)	39.119	40.071	27.992	41.142	43.410	29.862
Smooth	**Joint Half (before experiments)**			**Joint Half (after experiments)**		
Steel	*PZT*	*LC*	*Comb.*	*PZT*	*LC*	*Comb.*
σ (μm)	0.387	0.424	0.574	0.357	0.438	0.566
η (μm^{-2})	3.63E-04	3.56E-04	3.59E-04	3.68E-04	3.55E-04	3.60E-04
R (μm)	194.631	163.532	125.204	210.931	167.981	131.403
Rough	**Joint Half (before experiments)**			**Joint Half (after experiments)**		
Steel	*PZT*	*LC*	*Comb.*	*PZT*	*LC*	*Comb.*
σ (μm)	1.848	1.863	2.624	1.608	1.714	2.351
η (μm^{-2})	3.23E-04	3.05E-04	3.14E-04	3.55E-04	3.51E-04	3.53E-04
R (μm)	38.780	41.249	28.254	44.928	42.586	30.908

Table 6.3. Bolt torque values used in the experiments, and corresponding normal preloads and mean pressures.

T_{bolt} (Nm)	P_{flat} (N)	p_{mean} (MPa)
0.192	331	2
0.305	526	3.2
0.418	721	4.4

Table 6.4. Average friction coefficient values for dry and lubricated contact conditions.

	μ^{Dry}, μ^{Lubed}		
Joint Sample	T_{bolt} =0.192 Nm	T_{bolt} =0.305 Nm	T_{bolt} =0.418 Nm
Smooth Al	0.31, 0.18	0.61, 0.24	0.52, 0.26
Rough Al	0.32, 0.30	0.59, 0.43	0.54, 0.40
Smooth St	0.42, 0.18	0.47, 0.17	0.57, 0.20
Rough St	0.68, 0.18	0.72, 0.22	0.53, 0.24

CHAPTER 7: APPLICATION OF THE FRICTION MODEL TO A SIMPLE DYNAMICAL SYSTEM

7.1. Introduction

Friction complicates the dynamics of many engineering applications. To exemplify, dynamical models and simulations of assembled structures lack predictive capability mainly due to the complicated contact mechanics-related phenomena occurring at the joint interfaces. Uncertainty associated with joint friction behavior is one of the biggest challenges to predictive modeling alongside surface degradation, contamination and wear [142]. Thorough investigations of the dynamics of structures necessitate large-scale spatial and temporal modeling, which in turn, necessitate the use of reduced-order friction models. However, reduced-order modeling usually compromises either the physical or predictive basis of the overall dynamical model. For instance, Coulomb's law of friction accounts for gross sliding of two contacting bodies relative to each other and couples the friction force to the clamping force by a constant called friction coefficient. This model, however, does not account for the friction force and associated energy dissipation before gross sliding occurs [133].

A good reduced-order friction model should account for four vital components of the physical response before its reliable use in structural dynamics simulations: i) micro-displacements occurring before sliding; ii) variable tangential stiffness (softening spring behavior); iii) history-dependence of loading/unloading/reloading responses; and iv) hysteresis and frictional energy loss [143]. The importance of components ii) and iv) are apparent since joints can change the overall stiffness and damping of jointed structures drastically and, hence, influence the dynamical response. Components i) and iii) are necessary for continuity of physical variables, such as displacements and forces. Note that in the case of a non-smooth dynamical system these components might be compromised. Most friction models utilized by researchers in the dynamics and controls areas either neglect several of these critical components (regularization of the Coulomb model, e.g., [8]) or introduce non-physical auxiliary dynamics to make up for the missing components [5]. Phenomenological friction models, on the other

hand, require curve-fitting and tuning of parameters with prior friction experiments (eg. Iwan beam elements [9] in series, parallel or combined configurations [144]).

Models proposed in Refs. [78,145] and LuGre model [6] initiated physics-based approaches to the pre-sliding friction problem. These approaches mainly build up the models from micromechanics of asperity-scale contact. The limitation of these models, however, is either unrealistic contact definitions or asperity-scale Coulomb friction laws. Recently, Eriten et al. [36] (referred to as the EPB model in this chapter) proposed a friction model for flat-on-flat elastic-plastic contacts. In addition to reproducing the critical physics of the frictional contact, this model uses only material properties, surface roughness parameters and loading conditions. No prior friction experiments, curve-fit or look-up parameters are needed when applying this model. Its single disadvantage is that it involves integrals and numerous parameters in friction force evaluations; thus, the computational time increases. This problem, however, can be resolved by simple analytical expressions to approximate those integrals (see [79] for such an approximation).

In this chapter, the physics-based EPB friction model is used in a single degree-of-freedom dynamical system. A comparison with two different friction models (regularized Coulomb [143], and Dankowicz [7]) is also provided for three different base excitations: i) impulsive, ii) ramp and iii) harmonic displacement.

7.2. Dynamical System

A single degree-of-freedom mass-spring-damper system is employed to model the tangential response *x(t)* of a jointed interface in the subjected to a displacement *y(t)* at its base.

With respect to a stationary reference plane, the equation of motion can be written as

$$m\ddot{x} + c\dot{x} + kx = ky + c\dot{y} - f_s \tag{7.1}$$

where f_s is the friction force between the mass and the plane. In fully-lubricated contact case, the friction force can be assumed negligible and, thus, the equation of motion simplifies to a second order linear ordinary differential equation (ODE).

Three types of base excitation are used in this work: i) impulsive, ii) ramp, and iii) harmonic displacement. Impulse response is studied to identify the direct influence of frictional contact on modal frequency and damping. To illustrate whether stick-slip oscillations can be reproduced by the chosen friction model, the ramp model is utilized. Harmonic base excitation is employed to study the response during sustained vibrations. Table 7.1 summarizes the non-dimensional governing equations of motion given in Eq. (7.1) for each of the base excitations with the non-dimensional variables defined as $u(t) = x(t)/A$, $\tau = \sqrt{\frac{k}{m}}\,t$, $\tilde{f} = \sqrt{\frac{m}{k}}\,f$ and $F_s = \frac{f_s}{kA}$, and, $u' = \frac{du}{d\tau}$, $u'' = \frac{d^2u}{d\tau^2}$ and $\varepsilon = \frac{c}{\sqrt{mk}}$ is the normalized damping parameter (note that for a structural beam element under uniaxial vibrations $\varepsilon << 1$).

7.3. Friction Models

In this chapter, three different friction models are used in the dynamical simulations. Regularized Coulomb and Dankowicz models are provided for comparison with the EPB model.

Regularized Coulomb Model. Regularized Coulomb friction models are commonly used in dynamic simulations to introduce energy dissipation. Regularization increases numerical stability of these simulations. The following smooth regularization will be used in this work (see [143] for details) for comparison with the EPB model; i.e.,

$$f_s\left(\dot{x}\right) = F_{\max}\tanh\left(k_{\tan}\dot{x}\right) \tag{7.2}$$

where F_{max} is the maximum friction force during gross sliding of the interface and k_{tan} is the slope of the friction force curve at zero velocity (determines how fast the maximum friction force is attained). The non-dimensional friction force is given by

$$F_s\left(\dot{u}\right) = \tilde{F}_{\max} \tanh\left(\tilde{k}_{\tan}\dot{u}\right) \tag{7.3}$$

where $\tilde{F}_{\max} = \frac{F_{\max}}{kA}$ and $\tilde{k}_{\tan} = k_{\tan}A\sqrt{\frac{k}{m}}$. As mentioned above, despite its practicality, this model cannot capture two of the essential constituents of pre-sliding friction dynamics: micro-displacements and variable tangential stiffness (softening spring) response. Furthermore, the parameters needed (k_{tan} and F_{max}) are determined by curve-fitting data from friction experiments for a particular contact configuration, which in turn alleviates the practical use and predictive capability of the model.

Dankowicz Model. A more rigorous and physics-based model is proposed by Dankowicz [7]. Unlike the Coulomb model, this model is able to account for micro-displacements and varying tangential stiffness before gross sliding through an auxiliary internal variable z. The dynamics of this variable is coupled to the global displacements by

$$\dot{z} = \dot{x}\left(1 - \frac{z}{\delta}\operatorname{sgn}\left(\dot{x}\right)\right) \tag{7.4}$$

The ratio of this internal variable to the maximum possible pre-sliding micro-displacement δ scales the friction force; i.e.,

$$f_s\left(z\right) = F_{\max}\frac{z}{\delta} \tag{7.5}$$

In non-dimensional form, these equations become

$$\dot{\zeta} = \dot{u}\left(1 - \frac{\zeta}{\tilde{\delta}}\operatorname{sgn}\left(\dot{u}\right)\right) \tag{7.6}$$

$$F_s\left(\zeta\right) = \tilde{F}_{\max}\frac{\zeta}{\tilde{\delta}} \tag{7.7}$$

One inherent issue with this model is the physical meaning of the auxiliary internal variable. Furthermore, the model parameters need to be evaluated by either friction experiments or by other physics-based pre-sliding friction models. Dankowicz [7] employs the latter method (uses Bjorklund model [78]) to estimate the parameters, and assumes linear spring behavior for asperities both in normal and tangential contact. The stiffness of asperities in normal and tangential directions is assumed to be comparable; i.e., $k_{\perp} \approx k_{||}$. However, asperity-scale contact involves nonlinear elasto-plastic deformations with considerably diverse normal and tangential stiffnesses [80,146]. The EPB model is built on a more rigorous and physics-based micromechanics foundation compared to the Dankowicz model.

Eriten-Polycarpou-Bergman (EPB) Model. The EPB model is based on the same modeling approach as Bjorklund's [78] model: a multiscale micromechanics-based friction model for flat contacts. This bottom-up modeling approach first solves the single asperity contact problem (Hertzian contact, [46]) and utilizes statistical summation to obtain the flat contact friction force (Greenwood and Williamson's approach [29], see Fig. 7.2).

In this model, the friction force for flat contact is given as

$$Q\left(\frac{u}{\tilde{\sigma}}, \frac{u_{\max}}{\tilde{\sigma}}; \lambda\right) = \eta A_0 \int_d^{\infty} Q_{asp}\left(z, \frac{u}{\tilde{\sigma}}, \frac{u_{\max}}{\tilde{\sigma}}; \lambda\right) \phi(z) dz \tag{7.8}$$

where $\tilde{\sigma}$ is the root-mean-square roughness normalized to the magnitude of the harmonic oscillations, A; η is areal density of asperities; A_0 is the nominal contact area; $\phi(z)$ is the probability density function of asperity heights z, and λ is the parameter vector (see Nomenclature for descriptions)

$$\lambda = \{G^*, E^*, H, \sigma_{rms}, R, \eta, P, d\} \tag{7.9}$$

History dependence of the pre-sliding friction is also implemented in this model by changing the direction of displacements and force when velocity changes sign; i.e.,

$$F_s\left(\frac{u}{\tilde{\sigma}},\dot{u},\frac{u_{\max}}{\tilde{\sigma}};\lambda\right)=\begin{cases} Q\left(\frac{u}{\tilde{\sigma}},\frac{u_{\max}}{\tilde{\sigma}};\lambda\right) & \dot{u}<0 \\ -Q\left(-\frac{u}{\tilde{\sigma}},\frac{u_{\max}}{\tilde{\sigma}};\lambda\right) & \dot{u}>0 \end{cases} \tag{7.10}$$

In this formulation, the maximum tangential displacement $u_{\max}$ is reset to the displacement value when the velocity changes sign. Bjorklund [78] assumes elastic contact conditions and uses a physics-based formulation and parameter set except for friction coefficient. However, asperities deform both elastically and plastically irrespective of how light or heavy the loading is, and the local Coulomb friction law is shown to neglect the critical interface physics [147,148].

Eriten et al. [36] employs Bjorklund's modeling approach with two major improvements as far as physical basis: i) removal of friction coefficient from the asperity-scale formulation, and ii) introduction of elastic-plastic deformation formulation. The first of these improvements is achieved by associating sliding inception with plastic flow. The latter improvement is achieved by utilization of Finite Element Analysis (FEA)-based elastic-plastic response of asperities (see [33] for details). Depending on contact conditions (lubricated, partial-slip or high-adhesion), the asperity-scale micromechanical response varies considerably. The EPB model is a general modeling approach which ensures accommodation of any specific asperity-scale response. Three different asperity-scale formulations are presented earlier by Eriten et al. [36] and the Brizmer et al. [88] formulation is used in dynamical simulations presented in the current work. This friction model is validated by friction experiments at asperity-scale [33] and by fretting of centimeter-scale lap joints at nominally flat contact-scale [36]. In addition, this model has been used to study the effects of surface roughness on energy dissipation characteristics of flat contact [149]. This friction model is easy to integrate into finite element models and dynamics simulations. This chapter illustrates an example of the latter.

The EPB model requires material properties, surface roughness parameters and loading conditions, but no curve-fit constants or look-up parameters. The material properties can be obtained either by

uniaxial tension/compression experiments or can be directly obtained from the suppliers. Surface roughness parameters can be extracted from surface profile measurements, and loading conditions are the state variables of the dynamical system. Therefore, no friction experiments are needed before implementation of the EPB model, i.e., the EPB is a physics-based predictive model (see the Appendix B for details).

7.4. Results

The simulation results presented in this section are generated by solving the non-dimensional equations shown in Table 7.1 using MATLAB's built-in numerical solver, **"ode23"** with absolute and relative tolerances of 1e-7 and 1e-6, respectively.

Simulation Parameters. In selecting the simulation parameters, a linear structural component experiencing frictional contact at one end is reproduced. A specific example can be a slender hardened-steel beam joined to a rigid surface by a large clamping force while a distant base excitation is applied to the beam at one end and the response of the jointed interface and friction behavior is studied at the other end (see Fig. 7.1 for details). There are two sets of roughness parameters; one for a rough and one for a smooth interface. Rough contact parameters are representative of standard surface machining products whereas smooth surface parameters are obtained by fine surface finishing techniques. The EPB friction model uses the rough contact parameters unless mentioned otherwise. Table 7.2 lists the simulation parameters used.

Note that the parameters $\tilde{k}_{\tan}, \tilde{F}_{\max}, \tilde{\delta}$ are needed for the requlatized Coulomb and Dankowicz models.

Impulse Response. Impulse response of the mass-spring-damper system is obtained as the solution of the corresponding equation listed in Table 7.1 with impulse duration of 0.1 non-dimensional time; i.e., $\omega = 10\pi$, which corresponds to less than 2% of the free vibration period of the mass (free vibration frequency = $1/2\pi$). The frictional contact is expected to cause increase in stiffness and damping when

compared to free vibrations under frictionless contact. The influence of friction can readily be studied by the power spectrum of the single-degree-of-freedom system response. In practice, this procedure is conducted by modal analysis using frequency response functions. The power spectra of the non-dimensional position of the mass with Coulomb and Dankowicz friction models are presented in Fig. 7.3. The power spectrum for the frictionless case is also given for comparison. Note that the frictionless case has the modal frequency at the non-dimensional frequency of $1/2\pi$. The model with the Coulomb friction shows immediate increase in damping, yet no change in modal frequency. This is due to the incapability of this model to capture micro-displacements and, thus, no additional stiffness is introduced by the contact. Although the model cannot account for micro-displacements, it accounts for viscous damping thanks to sign changes of velocity. The response with the Dankowicz friction model, in contrast, exhibits the expected rise in damping and modal frequency. Structural stiffness in combination with the contact stiffness controls the modal frequency, and the area inside the friction loop for each vibration cycle controls the modal damping. The modal frequency with the Dankowicz friction model increases up to 1.9 in contrast to $1/2\pi$ of the frictionless and Coulomb friction cases. The modal damping is obtained as 0.098 and 0.081 for the Coulomb and Dankowicz friction cases, respectively. Considering that the structural damping ratio is taken as 0.016 ($\zeta = \varepsilon/2$; for ε, see Table 7.2), the increase in modal damping is significant with both friction models.

Fig. 7.4 shows the power spectra of the EPB model with rough and smooth contact parameters. The EPB model clearly accounts for the expected increase in modal frequency and damping when compared to the frictionless case. Modal frequencies increase up to 2.3 and 3.6 for rough and smooth contacts, respectively. Besides, the modal damping increases to 0.076 for the rough case and 0.07 for the smooth case. Stoimenov et al. [150] studied the effect of roughness on the vibration mode of two steel plates in contact, and concluded that smooth contact is always stiffer. Similar observations on bolted lap joints were made by Sandia National Laboratories were smooth lap joints were found to dissipate more energy than their rough equivalents [95]. The physical basis of these experimental observations is the fact that

smoother surfaces result in larger real contact area than the rougher surfaces. Larger real contact area results in higher friction, stronger contact and more energy loss. Therefore, both the modal stiffness and damping increase when the contact is smoother. The EPB model can simulate these observations because of the multiscale modeling approach it uses. Expressing the macroscale contact force as a summation of contact forces that asperities carry automatically couples the surface roughness with the micromechanics and, thus, the overall dynamics of the structure experiencing friction. With the Coulomb and Dankowicz models, these physical observations cannot be simulated unless roughness-dependent re-evaluation of each model parameter is conducted by specific sets of additional experiments. Note that the EPB model necessitates surface roughness measurements a priori, but no other testing is needed provided that mechanical properties of the material (Young's modulus, Poisson's ratio, and yield strength/ hardness) are known.

Ramp Response. Next, we study the ramp response using the corresponding equation given in Table 7.1. The purpose of the ramp response is to check whether the friction model we propose is capable of simulating stick-slip behavior. For sustained stick-slip oscillations, reverse loading (unloading) of the mass needs to be investigated [151]. However, we also expect to see the transition from stick to slip by unidirectional ramp loading. The velocity of the base is set to unity; i.e., $\alpha = 1$, and the position of the mass is traced until the mass starts following the base motion.

Fig. 7.5 shows the ramp responses of the mass with the Coulomb, Dankowicz and EPB friction models. The EPB model is generated using the rough contact parameters. The EPB model with smooth contact parameters yields much stiffer contact than the Coulomb and Dankowicz models, and the stick period increases to the extent that comparison among the models becomes difficult. In addition to using different friction models, the structural stiffness value, k, is decreased to 10^4 from its default value of 10^5 N/m listed in Table 7.2. The purpose of this modification is to make the stick region more apparent. As one can clearly see, for softer structural stiffness values, both Dankowicz and EPB models exhibit stick behavior for more than 15 non-dimensional time units, whereas the Coulomb friction model show slips

even at the initial stages of loading. For harder structural stiffness, the duration of stick decreases to about 3 as expected, and after the stick period, the mass tracks the base motion; i.e., the response becomes parallel to the unit ramp curve. The post-stick period is referred to as the slip region. The oscillations while slipping are due to the overshoot resulting from the initial transition from the stick period, and they decay in time with the frictional and structural damping modeled in the mass-spring-damper system.

The Coulomb friction can in fact simulate stick-slip behavior only if the friction coefficient or the maximum friction force depends on the relative velocity of the contact [151]. The Dankowicz and EPB models, on the other hand, do not require any velocity dependence to simulate stick-slip. However, velocity-dependence of the parameters used by those models should also be investigated for a thorough modeling of friction.

Harmonic (Fretting) Response. The last loading case we study is harmonic loading, where the base is excited by a sinusoidal displacement input. The distant harmonic loading on a frictional contact results in cyclic loading and unloading. Due to irreversible micro-displacements occurring at each step, the friction force exhibits hysteretic behavior. This type of response is also called fretting response in the literature [36]. The fretting response of the mass is a periodic orbit at steady-state, and we study the steady-state portion only. Fig. 7.6 shows the phase-portraits of the steady-state response of the mass with the Coulomb (a) and Dankowicz (b) friction models as well as the corresponding friction forces as a function of position in Fig. 7.6.c and d, respectively. Note that the position values oscillate with magnitudes less than 2% of the magnitude of base excitations. These subtle oscillations are a trademark of fretting response in the dynamics of assembled structures such as gas turbines, lap joints, and riveted aircraft structures. The friction forces exhibit very different nature with respect to position. The Coulomb friction exhibits a viscous damping property with no clear micro-displacements before sliding, whereas the Dankowicz model clearly shows micro-displacements, varying tangential stiffness, and transition from loading to unloading. Both models exhibit hysteresis loops, the area of which is directly associated with the energy loss and, thus, friction damping.

Fig. 7.7 shows the equivalent of Fig. 7.6 for the EPB model with smooth and rough contact conditions. Smooth contact shows very limited range of motion when compared to the rough contact. This result is in line with the previous observations asserting that the smooth contact possesses larger real area of contact and, hence, friction is more pronounced. More friction means stiffer and more constrained contact and less micro-displacement. The friction loops validate this statement more clearly, especially since the average slope of the friction loop can be regarded as the strength of the contact interface. The areas inside these loops correspond to the energy loss per fretting cycle, and can be correlated to the damping ratio. The friction loop for the smooth contact parameters has a smaller area than that for rougher contact, which suggests that in a displacement controlled fretting experiment rougher contacts should possess higher damping ratios. However, force or energy controlled experiments and simulations such as the one given in the impulse response section suggest that smooth contact dissipates more energy. In other words, if one can match the maximum amplitude of the cyclic displacement for the smooth and rough contact cases; i.e., the phase portraits of both cases should look very similar, the smooth contact dissipates slightly more energy and introduces higher damping. This observation is in line with the experimental evidence in the literature [95,38].

Similar studies can be conducted with the EPB friction model to investigate the effects of different materials and contact and loading conditions on structural dynamics. For instance, polymers, aluminum and steel structures would have quite different damping, stiffness, Young's moduli, and hardness even if their surface roughnesses match. This variation in material properties influences the dynamic response, which can be studied by the EPB model. Experimental validation of the dynamical responses is currently being performed by the authors.

A last note on the EPB model requires mentioning the contact conditions. The simulations presented in this work use a highly-adhesive contact at asperity-scale (Brizmer et al. asperity-scale model, [88]). Should contacts with low adhesion and high slippage be modeled, different asperity-scale models such as

Kogut and Etsion [15] should be used. Nevertheless, the EPB modeling approach seems to be a powerful candidate in structural dynamics simulations involving friction.

7.5. Comparison

Table 7.3 gives a summary of the comparison among the friction models. As mentioned before, the regularized Coulomb friction model is the simplest and most efficient method to account for frictional contacts in large-scale structural dynamic simulations. However, it cannot account for the influence of friction on modal frequency and damping, and micro-displacements before gross sliding. Also, its parameters do not enable further investigation of the effects of loading conditions, material and roughness parameters.

The Dankowicz model, in contrast, is more advanced and capable in many of those crucial criteria listed in Table 7.3 except for the parameters used and the non-physical auxiliary state variable used in its formulation. Accounting for all the crucial physics and retaining a sufficient amount of parameters to enable the study of loading, material and roughness effects, the EPB model is a strong candidate for a reduced-order friction model in structural dynamics simulations.

7.6. Conclusion

In this chapter, a physics-based friction model (the EPB model) is presented and compared to two friction models from the literature in a simple dynamical system framework. Three types of loading cases were studied to demonstrate that the EPB model accounts for all the critical physics including the influence on modal frequencies and damping, the pre-sliding friction behavior, as well as stick-slip oscillations. In addition, the EPB model utilizes physical parameters (material properties, surface roughness parameters, loading conditions) without any curve-fit or look-up parameters. That, in turn, gives this model its predictive capability and facilitates dynamical studies of jointed structures with different materials, surface roughness and contact conditions.

7.7. Figures

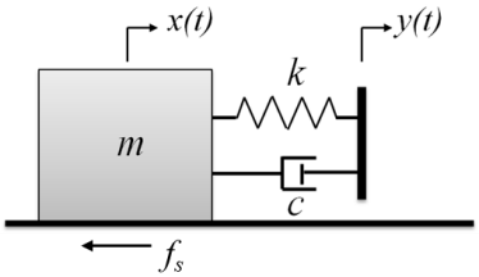

Fig. 7.1. Single degree-of-freedom dynamical system with friction

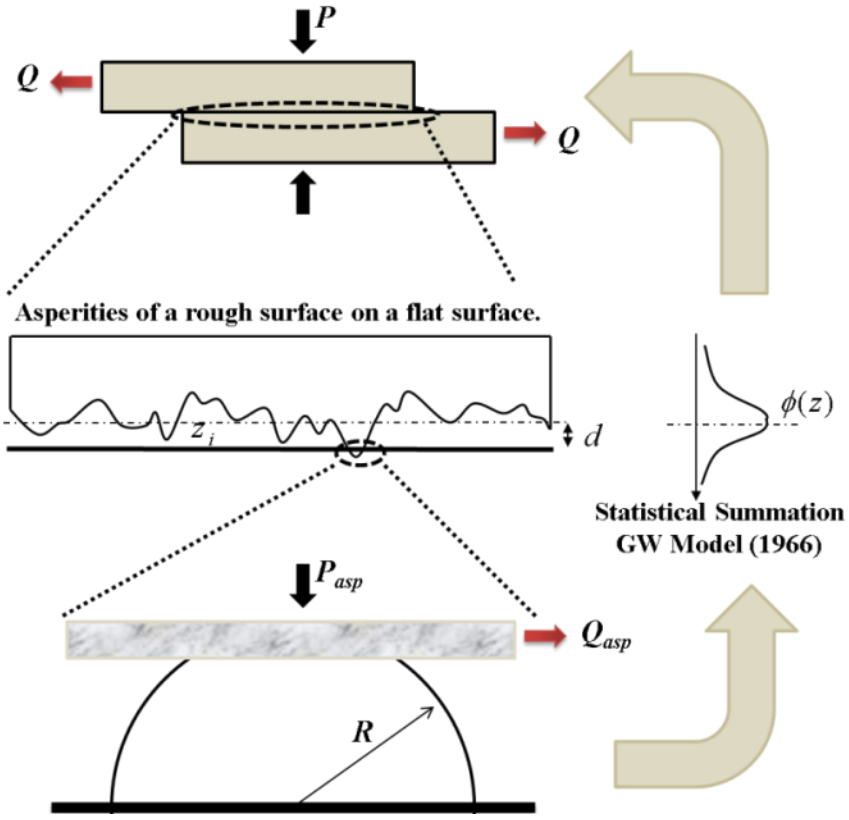

Fig. 7.2. Multiscale modeling approach proposed by Bjorklund [78]

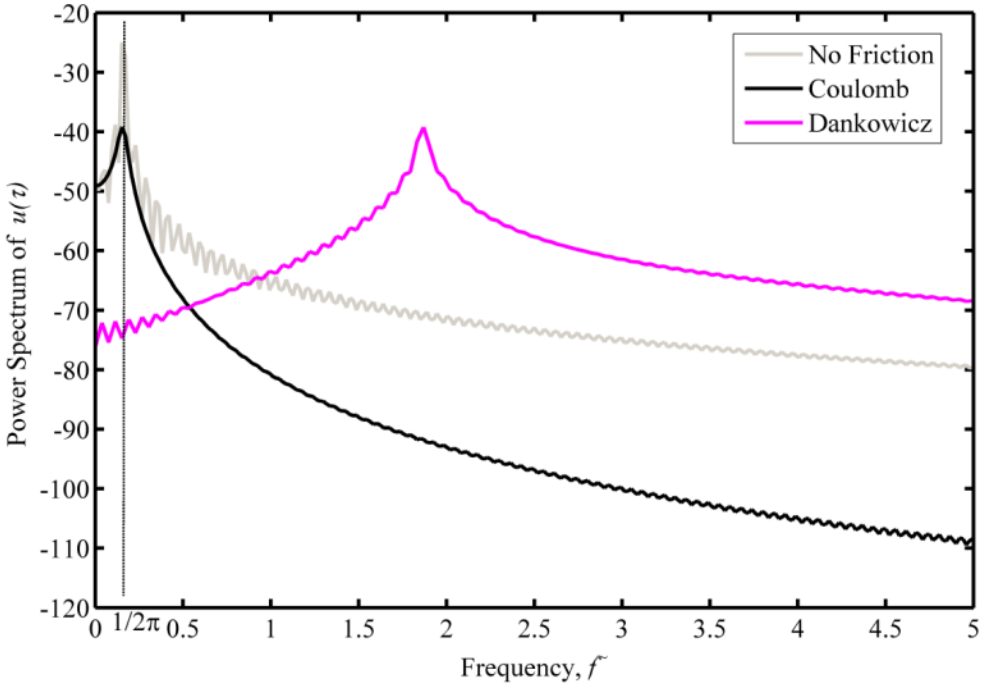

Fig. 7.3. Power spectra of the impulse response of the mass with Coulomb and Dankowicz friction models (no friction case is given for reference)

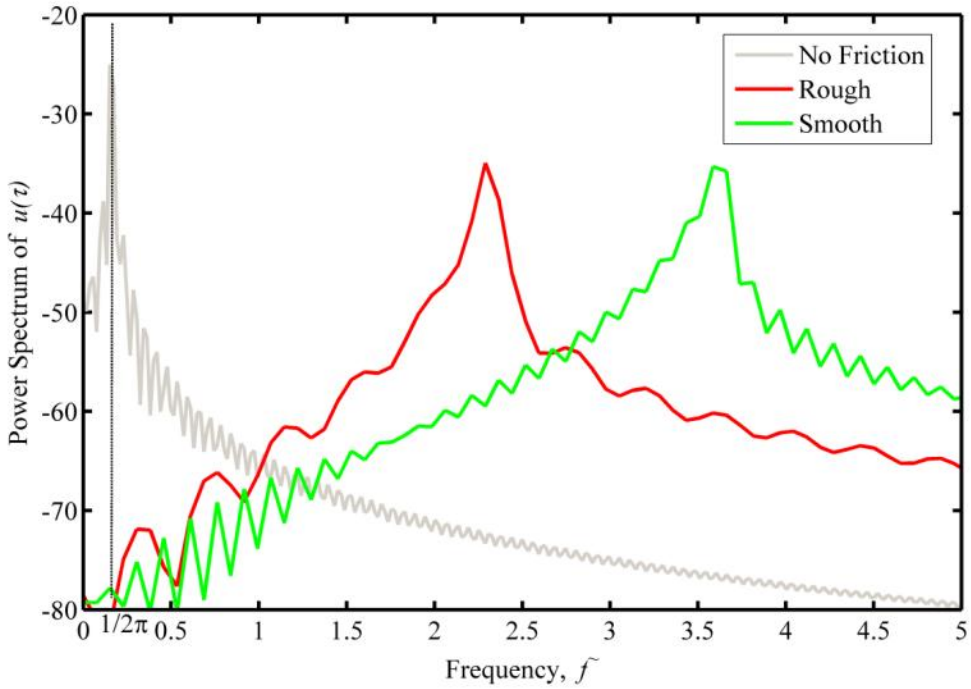

Fig. 7.4. Power spectra of the impulse response of the mass with EPB friction applied to rough and smooth surfaces (no friction case is given for reference)

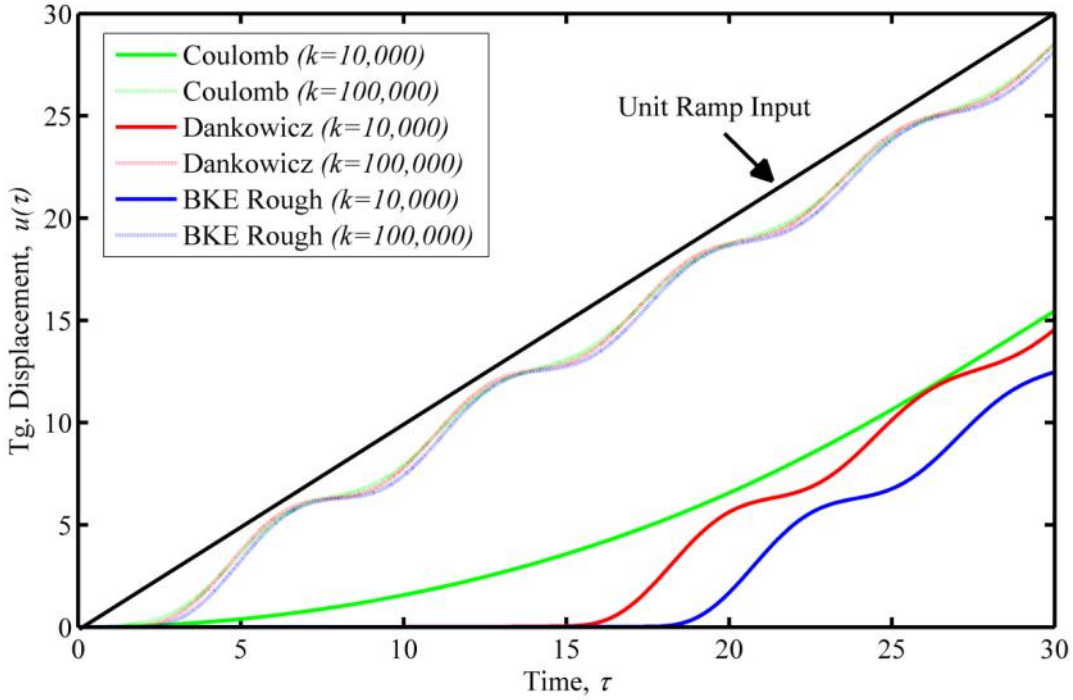

Fig. 7.5. Ramp response of the mass-spring-damper system with different friction models, and soft and hard structural stiffness

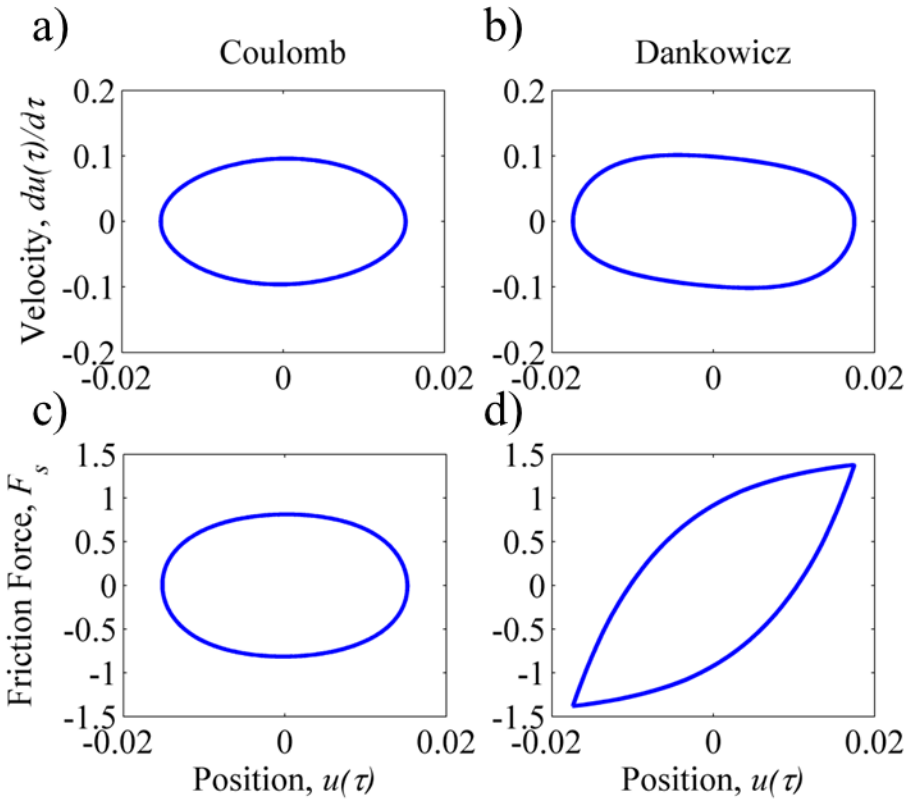

Fig. 7.6. Phase-portraits of the steady-state harmonic response of the mass with the Coulomb (a) and Dankowicz (b) friction models, and the corresponding friction forces as a function of position, c) and d), respectively.

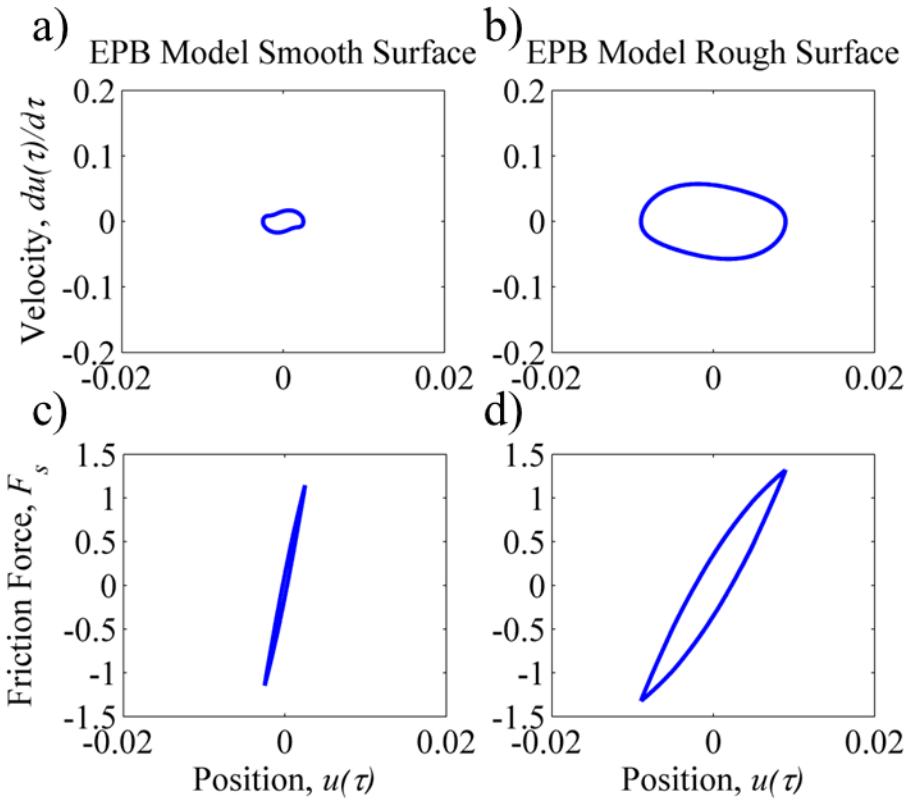

Fig. 7.7. Phase-portraits of the steady-state harmonic response of the mass with the EPB friction model using smooth (a) and rough (b) contact parameters, and the corresponding friction forces as a function of position, c) and d), respectively.

7.8. Tables

Table 7.1. Base excitation and corresponding equation of motion in non-dimensional form

Input	y(t)	EOM
Impulse	$y(t) = A\left[H(t) - H\left(t - \frac{\pi}{\omega}\right)\right]\sin(\omega t)$	$u'' + \varepsilon u' + u = \left[H(\tau) - H\left(\tau - \frac{\pi}{\omega}\right)\right]\sin(\omega \tilde{f}\tau) + \left[H(\tau) - H\left(\tau - \frac{\pi}{\omega}\right)\right]\omega \tilde{f}\varepsilon\cos(\omega \tilde{f}\tau) - F_s$
Ramp	$y(t) = \beta\, t$	$u'' + \varepsilon u' + u = \alpha\tau - F_s$
Sine	$y(t) = A\sin(\omega t)$	$u'' + \varepsilon u' + u = \sin(2\pi \tilde{f}\tau) + 2\pi \tilde{f}\varepsilon\cos(2\pi \tilde{f}\tau) - F_s$

Table 7.2. Parameters used in simulations

Parameter	Value
ε	0.032
$\tilde{f}$	1
$\tilde{k}_{\tan}$	6.32
$\tilde{F}_{\max}$	1.5
$\tilde{\delta}$	0.011
$\tilde{P}$	5
k	100000 (except for parametric study)
A	1
v	0.3
(G, E*, H)*	(22.9e9, 106e9,5.8e9)
$(\sigma_{rms}, R, \eta)_{smooth}$	(0.85e-6, 24.8e-6, 1.5e9)
$(\sigma_{rms}, R, \eta)_{rough}$	(2.7e-6, 30.1e-6, 2.9e8)

Table 7.3. Comparison table for the friction models studied (*Only with velocity-dependent parameters)

Criteria	Reg. Coulomb	Dankowicz (1999)	EPB (2011)
Modal Freq. & Damping	X	√	√
Stick-slip Vibrations	√*	√	√
Hysteresis (Cyclic loading)	X	√	√
Loading/Material/ Roughness	X	X	√
Computational Efficiency	√	√	√
Parameters Needed	F_{max}	δ, F_{max}	$\beta(\eta, R, \sigma), \phi^*, G^*, E^*, \nu, H, A_0, \delta$

CHAPTER 8: CONCLUSIONS AND FUTURE WORK

Modeling frictional contacts is a challenging task due to the complicated physics spanning multiple spatial and temporal scales. Detailed numerical models require extensive computational power to capture essential physics associated with the frictional interfaces. Hence, rather simple Coulomb friction is still the most ubiquitous model in the modeling and simulation literature. As an alternative, a reduced-order friction model built-up from micromechanics of surfaces is proposed in this thesis. Continuum scale formulation of presliding friction behavior is combined with material-strength-based friction coefficients to develop a physics-based friction model at asperity scale. Then, statistical summation technique is utilized to build a multiscale framework. A novel joint fretting setup is designed for friction experiments in a practical setting. Both asperity and rough surface friction models show good agreement with experimental data. The influences of materials, surface roughness and contact contamination on the frictional behavior are also studied. Finally, the developed models are incorporated into a simple dynamical system to illustrate broader applicability.

The models proposed in this work account for loading-history dependence, partial slip, gross slip, nonlinear stiffness and energy dissipation characteristics of frictional contacts. In doing so, the models require no curve-fit or look-up parameters. Instead, the formulations are developed from continuum mechanics, and the required parameters can be determined from simple tension/compression and surface roughness tests. In this sense, the developed models are physics-based and predictive. The following parameters are used in friction force-deformation formulations:

- Surface roughness parameters (mean areal density, mean asperity radius, rms roughness)
- Loading conditions (normal preload, maximum tangential displacement/force)
- Material properties (hardness, Young’s modulus, shear modulus, Poisson’s ratio)

The friction models are applied to macroscale rough surfaces after a statistical summation procedure. This requires the statistical characterization of roughness and the asperity height distribution. Simple

roughness tests provide the required characterization. After this, numerical integration is needed to obtain the friction force-deformation responses for flat contacts. Since the frictional contact of individual asperities and the asperity height distributions are modeled after mathematically bounded expressions, the integrands are well-defined and bounded. Therefore, the friction force formulations possess numerical stability, and common numerical integration schemes are sufficient for evaluation. In case the measured roughness profiles exhibit simple asperity height distributions, the integrals can be simplified to closed-form analytical expressions. Then, the developed models become as efficient numerically as Coulomb friction and power-law friction models. The friction models in their simplest forms provide a powerful predictive tool to simulate the effects of friction in electrical, mechanical, industrial systems and structures.

The friction models developed in this work depend on the contact conditions, surface roughness and material properties. For instance, the developed models use a dry-contact formulation at asperity-scale, and the macroscale friction predictions are tested only for dry contacts. However, the multiscale modeling approach can be applied to model the effect of lubrication provided that asperity-scale contact accounts for it. Besides, frictional contacts of certain materials exhibit severe adhesion, cold welding and galling behavior as demonstrated experimentally in Chapter 6. If these behaviors are modeled at asperity scale, then the friction at rough contact scale can be obtained by the same procedure presented in this work. This flexibility is another significant advantage of the proposed modeling approach.

Before future directions, a few reservations regarding the applicability of the friction models presented in this thesis as constitutive equations should be cleared. Constitutive equations, unlike governing equations in a solid, are derived through curve-fitting of experimental observations. Therefore, by definition, the constitutive equations developed here cannot be physics-based at atomistic scale. Since our models utilize continuum-scale curve-fit properties such as Young's modulus, Poisson's ratio, yield strength of a piece of solid, our claim that these models are physics-based holds only at continuum-scale, where the material is statistically uniform. Besides, we need to apply the general requirements (laws of

thermodynamics and objectivity [152]) for constitutive equations to these friction models. Beginning with the laws of thermodynamics requiring that the work done by the frictional stress corresponding to a given strain should result in a recoverable internal energy and/or dissipation and when a cycle of loading/unloading is completed and strain and internal energy state identical to the initial stage is achieved, the total work done should be positive. As can be seen in numerous experimental friction loops presented in this thesis, the physics of the frictional contact dictates that the energy input to the contact interface deforms the material elasto-plastically and some portion of that energy is dissipated manifesting itself as increasing contact temperature. The energy dissipation at each cycle can be measured directly by the area inside the corresponding friction loop and this energy loss can be directly correlated with the temperature increase over the contact with slight loss to convectional heating. Due to these losses, the total work done on the contact interface is always positive when total strain and stress in the material return to its original state. The friction models we proposed reproduce this behavior in force-deformation domain, but can be extended to the stress-strain domain over a given frictional area, and thus, the above argument on the laws of thermodynamics would hold for the models. The objectivity or material frame indifference criterion necessitates a constitutive equation transform correctly under a change of basis and translation of origin for the coordinate system used. Note that the friction models built in this dissertation assumes Mindlin's model as a basis, and Mindlin's model assumes a sticking region surrounded by a frictional slip region. The sticking region assumes continuity of materials and hence, the regular constitutive equations for a solid piece would hold across the interface with no discontinuity, and the frame indifference is not a concern. For the frictional slip region, local Coulomb friction law is assumed to hold in the direction of loading. The friction over this region imposes shear tractions predominantly along the friction direction, so the material segment undergoing frictional slip can be shown to be under simple shear. Using the same constitutive equation as the bulk material, one can obtain the corresponding strains, and Mindlin's formulation essentially achieves this in a closed-form solution. Therefore, the slipping portion of the asperities already assumes objectivity in formulation. Noting that the statistical summation procedure does not influence individual asperity-scale contacts, the material frame

indifference criterion can be assumed to hold for the rough contact friction models too. A more direct proof of this could follow from application of rotational transformation of the initial basis and stresses and strains, and showing that the friction relations presented transform accordingly. This straight-forward exercise is left to the reader.

There are several immediate extensions of the work presented in this thesis. The asperity scale contact formulation holds for continuum scale, but not for characteristic lengths of less than a few microns. Extension of the modeling approach presented here to nanoscale contact problems is a priority for future work. Material microstructure, discrete dislocations, adhesion, atomic interactions and surface chemistry will become critical in determining material response at this scale. Nevertheless, the modeling approach demonstrated in this thesis will remain the same. Therefore, an expected deliverable from such a study is a friction model associating sliding inception with fundamental material properties at nanoscale. No curve-fitting or look-up parameters would be used. All parameters will be physics-based. The multiscale modeling component might differ from the approach used in this thesis due to the limited number of asperities at nanoscale contacts. Yet, the essence of the modeling technique will remain untouched. Another long-term impact of this research would be to assist in the design of surfaces and materials in order to reduce or increase friction. By developing microstructure-based friction models, beneficial and detrimental effects of friction can be optimized in design. An example would be to optimize the dislocation densities at asperity-scale so that the frictional losses are minimal but sealing or electrical conductivity of the contact is superior. Another example would be to use the nanoscale contact formulation to design new materials with special crystal or grain structures to reduce friction.

REFERENCES

[1] Mang T., Bobzin K., and Bartels T., 2011, Industrial Tribology: Tribosystems, Wear and Surface Engineering, Lubrication, Wiley-VCH.

[2] Bowden F. P., and Tabor D., 1982, Friction: an introduction to tribology, R.E. Krieger Pub. Co.

[3] Cattaneo C., 1938, "Sul contatto di due corpi elastici: Distribuzione locale degli sforzi," Rc Accad. Naz. Lincei, **27**, pp. 474-478.

[4] Mindlin R., 1949, "Compliance of Elastic Bodies in Contact," J. of Appl. Mech., **16**, p. 259.

[5] Dahl P. R., 1968, A Solid Friction Model.

[6] Canudas de Wit C., Olsson H., Astrom K. J., and Lischinsky P., 1995, "A new model for control of systems with friction," IEEE Transactions on Automatic Control, **40**(3), pp. 419-425.

[7] Dankowicz H., 1999, "On the Modeling of Dynamic Friction Phenomena," ZAMM - Journal of Applied Mathematics and Mechanics / Zeitschrift für Angewandte Mathematik und Mechanik, **79**(6), pp. 399-409.

[8] Quinn D. D., 2004, "A New Regularization of Coulomb Friction," J. Vib. Acoust., **126**(3), pp. 391-397.

[9] Iwan W. D., 1966, "A Distributed-Element Model for Hysteresis and Its Steady-State Dynamic Response," J. Appl. Mech., **33**(4), pp. 893-900.

[10] Valanis K. C., 1970, A Theory of Viscoplasticity without a Yield Surface. Part 1. General Theory.

[11] Etsion I., 2010, "Revisiting the Cattaneo--Mindlin Concept of Interfacial Slip in Tangentially Loaded Compliant Bodies," J. Tribol., **132**(2), pp. 020801-9.

[12] Chang W. R., Etsion I., and Bogy D. B., 1987, "An elastic-plastic model for the contact of rough surfaces.," TRANS. ASME J.TRIBOLOGY, **109**(2), pp. 257-263.

[13] Chang W. R., Etsion I., and Bogy D. B., 1988, "Static Friction Coefficient Model for Metallic Rough Surfaces," Journal of Tribology, **110**(1), pp. 57-63.

[14] Chang W. R., Etsion I., and Bogy D. B., 1988, "Adhesion Model for Metallic Rough Surfaces," Journal of Tribology, **110**(1), pp. 50-56.

[15] Kogut L., and Etsion I., 2003, "A Semi-Analytical Solution for the Sliding Inception of a Spherical Contact," Journal of Tribology, **125**, p. 499.

[16] Kogut L., and Etsion I., 2004, "A Static Friction Model for Elastic-Plastic Contacting Rough Surfaces," Journal of Tribology, **126**, p. 34.

[17] Brizmer V., Kligerman Y., and Etsion I., 2006, "The effect of contact conditions and material properties on the elasticity terminus of a spherical contact," International Journal of Solids and Structures, **43**(18-19), pp. 5736-5749.

[18] Cohen O., Kligerman Y., and Etsion I., 2008, "A model for contact and static friction of nominally flat rough surfaces under full stick contact condition," Journal of Tribology, **130**(3).

[19] Hirano M., and Shinjo K., 1990, "Atomistic locking and friction," Phys. Rev. B, **41**(17), p. 11837.

[20] Mosey N. J., and Müser M. H., "Atomistic Modeling of Friction," pp. 67-124.

[21] Hurtado J. A., and Kim K.-S., 1999, "Scale effects in friction of single-asperity contacts. I. from concurrent slip to single-dislocation-assisted slip," Proceedings of the Royal Society A: Mathematical, Physical and Engineering Sciences, **455**(1989), pp. 3363-3384.

[22] Hurtado J. A., and Kim K.-S., 1999, "Scale Effects in Friction of Single-Asperity Contacts. II. Multiple-Dislocation-Cooperated Slip," Proceedings: Mathematical, Physical and Engineering Sciences, **455**(1989), pp. 3385-3400.

[23] Bhushan B., and Nosonovsky M., 2003, "Scale effects in friction using strain gradient plasticity and dislocation-assisted sliding (microslip)," Acta Materialia, **51**(14), pp. 4331-4345.

[24] Kogut L., and Etsion I., 2002, "Elastic-Plastic Contact Analysis of a Sphere and a Rigid Flat," Journal of Applied Mechanics, **69**, p. 657.

[25] Brizmer V., Zait Y., Kligerman Y., and Etsion I., 2006, "The effect of contact conditions and material properties on elastic-plastic spherical contact," JOMMS, **1**(5), pp. 865-879.

[26] Odfalk M., and Vingsbo O., 1992, "An elastic-plastic model for fretting contact," Wear, **157**, pp. 435-444.
[27] Johnson K. L., 1987, Contact mechanics, Cambridge University Press.
[28] Hills D. A., Nowell D., and Sackfield A., 1993, Mechanics of elastic contacts, Butterworth-Heinemann.
[29] Greenwood J. A., and Williamson J. B. P., 1966, "Contact of Nominally Flat Surfaces," Proceedings of the Royal Society A: Mathematical, Physical and Engineering Sciences, **295**, pp. 300-319.
[30] Majumdar A., and Bhushan B., 1991, "Fractal Model of Elastic-Plastic Contact Between Rough Surfaces," J. Tribol., **113**(1), pp. 1-11.
[31] Dini D., and Hills D. A., 2009, "Frictional Energy Dissipation in a Rough Hertzian Contact," Journal of Tribology, **131**, p. 021401.
[32] Kikuchi N., and Oden J. T., 1988, Contact Problems in Elasticity: A Study of Variational Inequalities and Finite Element Methods, SIAM.
[33] Eriten M., Polycarpou A. A., and Bergman L. A., 2010, "Physics-based modeling for partial slip behavior of spherical contacts," International Journal of Solids and Structures, **47**(18-19), pp. 2554-2567.
[34] Vakis A. I., Eriten M., and Polycarpou A. A., 2010, "Modeling Bearing and Shear Forces in Molecularly Thin Lubricants," Tribology Letters, **41**, pp. 573-586.
[35] Eriten M., Petlicki D., Polycarpou A. A., and Bergman L. A., 2011, "Influence of Friction and Adhesion on the Onset of Plasticity during Normal Loading of Spherical Contacts," Mechanics of Materials, **(in press)**.
[36] Eriten M., Polycarpou A. A., and Bergman L. A., 2011, "Physics-based modeling for fretting behavior of nominally flat rough surfaces," International Journal of Solids and Structures, **48**(10), pp. 1436-1450.
[37] Eriten M., Polycarpou A. A., and Bergman L. A., 2011, "Development of a Lap Joint Fretting Apparatus," Experimental Mechanics, **51**, pp. 1405-1419.
[38] Eriten M., Polycarpou A. A., and Bergman L. A., 2011, "Effects of surface roughness and lubrication on the early stages of fretting of mechanical lap joints," Wear, **271**(11-12), pp. 2928-2939.
[39] Lee C.-H., Eriten M., and Polycarpou A. A., 2010, "Application of Elastic-Plastic Static Friction Models to Rough Surfaces With Asymmetric Asperity Distribution," J. Tribol., **132**(3), pp. 031602-11.
[40] Eriten M., Polycarpou A. A., and Bergman L. A., 2011, "Surface roughness effects on energy dissipation in fretting contact of nominally flat surfaces," Journal of Applied Mechanics, Transactions ASME, **78**(2).
[41] Chandrasekar S., Eriten M., and Polycarpou A. A., "An Improved Normal Contact Model Accounting for Asperity Interaction," Journal of Applied Mechanics, **(submitted)**.
[42] Eriten M., Polycarpou A. A., and Bergman L. A., 2011, "A Physics-based Friction Model and Integration to a Simple Dynamical System," ASME J. Vibration and Acoustics, **(in press)**.
[43] Truster T. J., Eriten M., Polycarpou A. A., Bergman L. A., and Masud A., 2011, "A New Computational Method for Mechanical Joints: Physics-Based Models and Variationally Consistent Embedding," International Journal of Solids and Structures, **(in press)**.
[44] Eriten M., Lee C.-H., and Polycarpou A. A., 2011, "Tangential Stiffness of Mechanical Joints: Direct Measurements versus Contact Resonance Method," Journal of Vibration and Acoustics, Transactions of the ASME, **(in press)**.
[45] Hills D. A., and Nowell D., 1994, Mechanics of fretting fatigue, Springer.
[46] Hertz H., 1882, "Ueber die Berührung fester elastischer Körper.," Journal für die reine und angewandte Mathematik (Crelles Journal), **1882**(92), pp. 156-171.
[47] Bowden F. P., and Tabor D., 1964, The friction and lubrication of solids, Clarendon Press.

[48] McFarlane J. S., and Tabor D., 1950, "Relation between Friction and Adhesion," Proceedings of the Royal Society of London. Series A. Mathematical and Physical Sciences, **202**(1069), pp. 244 - 253.
[49] Burwell J. T., and Rabinowicz E., 1953, "The Nature of the Coefficient of Friction," Journal of Applied Physics, **24**, p. 136.
[50] Brizmer V., Kligerman Y., and Etsion I., 2006, "Elastic–plastic spherical contact under combined normal and tangential loading in full stick," Tribology Letters, **25**, pp. 61-70.
[51] Hirth J. P., and Kubin L., 2009, Dislocations in Solids, Elsevier.
[52] Greenwood J. A., and Tripp J. H., 1967, "The elastic contact of rough spheres," J. of Appl. Mech., **89**, p. 153.
[53] Goodman L. E., 1962, "Contact Stress Analysis of Normally Loaded Rough Spheres," ASME J. Appl. Mech., **29**, pp. 515-522.
[54] Spence D. A., 1968, "Self Similar Solutions to Adhesive Contact Problems with Incremental Loading," Proceedings of the Royal Society of London. Series A. Mathematical and Physical Sciences, **305**(1480), pp. 55 -80.
[55] Kogut L., and Etsion I., 2002, "Elastic-plastic contact analysis of a sphere and a rigid flat," Journal of Applied Mechanics, Transactions ASME, **69**(5), pp. 657-662.
[56] Naboulsi S., 2003, "Limitations of the Coulomb friction assumption in fretting fatigue analysis," International Journal of Solids and Structures, **40**, pp. 6497-6512.
[57] Oden J., and Martins J., 1985, "Models and computational methods for dynamic friction phenomena☆," Computer Methods in Applied Mechanics and Engineering, **52**, pp. 527-634.
[58] Mindlin R. D., Mason W. P., Osmer T. F., and Deresiewicz H., 1952, "Effects of an oscillating tangential force on the contact surfaces of elastic spheres," Proceedings of the First US National Congress of Applied Mechanics, **1951**, pp. 203-208.
[59] Johnson K. L., 1955, "Surface Interaction between Elastically Loaded Bodies under Tangential Forces," Proceedings of the Royal Society A: Mathematical, Physical and Engineering Sciences, **230**, pp. 531-548.
[60] Halling J., 1975, Principles of tribology, Macmillan.
[61] Comninou M., 1983, "Frictional slip between a layer and a substrate due to a periodic tangential surface force," International Journal of Solids and Structures, **19**, pp. 533-539.
[62] Sackfield A., Mugadu A., and Hills D. A., 2002, "The influence of an edge radius on the local stress field at the edge of a complete fretting contact," International Journal of Solids and Structures, **39**(17), pp. 4407-4420.
[63] Sneddon I. N., 1965, "The relation between load and penetration in the axisymmetric boussinesq problem for a punch of arbitrary profile," International Journal of Engineering Science, **3**(1), pp. 47-57.
[64] Spence D. A., 1975, "The hertz contact problem with finite friction," Journal of Elasticity, **5**(3-4), pp. 297-319.
[65] Evseev D., Medvedev B., and Grigoriyan G., 1991, "Modification of the elastic-plastic model for the contact of rough surfaces," Wear, **150**, pp. 79-88.
[66] Zhao Y., Maietta D. M., and Chang L., 2000, "An Asperity Microcontact Model Incorporating the Transition From Elastic Deformation to Fully Plastic Flow," J. Tribol., **122**(1), pp. 86-93.
[67] Rabinowicz E., 1995, Friction and wear of materials, Wiley.
[68] Gieck K., and Gieck R., 1997, Engineering formulas, McGraw-Hill Professional.
[69] Davis J. R., 1997, Concise metals engineering data book, ASM International.
[70] Hamilton G. M., 1983, "Explicit equations for the stresses beneath a sliding spherical contact," ARCHIVE: Proceedings of the Institution of Mechanical Engineers, Part C: Mechanical Engineering Science 1983-1988 (vols 197-202), **197**(1983), pp. 53-59.
[71] Varenberg M., Etsion I., and Halperin G., 2004, "Slip index: A new unified approach to fretting," Tribology Letters, **17**(3), pp. 569-573.

[72] Kogut L., and Etsion I., 2003, "Adhesion in elastic–plastic spherical microcontact," Journal of Colloid and Interface Science, **261**, pp. 372-378.
[73] Hutson A., Lee H., and Mall S., 2006, "Effect of dissimilar metals on fretting fatigue behavior of Ti–6Al–4V," Tribology International, **39**, pp. 1187-1196.
[74] Nowell D., Hills D. A., and Sackfield A., 1988, "Contact of dissimilar elastic cylinders under normal and tangential loading," Journal of the Mechanics and Physics of Solids, **36**, pp. 59-75.
[75] Rajeev P. T., and Farris T. N., 2002, "Numerical analysis of fretting contacts of dissimilar isotropic and anisotropic materials," Journal of Strain Analysis for Engineering Design, **37**(6), pp. 503-517.
[76] Comninou M., 1976, "Stress singularity at a sharp edge in contact problems with friction," Zeitschrift für angewandte Mathematik und Physik ZAMP, **27**, pp. 493-499.
[77] Eid H., and Adams G. G., 2007, "An elastic–plastic finite element analysis of interacting asperities in contact with a rigid flat," Journal of Physics D: Applied Physics, **40**, pp. 7432-7439.
[78] Björklund S., 1997, "A random model for micro-slip between nominally flat surfaces," Journal of Tribology, **119**(4), pp. 726-732.
[79] Polycarpou A. A., and Etsion I., 1999, "Analytical Approximations in Modeling Contacting Rough Surfaces," J. Tribol., **121**(2), pp. 234-239.
[80] Shi X., and Polycarpou A. A., 2005, "Measurement and Modeling of Normal Contact Stiffness and Contact Damping at the Meso Scale," J. Vib. Acoust., **127**(1), pp. 52-60.
[81] Dowson D., 1989, Tribological design of machine elements, Elsevier.
[82] Stolarski T. A., 1999, Tribology in Machine Design, Butterworth-Heinemann.
[83] Yu N., and Polycarpou A. A., 2002, "Contact of rough surfaces with asymmetric distribution of asperity heights," Journal of Tribology, **124**(2), pp. 367-376.
[84] McCool J. I., 1986, "Comparison of models for the contact of rough surfaces," Wear, **107**(1), pp. 37-60.
[85] Eriten M., Polycarpou A. A., and Bergman L. A., 2011, "Surface Roughness Effects on Energy Dissipation in Fretting Contact of Nominally Flat Surfaces," J. Appl. Mech., **78**(2), pp. 021011-8.
[86] Berthoud P., and Baumberger T., 1998, "Shear stiffness of a solid–solid multicontact interface," Proceedings of the Royal Society of London. Series A: Mathematical, Physical and Engineering Sciences, **454**(1974), pp. 1615 -1634.
[87] Blau P. J., 2009, Friction Science and Technology: from Concepts to Applications, CRC Press.
[88] Brizmer V., Kligerman Y., and Etsion I., 2006, "Elastic–plastic spherical contact under combined normal and tangential loading in full stick," Tribology Letters, **25**, pp. 61-70.
[89] Zhou Z. R., Nakazawa K., Zhu M. H., Maruyama N., Kapsa P., and Vincent L., 2006, "Progress in fretting maps," Tribology International, **39**(10), pp. 1068-1073.
[90] Waterhouse R. B., 1972, Fretting Corrosion (Materials Science & Technology Monographs), Pergamon Press.
[91] Wagle S., and Kato H., 2010, "Size Estimation of Fatigue Crack Appearing at Bolt Joints of Aluminum Alloy Plates by Synchronized SAW Measurement," Experimental Mechanics, **51**, pp. 869-878.
[92] Ryu J.-J., Dayal V., and Shrotriya P., 2007, "Onset of Surface Damage in Modular Orthopedic Implants: Influence of Normal Contact Loading and Stress-assisted Dissolution," Experimental Mechanics, **47**, pp. 395-403.
[93] Attia M. H., 1992, Standardization of fretting fatigue test methods and equipment, ASTM International.
[94] Ramalho A., and Celis J. P., 2003, "Fretting Laboratory Tests: Analysis of the Mechanical Response of Test Rigs," Tribology Letters, **14**(3), pp. 187-196.
[95] Segalman D. J., Gregory D. L., Starr M. J., Resor B. R., Jew M. D., and Lauffer J. P., 2009, Handbook on dynamics of jointed structures, Sandia National Laboratories, Albuquerque.
[96] National Research Council, NMAB, 1977, Control of Fretting Fatigue, National Academy of Science, Washington, DC.

[97] Bograd S., Schmidt A., and Gaul L., 2009, "Joint damping prediction by thin layer elements," Conference Proceedings IMAC XXVI: A Conference & Exposition on Structural Dynamics—Technologies for Civil Structures, Orlando, FL, USA.
[98] Segalman D. J., Bergman L. A., and Ewins D. J., International workshop on joint mechanics, Sandia National Laboratories, Arlington.
[99] Garcia-Prieto I., Faulkner M. D., and Alcock J. R., 2004, "The influence of specimen misalignment on wear in conforming pin on disk tests," Wear, **257**(1-2), pp. 157-166.
[100] Ungar E. E., 1964, Energy Dissipation at Structural Joints; Mechanisms and Magnitudes.
[101] Rogers P. F., and Boothroyd G., 1975, "Damping at Metallic Interfaces Subjected to Oscillating Tangential Loads," J. Eng. for Industry, **97**(3), pp. 1087-1093.
[102] Padmanabhan K. K., and Murty A. S. R., 1991, "Damping in structural joints subjected to tangential loads," ARCHIVE: Proceedings of the Institution of Mechanical Engineers, Part C: Journal of Mechanical Engineering Science 1989-1996 (vols 203-210), **205**, pp. 121-129.
[103] Ren Y., and Beards C. F., 1994, "An experimental study on the dynamic response of a beam structure containing a pseudo joint," ARCHIVE: Proceedings of the Institution of Mechanical Engineers, Part C: Journal of Mechanical Engineering Science 1989-1996 (vols 203-210), **208**, pp. 321-328.
[104] Gaul L., 1985, "Analytical and experimental study of the dynamics of structures with joints and attached substructures," Proceedings of the ASME Biennial Conference on Vibration and Noise, Cincinnati, OH.
[105] Gaul L., and Lenz J., 1997, "Nonlinear dynamics of structures assembled by bolted joints," Acta Mechanica, **125**, pp. 169-181.
[106] Varenberg M., Halperin G., and Etsion I., 2002, "Different aspects of the role of wear debris in fretting wear," Wear, **252**(11-12), pp. 902-910.
[107] Ovcharenko A., Halperin G., Etsion I., and Varenberg M., 2006, "A novel test rig for in situ and real time optical measurement of the contact area evolution during pre-sliding of a spherical contact," Tribology Letters, **23**, pp. 55-63.
[108] Kartal M. E., Mulvihill D. M., Nowell D., and Hills D. A., 2010, "Determination of the Frictional Properties of Titanium and Nickel Alloys Using the Digital Image Correlation Method," Experimental Mechanics, **51**, pp. 359-371.
[109] Hoeppner D. W., Chandrasekaran V., and Elliott C. B., 2000, Fretting fatigue: current technology and practices, ASTM International.
[110] Ramesh R., and Gnanamoorthy R., 2006, "Development of a fretting wear test rig and preliminary studies for understanding the fretting wear properties of steels," Materials & Design, **27**(2), pp. 141-146.
[111] Gaspar M. C., and Ramalho A., 2002, "Fretting behaviour of galvanised steel," Wear, **252**(3-4), pp. 199-209.
[112] Mohrbacher H., Celis J.-P., and Roos J. R., 1995, "Laboratory testing of displacement and load induced fretting," Tribology International, **28**(5), pp. 269-278.
[113] Bickford J., 2009, An Introduction to the Design and Behavior of Bolted, CRC Press.
[114] Goodman L. E., and Brown C. B., 1962, "Energy Dissipation in Contact Friction: Constant Normal and Cyclic Tangential Loading," J. Appl. Mech., **29**(1), pp. 17-22.
[115] Smallwood D., Gregory D. L., and Coleman R. G., 2001, "A three parameter constitutive model for a joint which exhibits a power law relationship between energy loss and relative displacement," Proceedings of the 72nd Shock and Vibration Symposium, San Destin, FL.
[116] Hartwigsen C. J., Song Y., McFarland D. M., Bergman L. A., and Vakakis A. F., 2004, "Experimental study of non-linear effects in a typical shear lap joint configuration," Journal of Sound and Vibration, **277**(1-2), pp. 327-351.
[117] Ovcharenko A., and Etsion I., 2009, "Junction Growth and Energy Dissipation at the Very Early Stage of Elastic-Plastic Spherical Contact Fretting," J. Tribol., **131**(3), pp. 031602-8.
[118] Thomas T. R., 1999, Rough surfaces, Imperial College Press.

[119] Smith G. T., 2002, Industrial metrology: surfaces and roundness, Springer.
[120] Jindal U. C., 2010, Machine Design, Pearson Education India.
[121] Fuller K. N. G., and Tabor D., 1975, "The Effect of Surface Roughness on the Adhesion of Elastic Solids," Proceedings of the Royal Society A: Mathematical, Physical and Engineering Sciences, **345**, pp. 327-342.
[122] Pashley M. D., Pethica J. B., and Tabor D., 1984, "Adhesion and micromechanical properties of metal surfaces," Wear, **100**(1-3), pp. 7-31.
[123] Bryggman U., and Soderberg S., 1986, "Contact conditions in fretting," Wear, **110**, pp. 1-17.
[124] Ciavarella M., Greenwood J., and Paggi M., 2008, "Inclusion of 'interaction' in the Greenwood and Williamson contact theory," Wear, **265**, pp. 729-734.
[125] Yeo C.-D., Katta R. R., Lee J., and Polycarpou A. A., 2010, "Effect of asperity interactions on rough surface elastic contact behavior: Hard film on soft substrate," Tribology International, **43**(8), pp. 1438-1448.
[126] Dulias U., Fang L., and Zum Gahr K.-H., 2002, "Effect of surface roughness of self-mated alumina on friction and wear in isooctane-lubricated reciprocating sliding contact," Wear, **252**(3-4), pp. 351-358.
[127] Proudhon H., Fouvry S., and Buffière J.-Y., 2005, "A fretting crack initiation prediction taking into account the surface roughness and the crack nucleation process volume," International Journal of Fatigue, **27**(5), pp. 569-579.
[128] Raeymaekers B., and Talke F. E., 2010, "The effect of laser polishing on fretting wear between a hemisphere and a flat plate," Wear, **269**(5-6), pp. 416-423.
[129] Billi F., Sangiorgio S. N., Aust S., and Ebramzadeh E., 2010, "Material and surface factors influencing backside fretting wear in total knee replacement tibial components," Journal of Biomechanics, **43**(7), pp. 1310-1315.
[130] Kubiak K. J., Mathia T. G., and Fouvry S., 2010, "Interface roughness effect on friction map under fretting contact conditions," Tribology International, **43**(8), pp. 1500-1507.
[131] Kubiak K. J., and Mathia T. G., 2009, "Influence of roughness on contact interface in fretting under dry and boundary lubricated sliding regimes," Wear, **267**(1-4), pp. 315-321.
[132] Zhou Z. R., and Vincent L., 1999, "Lubrication in fretting - A review," Wear, **225-229**(PART II), pp. 962-967.
[133] Gaul L., and Nitsche R., 2001, "The Role of Friction in Mechanical Joints," Appl. Mech. Rev., **54**(2), pp. 93-106.
[134] Owens J. F. P., and Lee-Sullivan P., 2000, "Stiffness behaviour due to fracture in adhesively bonded composite-to-aluminum joints: II. Experimental," International Journal of Adhesion and Adhesives, **20**(1), pp. 47-58.
[135] Owens J. F. P., and Lee-Sullivan P., 2000, "Stiffness behaviour due to fracture in adhesively bonded composite-to-aluminum joints: I. Theoretical model," International Journal of Adhesion and Adhesives, **20**(1), pp. 39-45.
[136] Chakherlou T. N., Mirzajanzadeh M., and Vogwell J., 2009, "Effect of hole lubrication on the fretting fatigue life of double shear lap joints: An experimental and numerical study," Engineering Failure Analysis, **16**(7), pp. 2388-2399.
[137] Eriten M., Polycarpou A. A., and Bergman L. A., 2011, "Development of a Lap Joint Fretting Apparatus," Exp Mech.
[138] Davis J. R., and Committee A. I. H., 1994, Stainless steels, ASM International.
[139] Mang T., and Dresel W., 2007, Lubricants and Lubrication, Wiley-VCH.
[140] Suh A. Y., Patel J. J., Polycarpou A. A., and Conry T. F., 2006, "Scuffing of cast iron and Al390-T6 materials used in compressor applications," Wear, **260**(7-8), pp. 735-744.
[141] Costello M. T., 2005, "Effects of basestock and additive chemistry on traction testing," Tribology Letters, **18**(1), pp. 91-97.
[142] Ibrahim R. A., and Pettit C. L., 2005, "Uncertainties and dynamic problems of bolted joints and other fasteners," Journal of Sound and Vibration, **279**(3-5), pp. 857-936.

[143] Andersson Söderberg A., and Björklund S., 2007, "Friction models for sliding dry, boundary and mixed lubricated contacts," Tribology International, **40**(4), pp. 580-587.
[144] Song Y., Hartwigsen C. J., McFarland D. M., Vakakis A. F., and Bergman L. A., 2004, "Simulation of dynamics of beam structures with bolted joints using adjusted Iwan beam elements," Journal of Sound and Vibration, **273**(1-2), pp. 249-276.
[145] Ulf O., 1995, "Cyclic micro-slip under unlubricated conditions," Tribology International, **28**(4), pp. 207-217.
[146] Filippi S., Akay A., and Gola M. M., 2004, "Measurement of Tangential Contact Hysteresis During Microslip," J. Tribol., **126**(3), pp. 482-489.
[147] Shi X., and Polycarpou A. A., 2006, "Adhesive effects on dynamic friction for unlubricated rough planar surfaces," Journal of Tribology, **128**(4), pp. 841-850.
[148] Shi X., and Polycarpou A. A., 2008, "Investigation of Contact Stiffness and Contact Damping for Magnetic Storage Head-Disk Interfaces," J. Tribol., **130**(2), pp. 021901-9.
[149] Eriten M., Polycarpou A. A., and Bergman L. A., 2011, "Surface Roughness Effects on Energy Dissipation in Fretting Contact of Nominally Flat Surfaces," Journal of Applied Mechanics, **78**, p. 021011.
[150] Stoimenov B. L., Maruyama S., Adachi K., and Kato K., 2007, "The roughness effect on the frequency of frictional sound," Tribology International, **40**(4), pp. 659-664.
[151] Guran A., Pfeiffer F., and Popp K., 2001, Dynamics with friction: modeling, analysis and experiment, World Scientific.
[152] Bower A. F., 2009, Applied mechanics of solids, CRC Press.

Appendix A

Cyclic tangential loading responses are quantified by the following equations:

CFC:

$$\delta^* = 0.284\omega^*\left[-1-\left(1-\frac{3.52Q_m^*}{\omega^{*3/2}}\right)^{2/3}+2\left(1+\frac{1.76\left(Q^*-Q_m^*\right)}{\omega^{*3/2}}\right)^{2/3}\right] \tag{A.1}$$

CEB:

$$\omega^* \le 0.95 \Rightarrow$$

$$\delta^* = \left(0.112\omega^*-0.047\sqrt{-4.5\omega^{*2}+72\omega^*}\right)\left[1+\left(1+\frac{Q_m^*}{0.112\omega^{*3/2}-0.047\omega^*\sqrt{72-4.5\omega^*}}\right)^{2/3}-2\left(1+\frac{0.5\left(Q_m^*-Q^*\right)}{0.112\omega^{*3/2}-0.047\omega^*\sqrt{72-4.5\omega^*}}\right)^{2/3}\right] \tag{A.2}$$

$$\omega^* > 0.95 \Rightarrow$$

$$\delta^* = 1.245\sqrt{\omega^*-\omega^{*2}}\left[-1-\left(1-\frac{0.803Q_m^*}{\omega^*\sqrt{1-\omega^*}}\right)^{2/3}+2\left(1-\frac{0.402\left(Q_m^*-Q^*\right)}{\omega^*\sqrt{1-\omega^*}}\right)^{2/3}\right] \tag{A.3}$$

KE:

$$\delta^* = \sqrt{\omega^*}\left(0.536-0.0186\omega^*\right)\left[-1-\left(1-\frac{1.87Q_m^*}{\omega^*\left(1-0.035\omega^*\right)}\right)^{2/3}+2\left(1-\frac{0.94\left(Q_m^*-Q^*\right)}{\omega^*\left(1-0.035\omega^*\right)}\right)^{2/3}\right] \tag{A.4}$$

BKE:

$$\delta^* = 0.267\omega^*\coth\left(0.306\omega^{*0.46}\right)\left[-1-\left(1-\frac{3.75Q_m^*\tanh\left(0.306\omega^{*0.46}\right)}{\omega^{*3/2}}\right)^{2/3}+2\left(1-\frac{1.88\left(Q_m^*-Q^*\right)\tanh\left(0.306\omega^{*0.46}\right)}{\omega^{*3/2}}\right)^{2/3}\right] \tag{A.5}$$

Energy dissipation per fretting cycle responses are given as follows:

CFC:

$$\Delta W^* = \omega^{*5/2}\left[\left(1-\left(1-\frac{3.52Q_m^*}{\omega^{*3/2}}\right)^{5/3}\right)-2.935Q_m^*\omega^*\left(1+\left(1-\frac{3.52Q_m^*}{\omega^{*3/2}}\right)^{2/3}\right)\right] \quad \text{(A.6)}$$

CEB:

$\omega^* \le 0.95 \Rightarrow$

$$\Delta W^* = 0.9\omega^{*5/2}\left(0.112-0.047\sqrt{\frac{72}{\omega^*}-4.5}\right)^2\left[1-\left(1+\frac{Q_m^*}{\left(0.112-0.047\sqrt{\frac{72}{\omega^*}-4.5}\right)\omega^{*3/2}}\right)^{5/3}-\right.$$

$$\left.\frac{5Q_m^*}{6\left(-0.112+0.0467\sqrt{\frac{72}{\omega^*}-4.5}\right)\omega^{*3/2}}\left(1+\left(1+\frac{Q_m^*}{\left(0.112-0.0467\sqrt{\frac{72}{\omega^*}-4.5}\right)\omega^{*3/2}}\right)^{2/3}\right)\right] \quad \text{(A.7)}$$

$\omega^* > 0.95 \Rightarrow$

$$\Delta W^* = 1.4\left(-1+\frac{1}{\omega^*}\right)\omega^{*5/2}\left[1-\left(1-\frac{0.803Q_m^*}{\omega^*\sqrt{1-\omega^*}}\right)^{5/3}-\frac{0.67Q_m^*}{\omega^*\sqrt{1-\omega^*}}\left(1+\left(1-\frac{0.803Q_m^*}{\omega^*\sqrt{1-\omega^*}}\right)^{2/3}\right)\right] \quad \text{(A.8)}$$

KE:

$$\Delta W^* = 0.9\left(0.536-0.019\omega^*\right)^2\omega^{*3/2}\left[1-\left(1-2\frac{Q_m^*}{\omega^*-0.035\omega^{*2}}\right)^{5/3}-\right.$$

$$\left.\frac{10Q_m^*\left(1+\left(1-2\frac{Q_m^*}{\omega^*-0.035\omega^{*2}}\right)^{2/3}\right)}{6\left(\omega^*-0.035\omega^{*2}\right)}\right] \quad \text{(A.9)}$$

BKE:

$$\Delta W^* = 0.064\omega^{*5/2}\left(\coth\left(0.306\omega^{*0.46}\right)\right)^2\left[1-\left(1-\frac{3.748Q_m^*\tanh\left(0.306\omega^{*0.46}\right)}{\omega^{*3/2}}\right)^{5/3}-\right.$$
$$\left.\frac{3.123Q_m^*\tanh\left(0.306\omega^{*0.46}\right)}{\omega^{*3/2}}\left(1+\left(1-\frac{3.748Q_m^*\tanh\left(0.306\omega^{*0.46}\right)}{\omega^{*3/2}}\right)^{2/3}\right)\right] \quad \text{(A.10)}$$

Appendix B

Details of the sphere-on-flat contact formulation:

B.1. Normal Contact of Single (Spherical) Asperities

Hertz:
$$P_H\left(\omega;P_c,\omega_c\right)=P_c\left(\omega/\omega_c\right)^{1.5} \tag{B.1}$$

CEB:
$$P_{CEB}\left(\omega;P_c,\omega_c\right)=P_c\begin{cases}\left(\omega/\omega_c\right)^{1.5} & \omega/\omega_c\le 1\\ 3\left(\omega/\omega_c-0.5\right) & \omega/\omega_c>1\end{cases} \tag{B.2}$$

KE:
$$P_{KE}\left(\omega;P_c,\omega_c,\nu\right)=P_c\begin{cases}\left(\omega/\omega_c\right)^{1.5} & \omega/\omega_c\le 1\\ 1.03\left(\omega/\omega_c\right)^{1.425} & 1<\omega/\omega_c\le 6\\ 1.4\left(\omega/\omega_c\right)^{1.263} & 6<\omega/\omega_c\le 110\\ 3/K\omega/\omega_c & 110<\omega/\omega_c\end{cases} \tag{B.3}$$

BKE:
$$P_{BKE}\left(\omega;P_c,\omega_c,\nu\right)=\frac{\bar{l}_c P_c}{\bar{\delta}_c^{1.5}}\begin{cases}\left(\omega/\omega_c\right)^{1.5} & \omega/\omega_c\le\bar{\delta}_c\\ \left(\omega/\omega_c\right)^{1.5}\left(1-\exp\left(\bar{\delta}_c^{\alpha}/\left(\bar{\delta}_c^{\alpha}-\left(\omega/\omega_c\right)^{\alpha}\right)\right)\right) & \omega/\omega_c>\bar{\delta}_c\end{cases} \tag{B.4}$$

and contact radius-penetration relationships

Hertz:
$$a_H\left(\omega;a_c,\omega_c\right)=a_c\left(\omega/\omega_c\right)^{0.5} \tag{B.5}$$

CEB:
$$a_{CEB}\left(\omega;a_c,\omega_c\right)=a_c\begin{cases}\left(\omega/\omega_c\right)^{0.5} & \omega/\omega_c\le 1\\ \left(2\omega/\omega_c-1\right)^{0.5} & \omega/\omega_c>1\end{cases} \tag{B.6}$$

KE:
$$a_{KE}\left(\omega;a_c,\omega_c\right)=a_c\begin{cases}\left(\omega/\omega_c\right)^{0.5} & \omega/\omega_c\le 1\\ 0.96\left(\omega/\omega_c\right)^{0.57} & 1<\omega/\omega_c\le 6\\ 0.97\left(\omega/\omega_c\right)^{0.57} & 6<\omega/\omega_c\le 110\\ 1.41\left(\omega/\omega_c\right)^{0.5} & 110<\omega/\omega_c\end{cases} \tag{B.7}$$

BKE:
$$a_{BKE}\left(\omega;a_c,\omega_c,\nu\right)=\frac{a_c}{\bar{\delta}_c^{0.5}}\begin{cases}\left(\omega/\omega_c\right)^{0.5} & \omega/\omega_c\le\bar{\delta}_c\\ \left(\omega/\omega_c\right)^{0.5}\left(1+\exp\left(\bar{\delta}_c^{\gamma}/\left(\bar{\delta}_c^{\gamma}-\left(\omega/\omega_c\right)^{\gamma}\right)\right)\right)^{0.5} & \omega/\omega_c>\bar{\delta}_c\end{cases} \tag{B.8}$$

where the critical interference, ω_c, contact radius, a_c, and normal load, P_c, are defined at the inception of plastic deformation as functions of Poisson's ratio, ν; hardness factor, $K = 0.454 + 0.41\nu$; hardness of the softer material in contact, H; combined Young's modulus, $E^* = \left((1-\nu_1^2)/E_1 + (1-\nu_2^2)/E_2\right)^{-1}$; and combined radius of curvature, $R = \left(1/R_1 + 1/R_2\right)^{-1}$ as

$$\begin{aligned} \omega_c &= \left(\frac{\pi KH}{2E^*}\right)^2 R \\ a_c &= \sqrt{\omega_c R} = \frac{\pi KHR}{2E^*} \\ P_c &= \frac{2}{3} KH\pi a_c^2 = \frac{2}{3} KH\pi\omega_c R \end{aligned} \tag{B.9}$$

Note that $\bar{l}_c = 8.88\nu - 10.13\left(\nu^2 + 0.089\right)$, $\bar{\delta}_c = 6.82\nu - 7.83\left(\nu^2 + 0.0586\right)$, $\alpha = 0.174 + 0.08\nu$ and $\gamma = 0.25 + 0.125\nu$.

B.2. Tangential Contact of Single (Spherical) Asperities

Friction coefficient models:

CFC:
$$\mu_{CFC}(s,H) = \frac{Q_{\max}}{P_{\max}} = \frac{\tau_{Av}A_r}{HA_r} = \frac{\tau_{Av}}{H} \approx \frac{s}{H} \tag{B.10}$$

CEB:
$$\mu_{CEB}(\omega;\omega_c,\nu,\zeta) = \min\left(\frac{0.2045}{K|c_1|}\left(\frac{\omega_c}{\omega} - 1\right)^{1/2}, \frac{-c_4 + \sqrt{c_4^2 - 4c_3c_5}}{2c_3}\right) \tag{B.11}$$

KE:
$$\mu_{KE}(\omega;\omega_c) = \begin{cases} 0.536\left(\omega/\omega_c\right)^{-0.5} - 0.0186\left(\omega/\omega_c\right)^{0.5} & \omega/\omega_c \le 1 \\ -0.007\left(\omega/\omega_c\right)^3 + 0.085\left(\omega/\omega_c\right)^2 - 0.389\left(\omega/\omega_c\right) + 0.822 & 1 \le \omega/\omega_c \le 6.2 \end{cases} \tag{B.12}$$

BKE:
$$\mu_{BKE}(\omega;\omega_c,\nu) = 0.26\coth\left(0.27\left(\bar{\delta}_c^{-1}\omega/\omega_c\right)^{0.46}\right) \tag{B.13}$$

where $c_1 = -1 + \frac{3}{2}\zeta\tan^{-1}(1/\zeta) - \frac{\zeta^2}{2(1+\zeta^2)}$, $c_3 = \frac{9\pi^2}{16}\left(2 - \frac{\nu}{2} + \frac{7}{8}\nu^2\right)$, $c_4 = \frac{9\pi}{4}(1-2\nu)(1-\nu/2)$ and $c_5 = \frac{3}{2}(1-2\nu)^2 - \frac{0.56\omega_c}{K^2\omega}$. Note that ζ is the normal direction location of the plastic yield normalized by the contact radius and is found to be approximately 0.48 with a Poisson's ratio of 0.3.

The tangential response of contacting spheres with nondimensional force $\tilde{Q} = Q/(\mu P)$ and nondimensional displacement $\tilde{\delta} = 16G^* a\delta/(3\mu P)$ is given by:

Full Stick: $$\tilde{\delta} = \frac{2}{3}\tilde{Q} \tag{B.14}$$

Partial Slip (increasing Q): $$\tilde{\delta} = 1-\left(1-\tilde{Q}\right)^{2/3} \tag{B.15}$$

Partial Slip (unloading Q): $$\tilde{\delta} = 2\left(1-\left(\tilde{Q}_{\max}-\tilde{Q}\right)/2\right)^{2/3} - \left(1-\tilde{Q}_{\max}\right)^{2/3} - 1 \tag{B.16}$$

Partial Slip (reloading Q): $$\tilde{\delta} = -2\left(1-\left(\tilde{Q}_{\max}+\tilde{Q}\right)/2\right)^{2/3} + \left(1-\tilde{Q}_{\max}\right)^{2/3} + 1 \tag{B.17}$$

where $G^* = \left(\left(2-\nu_1\right)/G_1 + \left(2-\nu_2\right)/G_2\right)^{-1}$ is the combined shear modulus.

The energy dissipation per fretting cycle, ΔW_i for an individual asperity can be computed by the difference of energy required to reload the contact and the energy released while unloading; i.e., the area inside the fretting loop

$$\Delta W = \int_{-\delta_{\max}}^{\delta_{\max}} \left(Q_{RL} - Q_{UL}\right) d\delta \tag{B.18}$$

The nondimensional energy dissipation $\Delta\tilde{W} = \frac{10G^* a}{9(\mu P)^2}\Delta W$ is given as

$$\Delta\tilde{W} = 1-\left(1-\tilde{Q}_{\max}\right)^{5/3} - \frac{5\tilde{Q}_{\max}}{6}\left(1+\left(1-\tilde{Q}_{\max}\right)^{2/3}\right) \tag{B.19}$$

Assuming small tangential loading $\varepsilon << 1$, this expression can be expanded using binomial series giving, after some manipulation

$$\Delta\tilde{W} = \frac{5\tilde{Q}_{\max}^3}{162}\left(1+\frac{2\tilde{Q}_{\max}}{3}\right) + O\left(\tilde{Q}_{\max}^5\right) \tag{B.20}$$